ALPHA(V)BETA(3)-TARGETED NANOPROBES FOR IN VIVO IMAGING OF TUMOR ANGIOGENESIS

APPROVED BY SUPERVISORY COMMITTEE

Jinming Gao, Ph.D.

David A. Boothman, Ph.D.

Kathlynn Brown, Ph.D.

Jerry Shay, Ph.D.

DEDICATION

To my wife Jessica, my mother Rochelle and my father William.

ALPHA(V)BETA(3)-TARGETED NANOPROBES FOR IN VIVO IMAGING OF TUMOR ANGIOGENESIS

by

CHASE WILLIAM KESSINGER

DISSERTATION

Presented to the Faculty of the Graduate School of Biomedical Sciences

The University of Texas Southwestern Medical Center at Dallas

In Partial Fulfillment of the Requirements

For the Degree of

DOCTOR OF PHILOSOPHY

The University of Texas Southwestern Medical Center at Dallas

Dallas, Texas

August, 2010

ACKNOWLEDGEMENTS

The work presented in this dissertation would not have been possible without the support and guidance I received from many people. First, I would like to thank my graduate advisor, Dr. Jinming Gao, who shared with me his knowledge and taught me skills I needed to become a successful researcher, and for always expecting the best. He helped me develop as a bioengineer and a scientist in the exciting interdisciplinary research field of nanomedicine and cancer biology, and for that I am eternally grateful.

I would also like to acknowledge my committee members, Dr. David A. Boothman, Dr. Kathlynn C. Brown, and Dr. Jerry Shay, who not only took the time to serve on this committee but also provided advice and guidance throughout this process. I would also like to thank my undergraduate mentors, Drs. Rita Moyes and Cherie Oubre, who sparked my interest in research and guided my first project as an undergraduate researcher.

I would also like to thank all former and present lab members from the Boothman, Brown and Gao labs for their input and support throughout the years. Specifically, Dr. Chalermchai Khemtong for his friendship and advice regarding the project; Dr. Erik A. Bey for his friendship and expertise in animal models; Drs. Masaya Takahashi and Osamu Togao for their friendship, help in imaging on the 7T MRI scanner and their critical input regarding all imaging experiments; Drs. Vikram Kodibagkar, Jinmin Ren, Angelo Lubag and for their help on the 4.7 MRI scanner; and Mark Thompson and Kelly Tsai for their unwavering administrative assistance in ordering supplies and today-to-today maintenance of vital core equipment. Without any one of these people this work would not have been possible.

Without my family I would not be where I am today, they have always supported and encouraged me to continue with my research. And for that, I am extremely grateful to my parents, who inspired and motivated me throughout my life to achieve my goals, as well as buying me my first microscope that Thomas and I would use to look at protozoa from the pond in the summer. Thank you. To my younger brother Thomas for always joking with me about science and encouraging me to complete this endeavor, and to my ever growing family, Paul, Sherie, Allen, David, Peter, Reeder, and Laura thank you for your support.

Finally, I would like to thank my wife, Jessica, who was my inspiration, moral support and friend throughout my high school, college and graduate years and has always kept me focused and working towards the completion of this dissertation. Without her loving support, understanding, patience and friendship, I could not have completed this work.

ALPHA(V)BETA(3)-TARGETED NANOPROBES FOR IN VIVO IMAGING OF TUMOR ANGIOGENESIS

CHASE WILLIAM KESSINGER

The University of Texas Southwestern Medical Center at Dallas, 2010

JINMING GAO, Ph.D.

Lung cancer is the leading cause of cancer-related deaths in the US and abroad (WHO, 2010). Early detection of the disease has increased patients' five-year survival rates from 4% to over 50% (NCI SEER, 2010). Angiogenesis plays a critical role in the carcinogenesis and cancer metastasis of solid tumors. Integrin αvβ3 is a well-established overexpressed biomarker of angiogenesis and has recently been exploited in the clinical stratification of different types of cancer. Although magnetic resonance imaging (MRI) is not a first-line clinical imaging modality for the detection and diagnosis of lung cancer, recent advances in theranostic polymeric nanoplatforms and the development of ultrasensitive contrast agents, such as superparamagnetic iron oxide (SPIO) nanoparticles, has greatly broadened the application of MRI in cancer detection and

molecular imaging. The objective of this work is to develop superparamagnetic polymeric micelle (SPPM) nanoprobes that can noninvasively image tumor angiogenesis in vivo using conventional T2/T2*-weighted and off-resonance saturation (ORS) MRI methods. Therefore, we hypothesized that the inclusion of an αvβ3-specific ligand, cRGD (cyclic Arg-Gly-Asp) peptide and encapsulation of a cluster of SPIO in the SPPM nanoprobe formulation would allow the specific imaging of tumor angiogenesis.

SPPM nanoprobes are small (50-70 nm), and contain a cluster of SPIO in the core while maintaining the micelle core-shell architecture. In vitro examination of αvβ3-targeted cRGD-SPPM demonstrate an increase cellular uptake in αvβ3 overexpressing cells over control SPPM formulations. Upon translation to in vivo subcutaneous lung tumor models in mice, cRGD-SPPM is able to noninvasively image and quantitate tumor angiogenesis and demonstrate in vivo colocalization with αvβ3 integrin. In parallel with SPPM characterization, the ORS imaging method was validated in vitro and was successfully applied in vivo for imaging tumor angiogenesis and demonstrated an increased sensitivity and specificity for SPPM over conventional T2*-weighted MR imaging. Application of high temporal resolution (HTR) - MRI, combined with the ultrasensitivity of the SPPM nanoprobe, allows for the kinetic analysis of cRGD-SPPM targeting to angiogenic regions in vivo. Finally, SPPM shows the ability to detect small lung cancer nodules (<700 μm - 3 mm) in tail-vein induced orthotopic lung cancer models using convention T2-weighted and ORS MRI. The results presented herein, provide the characterization and proof-of-principle experiments that point towards the diagnostic potential of SPPM nanoprobes for the early detection of lung cancer.

TABLE OF CONTENTS

PRIOR PUBLICATIONS

Kessinger, C.W.; Khemtong, C.; Togao, O.; Takahashi, M.; Sumer, B.D.; Gao, J. "In Vivo Angiogenesis Imaging of Solid Tumors by $\alpha_v\beta_3$-Targeted, Dual-Modality Micellar Nanoprobes". *Exp. Biol. Med.* 2010, 235, 957-65.

Cohen E.M.; Ding, H.; Kessinger, C.W.; Gao, J.; Sumer, B.D. "Polymeric micelle nanoparticles for photodynamic treatment of head and neck cancer cells". *Otolaryngol. Head Neck Surg.* 2010, 143(1), 109-15.

Blanco, E.; Bey, E.A.; Khemtong, C.; Yang, S-G.; Setti Guthi, J.; Chen, H.; Kessinger, C.W.; Carnevale, K.A..; Bornmann, W.G.; Boothman, D.A.; Gao, J. "β-Lapachone Micellar Nanotherapeutics for Non–Small Cell Lung Cancer Therapy". *Cancer Res.* 2010, 70(10), 3896-904.

Setti Guthi, J.; Yang, S-G.; Huang, G.; Li, S.; Khemtong, C.; Kessinger, C.W.; Peyton, M.; Minna, J.D.; Brown, K.C., Gao, J. "MRI-Visible Micellar Nanomedicine for Targeted Drug Delivery to Lung Cancer Cells". *Mol. Pharm.* 2010, 7(1), 32-40.

Khemtong, C.; Kessinger, C.W.; Gao, J. "Nanocomposite Particles for Cancer MR Imaging and Drug Delivery". *Chem. Comm.* 2009, 24, 3497-3510.

*Khemtong, C.; *Kessinger, C.W.; Ren, J.; Bey, E.A.; Yang, S.; Setti Guthi, J.; Boothman, D.A.; Sherry, A.D.; Gao, J. "*In Vivo* Off Resonance Saturation Magnetic Resonance Imaging of αvβ3-Targeted Superparamagnetic Nanoparticles". *Cancer Res.* 2009, 69, 1651-58.

*Contributed equally

Blanco, E.; Kessinger, C.W.; Sumer, B.D.; Gao, J.; "Multifunctional micellar nanomedicine for cancer therapy". *Exp. Biol. Med. (Maywood)* 2009, 234(4), 123-31.

Mukherjee, B.; Kessinger, C.W.; Kobayashi, J.; Chen, B.P.; Chen. D.J.; Chatterjee, A.; Burma, S. "DNA-PK phosphorylates histone H2AX during apoptotic DNA fragmentation in mammalian cells". DNA Repair 2006, 5(5), 575-90.

LIST OF FIGURES

LIST OF TABLES

LIST OF APPENDICES

LIST OF DEFINITIONS

7T -7 Tesla

BLI - bioluminescence imaging

CCD - charge-coupled device

CEST - chemical exchange saturation transfer

CEU - contrast-enhanced ultrasound

CNR - contrast-to-noise ratio

cRGD - cyclic(Arg-Gly-Asp-D-Phe-Lys) or cRGDfK

CT - computed tomography

CXR - chest x-ray

DAPI - 4',6-diamidino-2-phenylindole

DCE-MRI - dynamic contrast enhanced - magnetic resonance imaging

DOTA - 1,4,7,10- tetraazacyclododecane-N,N',N'',N'''-tetraacetic acid

DS - dummy scan

DSPE-PEG - 1,2-distearoyl-sn-glycero-3-phosphoethanolamine-N-[amino(polyethylene glycol)

ECM - extracellular matrix

ETL - echo train length

Fe(III) - iron 3^{+}

FDG - ^{18}F-fluorodeoxyglucose

FID - free induction decay

FOV - field-of-view

FSPPM - fluorescent superparamagnetic polymeric micelle

Gd(III) - gadolinium 3^+

Gd-DPTA - Gd(III)-diethylenetriamine pentaacetic acid

H & E - hematoxylin and eosin

Hb - deoxy-hemoglobin

HbO_2 - oxy-hemoglobin

HEPES - 4-(2-hydroxyethyl)-1-piperazineethanesulfonic acid

HPLC - high performance liquid chromatography

HTR - high temporal resolution

k_a - accumulation rate - $k_{accumulation}$

LDCT - low dose helical computed tomography

Mal - maleimide

MeO - methoxy

MRI - magnetic resonance imaging

msMRI - magnetic susceptibility magnetic resonance imaging

MT - magnetic transfer

MVD - microvascular density

NEX - number of excitation or NA - number of averages

NIR - near infared

NIRF - near infared fluorescence

NLST - national lung screening trial

NMR - nuclear magnetic resonance

NMV - net magnetic vector

NSCLC - non-small cell lung cancer

OCT - optimal cutting temperature

ORS - off-resonance saturation

PBS - phosphate buffered saline

PD-w - proton density - weighted

PEG - poly(ethylene glycol)

PET - positron emission tomography

PLA - poly(lactic acid)

PTA - phosphotungstic acid

QD - quantum dot

RF - radiofrequency

RES - reticuloendothelial system

ROI - region-of-interest

SNR - signal-to-noise ratio

SPECT - single photon emission computed tomography

SPIO - superparamagnetic iron oxide

SPPM - superparamagnetic polymeric micelle

T1-w - T1-weighted

T2-w - T2-weighted

T2*-w - T2*-weighted

TE - echo time

TEM - transmission electron microscopy

THF - tetrahydrofuran

TMR - tetramethylrhodamine

TR - repetition time

US - ultrasound imaging

WGA - wheat germ agglutinin

CHAPTER ONE
Introduction

1.1 A History and Significance of Lung Cancer

Cancer is a leading cause of death worldwide and in 2004 accounted for 7.4 million deaths, roughly 13% of all deaths worldwide. By 2030, it is estimated that cancer will attribute to 12 million deaths worldwide.[1] In the United States, over 1.5 million new cases of cancer will be diagnosed with over 560,000 cancer-related deaths in 2009. Of the new cases, male prostate and female breast cancer will account for 25% and 27% of all new cases, respectively.[2] However, lung cancer is the leading cause of all cancer-related deaths in men and women (Figure 1.1). Highlighting the severity of the disease, the one and two year survival rates have remained constant with 65% succumbing to the disease after one year and 73% after two.[3] Lung cancer is classified into two different types. Small cell lung cancer consists of 20% of presented lung cancer cases and arises from tissues such as the bronchi. Non-small cell lung cancer (NSCLC) accounts for the remaining and is subdivided into three groups including squamous cell lung carcinoma, adenocarcinoma and large cell lung carcinoma.[4]

1.2 Clinical Detection of Lung Cancer

Although the incidence rate of lung cancer have started to decline recently, five-year survival rates for local, regional, and distant disease have remained constant at 52.9%, 24.0%, and 3.5%, respectively.[3] At diagnosis, most lung cancers are at an advanced state (56%), i.e. regional or distant (metastatic) stage.[3] In light of the disparaging statistics, it is apparent that early stage lung cancer patients have a much higher five-year survival rate. Early detection and therapeutic invention such as surgical

Ten Leading Cancer Types for Cancer Deaths Worldwide and in the United States

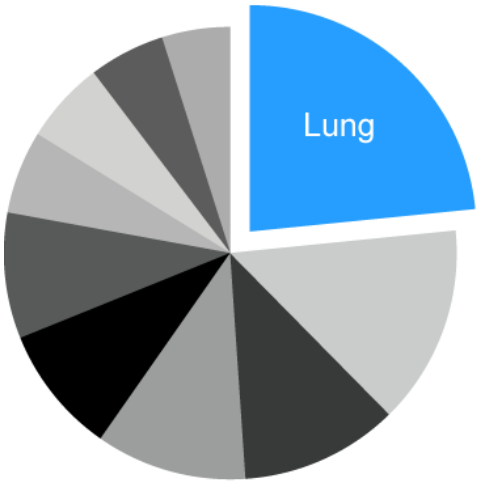

Worldwide

Cancer Type	Deaths in 2004**
Lung	1321
Stomach	802.2
Colorectal	637.9
Liver	608.8
Breast	517.8
Esophagus	507.8
Mouth	334.8
Lymphoma*	331.7
Prostate	276.1
Leukemia	267.9

**Deaths in thousands
*Includes myelomas

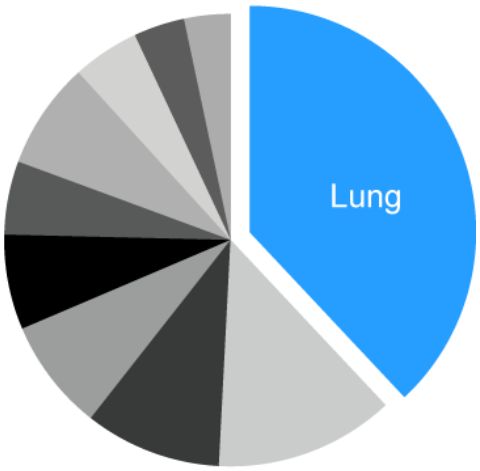

United States

Cancer Type	Deaths in 2006**
Lung	159
Colorectal	53.5
Breast	40.8
Pancreas	33.5
Prostate	28.4
Leukemia	21.9
Lymphoma*	20.3
Liver	20.0
Ovary	15.2
Bladder	13.9

**Deaths in thousands
*Includes myelomas

Figure 1.1 - Ten leading cancer types for cancer-related deaths worldwide and in the United States.

resection and adjuvant chemotherapy may provide a cure and strengthen the potential benefit of lung cancer screening. Based on the premise that early detection of lung cancer may save lives, the National Cancer Institute launched a National Lung Screening Trial (NLST) in 2002. This randomized screen for lung cancer enrolled nearly 50,000 current or former smokers, and compared the effectiveness of low dose helical computed tomography (LDCT) with that of chest x-ray (CXR) imaging of enrollees who are at high risk for developing lung cancer. Participants will receive an initial screening and two subsequent annual screening, and will be observed for a minimum of 4.5 years. Although the NLST is still ongoing and no data has been published, other smaller lung cancer screening trials, which lead to the design and enactment of NLST, have been reported. In the 1980's, however, lung cancer screening was shown to be ineffective in reducing lung cancer mortality.[5-8] In the 1990 and early 2000's, after the introduction of LDCT imaging, lung cancer screens in Japan and from the Early Lung Cancer Action Project, Mayo Clinic and Lung Screening Study reported that LDCT could detect lung cancer in asymptomatic patients, although, some studies reported 10-20% false positive screening rates (i.e. a positive screen with no resulting lung cancer diagnosis).[9-13] High false positive rates represent a public health burden not only in terms of screening costs and unnecessary and potentially harmful surgical biopsies but also the emotional stress and other unrealized drawbacks of ionizing radiation to the patients after LDCT and CXR screenings.

Positron emission tomography (PET) and ^{18}F-fluorodeoxyglucose (FDG) are also clinically used for staging and diagnosis of lung cancers. Although PET/FDG permits the diagnosis of lung nodules greater than 1 cm with 96.8% sensitivity and 77.8% specificity

for malignancy, it has high false negative rates for smaller nodules.[14-17] In 2004, Nomori and coworkers reported that all 20 lung nodules less than 1 cm in diameter were negative on PET regardless of the type of lung cancer. The authors also found that PET failed to detect 90% of well-differentiated adenocarcinomas bigger than 1 cm. The high false positive rates, due to detection of active inflammation in the lung, and high false negative rates, due to low glucose consumption of well-differentiated adenocarcinoma, combined with poor spatial resolution (7-8 mm) are major limitations in the use of PET for early detection of lung cancer.[14,15,18]

Therefore, new tools and technologies that are less invasive and can detect malignant lesions from benign lung structures are necessary to follow up after screening for lung cancer. Such new technologies include the discovery of novel biomarkers specific for lung cancer and other solid cancer biomarkers like integrin αvβ6 and αvβ3, respectively.[19-21]

1.3 Integrin αvβ3: A Biomarker for Molecular Imaging of Tumor Angiogenesis and Cancer

Integrins are a large family of heterodimeric cell surface transmembrane glycoproteins, which bind to extracellular matrix proteins (ECM) and mediate cell-to-cell adhesion by binding to arginine-glycine-aspartic acid (RGD) peptide sequence or a non-RGD sequence in ECM proteins such as vitronectin, collagen, laminin, fibronectin and others.[22,23] In humans, there are at least 24 distinct integrin heterodimers comprised of one of 18 α subunits with one of 8 β subunits. The α and β subunit are non-covalently bound with each subunit having a large extracellular domain, a single membrane spanning domain and a short cytoplasmic domain that can connect to the cytoskeleton of

the cell. Integrin binding to its ligand can trigger outside-in intracellular events that can induce gene expression thus stimulating cell proliferation, migration or apoptosis.[20,24-26] The role of integrins in cancer growth is very complex and differs among different cancer types.[27,28] Studies have also shown that expression levels can fluctuate during growth and can be different between primary and metastatic sites.[29,30]

Angiogenesis plays a critical role in carcinogenesis and cancer metastasis.[31] The formation of new blood vessels from an existing vasculature network is necessary for sustained tumor growth, metastasis, and the exchange of nutrients and metabolic waste. Integrin $\alpha_v\beta_3$, also known as vitronectin receptor, is a well-established angiogenesis marker that is overexpressed on the surface of neovascular endothelial cells and weakly expressed on non-angiogenic endothelial cells.[21] Specifically, $\alpha_v\beta_3$ integrin expression has been correlated with tumor stage, and the malignant potential of several types of cancer, including lung, breast, colon, and malignant melanoma and squamous cell carcinomas of the skin.[32-34] Therefore, αvβ3 is an ideal target for diagnosing cancer as well as a therapeutic target for cancer therapy. Based on the RGD tripeptide sequence, numerous peptides have been designed as ligands to target αvβ3 integrin. Kessler and coworkers showed that particularly cyclic pentapeptides containing the RGD sequence have a higher affinity for αvβ3. The cyclic(Arg-Gly-Asp-D-Phe-Lys), cRGDfK, is a 100-fold better inhibitor of cell adhesion to vitronectin compared to the linear RGD peptide and has a nanomolar affinity for αvβ3.[35] Blocking of αvβ3 specifically with RGD-containing peptide mimics, or anti-αvβ3 antibodies induces tumor regression and display anti-angiogenesis properties by disrupting newly formed vasculature while leaving non-angiogenic vessels unaffected.[20,24,36]

Although known as an angiogenic biomarker, αvβ3 is also highly expressed on mature osteoclasts, activated macrophages, and migrating smooth muscle cells, which are involved with bone reabsorption, inflammation and angiogenesis process, respectively. To determine the major role of αvβ3, knockout mice have been used. Although knocking out all αv integrins in mice led to developmental abnormalities of the placenta, intracerebral vasculature and formation of the palate, 20% of the progeny survived until birth.[37] In cases where β3 and β5 integrins were knocked out separately, mice were viable.[38,39] More interestingly, these mice lacking β3 or β5 integrins showed enhanced tumor growth and angiogenesis in subcutaneous human tumor xenograft models.[40] One possible explanation is that when integrins are bound to the ECM a pro-survival signal is triggered, whereas in the absence of ECM binding an apoptotic signal is activated leading to cell death and anti-angiogenic activity. However absence of β3 and β5 integrins leads to the loss of the ability to sense ECM binding thus resulting in increased pathological angiogenesis.[41]

1.4 Molecular Imaging Modalities for Imaging αvβ3 Integrin Using Nanoparticles

"Molecular imaging is defined as the visualization, characterization and measurement of biological processes at the molecular and cellular level in living systems."[42] With the recent advances in imaging probe design, molecular imaging of cancer biomarkers is poised to become a key component in cancer diagnosis and management.

Current imaging modalities can be separated based on the type of information obtained (i.e., molecular, physiological or anatomical), the energy used to visualize an image (X-rays, gamma rays, radio- and ultrasound waves) or the spatial resolution

(microscopic ranging to macroscopic) of the resultant image generated (Table 1.1).[43] The following sections of the dissertation contain a description of how each imaging modality works and what contrast agents have been developed to image tumor angiogenesis.

Most imaging studies of αvβ3 have utilized RGD peptides as the targeting ligand. However, RGD peptide-based agents bind to both αvβ3 on the tumor endothelium surface as well as the tumor cells, thus not strictly representing the angiogenesis in the tissue. Numerous nanoparticles have been developed to target αvβ3 for imaging. Due to their larger size (20-1000 nm) , these probes are greatly restricted to the vascular compartment and thus mainly target angiogenic endothelium expressing αvβ3. Although some nanoparticles show penetration into tumor parenchyma, nanoparticles are vastly reduced compared to small peptide-based agents in their diffusion in tumors.

Although most of the data presented in this dissertation was obtained using an MRI scanner to image tumor angiogenesis via integrin αvβ3, it is appropriate to discuss briefly the other modalities used for imaging angiogenesis and its biomarkers.

1.4.1 *X-ray and computed tomography (CT)*

X-ray imaging has been used for many decades and still serves an imaging solution for numerous disease states and medical conditions due to it simple principles, speed and cost of image acquisition. When x-rays pass through the body they are attenuated by varying tissue thickness and densities. These intrinsic tissues differences, such as bone and fat provide the contrast in anatomical structures at a relatively high resolution. CT is an imaging method employing x-ray techniques to gain 3-dimensional tomographic information. In CT, a rotating frame has an array of x-ray tubes mounted on one side and the detectors on the opposite side. The frame spins and takes multiple 2D

Table 1.1 - Overview of current small animal molecular imaging modalities

Modality	Target	Resolution*	Depth	Measured signal	Molecular contrast agents
X-ray, CT	Anatomical, physiological	50 μm	No limit	transmitted x-rays	Iodinated molecules, gold-based nanoparticles
MRI	Anatomical, physiological, molecular	10-100 μm	No limit	MRI active nuclei	Gd^{3+}-chelates, SPIO, FePt, FeCo
US	Anatomical, physiological	50 μm	cm	Reflected sound waves	Microbubbles, liposomes
PET	Physiological, molecular	1 - 2 mm	No limit	Positron (β) emissions	^{11}C, ^{13}N, ^{18}F, ^{94m}Tc, ^{124}I - labeled compounds
SPECT	Physiological, molecular	1 - 2 mm	No limit	Gamma emissions	^{99m}Tc, ^{111}In, ^{123}I, ^{125}I - labeled compounds
Optical	Physiological, molecular	1 μm	<400 μm - cm	Fluorescence or bioluminence from exogenous agents	Fluorophores: NIR, photoproteins, luciferins

*Clinical imaging scanner may have less resolution

images or projection images around a single axis of rotation where the patient is located. These projection images are then compiled and fitted using reconstruction algorithms via a dedicated computer to yield a three dimensional data set.

Limitations of CT include poor soft tissue contrast, generally not able to differentiate between malignant vs. surrounding normal tissue. Recently nanoprobe contrast agents have been published using gold-based nanoparticles for blood pool CT imaging.[44-48] In 2008, Kopelman and coworkers reported the first molecular CT imaging agent targeted to head and neck cancer biomarker A9 antigen. Although only in vitro data was presented, the promise of gold-based nanoprobes is foreseeable in the near future for their application as molecular agents targeting angiogenesis and other cancer imaging applications. Conventional CT contrast agents are iodine-based and are used in very high concentrations only limited by toxicity. However, clinical procedures using these agents are routine.

1.4.2 *Radionuclide imaging*

Radionuclide imaging or commonly referred to as nuclear medicine imaging detects emitted gamma rays directly or indirectly from radioactive decay of radiopharmaceuticals, and is considered the "gold standard" for molecular imaging, due its quantitative nature and very high sensitivity. Single photon emission computed tomography (SPECT) and PET are the two major types of nuclear medicine imaging in clinical use.

SPECT directly detects gamma radiation emitted from radionuclide using a gamma camera that is rotated around the patient. Collecting two-dimensional (2D) images or projection images from multiple angles, a computer then applies a tomographic

reconstruction algorithm combining all 2D images yielding a three-dimensional data set. Radioisotopes used in SPECT imaging include technetium-99m, indium-111 and iodine-123. In contrast to SPECT, PET indirectly measures radioactive decay by radionuclide through gamma radiation. In PET, a radionuclide emits a positron which annihilates with an electron, causing two gamma photons to be emitted 180-degrees to one another. Those two photons are then detected in tandem by a ring of gamma cameras. If photons that are not detected in timed pairs (within a few nanoseconds) they are ignored. To create the images the paired events are grouped into projection images, and then reconstructed similarly to SPECT images. Radioisotopes used in PET are nitrogen-13, carbon-11, fluorine-18, iodine-124, copper-64, and technetium-94m.

Contrast agents or radiotracers in PET/SPECT applications of imaging αvβ3 integrin have been based on the radiolabeling of RGD peptides with minimal chemical structure alterations, peptidomimetics and RGD peptide carbohydrate conjugates.[49] Major contributions to the field come from works by Haubner and coworkers where they first evaluated in vivo cyclic RGD (cRGD) peptides as a radionuclide functionalized particle for noninvasive PET imaging. Based on the lead compound cyclo(Arg-Gly-Asp-D-Tyr-Val), these compounds where quickly cleared via the liver and finally though the intestines.[50] Further work by the group conjugated the agents with glucose and galactose to allow kidney clearance of the agent instead. Studies in mice xenografts of melanoma using M21 cells showed 4-fold increase in tumor uptake in glycosylated-RGD agents over non-glycosylated agents.[51,52] Clinically, this ^{18}F-galacto-RGD was extensively characterized in cancer patients and showed good tumor/background ratios, or signal-to-noise ratio (SNR), and PET signal was correlated to αvβ3 expression levels in biopsied

tumor tissue.[30] In SPECT, Janssen and coworkers were the first to synthesize dimeric RGD agents. The agent was two c(RGDfK) peptides linked by an glutamic acid residue resulting in the peptide E-[c(RGDfK)]$_2$. From these studies, they found that dimerization resulted in greater accumulation in αvβ3 expressing tumors, presumably through a multivalent interaction.[53,54] The group specifically analyzed the enhancement of monomer, dimeric and tetrameric compounds in mice with a SK-RC-52 xenograft, and found 8 hours after injection tetrameric accumulation was significantly high than dimeric and monmeric at 7.4, 5.2, and 2.3% ID/g of tumor, respectively.[55] Recently, these scaffolds have been increased to octameric peptides and showed increase is tumor accumulation (~ 2-fold) greater than tetrametric scaffold.[56]

Nanoparticle-based radionuclide particles targeted to αvβ3 integrin include ^{111}In-perfluorcarbon nanoparticles and superparamagnetic iron oxide (SPIO) based PET/MRI sensitive nanoparticles. ^{111}In-perfluorcarbons were tested for the detection of angiogenesis in a VX-2 tumor model in New Zealand white rabbits. The nanoparticles had a payload of 10 ^{111}In atoms per particle, and compared to control nanoparticles had a 4-fold increase in mean tumor radioactivity. They also demonstrated that the same particle with only one ^{111}In atom per particle was much less sensitive to the larger payload particles.[57] In the case of the SPIO-based PET agent, a macrocyclic chelating agent 1,4,7,10-tetraazacyclododecane-N,N',N'',N'''-tetraacetic acid (DOTA) and cRGD were covalently bound to a single SPIO nanoparticle. ^{64}Cu, a positron-emitting radionuclide, was then chelated with DOTA to make a PET/MRI sensitive nanoparticle. Imaging of αvβ3 integrin was performed on mice bearing U87, a human glioblastoma cell line, subcutaneous xenografts and PET analysis showed a 2-fold

increase in tumor uptake over control particles, cRGD-free and competitive inhibition groups.[58]

1.4.3 *Ultrasound imaging (US)*

Ultrasound imaging is based on detecting reflected and transmitted sound waves from tissues in response to high frequency sound emitted from a transducer. The transducer also detects reflected waves as they bounce off these tissues. Differences in tissue pathology cause the reflected waves to have different signature that is measured and transformed into an image. US is commonly used as a very low cost imaging modality for reporting on anatomy and physiological properties of tissues. It is portable and has a millimeter resolution and is a form of non-ionizing radiation. Contrast-enhanced US (CEU) with microbubbles has been used specifically in report angiogenesis status before and after treatment with anti-angiogenesis therapies.[59] Microbubbles (3-4 μm in diameter) are usually colloidal particles made of aqueous dispersion of decalfluorbutane or perfluoropropane with PEGylated phospholipids. They considered to be intravascular tracers and can report on microvascular perfusion of most organs.[60] Microbubbles are mainly conjugated with echistatin peptides, which bear a RGD sequence the targets αvβ3. Studies using orthotopic U87 brain tumor models showed that targeted microbubbles could target to the tumor and report on the spatial distribution and extent of angiogenesis, with the highest CEU signal found in the tumor periphery, which correlated with immunohistochemitry.[61,62]

1.4.4 *Optical imaging*

Optical imaging is based on the projection of light onto a sample of interest and/or detecting the scattered, reflected, emitted, or attenuated light from the sample.

Two major methods employed in optical imaging include fluorescence and bioluminescence imaging. In the case of fluorescence imaging, if the light and the detector are on the same side in relation to the sample, it is called fluorescence reflectance imaging, and if they are on opposite sides it is called translumination fluorescence imaging. Fluorescence is the process by which fluorophores absorb energy in the form of light at a specific wavelength and then emit light of a specific lower energy and longer wavelength (Figure 1.2). More specifically, when photons of a specific energy (hv1) encounter a fluorophore residing at equilibrium in a ground state S0, the electrons are excited to a higher energy level S1. Photon emission (hv2), or fluorescence, is generated by the relaxation of these electrons back to their ground state.

In biological tissues there are a plethora of endogenous light absorbing molecules. Fluorescence from these endogenous molecules, termed autofluorescence, decreases the signal-to-noise ratio (SNR) of exogenous fluorophores absorbing and emitting light in the same region. As shown in Figure 1.3, light with wavelengths between 400 – 600 nm are readily absorbed by oxy-hemoglobin and deoxy-hemoglobin, limiting the distance light can travel through the body to a few millimeters. However, fluorophores in the near infrared spectrum region, 650-950 nm, enable practical detection even after several centimeters in tissue. Clinical studies using NIR fluorophores have shown light penetration from 3 to greater than 10 cm in the muscle/brain and breast, respectively.[63-65] Moreover, since little to no endogenous fluorophores absorbs or emits light in this region there is less background light from the tissue thus increasing the inherent SNR of the acquired images.

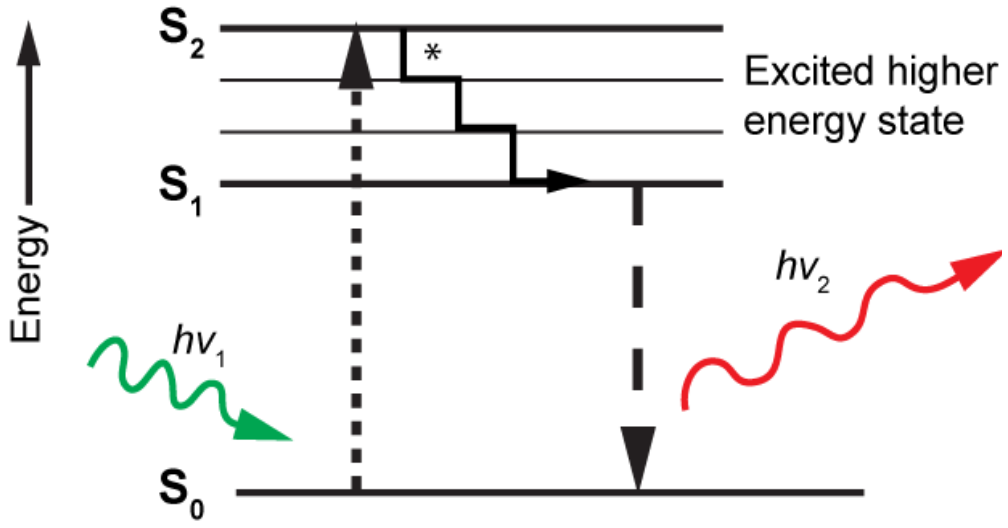

Figure 1.2 - Simplified Jablonski diagram of fluorescence where * represents partial dissipation of absorbed energy.

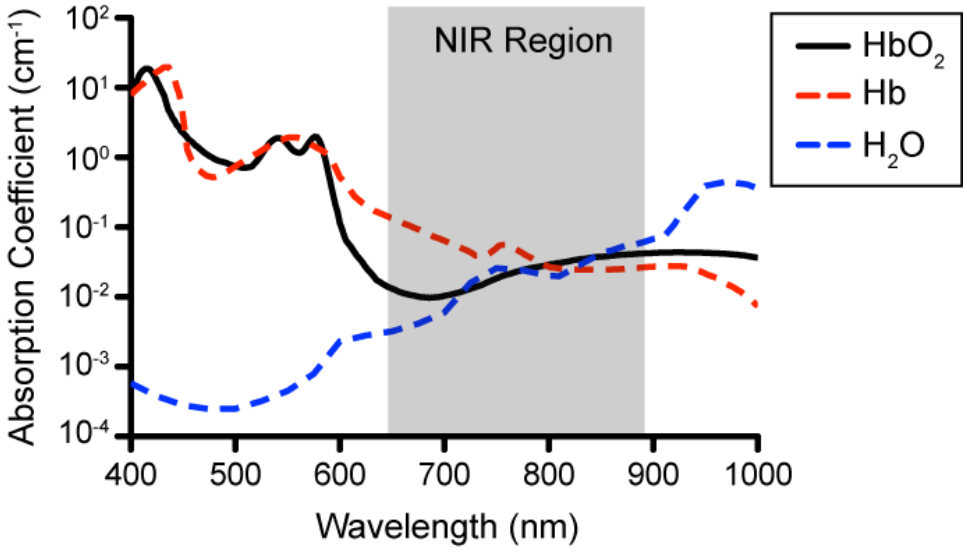

Figure 1.3 - Absorbtion coeffients of oxy-hemoglobin (HbO2) and deoxy-hemoglobin (Hb) and water. Near infrared (NIR) region is shaded.

Similar to PET agents, αvβ3 targeted fluorescence imaging agents have been based on the labeling of RGD peptides with NIR fluorophores for noninvasive optical imaging. Chen and coworkers first published the use of cyanine dyes for the detection of αvβ3. [53,54] Their study showed that by conjugating a cRGD peptide with Cy5.5 could detect a subcutaneous U87 tumor xenograft as far out as 24 hours after injection, and followed the work by showing the increased targeting effect of multimers of RGD peptides labeled with Cy5.5 and Cy7.[66,67] Results were consistent with PET multimer studies. Exploiting the noninvasive nature of NIRF imaging, Chen and coworkers synthesized a NIRF-RGD nanoparticle targeted to αvβ3 that utilized NIRF quantum dots. Quantum dots are inorganic fluorescent semiconductor nanoparticles that can range is size and have optimal optical properties (high quantum yields and strong resistance to photobleaching). The final nanoparticle ranged in size from 15-20 nm and showed specific targeting to a subcutaneous U87 tumor 6 hours post-injection. In vitro uptake studies showed increasing amount of fluorescence with higher αvβ3 expression. Recently, a multimodal paramagnetic quantum dot nanoparticle has also shown αvβ3 targeting in vitro with both optical NIRF and T1-weighted MRI sensitivity.[68]

1.4.5 *MRI*

Known for its high spatial resolution and excellent soft tissue contrast, MRI allows clinicians to noninvasively visualize anatomy, pathology and physiology of a patient. Despite the first MR image being published in 1973, nearly 40 years later, MRI is still developing novel applications at a rapid pace.

1.4.5.1 Principles of MRI

MRI is based on the imaging of nuclear magnetic resonance (NMR) signals of MR active nuclei to report on physical and chemical attributes of an object. MR active nuclei are nuclei with unpaired nuclear spins or spin ½ (Table 1.2). Due to its high natural abundance and that humans are 50-70% water, the hydrogen atom (^{1}H) or proton is the most common MR active nuclei imaged using MRI. Under a strong static external electromagnetic field of the MRI scanner, protons align their magnetic moment parallel (spin-up nuclei, low-energy state) or anti-parallel (spin-down nuclei, high-energy state) with the main magnetic field (B_0). The net magnetic moment or net magnetic vector (NMV) reflects the balance between low-energy spin-up and high-energy spin-down populations. At high magnetic field strength (i.e. 7T versus 3T) the energy difference between the energy states increases so fewer nuclei can populate the spin-down high-energy state; thus, at high field the NMV increases resulting in improved signal. Thermal energy also affects the NMV but will not be discussed herein. In quantum physics, every nucleus is spinning, however when in a static B_0 field an additional spin of the nuclei's magnetic moment around the axis of the B_0 is introduced, this is called precession and the speed at which the magnetic moment spins is the precessional or Larmor frequency (ω_0, MHz). All magnetic moments move on circular precessional path. The precessional frequency of a given nuclei at a given magnet field strength is governed by the Larmor equation:

$$\omega_o = B_o \bullet \lambda \qquad \text{(Equation 1)}$$

where λ is the gyromagnetic ratio which is the Larmor frequency of a MR active nuclei at 1T (Table 1.2). As seen from the Larmor equation as B_0 increases, as does ω_0. The energy of the precessional frequency of all MR active nuclei at all clinical and preclinical

Table 1.2 - Properties of Common MRI Active Nuclei

Nucleus	Spin	Relative Sensitivity*	Gyromagnetic Ratio γ (MHz/T)	Frequency (MHz) at 4.7T / 7T
^{1}H	1/2	1.000	42.58	200.13 / 298.06
^{13}C	1/2	0.016	10.71	50.34 / 74.97
^{19}F	1/2	0.870	40.05	188.24 / 280.35
^{31}P	1/2	0.093	17.24	81.03 / 120.68

*Calculated at constant field for an equal number of nuclei

MRI scanner field strengths (0.2T-11T) corresponds to the radio-frequency (RF) band in the electromagnetic spectrum (Figure 1.4). Resonance is the phenomenon where a MR nucleus is perturbed by an oscillating electromagnetic wave with the same precessional frequency. It is important to note that, the nucleus gains energy and resonates only if the energy is delivered at exactly the same precessional frequency of the MR nucleus. If energy is not delivered at that frequency no energy is gained. To achieve this gain of energy an RF pulse is utilized. In the case of protons at 7T, a 300 MHz RF pulse would be introduced causing excitation of the protons at the Larmor frequency at 7T. This absorption of energy causes nuclei to flip to the high-energy spin down population thus changing the NMV. Depending on the duration and amplitude of the RF pulse, the NMV is moved out of alignment with the B_0 (longitudinal plane). The amount of displacement is called the flip angle. If the flip angle is exactly 90°, then all of the NMV will lie in the transverse plane, which is perpendicular to the B_0. During resonance all magnetic moments move into phase with one another. Phase is the position a magnetic moment is in on the precessional path. Nuclei's magnetic moments that are in-phase with each other are at the same location on the precessional path, whereas magnetic moments that are not in-phase are termed out-of-phase. After a RF pulse and resonance occurs, all magnetic moments are in-phase.

In order to detect the NMV, MRI utilizes Faraday's law of induction, which states that if a conductive loop, i.e. a receiver coil is placed in an area of an alternating magnetic field, i.e. the NMV precessing in the transverse plane, a voltage is induced in the coil. Thus, the voltage created in the coil due to the NMV cutting across the coil is

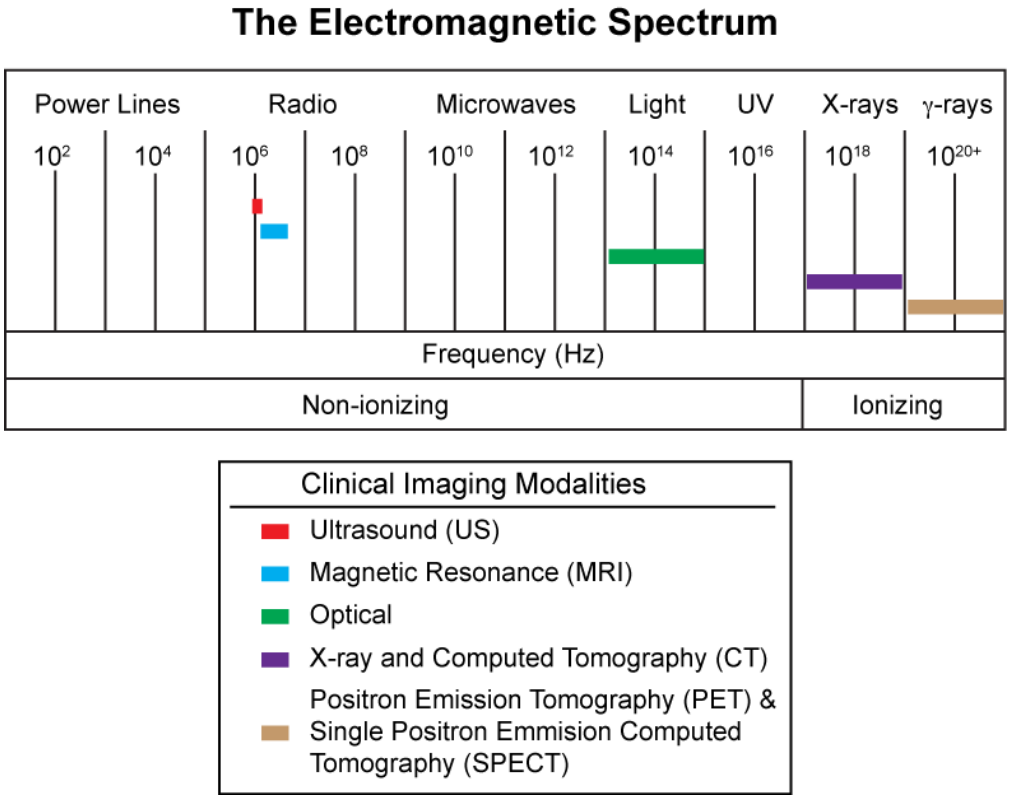

Figure 1.4 - The electromagnetic spectrum and corresponding imaging modalities at different energy levels.

the MR signal, which is only present when the NMV is flipped by an RF pulse into the transverse plane. It is important to remember that NMV is a vector quantity and has components in the longitudinal and transverse planes. Once the RF pulse is removed the NMV is again influenced by the B_0 and tries to realign with B_0. To return, the NMV must lose energy, this process is termed relaxation. During relaxation, NMV gradually increases in the longitudinal plane called T1 recovery, while in the transverse plane NMV gradually decreases called T2 decay. Both T1 recovery and T2 decay affect the NMV during relaxation. Induction lost in the receiver coil during relaxation processes is termed the free induction decay (FID) signal. T1 recovery occurs by the nuclei giving up energy to its surround environment or lattice and is termed spin lattice, longitudinal or T1 relaxation, and is governed by Equation 2 below:

$$M_{z(t)} = M_{z(0)}(1 - e^{-t/T_1}) \qquad \text{(Equation 2)}$$

where $M_{z(t)}$ is the NMV along the longitudinal plane, *z*, at given time after an RF-pulse and $M_{z(0)}$ is the initial NMV before RF pulse excitation and T_1 is the T1 relaxation time of the substance. T2 decay occurs when the nuclei exchanges energy with neighboring nuclei and is termed spin-spin, transverse or T2 relaxation, and is governed by Equation 3 below:

$$M_{xy(t)} = M_{xy(0)} \bullet e^{-t/T_2} \qquad \text{(Equation 3)}$$

where $M_{xy(t)}$ is the NMV along the transverse plane, *xy*, at given time after an RF-pulse and $M_{xy(0)}$ is the initial NMV before RF pulse excitation and T_2 is the T2 relaxation time of the substance. Induction lost in the receiver coil is recorded and is termed the free induction decay (FID) signal.

Both processes, T1 and T2 relaxation, are exponential and can yield relaxation time constants of a tissue. The T1 relaxation time of a tissue is defined as the time it takes for the longitudinal NMV to recovery to 63% after removal of RF pulse. T2 relaxation time of a tissue is defined as the time it takes for the transverse NMV to decay to 37% after removal of RF-pulse. In Table 1.3, T1 and T2 times for tissues are listed.

Image formation is made possible by the spatial encoding principles called zeugmatography. These principles enable the MRI scanner to uniquely encode spatial information into MR signals that can be detected outside of the object. Although MRI is a tomography imaging technique it does not rely on the processing of multiple 2D projection images to provide tomographic information unlike PET, SPECT, and CT. Briefly, a magnetic field gradient is induced in the bore of the MRI in line with the B_0 field. This gradient encodes the nuclei's magnetic moment spins and RF-pulses with spatial information allowing for the tomographic data collection and reconstruction.

1.4.5.2 Weighting MR images

When visualizing MR images the signal intensities in different tissues have been simultaneously influenced by three intrinsic contrast generating mechanisms: T1, T2 and proton density. The proton density of a tissue is the amount of protons per unit volume in the tissue imaged. This simultaneous contribution makes it very difficult to determine the relative contribution of each parameter to the image contrast presented. So in order evaluate one contrast mechanism over another, the image contrast is weighted towards one of the parameters and away from the others. This is achieved by controlling the extrinsic contrast parameters such as the repetition time (TR) between each RF-pulse, or the echo time (TE), which is the time waited after the RF-pulse to collect the FID echo.

Table 1.3 - Relaxation times for various tissues at 1.5T

Tissue Type	T1 / msec	T2 / msec
Adipose tissue	250	60 - 80
Whole blood (deoxygenated)	1350	50
Whole blood (oxygenated)	1350	200
Cerebrospinal fluid / pure water	2200 - 2400	500-1400
Gray matter / cerebrum	920	100
White matter / cerebrum	780	90
Liver	490	40
Kidneys	650	60-75
Muscles	860 - 900	50

http://en.wikipedia.org/wiki/Relaxation_(NMR)

In T1-weighted (T1-w) images, the contrast is dependent predominately in the difference in T1 relaxation times of the tissue. Since T1 relaxation involves the realignment of the NMV with the B_0 along the longitudinal plane, T1-w images utilize a short TR to accentuate the differences in T1 relaxation times in the tissues. If the TR is too long, then all tissues would return to the initial NMV, and thus have no contrast between one another (Figure 1.5A). In T2-weighted (T2-w) images, a long TE is used to accentuate the differences in T2 relaxation times in the tissues (Figure 1.5B). This difference is due to the increased spin-spin interactions some tissues over others, thus maximizing the differences in T2 decay. In proton density weighted (PD-w) images, a long TR and very short TE are utilized to diminish the T1 contrast and T2 contrast contribution, respectively, thus imaging only the amount of proton distribution in the image. Contrast agents that can specifically affect the T1 or T2 relaxation of the local protons have proven to be useful for cancer diagnosis, reporting on vascular transfer kinetics and angiography in the clinic.

1.4.5.3 MRI contrast agents

T1 contrast agents shorten T1 relaxation times of surrounding protons, and its ability to achieve this change in called T1 relaxivity, r_1. The higher the r_1 of the contrast agent the less concentration is needed to speed the recovery of the longitudinal NMV of the surrounding protons. Equation 4 shows the T1 relaxation rate, $1/T_1$, as a function of r_1 and contrast agent concentration, $[CA_{T1}]$, where T_{1H2O} is the relaxation time of pure water.

$$\frac{1}{T_1} = \frac{1}{T_{1,H_2O}} + r_1[CA_{T1}] \qquad \text{(Equation 4)}$$

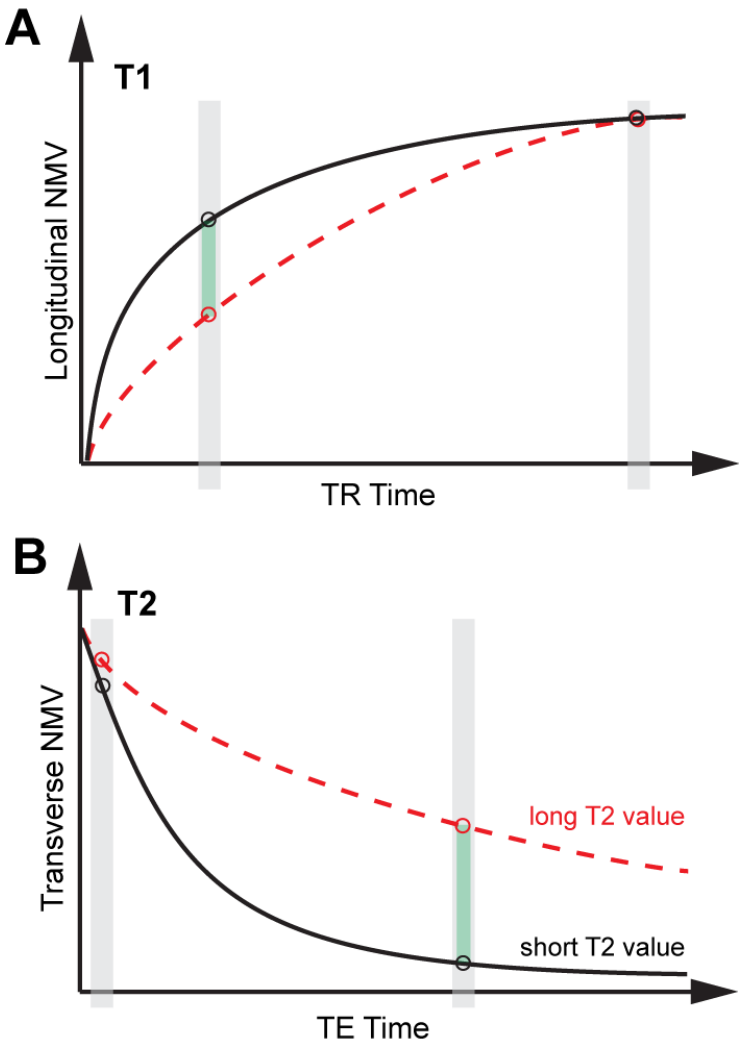

Figure 1.5 - Simulated T1 (A) and T2 (B) difference between fat (black line) and water (dot line). Shade area equal proposed acquisitions. In the case of T1 (A) short TR times are needed and for T2, long TE times are needed to maximize the difference between fat and water.

Protons influenced by a T1 contrast agent would appear brighter (signal intensity gain) than protons not in the vicinity of the contrast agent on a T1-w image.

The most common T1 contrast agents are Gd(III)-based chelating complexes. Due to the seven unpaired electrons of Gd(III) it is strongly paramagnetic. Chelating moieties are necessary for Gd(III) use in vivo due to it being highly toxic in its ionic form. It was found that linear and cyclic forms of diethylene triamine backbones with carboxylic acids bound strongly to Gd(III), the first clinically approved complex was Gd-DPTA or Magnevist® (Gd(III)-diethylenetriamine pentaacetic acid) others include Omniscan™, Dotarem®, Prohance®, Evoist® and Multihance®. Due to the clearance of these complexes through the kidneys and blood half-time is relatively short, however if one has a problem with kidney filtration, i.e. chronic kidney disease, Gd(III) complexes have shown to cause nephrogenic systemic fibrosis in select patients.[69] This has raised concern over the future application of Gd(III) complexes and has inspired researchers to develop new modalities of imaging that are independent of Gd(III). Common application for Gd(III) in MRI, are MR angiography, dynamic contrast enhanced MRI (DCE-MRI), and interrogating brain pathology in cancer and non-cancer presenting patients.

Targeted nanoparticle applications for noninvasive MR imaging of angiogenesis and $\alpha v\beta 3$ expression where first demonstrated using Gd(III)-containing polymerized paramagnetic liposomes (300-350 nm in diameter). In this study, Sipkins and coworkers conjugated biotinylated antibodies against $\alpha v\beta 3$ to the surface of the liposome via avidin linker. Using a rabbit carcinoma model (syngeneic Vx-2 tumor in the thigh), they showed T1 enhancement around the periphery of the tumor 24 hours after injection of the

targeted-liposomes whereas minimal enhancement was seen in control animals.[70] Work by the Lanza group as also shown αvβ3 T1 enhanced imaging of αvβ3 using peptidomimetics targeted specifically to αvβ3 or both αvβ3/αvβ5 conjugate to a $Gd(III)^{-}$ loaded paramagnetic perfluorcarbon nanoparticle.[71] Further work using the same nanoparticle formulation with the addition of an anti-angiogenesis therapeutic, fumagillin, showed that the imaging nanoparticle could show differences in enhanced pre- and post-treatment with the therapeutic nanoparticles and allow the modeling of the angiogenesis.[72,73] Athymic nude mice bearing melanoma xenografts also were successfully imaged with the αvβ3-targeted perfluorcarbon nanoparticle.[74] Multimodal paramagnetic particles have also been utilized to image angiogenesis via αvβ3 with Gd(III) has the MRI sensitive agent combined with a QD or fluorescein dye.[68,75]

T2 contrast agents are based on superparamagnetic nanoparticles. These agents act as nanosized magnets when placed in a static B_0 field causing local distortions in the B_0 field homogeneity. The direct consequence of which is the in spin-spin interactions between protons and a faster T2 relaxation of protons in the vicinity of T2 contrast agents. Compared to T1 contrast agents where a chemical exchange between bound and free water protons is required for increased T1 relaxation, T2 contrast agents affect a larger population of water protons due to local magnetic distortions in the B_0 field. This translates into conventional T2 contrast agents having detection limits in the micromolar to nanomolar concentrations, while T1 contrast agents have detection limits in the millimolar to micromolar range.[76,77] T2 relaxivity, r_2, is the measure of a contrast agent's ability to affect T2 relaxation rates. Equation 5 shows the T2 relaxation rate, $1/T_2$, as a

function of r_2 and contrast agent concentration, $[CA_{T2}]$, where T_{2H2O} is the relaxation time of pure water.

$$\frac{1}{T_2} = \frac{1}{T_{2,H_2O}} + r_2[CA_{T2}] \qquad \text{(Equation 5)}$$

Faster T2 relaxation of protons in the vicinity of a T2 contrast agent causes a darken area (signal intensity loss) in T2-w images.

Unlike the low molecular weight, paramagnetic metal chelates such as Gd-DTPA (T1 contrast agent), SPIO nanoparticles are considered T2-negative contrast agents with substantially higher T1 and T2 relaxivity compared to T1 agents.[78] Clinically, superparamagnetic iron oxide (SPIO) nanoparticles are the most commonly used T2 contrast agent. Feridex® is a clinically approved contrast agent with a 5 nm SPIO core coated in dextran yielding a nanoparticle with a hydrodynamic radius of 80-150 nm with a T2 relaxivity of 98.3 Fe $mM^{-1}s^{-1}$.[79] Recently, novel synthetic schemes have been able to fabricate well-defined, monodisperse SPIO nanoparticle with tunable sizes from 4 to 20 nm in diameter.[80] Investigations into increasing the r_2 of SPIO nanoparticles has yielded SPIO doped with other M^{2+} metals following the formula MFe_2O_4, where M = Fe^{2+}, Co^{2+}, Mn^{2+} or Zn^{2+}. Specifically, partially doped $Zn_xFe_{3-x}O_4$ ($x < 0.5$) nanoparticles have demonstrated a 2.5 fold increase in r_2, over similar sized Fe_3O_4 nanoparticles.[81,82] Other metal alloy based nanoparticles, such as FeCo and FePt, also exhibit high T2 relaxivities for T2 contrast agents.[83-85] One major consideration in the development of iron oxide based nanoparticles is to create a compatible imaging agent that when degraded has low to no acute or chronic toxicity.

Recently, T2 contrast agents targeted to αvβ3 have been used in the molecular imaging of angiogenesis in vivo. In 2007, Kiessling and coworkers synthesized an ultrasmall SPIO conjugated with cRGD peptides and reported the ability to distinguish between tumors with differing degrees of αvβ3 expression on a clinically relevant 1.5T MRI scanner.[86] Work from our lab and work presented in this dissertation has shown the ability to use cRGD conjugate polymeric micelle nanoparticles loaded with a cluster of SPIO can greatly increase T2 MRI sensitivity of the nanoparticle to noninvasively image αvβ3 and angiogenesis in vivo.[87,88] Previously mentioned dual modality nanoparticles for PET/MRI have been developed, as well as dual modality probes that incorporate fluorescent moieties for MRI/optical imaging, presented in this dissertation.[58]

It is important to note that most of the nanoparticles and conjugates aforementioned can and have been adapted for the molecular imaging of other disease states and biomarkers. For cancer, both T1 and T2 contrast agents have been explored in imaging cancer markers such as Her2-Neu, transferrin receptors, epidermal growth factor receptors, αv integrins, matrix metalloproteases and many others.

1.5 Polymeric Micelles as Nanomedicine Platforms for Molecular Imaging

Recently polymeric micelles have emerged as a novel multifunctional platform for therapeutic and diagnostic applications. Currently, biocompatible and biodegradable block copolymers are used in fabricating the micelle nanoplatform. Each copolymer consists of a hydrophilic segment and hydrophobic segment. Poly(ethylene glycol) (PEG) segments with molecular weights 2 to 15 kD are most often utilized for the hydrophilic segment. Whereas a variety of polymers such as poly(propylene), poly(lactic acid), poly(ε-caprolactone), poly(β-benzoyl-L-aspartate), poly(γ-benzyl-L-glutamate) and other

poly(amino acids) are used to from the hydrophobic segment.[89,90] The distinct chemical nature of the two segments results in thermodynamic phase separation in aqueous solution. In water, the hydrophobic segment of the block copolymer self-associates into a semi-solid core with the hydrophilic segment forming a brush-like coronal layer. The resulting core-shell architecture of the supramolecular micelle nanoparticle is important because the hydrophobic core can act as a carrier for hydrophobic therapeutic or diagnostic agents, while the PEG coronal layer protects the micelle from rapid clearance. Without the coronal layer, the micelle would undergo opsonization and rapid phagocytic clearance by the reticuloendothelial system (RES).[91] Dissociation of the micelle into unimers, or single copolymers, can be assessed by the critical micelle concentration, which is typically very low for the micelle (10^{-6} – 10^{-7} M), thus resulting in stable nanoparticles that are not easily dissociated in vivo.

Polymeric micelles have several advantages when compared to small molecular contrast agent and other nanoplatforms. First, their nanoscopic size can be easily controlled by varying the PEG or hydrophobic segment lengths. Nanoparticle size plays an important role in biodistribution and tumor targeting in vivo. Second, micelles have prolonged blood half-lives over small molecules because PEG coronas can effectively hinder micelle uptake by the RES, and micelles (>10^6 Da) are above the threshold limit (~70 kD) of filtration in the kidneys.[92] This allows for more contrast agent to reach its target. Third, a cluster of hydrophobic SPIO can be encapsulated in the micelle, increasing the T2 relaxivity for molecular imaging applications.[87] Finally, the micelle presentation of a targeting ligand is multivalent, which has been shown to increase affinity of nanoparticles to integrin $\alpha v\beta 3$.[53,56,70]

1.6 Current MR Imaging of SPIO

For molecular imaging it is imperative to have a sensitive agent. As discussed above the most sensitive contrast agents for MRI, currently, are SPIO-based probes, which are consistently more sensitive by one to two orders of magnitude over T1 contrast agents. Conventionally, SPIO T2 contrast agents are negative contrast agents, meaning they darken the signal intensity in an image, and are evaluated by T2- or T2* – weighted MR images. T2*-weighted (T2*-w) images are the gold standard for imaging SPIO containing tissue and is very sensitive to SPIO induced magnetic susceptibility. On the other hand, high concentrations of SPIO are difficult to differentiate from a tissue void or void-like signals caused by severe magnetic anisotropy at air-tissue and tissue-tissue interfaces. This is particularly challenging in lung imaging where 99% of the volume is air. Another issue with T2-w imaging of the lung and other organs, is the long echo times needed for quantitative T2 relaxation time calculations may lead to compromised image quality due to motion artifacts from breathing or the heart beat.

Recently, new alternative contrast mechanisms have been investigated for creating pseudo-positive contrast when imaging SPIO probes. These methods so-called white-marker method and off-resonance saturation (ORS) method take advantage of the local field gradient induced by the presence of SPIO and it water proton signal dispersion.[93,94] The white-marker method images the SPIO nanoparticles by imaging a narrow bandwidth of dephased water at a shifted frequency away from the bulk water while saturating all the signal outside of that narrow bandwidth including the bulk water signal. The resulting image shows only the SPIO-distributed regions as bright spots on a dimmed background however it suffers from low signal-to-noise ratios (SNR). In the

ORS method, a selective saturation pulse is applied at an off-resonance frequency from the peak position of bulk water signal, decreasing the total bulk water peak when SPIO is present. An image with the selective saturation ("ON") and an image without ("OFF") are collected and subtracted to generate an ORS contrast image displaying areas influenced by SPIO as a positive contrast.[87] In vivo studies utilizing ORS method to image tumor angiogenesis have been recently published and will be expanded on in this dissertation.[87]

1.7 Organization of Dissertation

By utilizing recent advancements in the fabrication of ultrasensitive MRI contrast agents and the development of novel off-resonance MR imaging, this work aims to establish a novel nanoprobe platform for tumor angiogenesis and lung cancer imaging. We hypothesize that combining these features into a dual modality fluorescent superparamagnetic polymeric micelle nanoprobe will enhance the detection of tumor angiogenesis and lung cancer in vivo, while also allowing one to study the binding kinetics noninvasively using high temporal resolution (HTR) MRI.

To achieve this end goal, the research consisted of several developmental stages, from nanoprobe fabrication, to in vitro and in vivo characterization as well as novel MRI method development, which comprise the chapters of this dissertation. Chapter two aims to establish the dual modality αvβ3-specific fluorescent superparamagnetic polymeric micelle nanoprobe as a non-invasive MRI contrast agent for imaging angiogenesis. Chapter three and four establish the ORS method as a viable MRI method for detecting SPIO in vivo with chapter three detailing the theory behind ORS imaging and chapter four applying the ORS method for in vivo imaging while comparing it to the current gold standard for imaging SPIO-based nanoparticles in vivo. Chapter five utilizes the

ultrasensitivity of the FSPPM nanoprobe and high temporal resolution MRI to report targeting kinetics of the FSPPM in vivo. Chapter six focuses on establishing, imaging and targeting of lung cancer in concert with targeted FSPPM nanoprobes and MRI. In chapter seven, a review of all major findings will be presented, along with a discussion on several new areas of investigation that can benefit from the results presented in this dissertation.

The work accomplished within this dissertation will contribute to the development of polymeric micelles as molecular imaging nanoprobes for the multimodality imaging of tumor angiogenesis and lung cancer. Results and knowledge gained from this work should assist in propelling T2-based MRI contrast agents toward the targeted and specific imaging of lung cancer as well as establishing a nanoplatform and MRI method for studying targeting kinetics of nanoprobes noninvasively in vivo.

1.8 Intended Audience

This dissertation is interdisciplinary in nature. It combines material science, bioengineering, cancer biology, preclinical imaging modalities, and MRI sequence development and optimization. For those working in biological sciences, this work features several technological advances in imaging that can have numerous applications in many areas of cancer biology, specifically biomarker imaging. For those working in biomedical engineering, this work illustrates the needs and challenges when working with a specific biological problem in vivo. The author sincerely hopes that this work can stimulate more conversations between scientists and engineers in life sciences, bioengineering and medical imaging, and that its readers will emerge from this with a collaborative spirit.

1.9 References

1. The global burden of disease: 2004 update.: WHO; 2008.
2. Jemal A, Siegel R, Ward E, Hao Y, Xu J, Thun MJ. Cancer statistics, 2009. CA Cancer J Clin 2009;59(4):225-249.
3. Altekruse SF KC, Krapcho M, Neyman N, Aminou R, Waldron W, Ruhl J, Howlader N, Tatalovich Z, Cho H, Mariotto A, Eisner MP, Lewis DR, Cronin K, Chen HS, Feuer EJ, Stinchcomb DG. SEER Cancer Statistics Review, 1975-2007. In: BK E, editor. National Cancer Institute. Bethesda, MD; 2010.
4. Collins LG, Haines C, Perkel R, Enck RE. Lung cancer: diagnosis and management. Am Fam Physician 2007;75(1):56-63.
5. Frost JK, Ball WC, Jr., Levin ML, et al. Early lung cancer detection: results of the initial (prevalence) radiologic and cytologic screening in the Johns Hopkins study. Am Rev Respir Dis 1984;130(4):549-554.
6. Melamed MR, Flehinger BJ, Zaman MB, Heelan RT, Perchick WA, Martini N. Screening for early lung cancer. Results of the Memorial Sloan-Kettering study in New York. Chest 1984;86(1):44-53.
7. Fontana RS, Sanderson DR, Woolner LB, Taylor WF, Miller WE, Muhm JR. Lung cancer screening: the Mayo program. J Occup Med 1986;28(8):746-750.
8. Kubik A, Polak J. Lung cancer detection. Results of a randomized prospective study in Czechoslovakia. Cancer 1986;57(12):2427-2437.
9. Sone S, Takashima S, Li F, et al. Mass screening for lung cancer with mobile spiral computed tomography scanner. Lancet 1998;351(9111):1242-1245.

10. Henschke CI, McCauley DI, Yankelevitz DF, et al. Early Lung Cancer Action Project: overall design and findings from baseline screening. Lancet 1999;354(9173):99-105.

11. Swensen SJ, Jett JR, Sloan JA, et al. Screening for lung cancer with low-dose spiral computed tomography. Am J Respir Crit Care Med 2002;165(4):508-513.

12. Gohagan JK, Marcus PM, Fagerstrom RM, et al. Final results of the Lung Screening Study, a randomized feasibility study of spiral CT versus chest X-ray screening for lung cancer. Lung Cancer 2005;47(1):9-15.

13. Gohagan J, Marcus P, Fagerstrom R, Pinsky P, Kramer B, Prorok P. Baseline findings of a randomized feasibility trial of lung cancer screening with spiral CT scan vs chest radiograph: the Lung Screening Study of the National Cancer Institute. Chest 2004;126(1):114-121.

14. Gould MK, Maclean CC, Kuschner WG, Rydzak CE, Owens DK. Accuracy of positron emission tomography for diagnosis of pulmonary nodules and mass lesions: a meta-analysis. JAMA 2001;285(7):914-924.

15. Nomori H, Watanabe K, Ohtsuka T, Naruke T, Suemasu K, Uno K. Evaluation of F-18 fluorodeoxyglucose (FDG) PET scanning for pulmonary nodules less than 3 cm in diameter, with special reference to the CT images. Lung Cancer 2004;45(1):19-27.

16. Allen-Auerbach M, Yeom K, Park J, Phelps M, Czernin J. Standard PET/CT of the chest during shallow breathing is inadequate for comprehensive staging of lung cancer. J Nucl Med 2006;47(2):298-301.

17. Knoepp UW, Ravenel JG. CT and PET imaging in non-small cell lung cancer. Crit Rev Oncol Hematol 2006;58(1):15-30.

18. Townsend DW. Physical principles and technology of clinical PET imaging. Ann Acad Med Singapore 2004;33(2):133-145.

19. Elayadi AN, Samli KN, Prudkin L, et al. A peptide selected by biopanning identifies the integrin alphavbeta6 as a prognostic biomarker for nonsmall cell lung cancer. Cancer Res 2007;67(12):5889-5895.

20. Brooks PC, Montgomery AM, Rosenfeld M, et al. Integrin alpha v beta 3 antagonists promote tumor regression by inducing apoptosis of angiogenic blood vessels. Cell 1994;79(7):1157-1164.

21. Brooks PC, Clark RA, Cheresh DA. Requirement of vascular integrin alpha v beta 3 for angiogenesis. Science 1994;264(5158):569-571.

22. Stupack DG, Cheresh DA. Get a ligand, get a life: integrins, signaling and cell survival. J Cell Sci 2002;115(Pt 19):3729-3738.

23. Beer AJ, Schwaiger M. Imaging of integrin alphavbeta3 expression. Cancer Metastasis Rev 2008;27(4):631-644.

24. Brooks PC, Stromblad S, Klemke R, Visscher D, Sarkar FH, Cheresh DA. Anti integrin alpha v beta 3 blocks human breast cancer growth and angiogenesis in human skin. J Clin Invest 1995;96(4):1815-1822.

25. Hynes RO. Integrins: versatility, modulation, and signaling in cell adhesion. Cell 1992;69(1):11-25.

26. Hood JD, Cheresh DA. Role of integrins in cell invasion and migration. Nat Rev Cancer 2002;2(2):91-100.

27. Jin H, Varner J. Integrins: roles in cancer development and as treatment targets. Br J Cancer 2004;90(3):561-565.

28. Mizejewski GJ. Role of integrins in cancer: survey of expression patterns. Proc Soc Exp Biol Med 1999;222(2):124-138.

29. Marshall JF, Rutherford DC, Happerfield L, et al. Comparative analysis of integrins in vitro and in vivo in uveal and cutaneous melanomas. Br J Cancer 1998;77(4):522-529.

30. Beer AJ, Haubner R, Sarbia M, et al. Positron emission tomography using [18F]Galacto-RGD identifies the level of integrin alpha(v)beta3 expression in man. Clin Cancer Res 2006;12(13):3942-3949.

31. Hanahan D, Weinberg RA. The hallmarks of cancer. Cell 2000;100(1):57-70.

32. Horak ER, Leek R, Klenk N, et al. Angiogenesis, assessed by platelet/endothelial cell adhesion molecule antibodies, as indicator of node metastases and survival in breast cancer. Lancet 1992;340(8828):1120-1124.

33. Meitar D, Crawford SE, Rademaker AW, Cohn SL. Tumor angiogenesis correlates with metastatic disease, N-myc amplification, and poor outcome in human neuroblastoma. J Clin Oncol 1996;14(2):405-414.

34. Vosseler S, Mirancea N, Bohlen P, Mueller MM, Fusenig NE. Angiogenesis inhibition by vascular endothelial growth factor receptor-2 blockade reduces stromal matrix metalloproteinase expression, normalizes stromal tissue, and reverts epithelial tumor phenotype in surface heterotransplants. Cancer Res 2005;65(4):1294-1305.

35. Aumailley M, Gurrath M, Muller G, Calvete J, Timpl R, Kessler H. Arg-Gly-Asp constrained within cyclic pentapeptides. Strong and selective inhibitors of cell adhesion to vitronectin and laminin fragment P1. FEBS Lett 1991;291(1):50-54.

36. Friedlander M, Brooks PC, Shaffer RW, Kincaid CM, Varner JA, Cheresh DA. Definition of two angiogenic pathways by distinct alpha v integrins. Science 1995;270(5241):1500-1502.

37. Bader BL, Rayburn H, Crowley D, Hynes RO. Extensive vasculogenesis, angiogenesis, and organogenesis precede lethality in mice lacking all alpha v integrins. Cell 1998;95(4):507-519.

38. Hodivala-Dilke KM, McHugh KP, Tsakiris DA, et al. Beta3-integrin-deficient mice are a model for Glanzmann thrombasthenia showing placental defects and reduced survival. J Clin Invest 1999;103(2):229-238.

39. Huang X, Griffiths M, Wu J, Farese RV, Jr., Sheppard D. Normal development, wound healing, and adenovirus susceptibility in beta5-deficient mice. Mol Cell Biol 2000;20(3):755-759.

40. Reynolds LE, Wyder L, Lively JC, et al. Enhanced pathological angiogenesis in mice lacking beta3 integrin or beta3 and beta5 integrins. Nat Med 2002;8(1):27-34.

41. Cheresh DA, Stupack DG. Integrin-mediated death: an explanation of the integrin-knockout phenotype? Nat Med 2002;8(3):193-194.

42. Mankoff DA. A definition of molecular imaging. J Nucl Med 2007;48(6):18N, 21N.

43. Weissleder R, Pittet MJ. Imaging in the era of molecular oncology. Nature 2008;452(7187):580-589.

44. Hainfeld JF, Slatkin DN, Focella TM, Smilowitz HM. Gold nanoparticles: a new X-ray contrast agent. Br J Radiol 2006;79(939):248-253.

45. Kim D, Park S, Lee JH, Jeong YY, Jon S. Antibiofouling polymer-coated gold nanoparticles as a contrast agent for in vivo X-ray computed tomography imaging. J Am Chem Soc 2007;129(24):7661-7665.

46. Kattumuri V, Katti K, Bhaskaran S, et al. Gum arabic as a phytochemical construct for the stabilization of gold nanoparticles: in vivo pharmacokinetics and X-ray-contrast-imaging studies. Small 2007;3(2):333-341.

47. Alric C, Taleb J, Le Duc G, et al. Gadolinium chelate coated gold nanoparticles as contrast agents for both X-ray computed tomography and magnetic resonance imaging. J Am Chem Soc 2008;130(18):5908-5915.

48. Cai QY, Kim SH, Choi KS, et al. Colloidal gold nanoparticles as a blood-pool contrast agent for X-ray computed tomography in mice. Invest Radiol 2007;42(12):797-806.

49. Haubner R, Wester HJ. Radiolabeled tracers for imaging of tumor angiogenesis and evaluation of anti-angiogenic therapies. Curr Pharm Des 2004;10(13):1439-1455.

50. Haubner R, Wester HJ, Reuning U, et al. Radiolabeled alpha(v)beta3 integrin antagonists: a new class of tracers for tumor targeting. J Nucl Med 1999;40(6):1061-1071.

51. Haubner R, Wester HJ, Burkhart F, et al. Glycosylated RGD-containing peptides: tracer for tumor targeting and angiogenesis imaging with improved biokinetics. J Nucl Med 2001;42(2):326-336.

52. Haubner R, Kuhnast B, Mang C, et al. [18F]Galacto-RGD: synthesis, radiolabeling, metabolic stability, and radiation dose estimates. Bioconjug Chem 2004;15(1):61-69.

53. Janssen M, Oyen WJ, Massuger LF, et al. Comparison of a monomeric and dimeric radiolabeled RGD-peptide for tumor targeting. Cancer Biother Radiopharm 2002;17(6):641-646.

54. Janssen ML, Oyen WJ, Dijkgraaf I, et al. Tumor targeting with radiolabeled alpha(v)beta(3) integrin binding peptides in a nude mouse model. Cancer Res 2002;62(21):6146-6151.

55. Dijkgraaf I, Kruijtzer JA, Liu S, et al. Improved targeting of the alpha(v)beta (3) integrin by multimerisation of RGD peptides. Eur J Nucl Med Mol Imaging 2007;34(2):267-273.

56. Li ZB, Cai W, Cao Q, et al. (64)Cu-labeled tetrameric and octameric RGD peptides for small-animal PET of tumor alpha(v)beta(3) integrin expression. J Nucl Med 2007;48(7):1162-1171.

57. Hu G, Lijowski M, Zhang H, et al. Imaging of Vx-2 rabbit tumors with alpha(nu)beta3-integrin-targeted 111In nanoparticles. Int J Cancer 2007;120(9):1951-1957.

58. Lee HY, Li Z, Chen K, et al. PET/MRI dual-modality tumor imaging using arginine-glycine-aspartic (RGD)-conjugated radiolabeled iron oxide nanoparticles. J Nucl Med 2008;49(8):1371-1379.

59. Korpanty G, Carbon JG, Grayburn PA, Fleming JB, Brekken RA. Monitoring response to anticancer therapy by targeting microbubbles to tumor vasculature. Clin Cancer Res 2007;13(1):323-330.

60. Lindner JR. Microbubbles in medical imaging: current applications and future directions. Nat Rev Drug Discov 2004;3(6):527-532.

61. Ellegala DB, Leong-Poi H, Carpenter JE, et al. Imaging tumor angiogenesis with contrast ultrasound and microbubbles targeted to alpha(v)beta3. Circulation 2003;108(3):336-341.

62. Leong-Poi H, Christiansen J, Klibanov AL, Kaul S, Lindner JR. Noninvasive assessment of angiogenesis by ultrasound and microbubbles targeted to alpha(v)-integrins. Circulation 2003;107(3):455-460.

63. Pogue BW, Poplack SP, McBride TO, et al. Quantitative hemoglobin tomography with diffuse near-infrared spectroscopy: pilot results in the breast. Radiology 2001;218(1):261-266.

64. Ntziachristos V, Yodh AG, Schnall M, Chance B. Concurrent MRI and diffuse optical tomography of breast after indocyanine green enhancement. Proc Natl Acad Sci U S A 2000;97(6):2767-2772.

65. Hoge RD, Franceschini MA, Covolan RJ, Huppert T, Mandeville JB, Boas DA. Simultaneous recording of task-induced changes in blood oxygenation, volume,

and flow using diffuse optical imaging and arterial spin-labeling MRI. Neuroimage 2005;25(3):701-707.

66. Chen X, Conti PS, Moats RA. In vivo near-infrared fluorescence imaging of integrin alphavbeta3 in brain tumor xenografts. Cancer Res 2004;64(21):8009-8014.

67. Cheng Z, Wu Y, Xiong Z, Gambhir SS, Chen X. Near-infrared fluorescent RGD peptides for optical imaging of integrin alphavbeta3 expression in living mice. Bioconjug Chem 2005;16(6):1433-1441.

68. Mulder WJ, Koole R, Brandwijk RJ, et al. Quantum dots with a paramagnetic coating as a bimodal molecular imaging probe. Nano Lett 2006;6(1):1-6.

69. Perazella MA. Current status of gadolinium toxicity in patients with kidney disease. Clin J Am Soc Nephrol 2009;4(2):461-469.

70. Sipkins DA, Cheresh DA, Kazemi MR, Nevin LM, Bednarski MD, Li KC. Detection of tumor angiogenesis in vivo by alphavbeta3-targeted magnetic resonance imaging. Nat Med 1998;4(5):623-626.

71. Winter PM, Caruthers SD, Kassner A, et al. Molecular imaging of angiogenesis in nascent Vx-2 rabbit tumors using a novel alpha(v)beta3-targeted nanoparticle and 1.5 tesla magnetic resonance imaging. Cancer Res 2003;63(18):5838-5843.

72. Winter PM, Schmieder AH, Caruthers SD, et al. Minute dosages of alpha(nu)beta3-targeted fumagillin nanoparticles impair Vx-2 tumor angiogenesis and development in rabbits. FASEB J 2008;22(8):2758-2767.

73. Schmieder AH, Caruthers SD, Zhang H, et al. Three-dimensional MR mapping of angiogenesis with alpha5beta1(alphavbeta3)-targeted theranostic nanoparticles in the MDA-MB-435 xenograft mouse model. FASEB J 2008;22(12):4179-4189.

74. Schmieder AH, Winter PM, Caruthers SD, et al. Molecular MR imaging of melanoma angiogenesis with alphanubeta3-targeted paramagnetic nanoparticles. Magn Reson Med 2005;53(3):621-627.

75. Mulder WJ, Strijkers GJ, Habets JW, et al. MR molecular imaging and fluorescence microscopy for identification of activated tumor endothelium using a bimodal lipidic nanoparticle. FASEB J 2005;19(14):2008-2010.

76. Mills PH, Ahrens ET. Theoretical MRI contrast model for exogenous T2 agents. Magn Reson Med 2007;57(2):442-447.

77. Ahrens ET, Rothbacher U, Jacobs RE, Fraser SE. A model for MRI contrast enhancement using T1 agents. Proc Natl Acad Sci U S A 1998;95(15):8443-8448.

78. Wang YX, Hussain SM, Krestin GP. Superparamagnetic iron oxide contrast agents: physicochemical characteristics and applications in MR imaging. Eur Radiol 2001;11(11):2319-2331.

79. Weissleder R, Stark DD, Engelstad BL, et al. Superparamagnetic iron oxide: pharmacokinetics and toxicity. AJR Am J Roentgenol 1989;152(1):167-173.

80. Sun S, Zeng H, Robinson DB, et al. Monodisperse MFe2O4 (M = Fe, Co, Mn) nanoparticles. J Am Chem Soc 2004;126(1):273-279.

81. Lee JH, Huh YM, Jun YW, et al. Artificially engineered magnetic nanoparticles for ultra-sensitive molecular imaging. Nat Med 2007;13(1):95-99.

82. Barcena C, Sra AK, Chaubey GS, Khemtong C, Liu JP, Gao J. Zinc ferrite nanoparticles as MRI contrast agents. Chem Commun (Camb) 2008(19):2224-2226.

83. Seo WS, Lee JH, Sun X, et al. FeCo/graphitic-shell nanocrystals as advanced magnetic-resonance-imaging and near-infrared agents. Nat Mater 2006;5(12):971-976.

84. Chen M, Liu JP, Sun S. One-step synthesis of FePt nanoparticles with tunable size. J Am Chem Soc 2004;126(27):8394-8395.

85. Sun S, Murray CB, Weller D, Folks L, Moser A. Monodisperse FePt nanoparticles and ferromagnetic FePt nanocrystal superlattices. Science 2000;287(5460):1989-1992.

86. Zhang C, Jugold M, Woenne EC, et al. Specific targeting of tumor angiogenesis by RGD-conjugated ultrasmall superparamagnetic iron oxide particles using a clinical 1.5-T magnetic resonance scanner. Cancer Res 2007;67(4):1555-1562.

87. Khemtong C, Kessinger CW, Ren J, et al. In vivo off-resonance saturation magnetic resonance imaging of alphavbeta3-targeted superparamagnetic nanoparticles. Cancer Res 2009;69(4):1651-1658.

88. Nasongkla N, Bey E, Ren J, et al. Multifunctional polymeric micelles as cancer-targeted, MRI-ultrasensitive drug delivery systems. Nano Lett 2006;6(11):2427-2430.

89. Adams ML, Lavasanifar A, Kwon GS. Amphiphilic block copolymers for drug delivery. J Pharm Sci 2003;92(7):1343-1355.

90. Sutton D, Nasongkla N, Blanco E, Gao J. Functionalized micellar systems for cancer targeted drug delivery. Pharm Res 2007;24(6):1029-1046.

91. Torchilin VP. PEG-based micelles as carriers of contrast agents for different imaging modalities. Adv Drug Deliv Rev 2002;54(2):235-252.

92. Delgado C, Francis GE, Fisher D. The uses and properties of PEG-linked proteins. Crit Rev Ther Drug Carrier Syst 1992;9(3-4):249-304.

93. Seppenwoolde JH, Viergever MA, Bakker CJ. Passive tracking exploiting local signal conservation: the white marker phenomenon. Magn Reson Med 2003;50(4):784-790.

94. Zurkiya O, Hu X. Off-resonance saturation as a means of generating contrast with superparamagnetic nanoparticles. Magn Reson Med 2006;56(4):726-732.

CHAPTER TWO

Angiogenesis Imaging of Solid Tumor by αvβ3-Targeted, Dual-Modality Micellar Nanoprobes

2.1 - Introduction

Angiogenesis plays a critical role in carcinogenesis and cancer metastasis. The formation of new blood vessels from an existing vasculature network is necessary for sustained tumor growth and the exchange of nutrients and metabolic wastes. Accurate detection and quantification of tumor angiogenesis is important for early diagnosis of cancer as well as post-therapy assessment of anti-angiogenic drugs. Established clinical methods of interrogating tumor angiogenesis rely heavily on the invasive measurement of intratumoral microvascular density (MVD) by the immunohistochemical staining of endothelial markers in biopsied tumor tissue. Although MVD correlations with tumor malignance, stage and invasiveness have been reported, they have shown varying degrees of success in predicting patient response and survival.[1,2] This could be due to the inherent limitation of MVD measurements to follow the dynamic changes in vessel density before, during and after therapeutic interventions. Recently, numerous clinical trials evaluating the utility of anti-angiogenic therapies incorporate the use of dynamic contrast enhancement magnetic resonance imaging (DCE-MRI) to non-invasively assess tumor angiogenesis.[3] In DCE-MRI, vascular permeability (e.g. K^{trans}, the transport rate between the vascular and extravascular compartments) of intravenously injected T1-shortening contrast agents (e.g. Gd-DTPA) is analyzed to assess tumor vascularity. Despite the clinical implementation, DCE-MRI is far from precise and specific due to variations in tumor location, size, pathophysiology and the lack of contrast sensitivity.[3]

Currently, new imaging methods that allow for highly specific and quantitative detection of angiogenesis-specific biomarkers are under intensive investigation. Novel contrast probes such as small molecular radiotracers, superparamagentic iron oxide (SPIO), and lipid- and polymer-based nanoparticles are being developed to target different biomarkers of angiogenesis.[4-11] However, current non-invasive methods for visualization and quantification of angiogenic biomarkers have been limited to radiolabeled PET tracers (e.g. VEGF and αvβ3).[12-14] Despite the high sensitivity of PET, inherent limitations in the spatial resolution (5-10 mm) and high background signals do not allow for 3D reconstruction and visualization of the angiogenic vasculature.

In this study, we report the development of αvβ3-specific dual-modality, fluorescent superparamagnetic polymeric micelles (cRGD-FSPPM, Figure 2.1) for angiogenic imaging of tumors. Integrin αvβ3 is a well-established angiogenesis marker that is overexpressed on the surface of neovascular endothelial cells and weakly expressed on non-angiogenic endothelial cells.[15] Specifically, αvβ3 integrin expression has been correlated with tumor stage, and the malignant potential of several types of cancer, including lung, breast, colon, and malignant melanoma and squamous cell carcinomas of the skin.[16-18] This nanocomposite probe design exploits the advantages of the MRI ultrasensitivity rendered by the clustered SPIO-loaded micelles, αvβ3 specificity by cRGD ligands and target validation by fluorescence functionality. Three dimensional tumor volume images from cRGD-FSPPM nanoprobes illustrate the interconnecting vascular network in A549 lung tumor xenografts *in vivo*. Furthermore, quantitative image analysis demonstrates that this nanoprobe is capable of providing highly specific

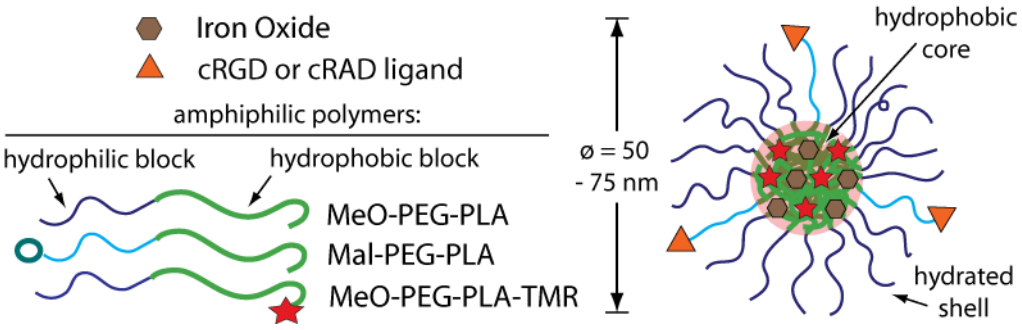

Figure 2.1 - Fluorescent superparamagnetic polymeric micelle (FSPPM) for molecular imaging of αvβ3 integrin expression in angiogenic vasculature of solid tumors. *Modified from EBM 2010, 235.*

and quantitative detection of angiogenic "hot-spots" over the non-targeted, cRAD-FSPPM, control.

2.2 Materials and Methods

2.2.1 Syntheses and characterization of PEG-PLA copolymers

Methoxy(MeO)-PEG-PLA and Maleimide(Mal)-PEG-PLA copolymers were synthesized by ring-opening polymerization of D,L-lactide using corresponding PEG-OH as macromolecular initiators in refluxing toluene.[19] The polymers were characterized by NMR spectroscopy and gel permeation chromatography (GPC). PEG-PLA-TMR copolymer was synthesized by conjugating tetramethylrhodamine-5-carbonyl azide (Invitrogen, Carlsbad, CA) to the hydroxyl group of MeO-PEG-PLA in anhydrous toluene at 80 °C for 4 h Figure 2.2.[20] The fluorescent polymer was first dissolved in THF, filtered, and then precipitated from cold hexane and diethyl ether. All resultant polymers had a total molecular weight of 10kD with 5kD PEG and 5kD PLA segments.

2.2.2 Production of FSPPM

SPIO nanoparticles were synthesized following published methods.[21] The SPIO nanoparticle size distribution was 9 ± 0.9 nm by TEM analysis (JEOL 1200 EX at 120 kV). Polymeric micelles were prepared by a solvent evaporation method.[19] Briefly, a mixture of SPIO (4 mg), MeO-PEG-PLA (6 mg), PEG-PLA-TMR (10 mg), and Mal-PEG-PLA (4 mg) in THF (2 mL) was added dropwise to 0.05 M HEPES buffer containing 0.01 M EDTA (pH 7.4, 18 mL) under sonication. The micelle suspension was then equally divided into two parts, and then shaken on an orbital shaker for 4 h to allow THF to evaporate. Each micelle solution was then added a solution of either thiol-terminated cRGDfK or cRADfK (0.4 μmole in 2 mL HEPES buffer) (Figure 2.2). The

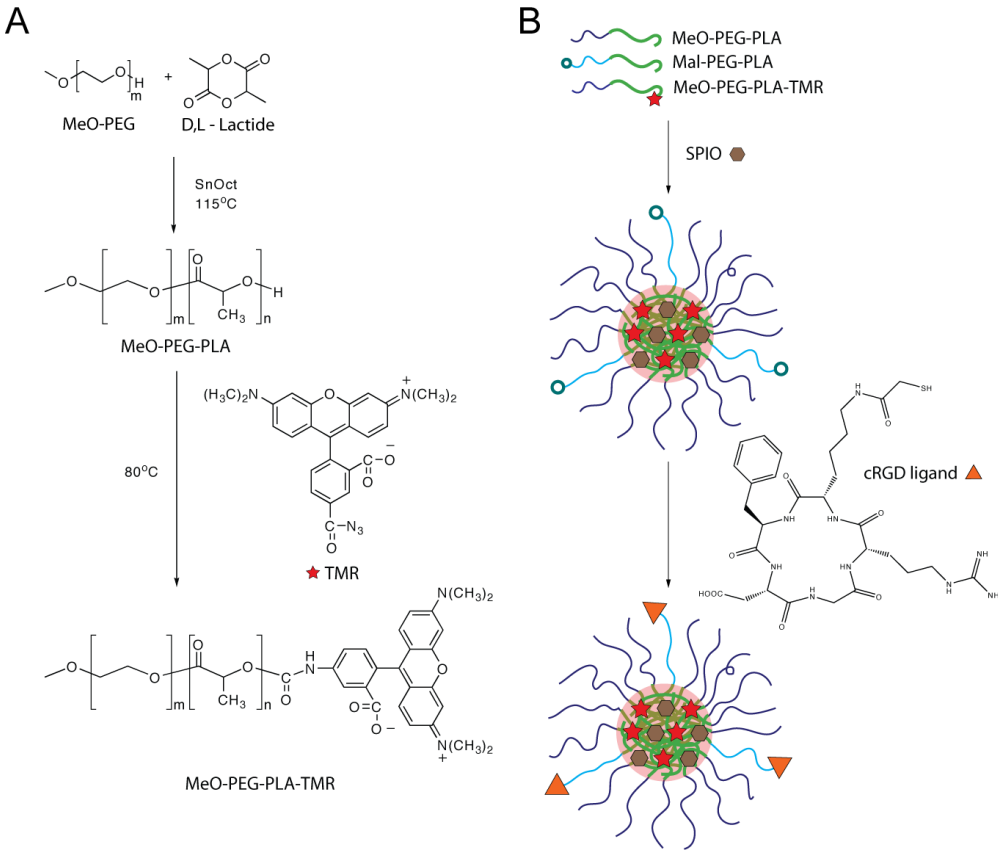

Figure 2.2 - The schemes for the synthesis of MeO-PEG-PLA-TMR copolymers (A) and the production of cRGD-FSPPM (B). *Modified from EBM 2010, 235.*

solutions were then shaken on an orbital shaker overnight for complete conjugations of peptides to maleimide-terminated micelles. Thiol-terminated cRGDfK and cRADfK were obtained by deprotections of thioacetate cRGDfK and cRADfK (Peptides International, Louisville, KY), followed by preparative HPLC purifications. Micelle formulations were filtered through 1.0 μm nylon syringe filters, purified and concentrated using centrifugal filters (100 kDa cutoff, Millipore, Billerica, MA).

2.2.3 Cellular uptake of targeted and non-targeted FSPPM

SLK cells, endothelial cells isolated from Kaposi's sarcoma, were incubated for 30 minutes with micelles and then washed and fixed in 4% paraformaldehyde (pH 7.4) after which they were stained with wheat germ agglutinin (WGA) AlexaFluor488 (W11261, Invitrogen) and mounted with DAPI containing media. Micrographs were collected using a Nikon C1 confocal laser scanning microscope and visualized using Nikon C1 free viewer software. For Prussian blue staining, cells were fixed in 30% acetone, 70% methanol solution. Cells were incubated in a mixture of 10% potassium ferrocyanide and 20% HCl for 30 minutes after which the nuclei and cytoplasm were counterstained with Nuclear Fast Red, dehydrated and mounted. For inhibition studies of endocytosis of the FSPPM, SLK cells were pre-incubated in 400 μM genistein or 20 μg mL^{-1} chlorpromazine for 15 minutes, and then fresh media, followed by micelles and inhibitors for 30 minutes. Cells were then stained with Hoechst 33342 and imaged.

2.2.4 Animal Studies

Female athymic nude mice were utilized for this study. All procedures were approved by the Institutional Animal Care and Use Committee at UT Southwestern

Medical Center in Dallas and carried out according to its guidelines. All imaging was performed under the inhalational anesthesia isoflurane (1%) mixed with pure oxygen, and administered to a free breathing mouse using a nose cone. Five million A549 non-small cell lung cancer cells were injected subcutaneously into the left flank of the animal to induce tumor formation. Tumors were randomized into groups (n=3 per group) and imaged at a volume of 300-400 mm^3. FSPPM was administered via tail vein (6 mg Fe kg^{-1}) and imaged using a 7T Varian horizontal bore small animal MRI scanner. T_2*-weighted (T_2*-w) images were acquired using a three-dimensional gradient echo sequence (TR=20 ms; TE=3 ms; flip angle = 45; NEX = 8; FOV=30mm x 30mm x 15mm; Matrix = 128 x 128 x 64). Images were then processed using ImageJ. 3D models were created using ITK-SNAP software.

2.2.5 Immunofluorescence and immunohistochemical histological analysis

After imaging, the tumor tissue was resected and embedded in OCT and flash frozen. The tissue was sectioned on a Leica 3050S cryostat at 8 μm and were fixed in -20 °C acetone. Immunofluorescene of murine endothelial marker CD31 (PECAM-1) and $\alpha_v\beta_3$ integrin via CD61 (β_3 integrin) was achieved following standardized protocols using BD Pharmagen primary antibodies 550274 and 550541, respectively. Fluorescently labeled secondary antibodies were obtained from Jackson Laboratories. Stained sections were mounted in a DAPI containing media. Images were collected using a Leica DM5500 microscope with proper excitation and emission filter sets. Prussian blue staining was achieved following protocol outlined above.

2.3 Results

2.3.1 Fluorescence and MR Characterization of FSPPM

The FSPPM nanoprobe was produced by encapsulating a cluster of SPIO (diameter: 9 ± 0.9 nm) in the core of polymeric micelles consisting of amphiphilic block copolymers consisting of PEG-PLA (Figure 2.1). To introduce fluorescence functionality, tetramethylrhodamine (TMR) was conjugated to the hydroxyl groups on the hydrophobic PLA segment of the copolymer (Figure 2.2). To optimize the FSPPM formulation for maximum fluorescence output, the weight ratio of PEG-PLA-TMR was varied from 1 to 20 w/w% over the non-fluorescent MeO-PEG-PLA copolymer. Emission spectra showed a maximal fluorescence at 584 nm, consistent with the TMR emission profile. Spectrofluorometric measurements showed relative fluorescence units (RFU) of 446, 607, 851 and 1212 for 1, 2, 5, and 20% at 584 nm, respectively (Figure 2.3A). Although lower loading percentages had greater fluorescence efficiency on a per dye basis, 20% PEG-PLA-TMR micelles showed the maximum fluorescence output on a per micelle basis and were therefore used for the remainder of the study. For all studies, SPIO was encapsulated in the FSPPM core at 20 wt%. Transmission electron micrographs revealed the spherical morphology of the FSPPM nanoprobes with diameters of 57±12 and 53±10 nm for cRGD- and cRAD-FSPPM, respectively (Figure 2.3B). Negatively stained samples highlighted the core-shell structure of the micelle with a cluster of SPIO loaded in the hydrophobic core (Figure 2.3B, inset). The hydrodynamic diameters measured by dynamic light scattering were consistent with TEM characterization with diameters of 58.4±9.7 and 55.4±9.8 nm for cRGD- and cRAD-FSPPM, respectively.

The MRI ultrasensitivity of the FSPPM was examined by obtaining the transverse relaxivity of the final formulation. A phantom with varying concentrations of

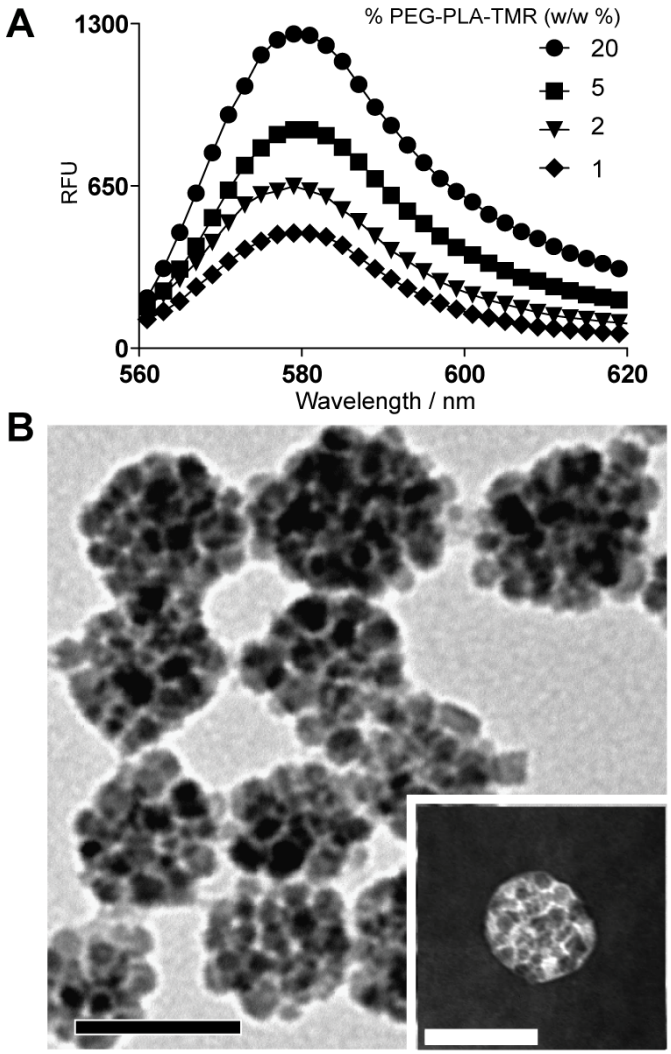

Figure 2.3 - Emission spectra of FSPPM formulations with 1, 2, 5 and 20% loading of PEG-PLA-TMR polymer (λ_{ex} = 534 nm, A). 20% blending of PEG-PLA-TMR (circles) ad the highest fluorescence output at 584 nm. (B) TEM micrograph of a representative FSPPM sample. The inset shows the same sample stained with 2% phosphotungstic acid. Black punctate structures are the SPIO nanoparticles in the micelle core. Scale bars = 50 nm. *Modified from EBM 2010, 235.*

FSPPM solutions was imaged using T_2-weighted (T2-w) spin echo sequences with variable TE times (TE = 10, 15, 30, 45, 60, 75, 90, 105, 200, 500, 1000ms; TR = 2s) on a 7T small animal MRI system (Figure 2.4). The T2-w images used to generate a T2 map of the phantom. The T2 times were 23.4 ±0.9, 41.6±1.4, 94.3±0.8 and 162.6±2.9 ms for 100, 50, 20 and 10 mM Fe, respectively, yielding a transverse relaxivity of 406.6 ± 9.1 $mM^{-1}s^{-1}$ Fe at 20° C for the FSPPM formulation (Figure 2.4, upper panel). The same phantom was imaged on a fluorescent scanner with an excitation laser of 534 nm and long pass detection at 575 nm (Typhoon 9200 variable scanner). The FSPPM showed a fluorescent profile similar to that of the T_2 times with the highest concentration, 100 μM Fe, showing the brightest fluorescence and the other concentrations showing a linear decrease in fluorescence as the concentration decreased (goodness of fit, R^2=0.97, Figure 2.4, lower panel).

2.3.2 αvβ3-targeting specificity of cRGD-FSPPM nanoprobes in vitro

The αvβ3-targeting specificity and cellular uptake of cRGD-FSPPM was examined in SLK cells, which have been shown to over-express αvβ3 integrin and facilitate αvβ3-mediated endocytosis *in vitro*. [22,23] To verify αvβ3 specificity, a non-targeted cRAD-FSPPM control and a competition control of free cRGD peptide co-incubated with cRGD-FSPPM were utilized. cRGD-FSPPM treated cells showed significantly greater uptake of FSPPM over the non-targeted cRAD-FSPPM control (Figure 2.5, red fluorescence). Moreover, competitive binding of $\alpha_v\beta_3$ by free cRGD peptide effectively reduced the amount of cRGD-FSPPM uptake to levels equivalent to cRAD-FSPPM treated cells. Plasma membrane labeling of sialic acid and other saccharides with fluorescently labeled WGA verified the internalization of the FSPPM in

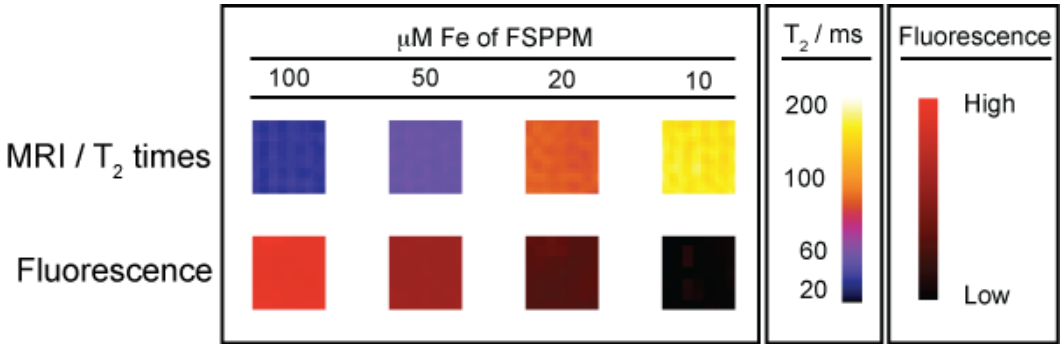

Figure 2.4 - MR and fluorescence imaging of FSPPM phantom with 100, 50, 20 and 10 μM Fe FSPPM solutions in PBS. MRI images are color coded to T2 time of each sample. T2-weighted spin echo images were collected on at 7T and variable TE times (TE = 10, 15, 30, 45, 60, 75, 90, 105, 200, 500, 1000ms; TR = 2s) were used to generate a T2 map of the phantom. The T2 times were 23.4 ±0.9, 41.6±1.4, 94.3±0.8 and 162.6±2.9 ms for 100, 50, 20 and 10 mM Fe, respectively (upper panel). The same phantom was imaged on a fluorescent scanner with an excitation laser of 534 nm and long pass detection at 575 nm (Typhoon 9200 variable scanner). The FSPPM showed a fluorescent profile similar to that of the T_2 times with the highest concentration, 100 mM Fe, showing the brightest fluorescence and the other concentrations showing a linear decrease in fluorescence as the concentration decreased (goodness of fit, R^2=0.97, lower panel). *Modified from EBM 2010, 235.*

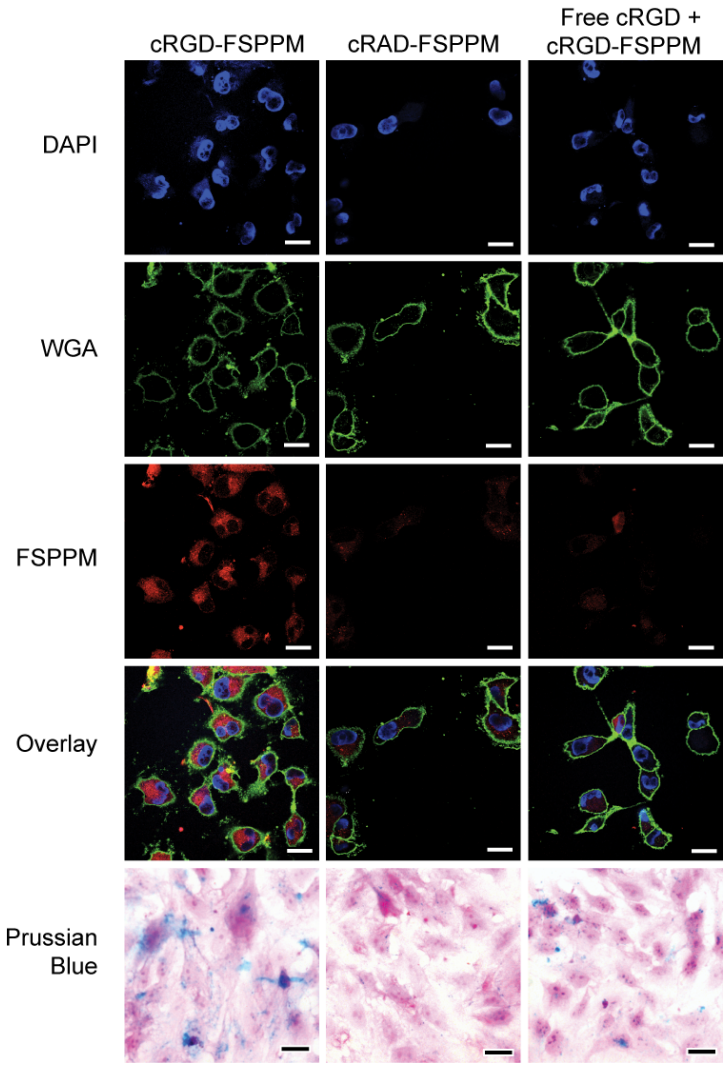

Figure 2.5 - αvβ3-specific cellular uptake of cRGD- and cRAD-FSPPM in SLK cells. SLK cells were incubated with cRGD-FSPPM, cRAD-FSPPM or free cRGD peptide + cRGD-FSPPM. Cells were co-stained with DAPI (blue) and wheat germ agglutinin (WGA) to show the nucleus and plasma membrane, respectively. FSPPM intracellular location was verified by Prussian blue and nuclear fast red staining. Higher uptake of cRGD-FSPPM (red fluorescence and blue granules) compared to other treatment groups is clearly indicated. Scale bar =10 µm. *Modified from EBM 2010, 235.*

cytoplasmic compartments. Prussian blue staining of the cells corroborated the internalized location of the intact FSPPM by staining for the iron in the SPIO (Figure 2.5). αvβ3-targeting specificity and cellular uptake of cRGD-FSPPM were further supported by flow cytometry and the measurement of T2 relaxation times of treated SLK cells resuspended in agarose gel (Figure 2.6). Furthermore, inhibitor studies of clathrin and caveolae-mediated endocytosis pathways by chlorpromazine and genistein, respectively, showed that FSPPM nanoprobes were internalized mainly through caveolae-mediated and not clathrin-mediated pathways (Figure 2.7).

2.3.3 In vivo imaging of αvβ3 integrin expression in tumor-bearing mice.

In vivo imaging of tumor angiogenesis using cRGD-FSPPM nanoprobes was evaluated in a murine subcutaneous A549 non-small cell lung cancer tumor xenograft model. FSPPM was injected intravenously via the tail vein and imaged using a 3D gradient echo sequence at pre-injection, and 4 and 24 hrs post-injection of FSPPM. Inspection of the coronal 2D images collected in the 3D data set showed differences in the distribution pattern and a number of "hot-spots", hypointense regions-of-interest (ROIs) or darkened areas compared to pre-injection images, in the tumor tissues (red dashed circles) of both cRGD-FSPPM and cRAD-FSPPM treated animals (Figure 2.8). cRGD-FSPPM treated tumors showed a connected network of hot-spots in the central and peripheral regions of the tumor, in addition to punctate hot-spots throughout the tumor tissue (Figure 2.8, bottom panel, red arrows). In contrast, cRAD-FSPPM treated tumors, showed less hypointense hot-spots with the majority of them at the skin-tumor interface (Figure 2.8, top panel, red arrows). Muscle and fat tissue contrast did not change over the duration of the study. Moreover in cRGD-FSPPM treated animals, tumor hot-spot signal

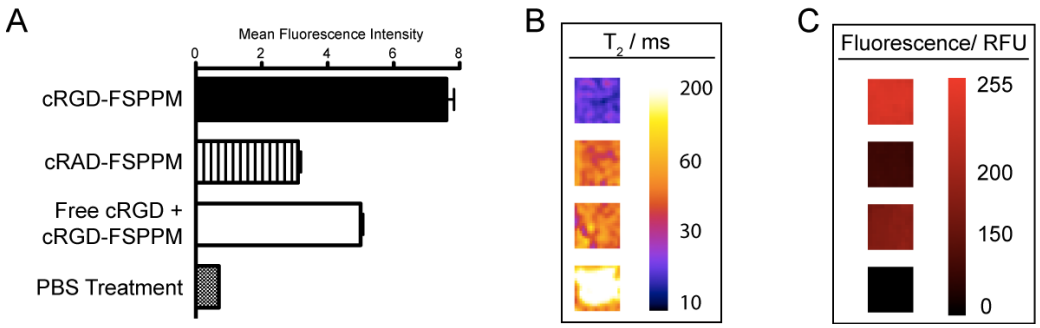

Figure 2.6 - Quantitative analysis of the cellular uptake of FSPPM in SLK cells using flow cytometry (A), MRI T2 relaxation times (B), and fluorescence imaging (C). For phantom analysis (B and C), cells were treated and suspended in 1% agarose in a 384 well plate. After treatment, the mean fluorescent intensity for the cells treated with cRGD-FSPPM was 7.9 ± 0.4 RFU, which was significantly ($p < 0.003$) higher than 3.2 ± 0.2 RFU and 5.0 ± 0.1 RFU for cRAD-FSPPM and free RGD co-treatment with cRGD-FSPPM treatment groups, respectively (A). These changes were also reflected in T_2 relaxation times where the mean relaxation time was 18 ± 4.4 ms for SLK cells incubated with cRGD-FSPPM. Cells incubated with cRAD-FSPPM or free RGD co-treatment with cRGD-FSPPM were 37 ± 2.5 ms and 45 ± 1.5 ms, respectively. PBS treated cells had a mean T_2 relaxation of 81 ± 25ms ($p < 0.009$, $R^2 > 0.99$ for T_2 curve fitting) (B). Similar trends in the fluorescent images of the phantoms were seen where the mean fluorescence was 102 ± 8.0 RFU for cRGD-FSPPM treated SLK cells and 61.8 ± 3.8 and 70.9 ± 0.8 RFU for cRAD-FSPPM and free RGD co-treatment with cRGD FSPPM treated cells, respectively ($p < 0.02$) (C). For all modalities: Mean ± SD of triplicate experiments. *Modified from EBM 2010, 235.*

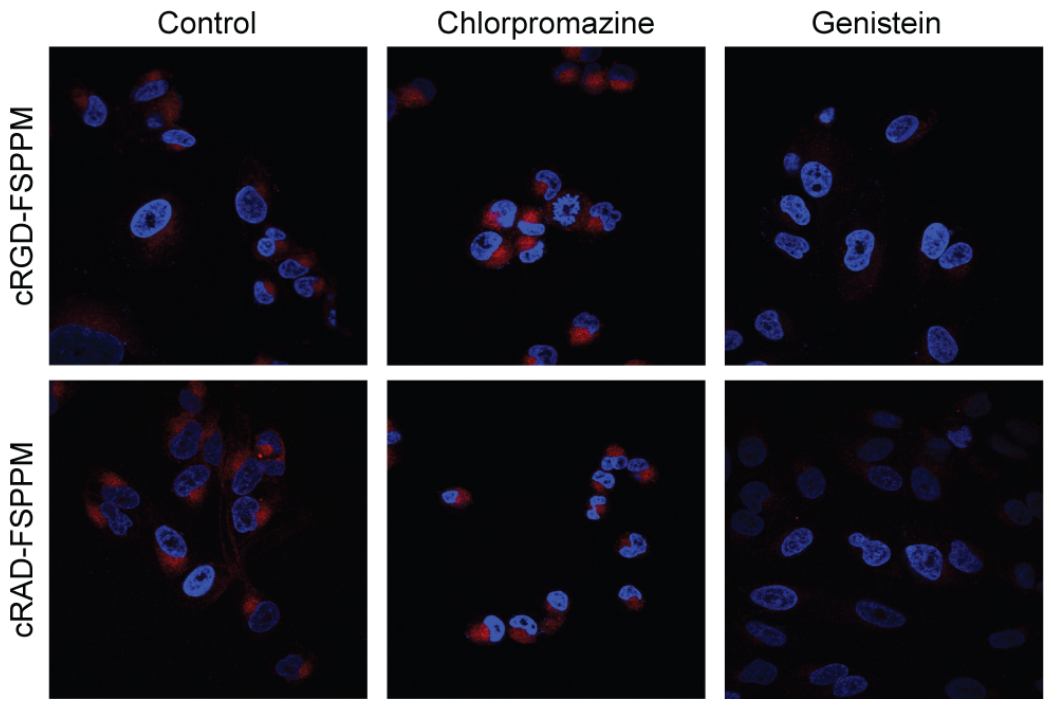

Figure 2.7 - Confocal micrographs of the endocytosis of FSPPM in SLK cells co-treated using inhibitors of clathrin- or caveolae- mediated endocytosis. SLK cell were pretreated with the inhibitors for 15 minutes and then co-incubated with FSPPM for 30 minutes. Chlorpromazine and genistein were used to inhibit clathrin- or caveolae- mediated endocytosis, respectively. Red fluorescence is from FSPPM and nuclei are stained with Hoechst 33342. *Modified from EBM 2010, 235.*

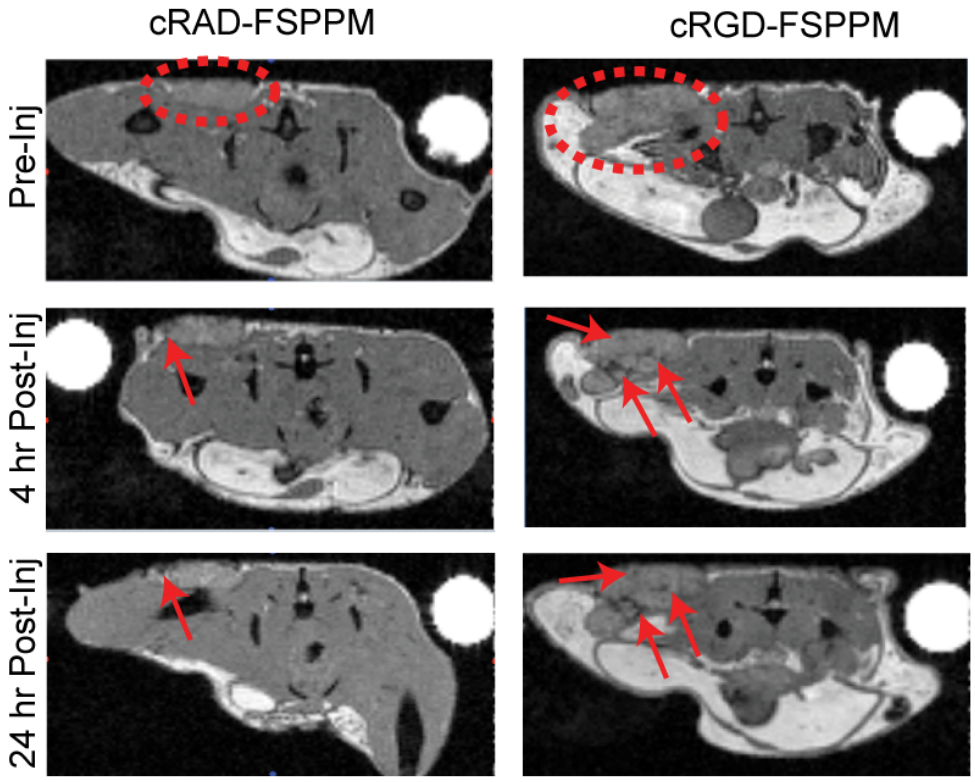

Figure 2.8 - T2*-weighted images of A549 tumor-bearing mice injected with cRAD-FSPPM (left column) or cRGD-FSPPM (right column). Dashed circles outline the location of tumor tissues, and red arrows indicate areas of FSPPM accumulation and signal intensity loss, compared to pre-injection images. In cRGD-FSPPM treated animals acculation was throughout the tumor tissue, whereas is the cRAD-FSPPM treated animals accumulation was at the tissue-skin interface. *Modified from EBM 2010, 235.*

intensity was preserved at the 4 and 24 hr time points, indicating an internalization or accumulation (no wash-out) of cRGD-FSPPM at those locations.

To validate that the MR hot-spots were a result of FSPPM localization, whole mount histological sections matching the MR images were stained with Prussian blue. All hot-spot regions on the MR images were matched with the presence of FSPPM (blue precipitate from Prussian blue staining). cRGD-FSPPM treated animals showed an accumulation of FSPPM associated with the tumor vasculature, while a diffuse staining pattern, likely attributed to the enhanced permeability and retention (EPR) effect, in the cRAD-FSPPM treated animals was observed at the tumor periphery at the skin-tumor interface (Figure 2.9). Although Prussian blue staining verifies the presence of iron and therefore SPIO at the location of MRI hot-spots, it cannot provide biological validation of αvβ3-expressing endothelial cells. To interrogate the αvβ3 targeting at these hot-spots, immunofluorescence images of adjacent tissue sections stained for vascular markers (PECAM-1, or CD31) and αvβ3 integrins (CD61, β3 integrin) showed cRGD-FSPPM (red fluorescence) to be closely associated with the vascular marker, and colocalized with the αvβ3 integrin fluorescence (Figure 2.10A, B). In contrast, cRAD-FSPPM nanoprobes showed little to no colocalization with αvβ3 integrins (Figure 2.10B, D). Further analysis of cRGD-FSPPM colocalization with αvβ3 integrin used Pearson's correlation coefficient for the red, cRGD-FSPPM, and green, αvβ3, channels in Figure 2.10B. The coefficient was 0.97 with values closer to 1 having maximal colocalization and the values closer to 0 having minimal colocalization.

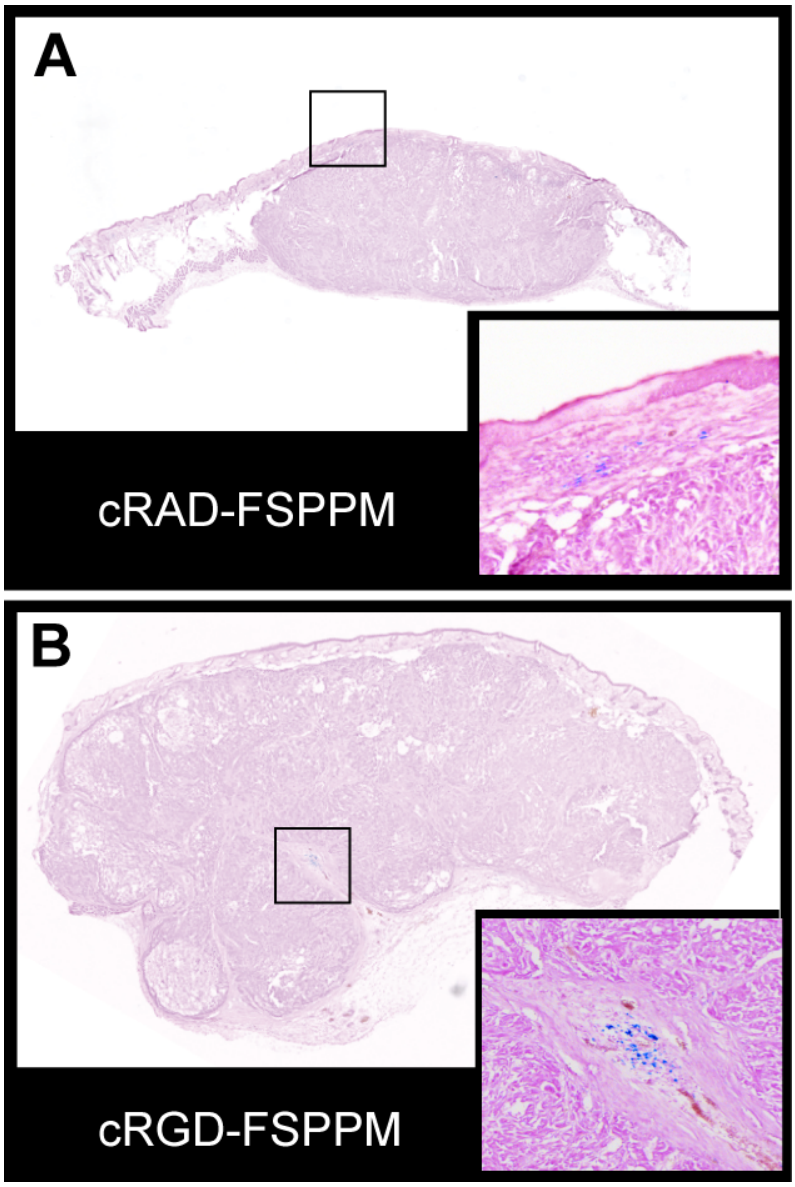

Figure 2.9 - Prussian blue staining of analogous tumor tissue sections of cRAD- (A) and cRGD-FSPPM (B) treated animals. The presence of FSPPM (blue precipitates) is seen in both cases. Inset images are magnifications of hot-spot areas that correlate with hypointense regions denoted in by red arrows in Figure 2.4. *Modified from EBM 2010, 235.*

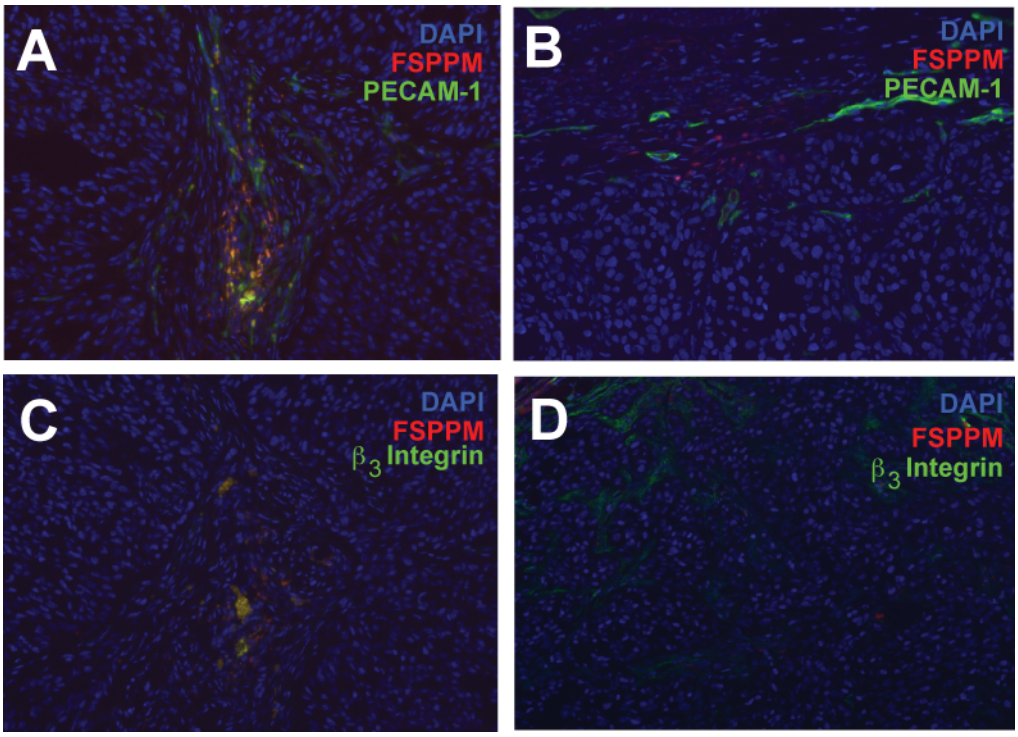

Figure 2.10 - Immunofluorescence of tissue sections stained for PECAM-1 (A, B) and αvβ3 via the β3 integrin (C,D) in cRGD- (A, C) and cRAD-FSPPM (B, D) treated animals, respectively. cRGD-FSPPM colocalizes with β3 integrin indicating target specificity of the targeted FSPM (C) compared to non-targeted FSPPM (D). *Modified from EBM 2010, 235.*

2.3.4 Visualization and quantification of tumor angiogenesis

To visualize and quantify the angiogenic regions in the tumor tissue, we constructed 3D volume filled models of the A549 tumor tissue (Figure 2.11, red volume) and hot-spots (Figure 2.11, green volume) at an isotropic spatial resolution of 234 μm^3 from the 3D gradient echo data sets. In this analysis, angiogenic hotspots were identified as voxels whose signal intensity was less than 40% of the tumor parenchyma. This threshold value was determined by the comparison of a histologically confirmed accumulation of FSPPM and a hypo-intense hot-spot in the tumor tissue of a cRGD-FSPPM treated animal (Figures 2.8 - 2.10). All hot-spots were located within the tumor boundaries. It is important to note that choosing the threshold value from a non-confirmed location in the tumor may lead to fluctuation in the angiogenic quantification. Multiple angles and varied opacities of the tumor volumes allows for the spatial localization of the hot-spot areas. In the pre-contrast images, sporadic hot-spot patterns were observed mostly on the surface of the solid tumors in both animals, which can be caused by magnetic susceptibility changes at the tissue/air or tumor tissue/fat tissue interfaces (Figure 2.11). In the post-contrast images (4 hrs after injection), cRGD-FSPPM treated tumors showed an extensively connected branching architecture of hot-spots throughout the tumor volume. In contrast, cRAD-FSPPM treated tumors showed the majority of the hot-spots were located in the highly perfused regions at the skin-tumor interface. Importantly, those punctate hot-spots in the 2D images can now be visualized as a continuation of an angiogenic hot-spot network. Furthermore, the volume-based tumor hot-spot density can be measured and compared pre- and post-injection to quantify

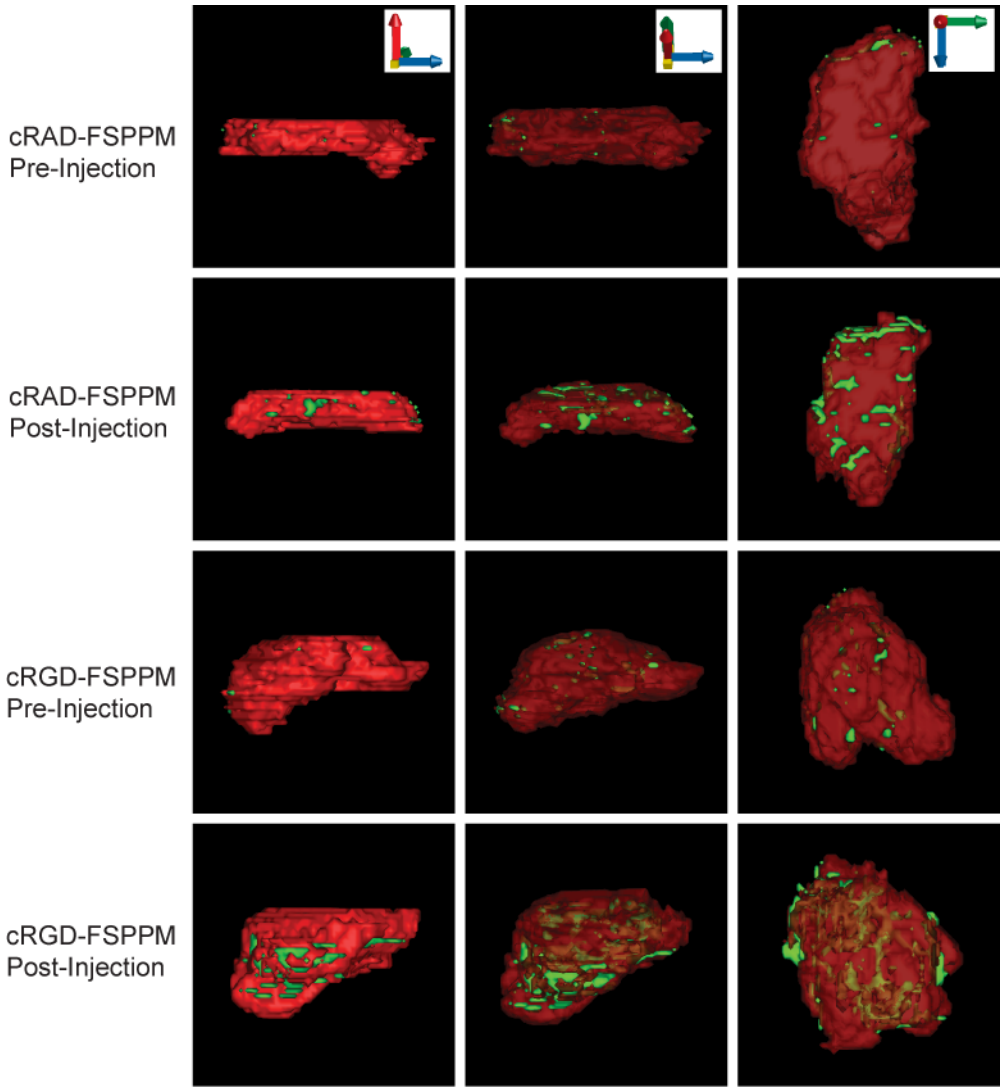

Figure 2.11 - 3D volume renderings of cRAD- and cRGD-FSPPM treated animals pre- and post-injection. Tumor volumes are shown in red and hot-spots in green. cRGD-FSPPM show more accumulation throughout the tumor tisse compared to cRAD-FSPPM treated tumors. The axis of the volumes was rotated and opacity of the tumor volume was decreased in the middle and right columns to help visualize the interior locations of the hot-spots. *Modified from EBM 2010, 235.*

the amount of angiogenesis in the tumor tissue (Figure 2.12, n=3 for each group). In pre-injection images, the percentage of hot-spot pixels to tumor volume pixels was 1.8±1.0% and 1.4±0.4% for cRAD- and cRGD-FSPPM treated animals, respectively (Figure 2.12, white boxes). In post-injection images, the amount of hot-spots increased to 3.7±1.0% and 11.8±4.3% in cRAD- and cRGD-FSPPM groups, respectively. Statistically significant differences (Student t-test, p-value = 0.03, **) in post-injection percentage between cRGD- and cRAD-FSPPM demonstrate the targeting and accumulation of cRGD-FSPPM in the areas of angiogenesis (Figure 2.12, black boxes) over cRAD-FSPPM. Comparison of the pre- and post-injection percentages also showed a significant difference in the cRGD-FSPPM group (p value = 0.01, *) and no difference in the cRAD-FSPPM group (p value = 0.09, ***).

2.5 Discussion

In this study, cRGD-FSPPM nanoprobes were developed and their ability to specifically bind to αvβ3 integrin expressing endothelial cells *in vitro* and *in vivo* was investigated using MRI and fluorescence imaging techniques. Moreover, 3D reconstruction of the T_2*-w MRI data sets allowed for the non-invasive visualization and quantification of angiogenic tumor vascular networks at an isotropic resolution of 234 μm^3.[12-14] Recently, Lanza and coworkers reported the ability to reconstruct 3D T1-weighted MRI data sets, with non-isotropic volumes greater than 390 μm^3, to visualize angiogenic vasculature using Gd-DOTA (~130,000 ions/particle) loaded perfluorcarbon emulsion nanoparticles targeted to both αvβ3 and αvβ5 integrins.[24] In this study, the ultrasensitive detection of superparamagnetic nanoparticles by the T_2*-w method allows

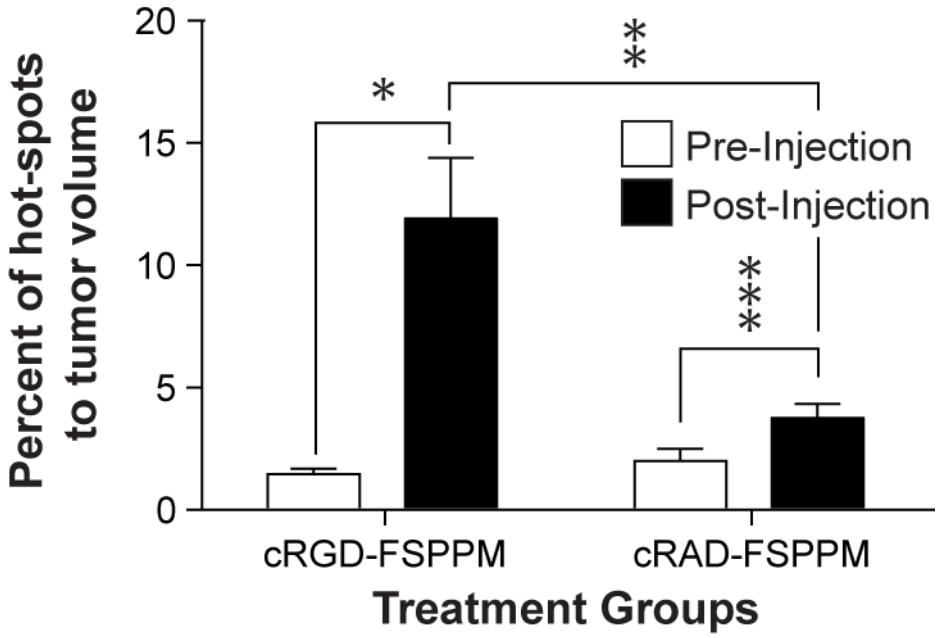

Figure 2.12 - Quantification and comparison of 3D volume-based hot-spot density from cRGD-FSPPM and cRAD-FSPPM groups. The p-values are 0.01 (*), 0.03 (**) and 0.09 (***) from paired groups of comparisons using the Student's t-test. *Modified from EBM 2010, 235.*

for detailed visualization and accurate 3D mapping of angiogenic vasculatures in the tumor tissue.

The use of polymer- and lipid-based platforms as nanocarriers of imaging agents has proven to be beneficial in increasing imaging sensitivity, prolonging blood circulation half-times, passive targeting of tumor tissues via the EPR effect, and the active targeting of cancer markers such as Her2-Neu, folate, transferrin receptors and αvβ3 integrin. [4-11,25-28] Although multiple imaging platforms have shown targeting efficacy *in vitro* and *in vivo*, it is only recently that these formulations have been adapted or combined for multimodality imaging applications. Recently, Sailor and coworkers have introduced SPIO and quantum dots (QDs) in the micellar systems to generate a dual-modality nanoprobe.[29] In our study, we chose to use a small hydrophobic molecular dye to maximize the payload of SPIO to increase MRI sensitivity of the FSPPM while avoiding possible cellular toxicity from QDs. Our FSPPM platform had several potential advantages compared to current molecular imaging agents. First, the clustering of uniform SPIO in the core of micelles has demonstrated MRI ultrasensitivity with detection limits in the nanomolar and picomolar concentration using conventional T_2-weighted and off-resonance saturation MR imaging sequences, respectively.[11,25,30] Conventional T_1-weighted contrast agents (e.g. Gd-DTPA) have detection limits in the millimolar to micromolar range.[31] Moreover, the FSPPM showed a 4.5 fold greater transverse relaxivity on a per iron atom basis than Feridex, a clinically approved SPIO formulation.[32] Second, the cRGD-FSPPM benefits from improved specificity for angiogenic vessels in the tumor tissue due to its active targeting to αvβ3 integrin via the cRGD ligands. Third, the incorporation of a fluorescent moiety allowed for the

validation of FSPPM targeting *in vitro* and *in vivo*, using fluorescence imaging techniques. Previous polymer- and lipid-based nanoprobes have also shown targeting via immunofluorescence analysis but have used externally displayed fluorophores.[4,8] In our nanocomposite design, the TMR dye is protected from inadvertent cleavage and protein interactions by its encapsulation in the core of the FSPPM. This characteristic could allow for the prolonged fluorescence output needed for other *in vivo* fluorescence imaging studies. Moreover, incorporation of hydrophobic near infrared fluorescent (NIRF) dyes could also allow for deeper tissue imaging using other non-invasive optical methods.

Specific targeting to αvβ3 integrins and subsequent receptor-mediated endocytosis of cRGD-FSPPM was demonstrated in SLK cells relative to studies of cRAD-FSPPM and the addition of free cRGD peptides to cRGD-FSPPM controls using both MR and fluorescence imaging techniques. In tumor bearing mice, differences in the intratumoral distribution of the targeted and non-targeted FSPPM were also compared. Most of cRGD-FSPPM was localized to vascular areas throughout the tumor volume and cRAD-FSPPM were found only at the tumor periphery. One of the limitations in displaying the angiogenic hot-spots in 2D slices is the lack of spatial context to appreciate the network structures of the tumor vasculature, which makes it difficult for the accurate quantification of tumor angiogenesis in the whole tumor volume. To overcome this limitation, isotropic 3D data were gathered to construct the volume filled models of the A549 tumors where an interconnecting vasculature network was demonstrated by cRGD-FSPPM nanoprobes. This αvβ3-targeted nanoprobe was further able to quantify the

extent of tumor angiogenesis by comparing the pre- and post-injection images over the cRAD-FSPPM control.

In summary, this study describes the development and application of dual modality nanoprobes for angiogenesis imaging of solid tumors. The combination of molecular targeting to an angiogenic biomarker (i.e. $\alpha v\beta 3$) and the dual modality imaging design allowed for an accurate and quantitative characterization of tumor angiogenesis. This new paradigm offers exciting opportunities for early detection of solid tumors and non-invasive post-therapy assessment of anti-angiogenic drugs.

2.6 References

1. Chandrachud LM, Pendleton N, Chisholm DM, Horan MA, Schor AM. Relationship between vascularity, age and survival in non-small-cell lung cancer. Br J Cancer 1997;76(10):1367-1375.
2. Weidner N, Semple JP, Welch WR, Folkman J. Tumor angiogenesis and metastasis--correlation in invasive breast carcinoma. N Engl J Med 1991;324(1):1-8.
3. O'Connor JP, Jackson A, Parker GJ, Jayson GC. DCE-MRI biomarkers in the clinical evaluation of antiangiogenic and vascular disrupting agents. Br J Cancer 2007;96(2):189-195.
4. Mulder WJ, Strijkers GJ, Habets JW, et al. MR molecular imaging and fluorescence microscopy for identification of activated tumor endothelium using a bimodal lipidic nanoparticle. FASEB J 2005;19(14):2008-2010.

5. Artemov D, Mori N, Okollie B, Bhujwalla ZM. MR molecular imaging of the Her-2/neu receptor in breast cancer cells using targeted iron oxide nanoparticles. Magn Reson Med 2003;49(3):403-408.

6. Sonvico F, Mornet S, Vasseur S, et al. Folate-conjugated iron oxide nanoparticles for solid tumor targeting as potential specific magnetic hyperthermia mediators: synthesis, physicochemical characterization, and in vitro experiments. Bioconjug Chem 2005;16(5):1181-1188.

7. Hogemann-Savellano D, Bos E, Blondet C, et al. The transferrin receptor: a potential molecular imaging marker for human cancer. Neoplasia 2003;5(6):495-506.

8. Koole R, van Schooneveld MM, Hilhorst J, et al. Paramagnetic lipid-coated silica nanoparticles with a fluorescent quantum dot core: a new contrast agent platform for multimodality imaging. Bioconjug Chem 2008;19(12):2471-2479.

9. Zhang C, Jugold M, Woenne EC, et al. Specific targeting of tumor angiogenesis by RGD-conjugated ultrasmall superparamagnetic iron oxide particles using a clinical 1.5-T magnetic resonance scanner. Cancer Res 2007;67(4):1555-1562.

10. Cai W, Chen X. Multimodality molecular imaging of tumor angiogenesis. J Nucl Med 2008;49 Suppl 2:113S-128S.

11. Khemtong C, Kessinger CW, Ren J, et al. In vivo off-resonance saturation magnetic resonance imaging of alphavbeta3-targeted superparamagnetic nanoparticles. Cancer Res 2009;69(4):1651-1658.

12. Cai W, Chen K, Mohamedali KA, et al. PET of vascular endothelial growth factor receptor expression. J Nucl Med 2006;47(12):2048-2056.

13. Zhang X, Xiong Z, Wu Y, et al. Quantitative PET imaging of tumor integrin alphavbeta3 expression with 18F-FRGD2. J Nucl Med 2006;47(1):113-121.

14. Chen X, Hou Y, Tohme M, et al. Pegylated Arg-Gly-Asp peptide: 64Cu labeling and PET imaging of brain tumor alphavbeta3-integrin expression. J Nucl Med 2004;45(10):1776-1783.

15. Brooks PC, Clark RA, Cheresh DA. Requirement of vascular integrin alpha v beta 3 for angiogenesis. Science 1994;264(5158):569-571.

16. Horak ER, Leek R, Klenk N, et al. Angiogenesis, assessed by platelet/endothelial cell adhesion molecule antibodies, as indicator of node metastases and survival in breast cancer. Lancet 1992;340(8828):1120-1124.

17. Meitar D, Crawford SE, Rademaker AW, Cohn SL. Tumor angiogenesis correlates with metastatic disease, N-myc amplification, and poor outcome in human neuroblastoma. J Clin Oncol 1996;14(2):405-414.

18. Vosseler S, Mirancea N, Bohlen P, Mueller MM, Fusenig NE. Angiogenesis inhibition by vascular endothelial growth factor receptor-2 blockade reduces stromal matrix metalloproteinase expression, normalizes stromal tissue, and reverts epithelial tumor phenotype in surface heterotransplants. Cancer Res 2005;65(4):1294-1305.

19. Nasongkla N, Bey E, Ren J, et al. Multifunctional polymeric micelles as cancer-targeted, MRI-ultrasensitive drug delivery systems. Nano Lett 2006;6(11):2427-2430.

20. Luo L, Tam J, Maysinger D, Eisenberg A. Cellular internalization of poly(ethylene oxide)-b-poly(epsilon-caprolactone) diblock copolymer micelles. Bioconjug Chem 2002;13(6):1259-1265.

21. Sun S, Zeng H. Size-controlled synthesis of magnetite nanoparticles. J Am Chem Soc 2002;124(28):8204-8205.

22. Rader C, Popkov M, Neves JA, Barbas CF. Integrin alpha v beta 3-targeted therapy for Kaposi's sarcoma with an in vitro-evolved antibody. FASEB Journal 2002;16(12):2000-2.

23. Nasongkla N, Shuai X, Ai H, et al. cRGD-functionalized polymer micelles for targeted doxorubicin delivery. Angew Chem Int Ed Engl 2004;43(46):6323-6327.

24. Schmieder AH, Caruthers SD, Zhang H, et al. Three-dimensional MR mapping of angiogenesis with alpha5beta1(alpha nu beta3)-targeted theranostic nanoparticles in the MDA-MB-435 xenograft mouse model. FASEB J 2008;22(12):4179-4189.

25. Ai H, Flask C, Weinberg B, et al. Magnetite-loaded polymeric micelles as ultrasensitive magnetic-resonance probes. Adv Mater 2005;17(16):1949-52.

26. Moghimi SM, Hunter AC, Murray JC. Long-circulating and target-specific nanoparticles: theory to practice. Pharmacol Rev 2001;53(2):283-318.

27. Hashizume H, Baluk P, Morikawa S, et al. Openings between defective endothelial cells explain tumor vessel leakiness. Am J Pathol 2000;156(4):1363-1380.

28. Maeda H. The enhanced permeability and retention (EPR) effect in tumor vasculature: the key role of tumor-selective macromolecular drug targeting. Adv Enzyme Regul 2001;41:189-207.

29. Park JH, von Maltzahn G, Ruoslahti E, Bhatia SN, Sailor MJ. Micellar hybrid nanoparticles for simultaneous magnetofluorescent imaging and drug delivery. Angew Chem Int Ed Engl 2008;47(38):7284-7288.

30. Mills PH, Ahrens ET. Theoretical MRI contrast model for exogenous T2 agents. Magn Reson Med 2007;57(2):442-447.

31. Ahrens ET, Rothbacher U, Jacobs RE, Fraser SE. A model for MRI contrast enhancement using T1 agents. Proc Natl Acad Sci U S A 1998;95(15):8443-8448.

32. Barcena C, Sra AK, Chaubey GS, Khemtong C, Liu JP, Gao J. Zinc ferrite nanoparticles as MRI contrast agents. Chem Commun (Camb) 2008(19):2224-2226.

CHAPTER THREE

Off-Resonance Saturation Method for SPIO Contrast Enhancement: Theory and Application

3.1 - Introduction

The growing use of SPIO nanoparticles as ultra-sensitive molecular imaging agents for MRI has resulted in the rapid development of novel SPIO formulations and imaging acquisition methods. SPIO nanoparticles with different compositions, particle size, coatings and targeting ligands have been extensively studied to increase the (1) efficiency in shortening T2 relaxation times; (2) product stability, safety and applicability (i.e. lessen aggregation, increase aqueous stability, lower toxicity, narrow size distribution, and lengthy blood half-life); (3) biodistribution to specific organs/tissues; and (4) specific molecular imaging applications.

Vital to SPIO imaging is the ability to accurately identify and quantify SPIO nanoparticles that are present in a given tissue. Conventionally, SPIO are evaluated using T2-w and T2*-w MR imaging sequences, showing as hypo-intense regions of signal intensity (i.e. negative contrast or dark spots). An issue with T2/T2*-w imaging is the SPIO-induced hypo-intense regions can be difficult to differentiate from a tissue void or void-like signal caused by severe magnetic anisotropy at tissue and air-tissue interfaces. Moreover, if the SPIO is located close to the skin-air interface it may lose contrast with the surrounding air background on the MR image and could also be confused as a magnetic susceptibility image artifact where the difference between air and skin causes a void-like signal loss in the image.

Recently, new alternative contrast mechanisms have been investigated for creating pseudo-positive contrast when imaging SPIO nanoparticles. These methods so-called white-marker method and off-resonance saturation (ORS) method take advantage of the local field gradient induced by the presence of SPIO and its water proton signal dispersion.[1,2] The white-marker method images SPIO nanoparticles by imaging a narrow bandwidth of dephased water at a shifted frequency away from bulk water while saturating all the signal outside of that narrow bandwidth including the bulk water signal. The regions containing SPIO appeared as bright spots on the resulted image with a high contrast-to-noise ratio, however, the signal-to-noise ratio is sacrificed as the bulk water signal was also suppressed. The second mechanism is named off-resonance saturation (ORS) method. In ORS imaging, a selective saturation pulse is applied at an off-resonance frequency from the peak position of bulk water signal, thus saturating this population of water and decreasing the total bulk water peak when SPIO nanoparticles are present. An image with the selective pre-saturation ("ON") and an image without ("OFF") are collected and subtracted to generate an ORS contrast image displaying areas influenced by SPIO as a positive contrast (Figure 3.1).[3]

In this chapter, the theory of ORS contrast generation will be proposed and validated at 4.7T and 7T using phantoms of single SPIO-loaded 1,2-distearoyl-*sn*-glycero-3-phosphoethanolamine-N-methoxy(polyethylene glycol) (DSPE-PEG) micelles suspended in aqueous solution (Figure 3.2). This model was chosen due to the ability to control the loading of the SPIO to one nanoparticle per micelle.

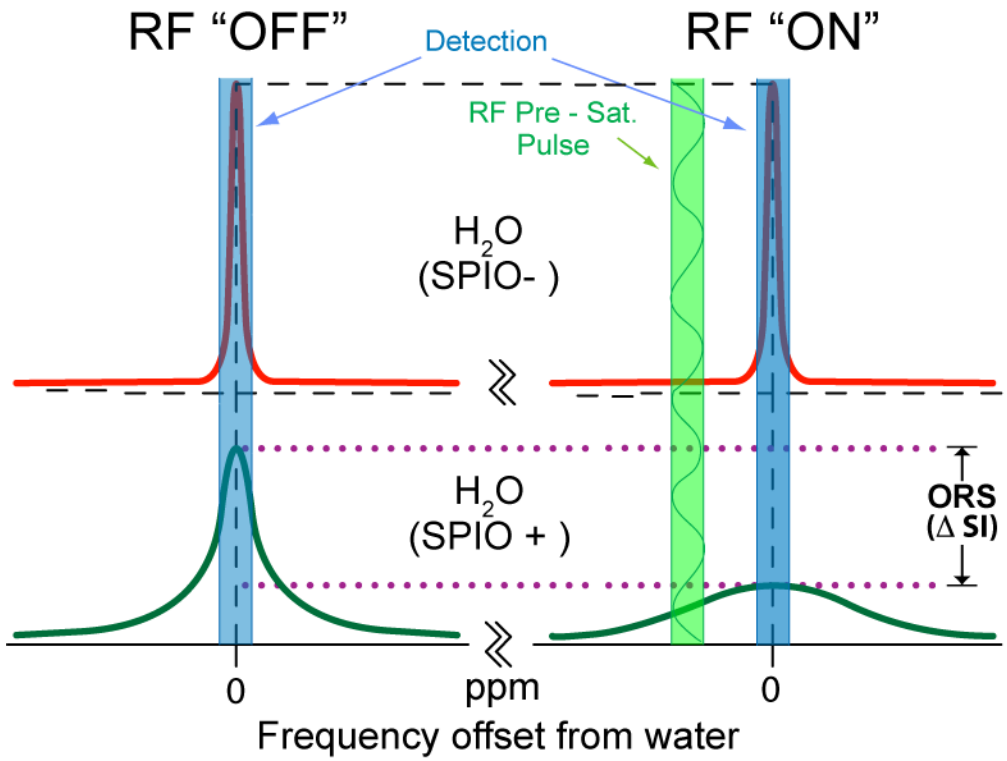

Figure 3.1 - Scheme of off-resonance saturation (ORS) method in the imaging of SPIO-based nanoparticles. This scheme depicts the NMR water peaks of water affected by SPIO (bottom) and not-affected by SPIO (top). The water affected by the SPIO has a broadened profile. This allows for the selective saturation of the broadened water population, water specifically effected by the SPIO, which generates ORS contrast when RF "ON" and RF "OFF" images are subtracted.

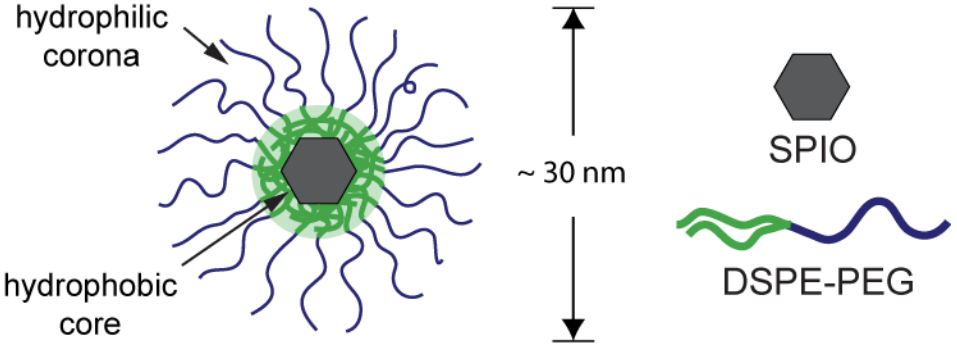

Figure 3.2 - Schematic of SPIO-loaded DSPE-PEG micelles.

3.2 Theoretical Model of ORS

In MRI numerous parameters are involved in creating an image's signal intensity and tissue contrast. To address the generation of ORS contrast a fast diffusing MR model must be taken into account. This model assumes that water molecules (protons) are fast diffusing rapidly between the hydrophilic shell of the SPIO-based nanoparticle and the bulk water population on a MR imaging time scale and can be characterized by a single set of T1 and T2 relaxation times.

To achieve an ORS effect a continuous wave pre-saturation RF pulse at power level of ω_1 (= $2\pi B_1$, B_1 in Hz) and frequency offset, Ω, from bulk water peak for a duration of t is applied, where the net magnetization vector (NMV) of the attenuated water signal can be described by the Bloch equation:[4]

$$\frac{dM(t)}{dt} = AM(t) + B \qquad \text{(Equation 1)}$$

where

$$M(t) = \begin{bmatrix} Mx(t) \\ My(t) \\ Mz(t) \end{bmatrix}, \qquad \text{(Equation 2)}$$

$$A = \begin{bmatrix} -\frac{1}{T_2} & -\Omega & 0 \\ \Omega & -\frac{1}{T_2} & -\omega_1 \\ 0 & \omega_1 & -\frac{1}{T_1} \end{bmatrix} \qquad \text{(Equation 3)}$$

and

$$B = \begin{bmatrix} 0 \\ 0 \\ Mz^0/T_1 \end{bmatrix} \qquad \text{(Equation 4)}$$

in which M_z^o is the equilibrium NMV in the z direction in the static external magnetic field along the longitudinal axis.

The solution for Bloch Equation can be expressed by:

$$M(t) = M^\infty + e^{At}(M^o - M^\infty) \qquad \text{(Equation 5)}$$

in which M^o is the NMV at initial state prior to saturation, and M^∞ is the so-called steady-state magnetization,

$$M^\infty = \begin{bmatrix} Mx^\infty \\ My^\infty \\ Mz^\infty \end{bmatrix} = -A^{-1}B, \qquad \text{(Equation 6)}$$

where the steady-state z-magnetization, Mz^∞, is given by:

$$Mz^\infty = \frac{(1+\Omega^2 T_2^2)Mz^o}{1+\Omega^2 T_2^2 + \omega_1^2 T_1 T_2} \qquad \text{(Equation 7)}$$

Note that the second term of Eq. 5 represents the difference of magnetization between the initial and steady-state, modulated by a time-dependent function e^{-At} (e^{-At} converges to 0 at $t \rightarrow \infty$).

A time dependent z-magnetization simulation illustrates the time-independence of the ORS effect (Mz/Mz^o) at several saturation pulse, B_1, power levels and T1 relaxation times (Figure 3.3). The curves indicate that an approximate full steady-state in Mz can be reached with an applied saturation pulse of sufficient time (a few hundred milliseconds to a few seconds). Moreover, increasing the B_1 power can facilitate the process of

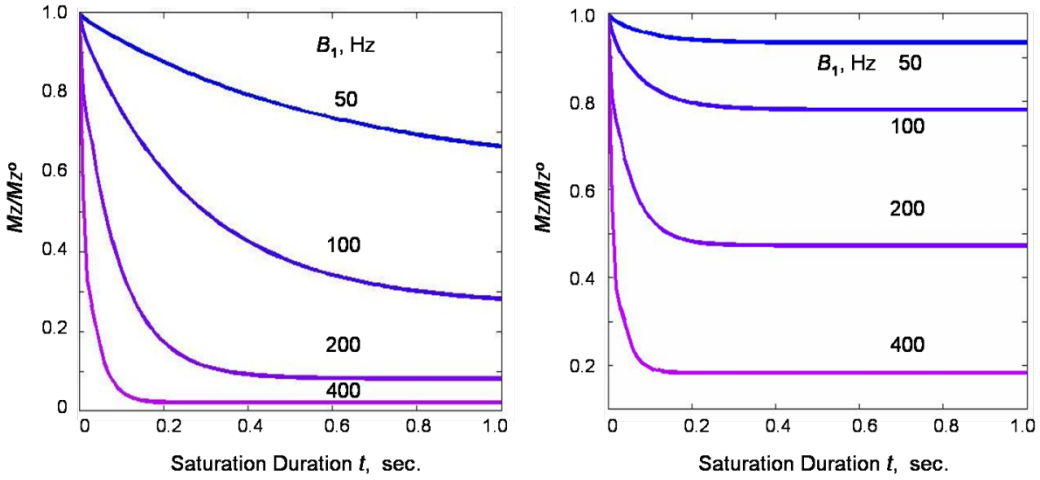

Figure 3.3 - Time dependence of the z-magnetization, *Mz*, at different B1 power levels. T1 = 1 s (left) and T1 = 0.1 s (right). Other simulation parameters are T2 = 10 ms and Ω = 600 Hz at 4.7T.

approaching a steady-state. Under these simulation conditions, a doubling in B_1 leads to roughly a 1-fold shortening in the approaching time for a steady–state. In regards to the T1 effect on steady-state, the longer the T1, the higher the saturation effect becomes and the longer it is required to reach steady state. The T1value not only affects the length of saturation pulse duration for a steady-state, but also the ORS level at the steady-state.

The steady-state z-magnetization equation (Equation 7) is of fundamental importance for understanding ORS effect and for optimization of experimental MRI parameters. It describes quantitatively how the ORS effect is dependent on RF saturation power B_1, saturation frequency offset Ω, and the relaxation times T1 and T2.

A simulated z-spectrum illustrates the Ω-dependency of the ORS effect (Mz/Mz^o) at three different T_2 conditions (10 ms, 1 ms and 0.1 ms), using the simulation data derived from Equation 7 (Figure 3.4). All the curves show that the attenuation of water signal, or ORS effect, increases as $|\Omega| \rightarrow 0$ ppm. However, a comparison among these different T2 curves indicates that, as $|\Omega| \rightarrow \infty$, the ORS effect of the long T2 component (10 ms) diminishes very rapidly while that of the short T2 component (0.1 ms) drops gradually. At Ω = 6 ppm, the attenuation remains above 30% for T2 = 0.1 ms but it almost fully disappears (0%) for T2 = 10 ms (Fig. 2). On the contrary, at the on-resonance saturation condition ($\Omega = 0$), a reversed order in signal attenuation is found for the T2 components. The data show a full saturation for T2 = 10 ms but only a ~60% saturation for T2 = 0.1 ms. One may further explore this on-resonance saturation method for imaging SPIO particles, for it is beyond the scope of this chapter.

Interestingly, when $|\Omega|$ is set in an intermediate frequency range, neither long (10 ms) nor short (0.1 ms) T2 signal experiences the largest attenuation. Instead, it is the intermediate T2 component (1 ms) which shows the largest signal saturation (Figure 3.4). Therefore, one can expect an optimal attenuation for a certain T2 at an appropriate $|\Omega|$ value. For a given T2 value, an optimal Ω value may be estimated by the following equation:

$$|\Omega|\ T_2 = 1 \qquad \text{(Equation 8)}$$

and the corresponding Mz/Mz^o value is $(1/(1 + \omega_1^2 T_1 T_2/2))$. On the other hand, if an improper Ω value is chosen, one may expect an undesirable ORS effect on the image contrast.

3.3 Materials and methods

3.3.1 Preparation of SPIO-loaded DSPE-PEG micelles

Fe_3O_4 nanoparticles (SPIO, 7±0.7 nm) were synthesized from iron(III) acetylacetonate in benzyl ether based on a published procedure.[5] The particles were size-selected by repeated precipitation with ethanol from hexane and subsequently characterized by transmission electron microscopy (TEM). Size distribution of SPIO nanoparticles was analyzed using ImageJ (National Institutes of Health, NIH). 1,2-Distearoyl-*sn*-glycero-3-phosphoethanolamine-*N*-methoxy-poly(ethylene glycol) (DSPE-PEG) with a PEG molecular weight of 5kDa were purchased from Avanti Polar Lipids, Inc. and used as received. SPIO-loaded micelles were prepared using a published procedure with slight modification.[6] Briefly, a mixture of SPIO (100 μg) and DSPE-PEG (2.5 mg) in THF was dried with a flow of argon generating a thin film. The film was rehydrated with pH 7.4 HEPES (10 mM) buffer that contains 150 mM NaCl (1 mL) at

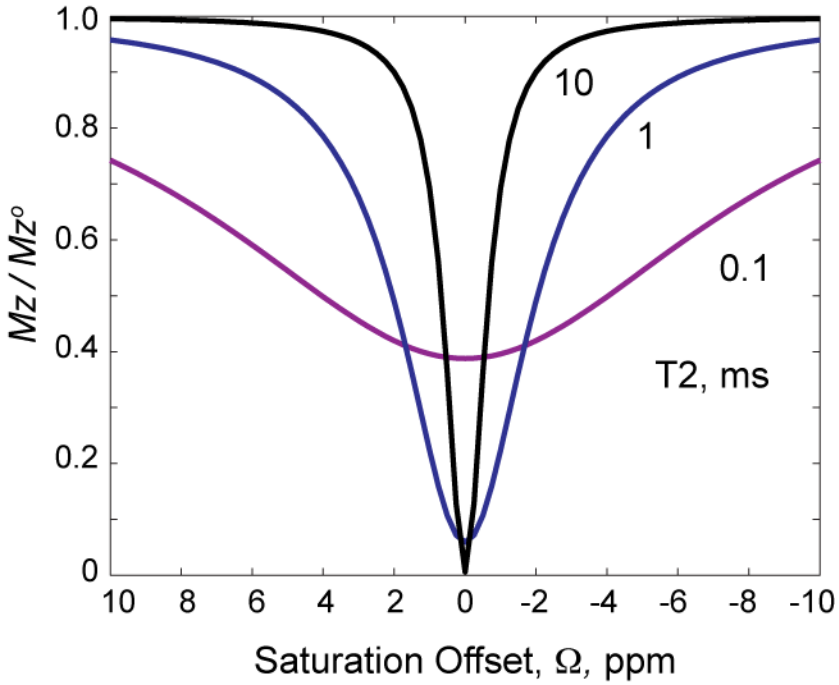

Figure 3.4 - Simulated z-spectrum at different T2 relaxation times. The faster the T2 the more broad the greater the ORS contrast at higher saturation offsets. Other simulation parameters are T1 = 10 ms, B_1 = 200 Hz and B_o = 7T.

70°C. The mixture was vortexed for 5 min and incubated at 70° C for 3 h with intermittent vortexing.

The resulting mixture was then diluted with deionized water (3 mL), filtered through a nylon filter membrane (size cutoff 0.2 μm), and then concentrated using Amicon Centrifugal Filter. The centrifugal concentration was repeated 2 cycles. Micelles were collected and the final volume was adjusted to 1 mL. Micelles were characterized by transmission electron microscopy (TEM) and dynamic light scattering (DLS). Sample preparation for TEM included staining carbon-coated grids containing micelles with 2% phosphotungstic acid (PTA, pH = 7.4). Iron concentration of the micelle solutions were measured using atomic absorption spectroscopy (AAS). First, a known volume of SPPM solutions were digested in aqua regia at 70 °C for 3 h. The solution was then diluted and the actual iron contents were determined using a Varian SpectrAA 50 (Varian) spectrometer. The calibration curve was obtained using an iron AA standard solution (Sigma Aldrich).

3.3.2 MRI phantom studies

All MRI experiments were conducted on a 4.7 or 7T Varian small animal horizontal bore MRI scanner a using a 40 mm i.d Litz coil (DOTY Scientific Inc.) or a 40 mm i.d. Millipede coil (Varian), respectively. For 4.7T analysis, a phantom was also constructed where micelles were put in micro-well plate in a 4x2 layout with increasing concentrations of micelle from bottom to top with the left column of wells filled with Eu(III) doped water. For 7T analysis, SPIO-loaded DSPE-PEG micelles were placed in a 1 mL plastic syringe with both ends sealed with paraffin wrap. The syringes containing

micelle solutions with different concentrations were inserted into a 10 mL plastic syringe, which was later filled with deionized water and sealed with paraffin. Once in the magnet the bulk water peak was shimmed to a line-width less than 100 MHz at both 4.7 and 7T.

At 4.7T, The T2 relaxation times of the phantom samples were measured by standard Carr-Purcell-Meiboom-Gill (CPMG) sequence with TR of 8.5 s and TE of 10, 14, 20, 34, 45, 65, 95 and 150 ms, respectively. The T1 relaxation rates of the samples were measured by the inversion recovery spin-echo pulse sequence with TR of 8.5 s, TE of 10 ms and TI of 100, 200, 400, 700, 1200, 2500 and 5000 ms. The null intensity point on the series of TI-varying MRI images for each solution was visually verified and was used to cross-check the T1 values obtained from data fitting the curves of MRI intensity *versus* TI. The 4.7T ORS study was carried out using a spin-echo pulse sequence modified by the addition of frequency-selective Gaussian-shaped pre-saturation pulse. The phantom studies were RF-irradiated at saturation B_1 power of 52 - 104 Hz at frequency offset of 2 kHz, 1 kHz, 800 Hz, 600 Hz, 400 Hz and 200 Hz (from bulk water signal, at low field side). A reference image was collected under the same condition but without saturation. The Mz/Mz^o division images were generated by pixel-by-pixel division of the saturation-on image by the reference image without pre-saturation. Other imaging parameters were given in the related figures and texts.

At 7T, T2 relaxation times of micelle solutions were determined using a fast spin echo pulse sequence with TR = 2s and TE of 7, 15, 20, 30, 45, 60, 90, 150, 300, 500 ms. ORS experiments were carried out using a spin echo (SE) pulse sequence (TR = 2s; TE = 8.5ms), with a saturation B_1 power of 2.6 μT for 0.5 s. The T1 relaxation times of the samples were measured by inversion recovery with a TR of 8.5 s, and TE of 10 ms and

the inversion times (TI) of 100, 200, 400, 700, 1200, 2500 and 5000 ms. The null intensity point on the series of TI-varying MRI images for each solution was visually verified and was used to cross-check the T1 relaxation times obtained from data fitting the curves of MRI intensity versus TI. ORS experiments were carried out using a spin echo (SE) pulse sequence (TR = 2s; TE = 8.5ms), with a saturation B_1 power of 2.6 μT (75.22 Hz at 7T) for 0.5 s. The saturation frequencies were 15, ±3, ±1.5, ±1.2, ±0.9, ±0.6, ±0.3, or 0 kHz from bulk water. The image obtained with the saturation frequency of 15 kHz (50 ppm) was used as a reference image. The Mz/Mz^o division images were generated by pixel-by-pixel division of the saturation-on image by the reference image without pre-saturation. Other imaging parameters were given in the related figures and texts. All experiments were conducted in triplicates.

3.3.3 RF pulse power calibration curve for 7T

A series of single pulses with a TR of 5 s were applied to a Gd phantom (0.125 mM, T1 = 1.3 s) at 7T. The RF pulse power, B_1, was set in dB. Flip angles were changed by adjusting pulse widths at each dB. An array of different pulse widths was applied and then the peak heights were recorded. A peak that shows maximum height corresponds to 90° RF pulse. The pulse width (at 90º time, μs) was then converted to 360° time by multiplying by four. Frequency (Hz) was calculated as the reciprocal of the 360° time (μs). B_1 (μT) was then obtained by dividing the frequency by 42.57 (1 Gauss = 100 μT; 1 Gauss = 4257 Hz; so 1 μT = 42.57 Hz). This calculation was performed at different dBs (ranging from 2 to 50 dB) to acquire the calibration curve (Figure 3.5).

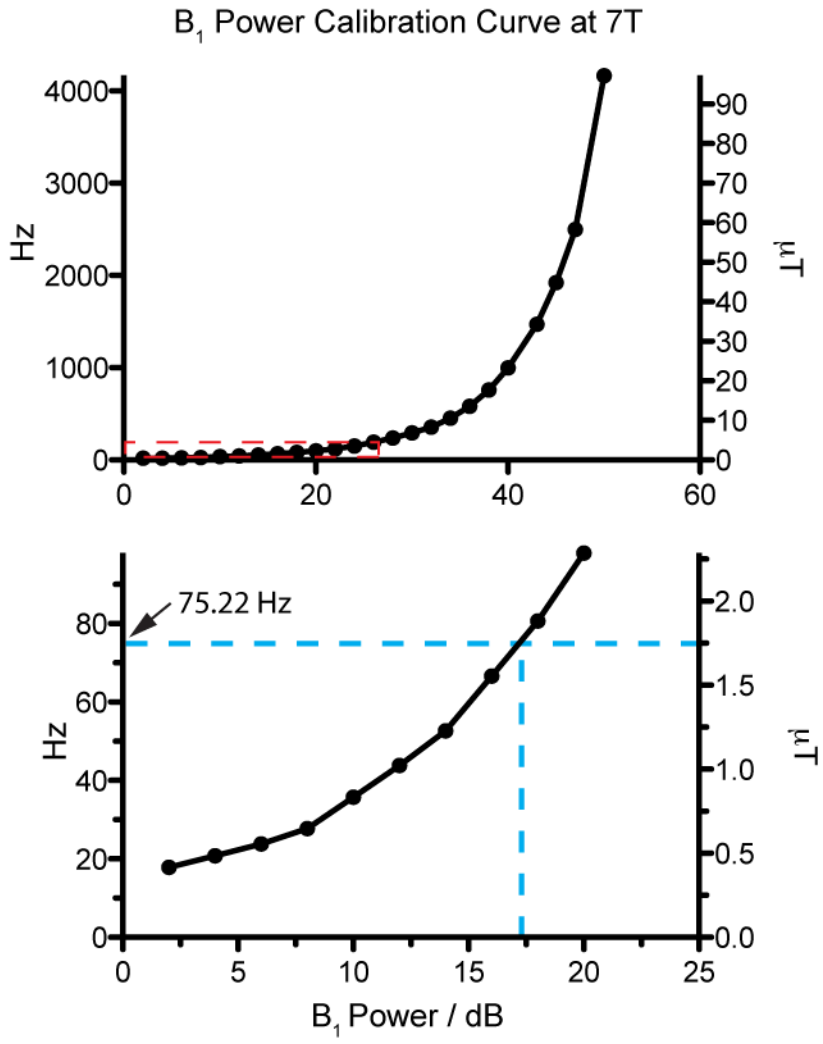

Figure 3.5 - RF-pulse power calibration curve for 7T Varian MRI scanner. (A) Graphs of the dB values from 0-60 (A) and 0-25 (B). Red box in A depicts the zoomed in region for B. dB values are set on the MRI console then converted from dB to Hz utilizing the power calibration curve, blue dashed line. For the simulations in Figure 3.4 a 75.22 Hz pre-saturation RF pulse was used in Equation 7 to calculate the ORS effect.

3.3.4 Data processing and MATLAB fitting of experimental ORS data

All MRI images were processed using ImageJ (free NIH software). All simulations of the ORS effects were done using an in-house program developed on Windows version of Matlab 7.0 (Mathworks). The m-code was then modified to incorporate and fit the experimental data using the theoretical model.

3.4 Results and discussion

3.4.1 Characterization of single SPIO-loaded DSPE-PEG micelles

Single SPIO-loaded DSPE-PEG micelles were produced by encapsulating a single SPIO (diameter: 7 ± 0.7 nm, Figure 3.6A) in the core of the phospholipid micelle. For all studies, SPIO was encapsulated in the micelle at 4 wt% to total lipid. Transmission electron micrographs revealed the spherical morphology of the DSPE-PEG micelle with diameters of 28.9 ± 3.4 nm (Figure 3.6B). Negatively stained samples highlighted the core-shell structure of the micelle with a single SPIO (black particle surrounded by white) loaded in the hydrophobic core (white area around SPIO) (Figure 3.6B and inset).

The MRI sensitivity of the SPIO-loaded DSPE-PEG was examined by obtaining the transverse relaxivity of the final formulation. A phantom with varying concentrations of micelle solutions was imaged using T2-weighted spin echo sequences with variable TE times at 7T. The transverse relaxivity of the micelle formulation was 109.4 $mM^{-1}s^{-1}$ Fe at 20° C.

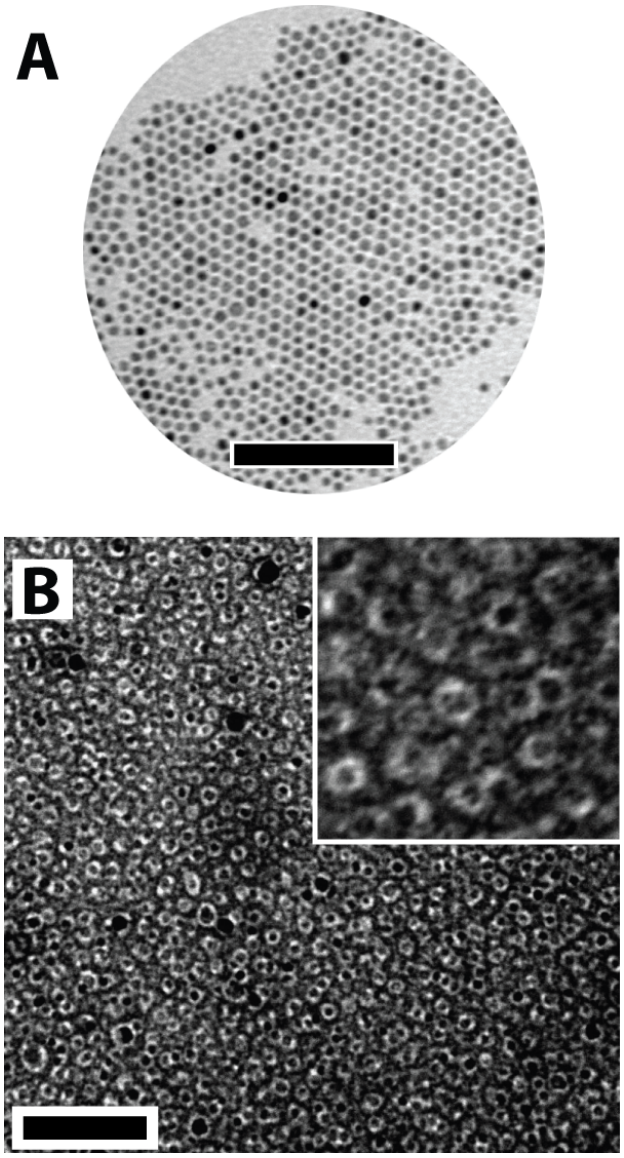

Figure 3.6 - TEM of synthesized SPIO (Fe_3O_4) (A) and SPIO-loaded DSPE-PEG micelles after staining with 2% PTA solution. Uniform loading of the micelle with a single SPIO nanoparticle can be seen. Inset is a magnification image of the same sample. Scale bars = 100 nm.

3.4.2 ORS model implications

The model simulations provide useful insights on the molecular mechanisms of ORS contrast and the identification of important parameters for ORS imaging. First, pre-saturation frequency offset, Ω, plays a critical role in ORS contrast. High Ω values will increase SPIO detection specificity, however, its sensitivity will be lessen due to the deceasing number of water protons at high Ω. On the other hand, low Ω values should provide a larger change in the proton density image (therefore larger ORS contrast), however, contrast at these Ω values is not linearly related to the T2 values, which makes the quantitative analysis of SPIO-based contrast agents concentration difficult. Therefore, lower T2 values (i.e. 100μs) will yield higher specificity for SPIO-based nanoparticles at high Ω values, leading to more sensitive and specific detection.

3.4.3 Experimental validation of ORS effect at 7T

The large dispersion of the transverse magnetization of the water proton's signal by SPIO-based nanoparticles allows for its detection by applying a B1 at a off-resonance frequency while keeping the non-SPIO containing water signal unaffected and silent (Figure 3.1). To explore the accuracy of our theoretical simulations, phantoms with SPIO-loaded micelles were utilized; (1) in an 8 micro-wells format and (2) in a 5 syringe phantom layout for 4.7T and 7T ORS imaging, respectively (Figures 3.7 and 3.8). In all cases the ORS effect was measured from ORS contrast images (Mz/Mz^o) generated from proton density-weighted (PD-w) images taken with (Mz) and without pre-saturation (Mz^o) while keeping other imaging parameters constant.

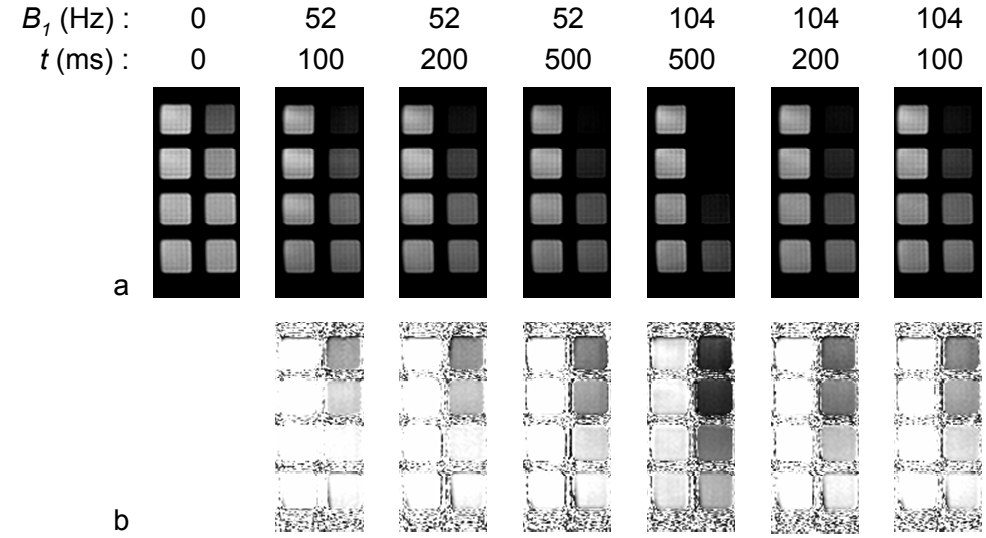

Figure 3.7 - Experimental analysis of the ORS effect at different pre-saturation pulse, B_1 power levels and durations, *t*. 4.7T PDw ORS RF "ON" images (a), and the corresponding ORS contrast images (b) of an SPIO phantom. For all the images, the left column contained Eu^{3+}- doped water and the right column contained SPIO encapsulated micelles with varying concentrations (0.08, 0.17, 0.41 and 0.83 mM Fe, from bottom to top). White represents no ORS enhancement (ratio = 1, as illustrated by the Eu^{3+}- doped water reference samples), while the black represents the largest ORS enhancement. Other MR acquisition parameters TR = 8.5 s, TE = 8 ms, resolution 0.3x0.3x6 mm^3 and Ω = 400 Hz.

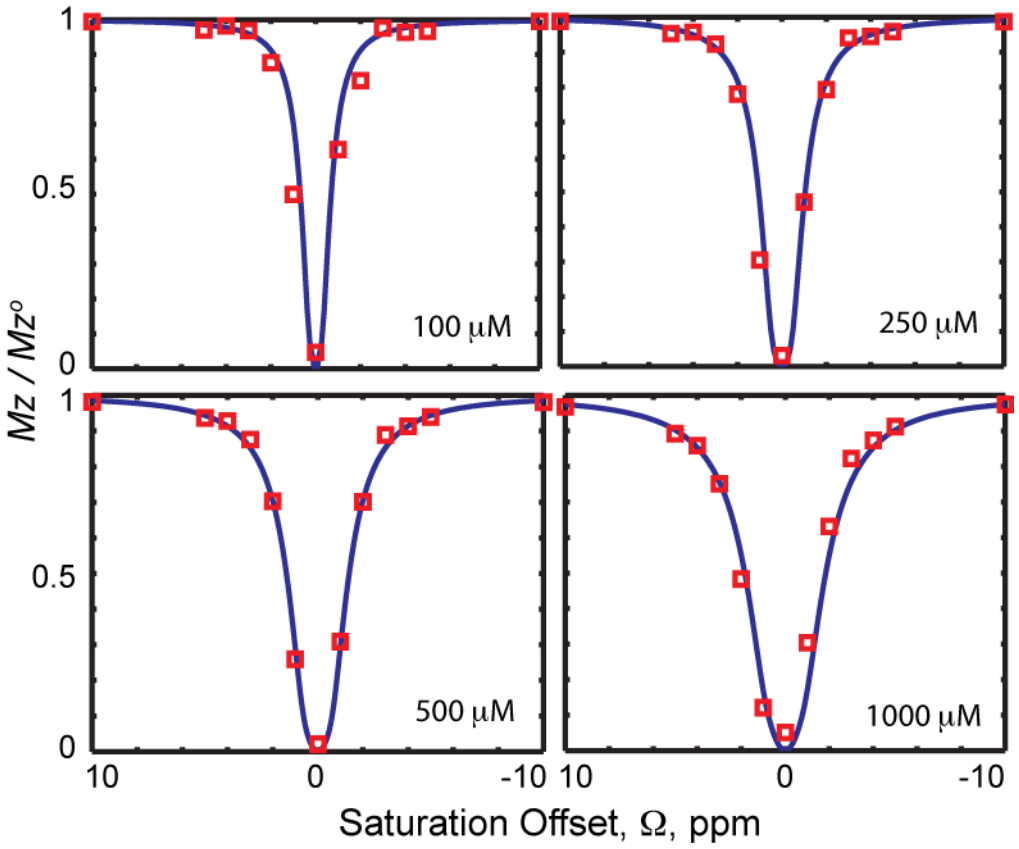

Figure 3.8 - Simulated and experimental Z-spectra from of SPIO-loaded DSPE-PEG micelle samples at 1000, 500, 250 and 100 μM Fe at 7T. Experimental data are shown as red squares and the curves were calculated using Equation 7 and with experimentally measured T1 and T2 relaxation times for the corresponding samples (Table 3.1). N = 3; mean values displayed.

In agreement with theoretical simulations (Figure 3.3), the 4.7T phantom study showed that increasing the RF pulse power (B_1) and duration (*t*), from and 52 to 104 Hz and 0 to 500 ms, respectively, causes the SPIO-loaded wells to progressively darken, while the brightness of the reference (Eu(III) dope water) remained unchanged, with the full steady-state in *Mz* being reached with a B_1 power of 104 Hz and a duration of 500 ms (Figure 3.7). PD-w images with a B_1 power 104 Hz and saturation durations ranging from 600 ms to 1 s showed no increase in the darkening of wells (data not shown). Thus, confirming that a steady-state in *Mz* can be reached as long as the saturation duration is of sufficient time. Furthermore, the increase in B_1 power level from 52 Hz to 104 Hz leads to a corresponding ORS effect increase, as expected from theoretical Equation 5 and Figure 3.3. Moreover, the amount of water signal attenuation is consistent with the SPIO-micelle concentrations, and in agreement with the results estimated from their T1 and T2 relaxation times.

In this study, the syringe phantom and the 7T MRI scanner were utilized to demonstrate the ORS effect on at the 7T magnetic field strength and equipment compatibility between 4.7T and 7T for ORS imaging. Specifically the phantom was used to demonstrate the off-resonance frequency, Ω, dependency of the ORS effect by imaging with a constant B1 at 75.22 Hz (Figure 3.5) at varying Ω values from 15 kHz to 300 Hz (i.e. from 50 ppm to 1 ppm) both on the high and low field sides of bulk water signal (0 ppm). The ORS effect could be measured at as far as 5 and 4 ppm up-field in the most concentrated sample, 1000 μM Fe (Figure 3.8). The predicted increase in darkening occurred in parallel with increases SPIO concentration compared across a single Ω value.

But for the most diluted micelle sample, 100 μM Fe, the ORS effect was not apparent until the Ω value approached 2ppm offset from the bulk water peak (i.e. same Mz/Mz^o value as the 1000 μM Fe sample at 5ppm). Thus, supporting the simulation data that the ORS effect is highly dependent on the T2 of the SPIO-based contrast agent and that an optimal Ω value may exist for each type of contrast agent as well. Moreover, the experimental data from the phantom at 7T (red squares, Figure 3.8) correlate with the predicted ORS effect outlined in Equation 7 (blue line, Figure 3.8). For each concentration examined the T1 and T2 rates where experimentally found and where incorparted into Equation 7 to predict the Mz/Mz^o curves (Table 3.1 and blue line in Figure 3.8).

In conclusion, we have validated the theoretical model and demonstrated MR imaging contrast generated by the ORS effect when imaging SPIO-loaded DSPE-PEG micelles in an in vitro phantom setting. The ORS effect can be quantified as the ratio of Mz/Mz^o, where Mz and Mz^o are the magnitudes of water z-magnetization (net magnetic vector (NMV) in the z-direction) with and without pre-saturation RF pulse (B_1), respectively. Lower Mz over Mz^o ratio results in larger ORS effect. The proper parameter settings, in particular B_1 power and duration and off-resonance frequency, Ω, are critical and highly dependent on inherent properties (i.e. relaxation rates T1 and T2) of the SPIO-based contrast agent, as described in Equation 7. Specifically, in our demonstration of the ORS effect, a soft saturation pulse with B_1 power of 50-100 Hz, duration of 500 ms and varying frequency offsets, Ω, were used, so that the observed ORS effect correlated well by the proposed fast diffusion model. Meanwhile, with short RF pulse saturation (~ ms) and large B_1 power (~ 1 kHz), the selectivity in saturation frequency may be

Table 3.1 - T1 & T2 relaxation rates of SPIO-loaded DSPE-PEG micelles

[SPIO] / μM Fe	T1 / ms	T2 / ms
50	2454 ± 62.4	145 ± 10
100	2252 ± 82.7	86.4 ± 9.6
250	1773 ± 193	34.9 ± 6.1
500	1229 ± 130	18.2 ± 2.3
1000	822.8 ± 173	9.19 ± 1.3

compromised and contribution from slow water diffusion may need to be considered. In such a case, a more comprehensive model cooperating the current fast diffusion model with other types of models might be more appropriate.[7,8] However, as long as specific absorption rate (SAR) for patient safety is assured, one can use a higher B_1, which will have the benefit of increasing the ORS effect and shortening the saturation duration. This, combined with clinically available fast sequences such as FLASH, as demonstrated by Hu and coworkers could make ORS a very powerful tool for evaluating SPIO-based nanoparticles in molecular imaging applications.[2]

Further phantom and in vivo validation of the ORS effect and its imaging contrast as an application for molecular imaging of tumor angiogenesis will be investigated in the Chapter 4. Ongoing work in the lab aims to correlate the structure-property and magneto-physical relationships of SPIO-based contrast agents and potential ORS effect.

3.5 References

1. Seppenwoolde JH, Viergever MA, Bakker CJ. Passive tracking exploiting local signal conservation: the white marker phenomenon. Magn Reson Med 2003;50(4):784-790.
2. Zurkiya O, Hu X. Off-resonance saturation as a means of generating contrast with superparamagnetic nanoparticles. Magn Reson Med 2006;56(4):726-732.
3. Khemtong C, Kessinger CW, Ren J, et al. In vivo off-resonance saturation magnetic resonance imaging of alphavbeta3-targeted superparamagnetic nanoparticles. Cancer Res 2009;69(4):1651-1658.

4. Hinton DP, Bryant RG. 1H magnetic cross-relaxation between multiple solvent components and rotationally immobilized protein. Magn Reson Med 1996;35(4):497-505.

5. Sun S, Zeng H, Robinson DB, et al. Monodisperse MFe2O4 (M = Fe, Co, Mn) nanoparticles. J Am Chem Soc 2004;126(1):273-279.

6. Dubertret B, Skourides P, Norris DJ, Noireaux V, Brivanlou AH, Libchaber A. In vivo imaging of quantum dots encapsulated in phospholipid micelles. Science 2002;298(5599):1759-1762.

7. Henkelman RM, Stanisz GJ, Graham SJ. Magnetization transfer in MRI: a review. Nmr Biomed 2001;14(2):57-64.

8. Yarnykh VL. Pulsed Z-spectroscopic imaging of cross-relaxation parameters in tissues for human MRI: Theory and clinical applications. Magnet Reson Med 2002;47(5):929-939.

CHAPTER FOUR

In Vivo Off-Resonance Saturation MRI of αvβ3-Targeted SPPM

4.1 Introduction

New contrast mechanisms and imaging probes have been actively pursued for cancer molecular imaging by magnetic resonance imaging (MRI). Chemical-exchange saturation transfer (CEST), a new contrast mechanism where a radiofrequency irradiation is used to noninvasively saturate agent protons that exchange with water, has led to many novel molecular imaging agents to monitor pH, glucose, and gene expression.[1-4] For most CEST probes and conventional T1 contrast agents (e.g. Gd-DTPA), however, their detection limits are above micromolar (μM) concentrations, which makes it a considerable challenge to visualize specific disease markers at much lower physiological concentrations (e.g., <nM).[3,4] Recently, superparamagnetic nanoparticles (e.g., Fe_3O_4, $MnFe_2O_4$, FeCo) have received considerable attention as molecular imaging probes with substantially higher molar relaxivities over small molecular T1 agents.[5-8] Once bound to a targeted marker or after internalization into a cell, superparamagnetic probes can create substantial disturbances in the local magnetic field leading to a rapid dephasing of protons and loss of MR signal intensity. Conventionally, T2*-weighted (T2*-w) method serves as the gold standard for the imaging of superparamagnetic probes where a pre-contrast scan and a post-contrast scan are required to visually detect contrast changes. This method is prone to image artifacts due to B_0 inhomogeneity and is quite limited when a slight position change occurs between MR scans, which can considerably deteriorate the detection accuracy of imaging probes in subtracted images.

In this report, we describe the use of superparamagnetic polymeric micelles (SPPM) in combination with an off-resonance saturation (ORS) method for in vivo molecular imaging of cancer (Figure 4.1A). Polymeric micelles are a new class of self-assembled nanoparticles with a core-shell architecture wherein the hydrophobic core serves as a natural carrier environment for hydrophobic agents and the hydrophilic shell provides particle stabilization and multi-valent molecular targeting.[9] Clustering of superparamagnetic iron oxide (SPIO) nanoparticles inside the hydrophobic core of a micelle dramatically increased the T2 relaxivity (e.g., r2 = 471 Fe $mM^{-1}s^{-1}$ at 1.5 T, >10 times increase over single SPIO particles at the same Fe concentration).[10] Surface functionalization of SPPM by a cyclic(RGDfK) ligand (cRGD) allowed the effective targeting of αvβ3 integrins on tumor endothelial cells and subsequent receptor-mediated endocytosis of micelles in vitro.[11] Here we employ a new off-resonance saturation (ORS) method for imaging of cRGD-encoded SPPM in angiogenic tumors in mice.[12] Similar to CEST, the ORS method applies a pre-saturation pulse that can turn "ON"/"OFF" the probe contrast. Unlike CEST where a specific exchangeable proton frequency is pre-saturated, the ORS method pre-saturates at an off-resonance frequency position away from the bulk water. This SPPM-induced ORS contrast is illustrated in Figure 4.1B. In the absence of SPPM, the pre-saturation RF pulse has little effect on the signal intensity of SPPM-free water (top panel in Figure 4.1B); in the presence of SPPM, the RF pulse can saturate a larger volume fraction of water molecules due to proton relaxation by SPPM, which can lead to a considerable decrease in signal intensity (ΔSI, bottom panel). Due to the rapid diffusion of water molecules, ORS contrast can be significantly amplified.[12] We illustrate that the ORS method can detect picomolar (10^{-12} M)

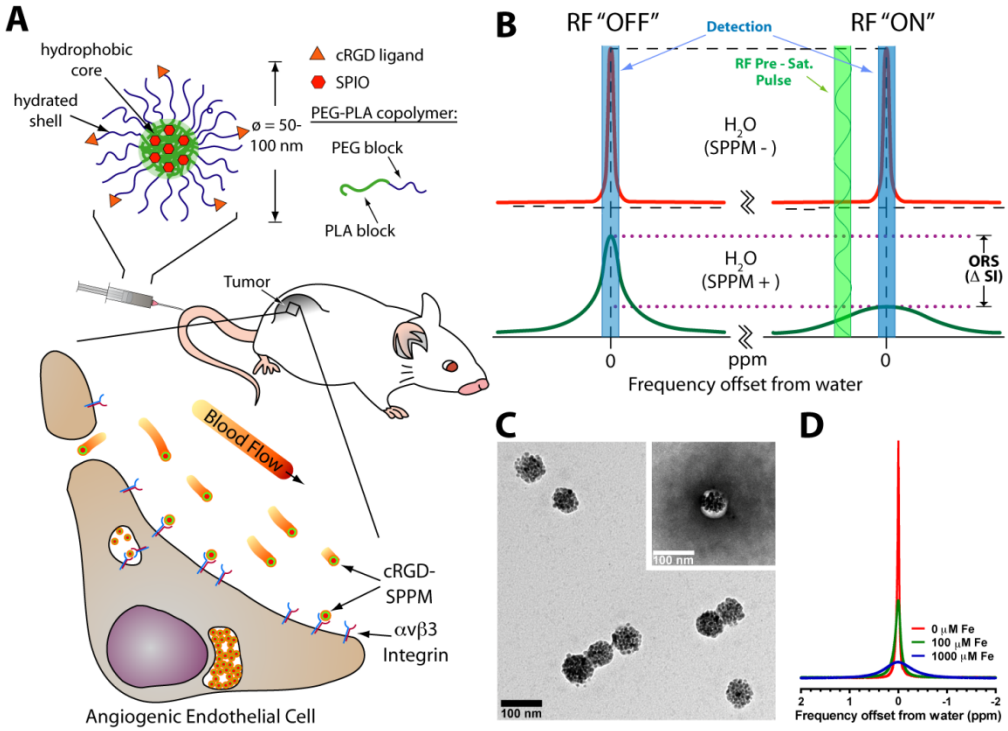

Figure 4.1 - Cancer molecular imaging using cRGD-encoded SPPM and off-resonance saturation (ORS) MRI. (A) Schematic illustration of a cRGD-encoded SPPM and its targeting to αvβ3-expressing endothelial cells in the tumor vasculature. (B) Mechanism of SPPM-induced ORS contrast. Pre-saturation RF pulse results in significant decrease in signal intensity (ΔSI) in SPPM(+) H_2O over SPPM(-) H_2O. (C) TEM image of a representative SPPM sample. The inset shows a SPPM particle after negative staining with 2% PTA solution. (D) ^1H NMR (300 MHz) spectra of water containing different concentrations of SPPM (in [Fe]/μM). *Modified from Cancer Res 2009 69(4).*

concentrations of SPPM in vitro, and demonstrate an improved ability to detect angiogenic tumors using cRGD-encoded SPPM probes over traditional T2*-w imaging method.

4.2 Materials and Methods

4.2.1 Production of cRGD-encoded and cRGD-free SPPM

cRGD-encoded and cRGD-free SPPM were prepared according to a previously published procedure.[11] Iron contents were determined on a Varian SpectrAA 50 spectrometer (air/acetylene flame). Amino acid quantities in the cRGD-encoded SPPM sample were analyzed by the W.M. Keck Facility, Yale University. Micelles were characterized by TEM, dynamic light scattering (DLS).

4.2.2 MRI parameters

All MRI experiments were conducted on a 4.7 T Inova horizontal scanner (Varian, Palo Alto, CA) using a Litz coil (diameter 4 cm, length 8 cm, DOTY Scientific Inc., NC) at either RT (~20°C) for the phantom samples or 37°C for the animal studies. Concentrations of SPPM in the phantoms, presented as molar concentrations of iron, were 0, 2, 5, 10, 20, 50 and 100 μM. Each SPPM solution (100 μL) was added into wells of 5 x 5 well plates. ORS experiments were carried out using a spin-echo (SE) pulse sequence (TR = 2 s, TE = 12 ms) modified by the addition of a frequency-selective Gaussian-shaped pre-saturation pulse. The phantom and animal studies were RF-irradiated at a saturation B_1 power of 3.85 μT for 0.5 s at frequency offsets of 0, ± 200, 400, 500, 600, 700, 800, 900, 1k, 2k and 4 kHz from bulk water. Reference images were collected using identical settings but without the pre-saturation pulse. The ORS contrast

images were generated by pixel-by-pixel subtraction of the saturation "ON" image by the reference image. The T2*-w method was acquired using a gradient echo sequence (TR = 400 ms, TE = 5, 10 and 20 ms, flip angle 20°). All MRI images were processed using ImageJ (NIH). The pre- and post-injection ΔORS images were displayed in the same scale using the phase LUT in ImageJ. The p values were calculated using the Student's two-tailed t-test ($p \leq 0.05$ is considered statistically significant).

4.2.3 Animal studies

All procedures were approved by the Institutional Animal Care and Use Committee at UT Southwestern Medical Center. A human non-small cell lung cancer A549 xenograft model in athymic female nude mice (18-22 g) was used, with 5 x 10^6 cells injected subcutaneously into both flanks. Tumors were allowed to reach adequate size (~200-400 mm^3) prior to injection of SPPM particles. For intratumoral studies, tumor-bearing mice were sacrificed before scanning to avoid the perfusion loss of SPPM nanoparticles. The animals were first imaged by the T2*-w and ORS methods to obtain the pre-injection images. SPPM particles (20 μL, 250 μg Fe/mL) were then directly injected into one tumor and the resulting animals were imaged again to obtain post-injection images. For intravenous studies, cRGD-encoded SPPM, cRGD-free SPPM, and a combination of cRGD-encoded SPPM and free cRGD peptide (18 molar excess) were injected at a dose of 6 mg Fe/kg through the tail vein. During MRI, mice were maintained under anesthesia with 1.5% isoflurane combined with 60:40 oxygen:nitrogen at a flow rate of 500-1000 mL/min delivered to the free-breathing animal via a face mask. Temperature was maintained using a warming blanket with circulating water at 37°C.

After MR imaging, mice were sacrificed and tumor tissues and other organs harvested for histological analysis.

4.2.4 Immunohistochemical staining for αvβ3 integrin

Dissected tumor tissue was snap-frozen in optimal cutting temperature media and sectioned at 5μm thickness. Sections were then fixed in -20 °C acetone, blocked, and reacted with a hamster anti-mouse β3 integrin antibody (BD Pharmingen #550541) and a secondary biotinylated anti-hamster antibody (BD Pharmingen #550335). To visualize the integrin, streptravidin - HRP peroxidase and DAB substrate were used (BD Pharmingen #550946 and #550880, respectively).

4.2.5 Pharmacokinetic and biodistribution of SPPM nanoprobes

Experiments involving radioactive materials were approved by the Radiation Safety Committee at UT Southwestern Medical Center. ^{3}H (or T)-labelled cRGD encoded and cRGD-free SPPMs were prepared from 75% MeO-PEG-PLA-C(O)CT_3 and 25% MAL-PEG-PLA. For the plasma concentration-time experiment, mice bearing A549 tumors were randomly divided into 2 groups (N = 4 for each group) for cRGD-encoded SPPM and cRGD-free SPPM. The mice were injected with SPPM solutions via tail vein. Blood was collected via ocular vein at 1 min, 1, 2 , 4 , 8 , 12, and 24 hrs after the injection. Plasma was isolated from red blood cells by centrifugation at 1000 rpm for 10 min. The plasma was subsequently mixed with a tissue solubilizer solution (1 mL, BTS-450, Beckman, CA) at room temperature for 5 hrs followed by an addition of a liquid scintillation cocktail (10 mL, Ready Organic™, Beckman, CA) for 12 hrs. Amount of radioactive isotope was measured by a liquid scintillation counter (Beckman LS 6000 IC). Biodistribution of SPPM particles in tumor and other tissues were

performed in a separate group of A549 tumor-bearing mice (n=3 for each SPPM group). Three formulations were examined: cRGD-encoded SPPM, cRGD-free SPPM and cRGD-encoded SPPM co-injected with free cRGD (18 molar excess). One hour after SPPM injection, mice were perfused with PBS buffer (~30 mL). Dissected organs were weighed, homogenized, and treated with scintillation cocktails. The SPPM distribution in different organs/tissues was calculated as the percentage of injected dose per gram of tissue.

4.2.6 Prussian blue staining of tumor tissue

Tumors were fixed in 10% formalin and cryoprotected with 10% and 18% sucrose solutions. Tissues were then snap-frozen in optimal cutting temperature medium and sectioned at 8 μm. For Prussian blue staining, sections were rinsed in distilled water and then incubated in a 1:1 solution of 10% aqueous solution of potassium ferrocyanide and 20% hydrochloric acid for 30 mins, and then rinsed and counterstained with nuclear fast red.

4.3 Results

4.3.1 Characterization of SPPM nanoprobes

To achieve the ultra-sensitivity of SPPM, we used a high loading density (33 wt%) of SPIO nanoparticles in poly(ethylene glycol)-block-poly(D,L-lactide) (PEG-PLA, MWs for PEG and PLA blocks are 5 kD) micelles. Hydrophobic, monodisperse SPIO nanoparticles (9.9±0.4 nm in diameter) were used in these studies (Figure 4.2). Figure 4.1C shows a bright field TEM image of a representative sample with each SPPM containing a cluster of SPIO nanoparticles (45±14 SPIO per SPPM, n = 72, ~9 x 10^5 Fe ions). The inset in Figure 4.1C shows the same SPPM sample after staining with an

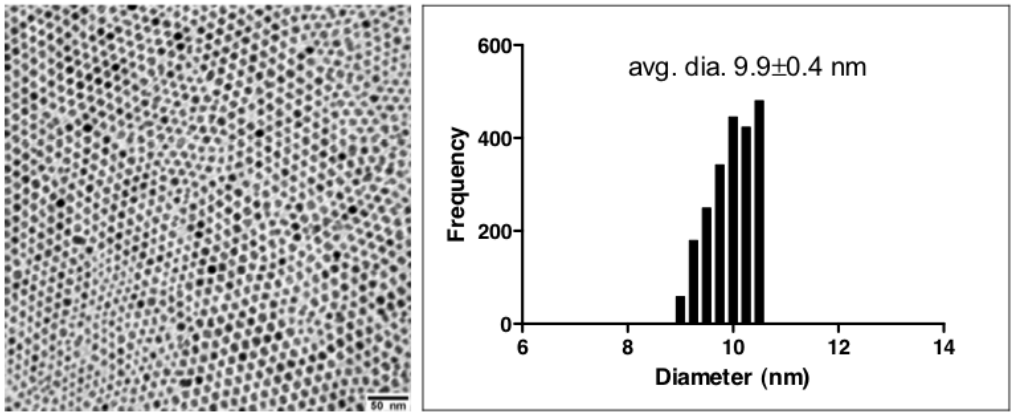

Figure 4.2 - TEM micrograph and size distribution of SPIO nanoparticles. Left panel shows TEM micrograph of synthesized SPIO nanoparticles on a carbon grid. Scale bar is 50 nm. Right panel is the size distribution of the SPIO nanoparticles pictured in left panel. The mean diameter of the SPIO were 9.9±0.4 nm (mean ± s.d.). *Modified from Cancer Res 2009 69(4).*

aqueous solution of 2% phosphotungstic acid (PTA). Due to their hydrophobic nature, micelle cores were not stained by PTA, and hence, showed up as white circles encapsulating a cluster of SPIO nanoparticles. The diameter of SPPM particles was 75±11 nm (n=52) as determined by TEM. Consistent with this analysis, DLS of SPPM solutions showed a single size distribution with an average hydrodynamic diameter of 70±11 nm. The slightly larger micelle diameter estimated by TEM compared to DLS (although not statistically significant) may reflect micelle spreading on the TEM grid during the sample drying process. ^{1}H-NMR (300 MHz) spectra of aqueous solutions containing different concentrations of SPPM particles are shown in Figure 4.1D. Significant peak broadening was observed with increasing Fe concentrations. The strong proton relaxation effects of the SPPM nanoparticles provided the physical basis for ORS imaging (Figure 4.1B).

4.3.2 Surface functionalization of SPPM with cRGD peptide

In a previous publication, we demonstrated that 1H NMR was able to follow the conjugation of cRGD (via the appearance of aromatic protons from D-Phe at δ = 7.4 ppm) to maleimide group (through the disappearance of its vinyl protons at δ = 6.75 ppm after conjugation) on the micelle surface.[13] In this study, we further quantified the amount of cRGD peptide on the SPPM by amino acid analysis. The cRGD-encoded SPPM was dissolved in a strong acid (6 N HCl) at an elevated temperature (115ºC) to ensure a complete hydrolysis of the peptide and dissociation from the polymer chains. The cRGD density on the surface of SPPM was calculated as a mole percentage of the peptide over that of the PEG-PLA copolymer. The density of the cRGD peptide was 18%, with approximately 1 in every 6 polymer chains conjugated with a cRGD peptide.

4.3.3 Imaging of SPPM phantoms

We first investigated the ORS contrast of SPPM particles in aqueous solutions (Figure 4.3A). The ORS experiment was performed using a spin-echo (SE) pulse sequence (TE = 12 ms, TR = 2 s) modified by the addition of a frequency-selective Gaussian-shaped pre-saturation pulse. Radiofrequency (RF) irradiation was applied using a B_1 of 3.85 μT for 0.5 s at frequency offsets of ±200, 400, 500, 600, 700, 800, 900, 1k, 2k and 4 kHz from bulk water. The frequency offsets correspond to ±1, 2, 2.5, 3, 3.5, 4, 4.5, 5, 10 and 20 ppm, respectively (only data from ±1, 2, 3 ppm were shown in Figure 4.3A). Reference (ORS OFF) images (left column in Figure 4.3A) were collected using identical settings, but without the pre-saturation pulse. Figure 4.3A shows that addition of a pre-saturation RF irradiation at the bulk water resonance frequency darkened the MR intensity for all samples including SPPM-free water. When a RF pulse was applied at an off-resonance frequency, MR intensity of SPPM-free water increased as the pre-saturation frequency was moved away from water and became comparable to that without the pre-saturation pulse. In comparison, in SPPM-containing samples, higher SPPM concentrations and smaller frequency offsets resulted in more pronounced image darkening effects and ORS contrast. To better illustrate ORS contrast, ORS subtraction images were calculated by pixel-by-pixel subtraction of intensities of pre-saturation images from those of corresponding reference images without pre-saturation (Figure 4.3B). Two general trends can be observed: (1) at the same offset frequency, higher SPPM concentrations yield greater ORS contrast; (2) at equivalent SPPM concentrations, a decrease in the value of the offset frequency leads to greater ORS contrast. It should be noted that it is the value, not the sign, of the saturation-pulse offset that affects the ORS

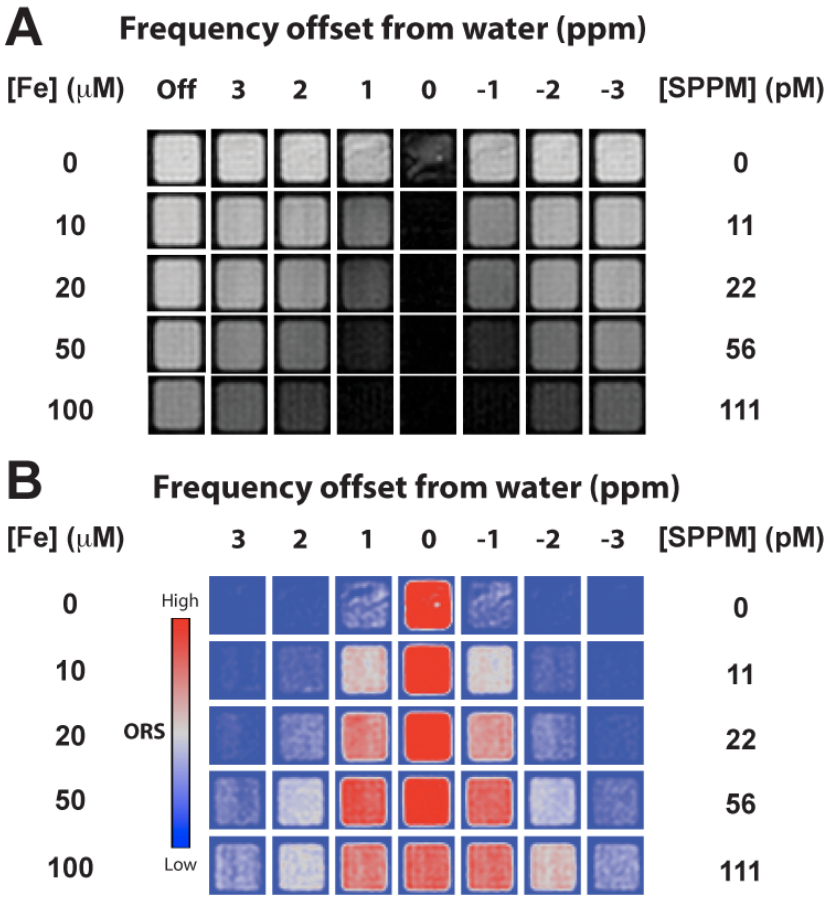

Figure 4.3 - ORS images of SPPM in aqueous solution. (**a**) ORS images of SPPM solutions at selected saturation frequency offsets (ORS ON) and reference images (ORS OFF) without pre-saturation (left-column). (**b**) ORS contrast images obtained by subtracting ORS ON images from the ORS OFF images. SPPM concentration was calculated by dividing [Fe] over the number of Fe ions per SPPM particle (i.e., 9 x 10^5). *Modified from Cancer Res 2009 69(4).*

contrast in the phantom samples (i.e., ORS contrast is symmetrical around the bulk water peak, see Figures. 4.3B and 4.4).

To quantitatively compare the imaging sensitivity between the ORS and T2*-w methods, we plotted the normalized signal intensity of SPPM sample to water as a function of Fe concentrations (Figure 4.5). Gradient echo sequence was used to acquire the T2*-w images (flip angle = 20°, TR = 400 ms, TE = 5, 10 and 20 ms). Longer TE times (TE > 30 ms) resulted in considerable image artifacts in T2*-w images (data not shown) and were not used. The same set of SPPM phantom samples (0, 2, 5, 10, 20, 50 and 100 μM [Fe]) were imaged at four independent times by the T2*-w and ORS methods, and the standard deviation from each sample was calculated to evaluate the imaging reproducibility. Data show that normalized signal intensity decreased with an increase in SPPM concentrations for both T2*-w and ORS methods. However, data variation is considerably greater with the T2*-w method (10-20%, Figure 4.5A) than the ORS method (2-10%, Figure 4.5B). We determined the values of S_{90} (SPPM concentration at which signal intensity decreased by 10% from water) from both methods. In the T2*-w method, the S_{90} values are 58 ± 21, 18.5 ± 7.5, and 7.5 ± 2.7 pM SPPM (n=4) for TE at 5, 10 and 20 ms, respectively (Figure 4.5A shows S_{90} as the vertical dashed lines in [Fe]). In the ORS method, the S_{90} values are 21.3 ± 3.7, 10.1 ± 0.8, and 6.1 ± 0.2 pM SPPM (n=4) for ORS OFF and ON at 3 and 2 ppm frequency offset, respectively (Figure 4.5B). It is worth noting that both methods can detect picomolar concentrations of SPPM nanoparticles, however, image reproducibility is much higher in the ORS method than the T2*-w method. In the following animal

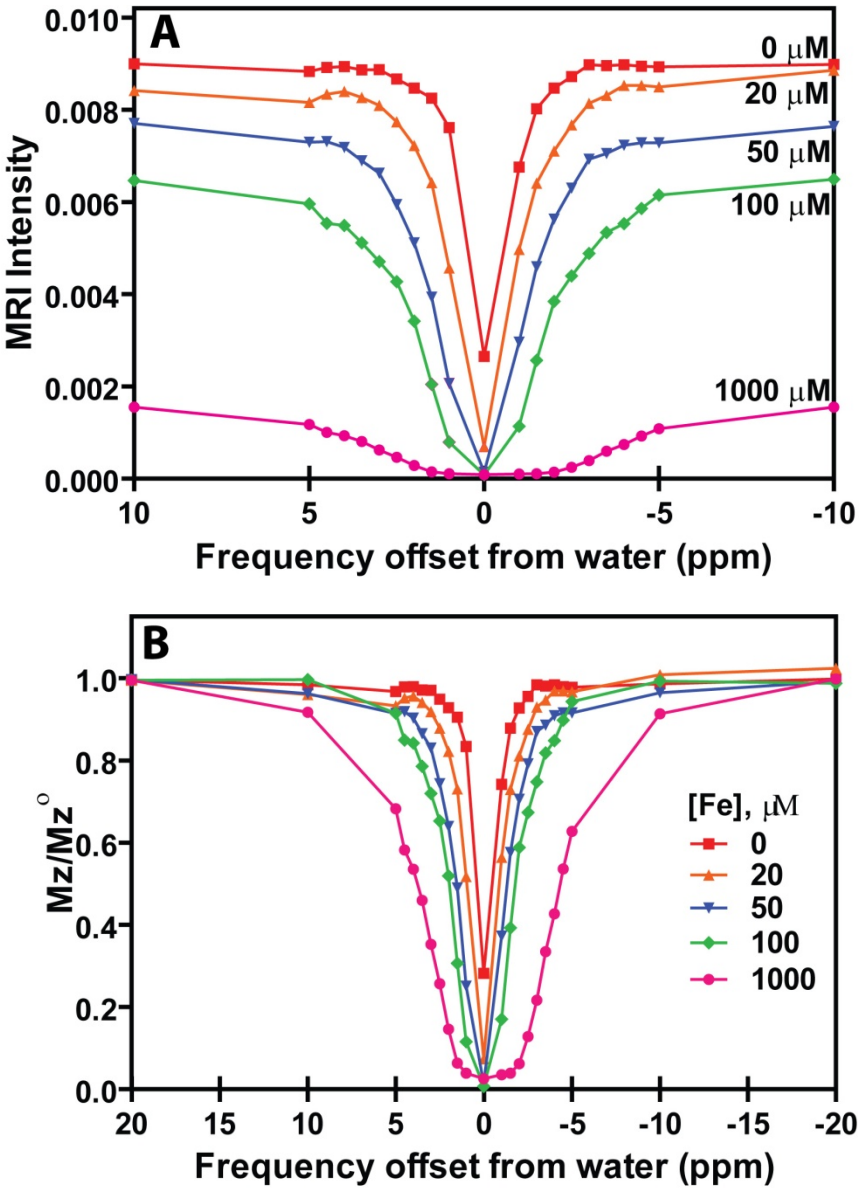

Figure 4.4 - MRI intensity (A) and Mz/Mz^o (B) of SPPM phantoms at 4.7T. Mz and Mz^o are the magnitudes of water z-magnetization with and without pre-saturation RF pulse, respectively. *Modified from Cancer Res 2009 69(4).*

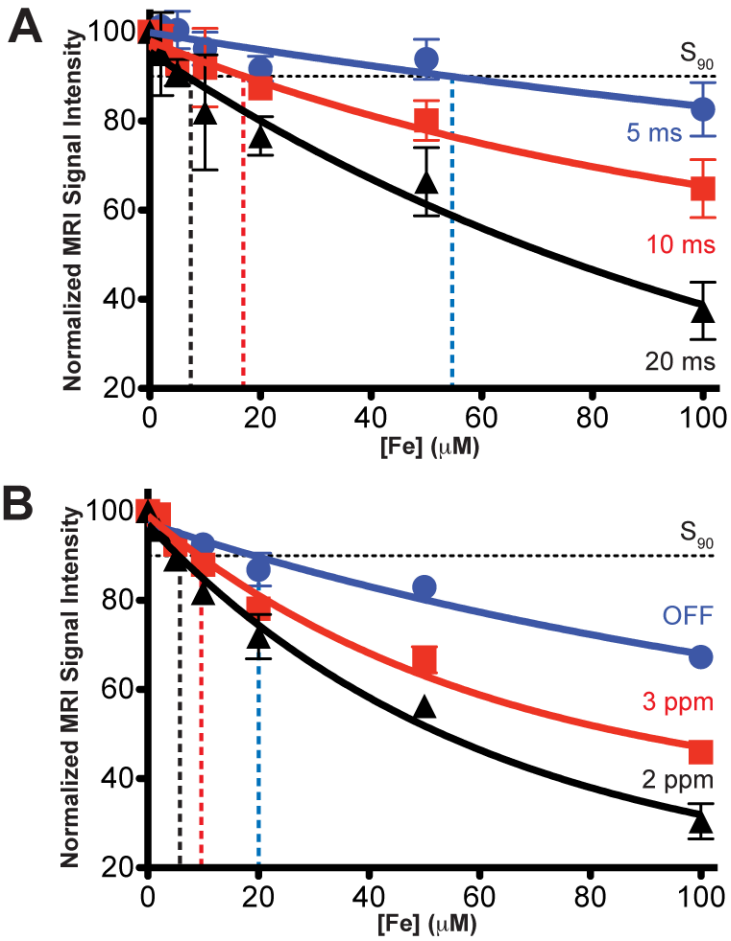

Figure 4.5 - Normalized signal intensity as a function of SPPM concentrations by T2*-w (A) and ORS imaging methods (B). The vertical dashed lines indicate different S_{90} values under different acquisition conditions for each method. (N=3, error bars are s.d.). *Modified from Cancer Res 2009 69(4).*

studies, we chose to use TE = 20 ms for the T2*-w method and 2 ppm frequency offset for the ORS method. These two conditions yielded similar sensitivity of SPPM detection in phantoms (e.g. the S_{90} values are 7.5 ± 2.7 and 6.1 ± 0.2 pM for the T2*-w and ORS methods, respectively).

4.3.4 In vivo imaging of SPPM nanoprobes in tumor-bearing mice

To validate the efficacy of the ORS method for SPPM imaging in vivo, we used animals bearing two A549 lung tumor xenografts (~300 mm^3) on each flank of an athymic nude mouse. SPPM nanoparticles (20 μL, 0.25 mg Fe/mL) were directly injected into one tumor (SPPM-t), and the other tumor was used as a SPPM-free control (control-t) (Figure 4.6A). To avoid perfusion loss of SPPM nanoparticles from the tumors, we sacrificed the animal prior to MRI experiments. After acquisition of ORS and T2*-w images, signal-to-noise ratio (SNR) was calculated by dividing the mean signal intensity of regions of interest (ROI) such as tumor or muscle tissues over noise. The background noise was calculated as the standard deviation for the largest possible ROI placed outside the animal in the image background. Contrast-to-noise ratio (CNR) was calculated as the contrast difference between the tumor and muscle tissues ($CNR_t = SNR_t - SNR_m$, where SNR_t and SNR_m are signal-to-noise ratios for tumor and muscle tissues, respectively).

Table 1 shows the values of SNR and CNR from different animals (n=3) before and after the injection of SPPM. Before SPPM injection, results show that the SNR/CNR values are not statistically significant ($p > 0.2$) between the two tumor xenografts by either imaging method. More specifically, the CNR_{SPPM-t} and $CNR_{control-t}$ are 3.7 ± 2.6

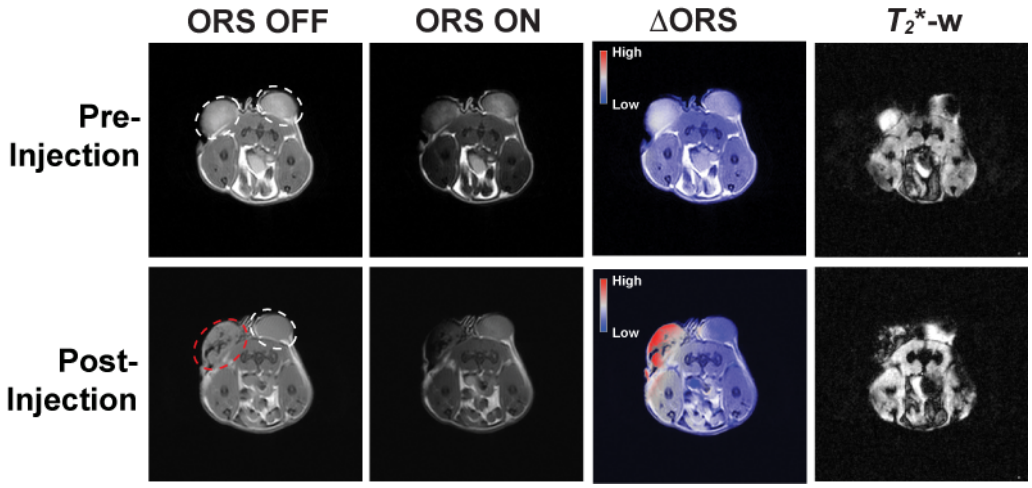

Figure 4.6 - Comparison of ORS and T2*-w imaging of SPPM intratumorally injected inside an A549 tumor xenograft in a mouse. ORS and T2*-w images of the transverse section of a representative mouse bearing two tumor xenografts (one for SPPM injection, the other as SPPM-free control) before and after the injection of SPPM. The red dashed circle in the post-injection image indicates the tumor injected with SPPM. The ΔORS images were obtained by pixel-by-pixel subtraction of ORS ON images from ORS OFF images, and overlayed with ORS OFF images. The T_2*-w images of the same animal sections were also shown. ORS condition: SE sequence with a 2 ppm ORS B_1 pulse at 0.385 mT for 0.5 s, TR = 2s, TE = 12 ms; T_2*-w condition: GE sequence, flip angle = 20°, TR = 400 ms, TE = 20 ms. Other imaging conditions are FOV = 50 mm, slice thickness = 2 mm, 128x128 matrix and NA = 2. *Modified from Cancer Res 2009 69(4).*

Table 1. Comparison of SNR and CNR of SPPM nanoprobes in tumor-bearing mice between T2*-w and ORS methods.

Animal Condition	Imaging Method	SNR[1]	CNR[2]
SPPM Pre-injection	**T2*-w**	15.1 ± 7.0 (SPPM-t) 13.4 ± 2.8 (Control-t) 18.8 ± 9.2 (Muscle)	3.7 ± 2.6 (SPPM-t) 6.3 ± 5.2 (Control-t)
	ORS	49.4 ± 11.4 (SPPM-t) 43.6 ± 16.6 (Control-t) 49.6 ± 16.8 (Muscle)	8.1 ± 4.6 (SPPM-t) 8.1 ± 10.1 (Control-t)
SPPM Post-injection	**T2*-w**	6.9 ± 2.9 (SPPM-t) 24.4 ± 13.6 (Control-t) 13.9 ± 4.7 (Muscle)	6.9 ± 2.2 (SPPM-t) 10.5 ± 12.8 (Control-t)
	ORS	78.1 ± 21.8 (SPPM-t) 44.2 ± 22.2 (Control-t) 40.7 ± 14.3 (Muscle)	37.4 ± 8.4 (SPPM-t) 7.8 ± 6.8 (Control-t)

[1]SNR was calculated as the mean signal intensity within the ROI of tissues of interest by noise. The standard deviation was obtained from n = 3.

[2]CNR was calculated as the tumor contrast over the muscle tissue ($CNR = |SNR_t - SNR_m|$). The standard deviation was obtained from n = 3.

Modified from Cancer Res 2009 69(4).

and 6.3 ± 5.2 for the T2*-w method ($p = 0.24$), and 8.1 ± 4.6 and 8.1 ± 10.1 for the ORS method ($p = 0.99$), respectively. These data suggest that the two tumor xenografts have comparable MR properties prior to SPPM injection. After SPPM injection, ORS data show that the $CNR_{SPPM\text{-}t}$ (37.4 ±8.4) is significantly higher than the $CNR_{control\text{-}t}$ of SPPM-free tumor control (7.8 ± 6.8, $p = 0.01$), as well as the same tumor before SPPM injection (8.1 ± 4.6, $p = 0.05$). In contrast, the CNRs by the T2*-w method did not show any significant differences ($p > 0.2$) between the paired comparisons described above (Figure 4.7). These data demonstrate that the ORS method significantly improves the imaging efficacy of SPPM nanoprobes over the T2*-w method. This conclusion is supported by the images shown in Figure 4.6 from a representative animal. The ΔORS images before and after SPPM injection clearly showed the ORS contrast in the injected tumors. However, contrast changes in the SPPM-injected tumors by the T2*-w method are difficult to interpret since considerable changes of signal intensity were also observed in the control tumors and background tissues (Figure 4.6, see also discussion below).

Finally, we evaluated the imaging efficacy of A549 tumors by intravenous injection of αvβ3-targeted SPPM probes. cRGD-encoded or cRGD-free SPPM were injected (6 mg Fe/kg) into mice bearing A549 tumor xenografts ($n = 4$ for each SPPM group). The third group of animals was co-injected with cRGD-encoded SPPM and free cRGD peptide (10 mg/kg, 18 molar excess).[14] Our previous studies demonstrated the effective targeting and receptor-mediated endocytosis of cRGD-encoded micelles in αvβ3-expressing tumor endothelial SLK cells in vitro.[11,13] Here, cRGD-encoded SPPM were employed to target the αvβ3-expressing angiogenic tumor vasculature in vivo

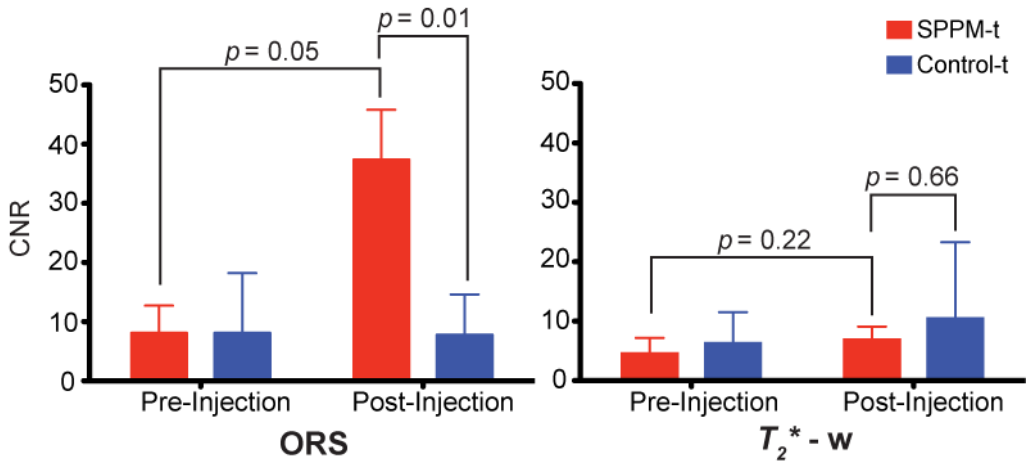

Figure 4.7 - Statistical comparison of CNRs of SPPM-injected vs. SPPM-free tumors by the ORS and T2*-w methods. The *p* values were calculated by the Student's t-test from three tumor samples under each condition. *Modified from Cancer Res 2009 69(4).*

(Figure 4.8 shows αvβ3 expression in A549 tumors). One hour after SPPM injection, ORS contrast images showed a clear identification of A549 tumors by cRGD-encoded SPPM probes (Figure 4.9). The CNR of the tumor over background muscle tissue was 10.7 ± 3.0 (n = 4) (Figure 4.10). Prussian blue staining of cRGD-encoded SPPM treated tumor tissues showed SPPM closely associated with the αvβ3 expressing tumor vasculature (Figure 4.9). In comparison, cRGD-free SPPM showed accumulation in the tumor parenchyma in a diffusive pattern, likely the result of passive targeting of SPPM to solid tumors through the enhanced permeation and retention (EPR) effect (Figure 4.9).[15] Correspondingly, a smaller CNR (5.1 ± 1.6, n = 4) was observed with the cRGD-free SPPM compared to that of the cRGD-encoded SPPM (10.7 ± 3.0, p = 0.02). In order to assess the specificity of the cRGD-encoded SPPM for αvβ3, blocking experiments, where an excess amount of free cRGD peptide was co-injected with cRGD-encoded SPPM, revealed that tumor accumulation of SPPM decreased, resulting in a decreased CNR (5.3 ± 0.7, p = 0.02 compared to that of cRGD-encoded SPPM) (Figure 4.10). Prussian blue staining of the tumor section showed a diffusive pattern of SPPM distribution similar to that of cRGD-free SPPM (Figure 4.9). These results highlight the efficacy of αvβ3-targeted SPPM nanoprobes in the imaging of angiogenic tumor vasculature in A549 tumor xenografts in vivo.

4.3.5 Blood circulation half-lives and biodistribution of SPPM.

We modified the hydroxyl (-OH) terminal group of MeO-PEG-PLA copolymer with a ^{3}H radioactive moiety ($-C(O)CT_3$) for the quantitative measurement of SPPM pharmacokinetics in vivo. Two groups of animals were injected with cRGD-encoded SPPM and cRGD-free SPPM. Plasma clearance studies showed a two-phase behavior

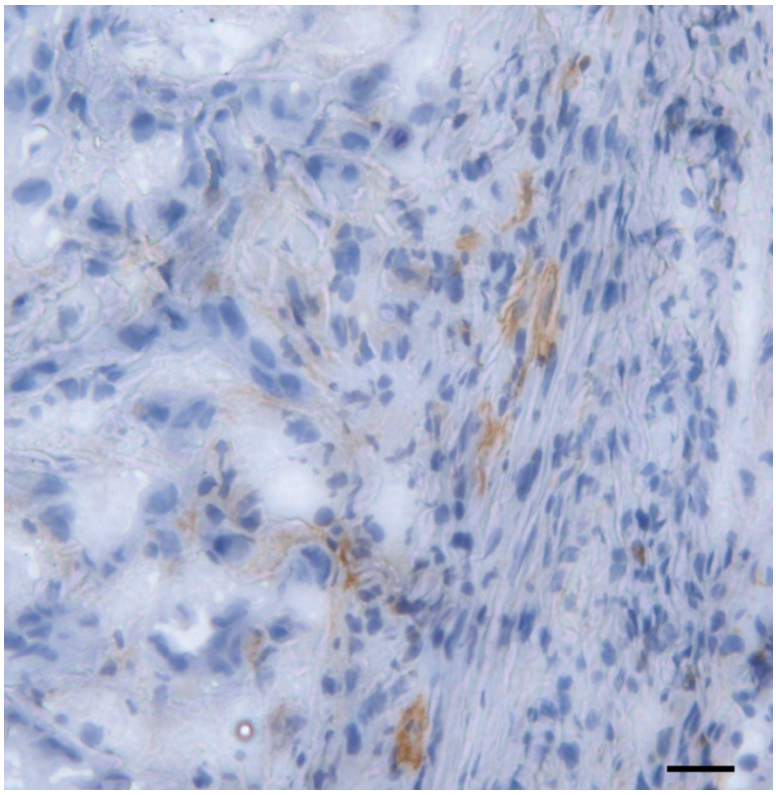

Figure 4.8 - Immunohistochemistry staining of the β3 subunit of αvβ3 in A549 tumor xenografts. Positive staining of β3 is shown in brown. Cell nuclei are counter-stained in blue. Scale bar 10 μm. *Modified from Cancer Res 2009 69(4).*

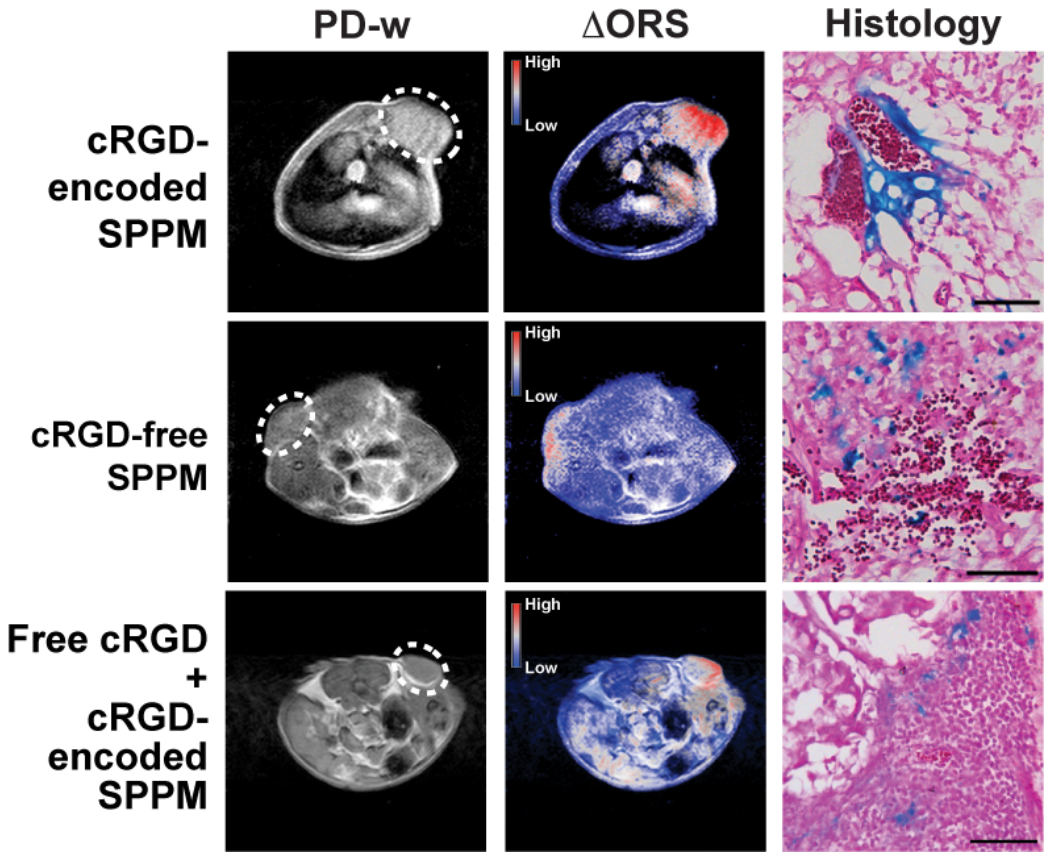

Figure 4.9 - *In vivo* ORS imaging of cRGD-encoded SPPM, cRGD-free SPPM, and a mixture of cRGD-encoded SPPM with free cRGD peptide injected intravenously in mice bearing A549 tumor xenografts (6 mg Fe/kg). The same phase LUT scale was used in both ΔORS images for direct contrast comparison. Histological sections by Prussian blue staining showed Fe presence from SPPM samples in tumor tissues. Scale bars = 50 μm. *Modified from Cancer Res 2009 69(4).*

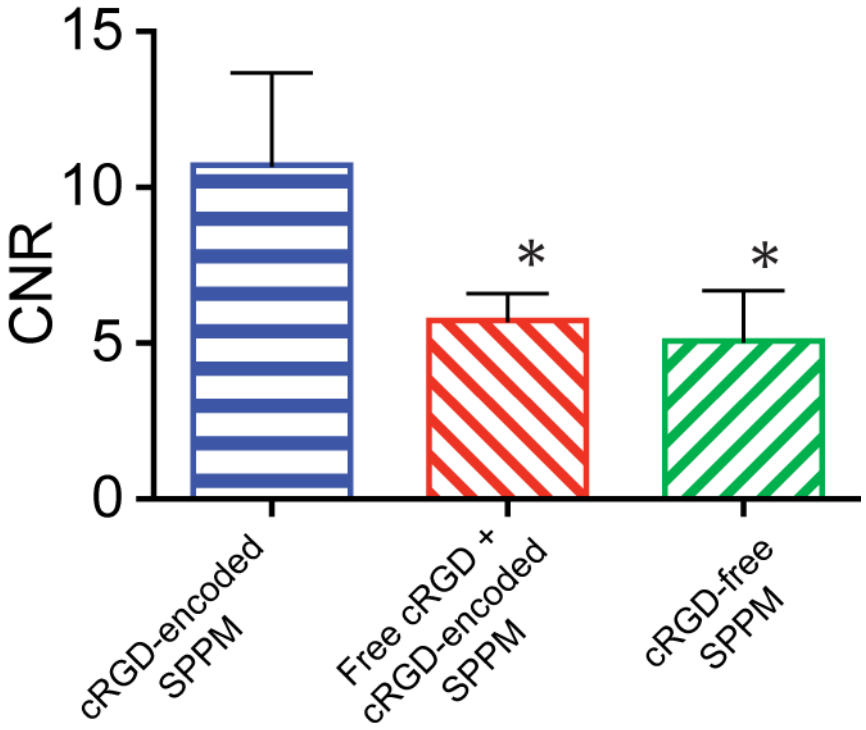

Figure 4.10 - CNRs of ΔORS images of A549 tumor xenografts (n=4) injected with cRGD-encoded SPPM, cRGD-free SPPM, and a mixture of cRGD-encoded SPPM with free cRGD peptide. The asterisks (*) indicate statistical significance (p values ≤ 0.05) between the SPPM group of interest and cRGD-encoded SPPM based on the Student's t-test. *Modified from Cancer Res 2009 69(4).*

over 24 hours. The plasma half-lives ($t_{1/2,\alpha}$) for the α-phase were 0.34±0.09 and 0.40±0.34 hrs for the cRGD-encoded and cRGD-free SPPM (n=4 for each SPPM formulation), respectively. The $t_{1/2,\beta}$ values for the β-phase were 3.9±0.8 and 9.2±0.8 hrs for the cRGD-encoded and cRGD-free SPPM (n=4), respectively (Figure 4.11).

To corroborate ORS imaging data, we performed biodistribution studies of different SPPM samples 1 hr after i.v. administration of the SPPMs. Spleen (~10% injected dose/g tissue (ID/g)) and liver (~4% ID/g) were the primary organs for SPPM uptake (Figure 4.12). It is important to note that cRGD-encoded SPPM accumulated significantly more in tumors than in the lung, muscle, and brain (Figure 4.12). Moreover, tumor uptake of cRGD-encoded SPPM (1.3±0.3% ID/g, n=3) was significantly higher than that of cRGD-free SPPM (0.6±0.3% ID/g, n=3). The co-injection of the free cRGD peptide decreased tumor accumulation of cRGD-encoded SPPM (0.6±0.1 % ID/g, n=3).

4.4 Discussion

Compared to optical and nuclear imaging methods, the lack of imaging sensitivity is a major limitation for MRI in molecular imaging applications.[16] Conventional small molecular T1 agents (e.g., Gd-DTPA) or new CEST probes (e.g., Eu-DOTA-4AmCE) have limited sensitivity of detection (>μM), which makes it difficult to image specific tumor markers at low physiological concentrations (<nM).[17] Superparamagnetic nanoparticles (e.g., Fe_3O_4) have demonstrated significantly improved sensitivity due to their strong perturbation to the local magnetic field. Currently, clinically used superparamagnetic agents are synthesized by aqueous precipitation of $FeCl_2$ and $FeCl_3$ in the presence of a dextran polymer (e.g., Feridex®). This method yields a variable size distribution of iron oxide nanoparticles (2-20 nm) and the loading of

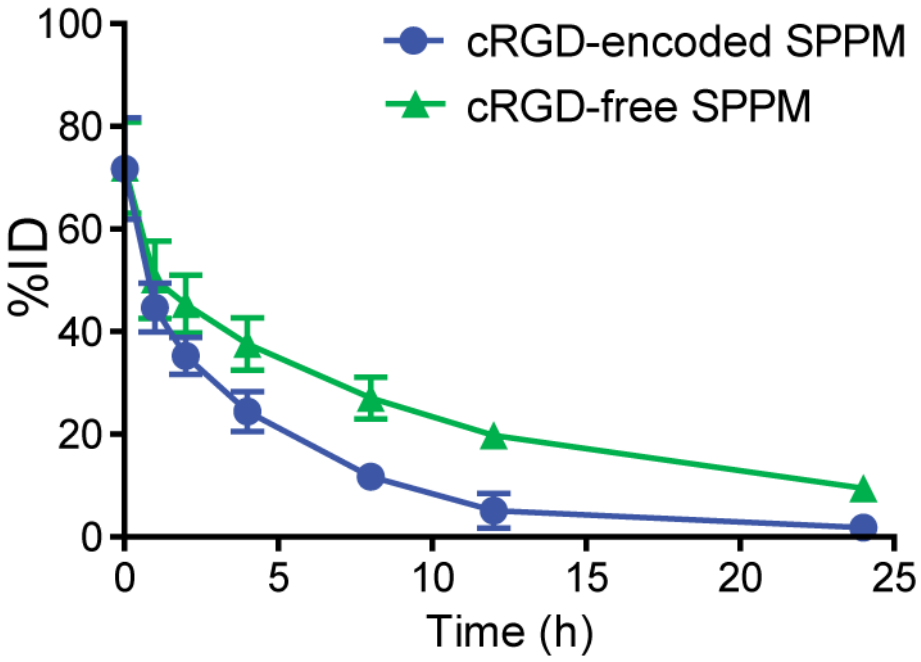

Figure 4.11 - Plasma concentration versus time relationships (n=4 for each SPPM group, 6 mg Fe/kg) for cRGD-encoded SPPM and cRGD-free SPPM. *Modified from Cancer Res 2009 69(4).*

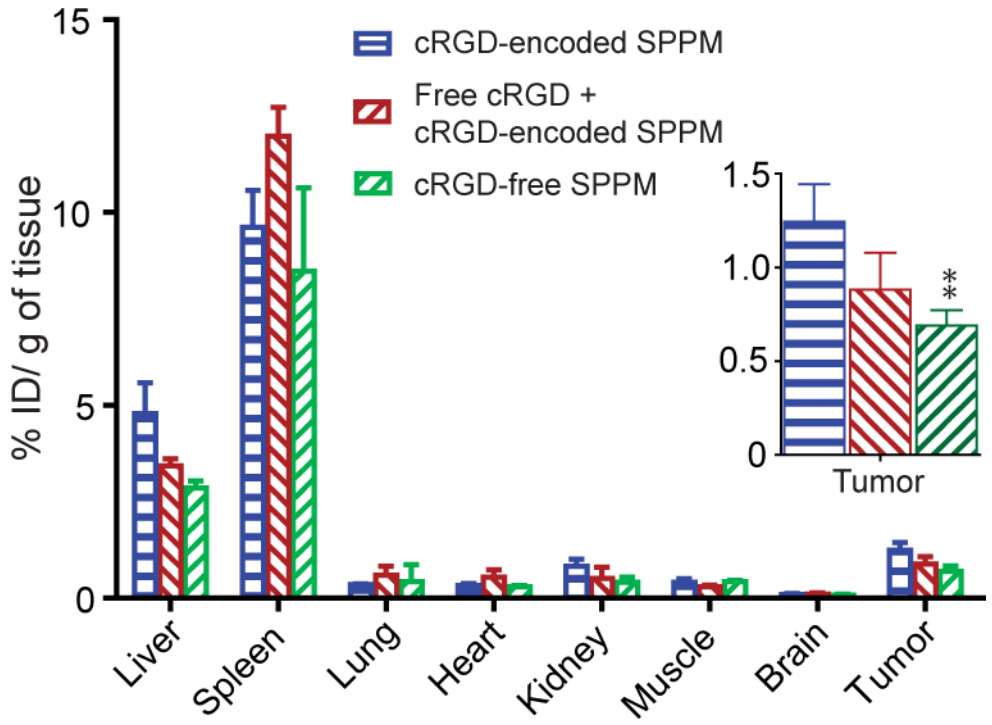

Figure 4.12 - Biodistribution profiles (n=3) of different SPPM formulations (cRGD-encoded SPPM, cRGD-free SPPM, and cRGD-encoded SPPM co-injected with free cRGD) 1 hr after intravenous administration. The asterisks (**) indicate statistical significance (p values ≤ 0.05) between the SPPM group of interest and cRGD-encoded SPPM based on the Student's t-test. *Modified from Cancer Res 2009 69(4).*

iron oxide per nanoparticle is low.[18] Compared to the Fe_3O_4-dextran system, our SPPM design had several distinctive advantages. First, the size distribution of Fe_3O_4 nanoparticles was monodisperse (e.g., 9.9±0.4 nm in diameter), which minimized variability between Fe_3O_4 nanoparticles. Secondly, clustering of highly compacted Fe_3O_4 particles inside micelle core considerably increased MR relaxivity. Previous study showed that over 10 times enhancement in T2 relaxivity per Fe was achieved when clustered Fe_3O_4 particles were loaded inside each micelle.[10] Thirdly, high loading of Fe_3O_4 (e.g., 33wt% in this study) effectively increased Fe content per micelle nanoparticle. Combination of increased molar relaxivity and high Fe loading per particle resulted in considerably increased sensitivity of SPPM probes. Indeed, results from this study demonstrated detection of picomolar concentrations of SPPM nanoparticles in phantom samples by MRI. Moreover, the SPPM samples demonstrated superb stability with long storage shelf-lives. These nanoparticles do not aggregate at 4°C even after one month of storage in PBS solution. Dynamic light scattering measurements also showed that particle size (~70 nm in diameter) did not change over this time period.

Pharmacokinetic studies showed that SPPM formulations had prolonged blood circulation times, which should allow for effective tumor targeting by the cRGD-encoded SPPM. Both cRGD-encoded and cRGD-free SPPM formulations had comparable α-phase plasma half-lives ($t_{1/2,\alpha}$) at 0.34±0.09 and 0.40±0.34 hrs, respectively. However, cRGD-free SPPM showed slower clearance in the β-phase as represented by longer $t_{1/2,\beta}$ (9.2±0.8 hrs) than cRGD-encoded SPPM (3.9±0.8 hrs). We attribute this variation to the different functionalization of peptides (i.e., cRGD vs Cys) on the SPPM surface. Since the ORS imaging study was performed 1 hr after SPPM injection, we do not anticipate

the different $t_{1/2,\beta}$ values will have a strong influence on the ORS contrast in the current study. Biodistribution studies showed relatively high accumulations of SPPM in the liver and spleen, which are commonly observed for nanoparticles in vivo.[19] In comparison, SPPM accumulations in other major organs such as lung, brain, muscle and kidney were minimal. More importantly, tumor accumulation of cRGD-encoded SPPM was significantly higher than that of cRGD-free SPPM and cRGD-encoded SPPM co-injected with free cRGD (Figure 4.12).

Currently, the T2*-w method is the gold standard for imaging superparamagnetic nanoparticles. Due to the strong magnetization and field perturbation by the superparamagnetic nanoparticles, the T2*-w method provides a much higher sensitivity for SPIO agents over conventional T1 agents (e.g. Gd-DTPA). Despite this advantage, T2*-w imaging suffers from several major limitations in molecular imaging applications. First, in T2*-w imaging, significant signal loss can arise due to B_0 inhomogeneity, magnetic susceptibility or spin-spin couplings. This will lead to signal variations that are independent of the superparamagnetic probes. For example, the pre-injection T2*-w image (Figure 4.6) showed considerably different image contrast (tumor ROI analyses showed 2.1±1.2 and 1.2±0.9 for the SPPM-t and control-t, respectively) between the two tumor xenografts in the same mouse before SPPM injection. After SPPM injection, the control tumor (SPPM-free) showed a relative increase in signal intensity (1.7±1.1) compared to its pre-injection image (1.2±0.9). Such signal variations can greatly complicate the interpretation of pre- and post-injection images to identify SPPM contrast on an individual animal basis. Secondly, T2* method is also sensitive to different magnetic susceptibility caused by air/tissue or hard/soft tissue interface present in internal

organs. This phenomena gives rise to signal distortion and can also complicate image analysis. Lastly, identification of SPIO requires a pre-contrast scan for image subtraction from a post-contrast scan. Small changes of animal positions can easily decrease the spatial resolution (>mm) for tumor detection. Compounded with the variations in signal intensity between the scans, the quality and accuracy of contrast images can be considerably deteriorated in subtracted images.

The off-resonance saturation (ORS) method overcomes the above limitations and offers many advantages. The most exciting aspect of ORS is its ability to turn "ON" and "OFF" the contrast of the SPPM probes after the contrast agents are injected. This ability greatly increases the imaging accuracy in detecting contrast changes in targeted tissues while saving the need of a pre-contrast scan as in the T2*-w method. Because ON and OFF imaging can be performed subsequently without the moving of the imaging subject, pixel-by-pixel subtraction between these images can be performed to provide the maximal spatial resolution in contrast images. In this case, the intrinsic resolution of MRI (e.g. ~100 μm for the 4.7 T scanner in the current study) can be maintained in the ORS contrast images (e.g. Figures 4.6 and 4.9). In contrast, it is impossible to perform accurate pixel-by-pixel subtractions between pre- and post-injection images in T2*-w method. It is also interesting to note that although the current acquisition conditions with T2*-w and ORS methods allowed for similar sensitivities (e.g., S_{90}) in phantom studies, results from animal studies demonstrated significantly improved SNR/CNR by the ORS method for SPPM detection than the T2*-w method (Table 1, Figures 4.5 and 4.7). This improvement indicates that the complex physiological environments may introduce more signal variations in T2*-w images than the ORS images.

One consideration in using the ORS method is that the ORS imaging protocol also introduces contrast effects by magnetization transfer (MT). The MT effect is dependent on cross-relaxation and/or chemical exchange between the "free" water and macromolecule-associated or "immobile" water while ORS effect primarily relies on the diffusion of water molecules among different compartments that are defined by magnetic field isosurfaces.[12,20-22] Our current study allows for a preliminary estimation of MT and ORS effects on SPPM contrast. The CNR for the SPPM-injected tumor is 37.4 ±8.4 (n = 3), which includes the compounded effects from both ORS and MT. The CNR for the SPPM-free tumors from the same animal is 7.8 ± 6.8, where the SPPM-induced ORS contribution is absent. The significantly higher CNR ($p = 0.01$) from SPPM-injected tumors suggest that ORS contrast can be effectively detected over the MT contrast. Precautions need to be taken when imaging lower concentrations of SPPM in tumor tissues when the contribution from MT effect becomes significant. Further studies are necessary to quantitatively evaluate the contributions of MT- and/or ORS-based effects on the detection of SPPM.

In conclusion, these studies demonstrate the synergy of ultra-sensitive SPPM design and ORS method for molecular imaging of cancer, and in particular, non-small cell lung cancer. Phantom studies show detection limit at picomolar (10-12 M) concentrations of SPPM nanoprobes, making them comparable in sensitivity to nuclear imaging probes. Results from the animal studies support our hypothesis that ORS method can significantly increase the contrast sensitivity and detection accuracy of SPPM particles in tumor tissues over the conventional T2*-w method. After intravenous injection, αvβ3-targeted SPPM nanoprobes demonstrate significantly increased ORS

imaging contrast in A549 tumors over the non-targeted SPPM. Pharmacokinetic studies showed prolonged blood circulation times of SPPM nanoparticles and verified the αvβ3-dependent targeting specificity by the cRGD-encoded SPPM. The combination of ORS imaging with cancer-targeted SPPM nanoparticles offers new opportunities in detecting biochemical markers at early stages of tumor development.

4.5 References

1. Ward KM, Aletras AH, Balaban RS. A new class of contrast agents for MRI based on proton chemical exchange dependent saturation transfer (CEST). J Magn Reson 2000;143(1):79-87.
2. Aime S, Delli Castelli D, Terreno E. Novel pH-reporter MRI contrast agents. Angew Chem Int Ed Engl 2002;41(22):4334-4336.
3. Zhang S, Trokowski R, Sherry AD. A paramagnetic CEST agent for imaging glucose by MRI. Journal of the American Chemical Society 2003;125(50):15288-15289.
4. Gilad AA, McMahon MT, Walczak P, et al. Artificial reporter gene providing MRI contrast based on proton exchange. Nat Biotechnol 2007;25(2):217-219.
5. Bulte JWM, Kraitchman DL. Iron oxide MR contrast agents for molecular and cellular imaging. NMR Biomed 2004;17(7):484-499.
6. Thorek DLJ, Chen A, Czupryna J, Tsourkas A. Superparamagnetic iron oxide nanoparticle probes for molecular imaging. Ann Biomed Eng 2006;34(1):23-38.
7. Lee JH, Huh YM, Jun Y, et al. Artificially engineered magnetic nanoparticles for ultra-sensitive molecular imaging. Nat Med 2007;13(1):95-99.

8. Seo WS, Lee JH, Sun X, et al. FeCo/graphitic-shell nanocrystals as advanced magnetic-resonance-imaging and near-infrared agents. Nat Mater 2006;5(12):971-976.

9. Sutton D, Nasongkla N, Blanco E, Gao J. Functionalized micellar systems for cancer targeted drug delivery. Pharm Res 2007;24(6):1029-1046.

10. Ai H, Flask C, Weinberg B, et al. Magnetite-loaded polymeric micelles as ultrasensitive magnetic-resonance probes. Adv Mater 2005;17(16):1949-1952.

11. Nasongkla N, Bey E, Ren J, et al. Multifunctional Polymeric Micelles as Cancer-Targeted, MRI-Ultrasensitive Drug Delivery Systems. Nano Letters 2006;6:2427-2430.

12. Zurkiya O, Hu X. Off-resonance saturation as a means of generating contrast with superparamagnetic nanoparticles. Magnetic Resonance in Medicine 2006;56(4):726-732.

13. Nasongkla N, Shuai X, Ai H, et al. cRGD-functionalized polymer micelles for targeted doxorubicin delivery. Angew Chem Int Ed Engl 2004;43(46):6323-6327.

14. von Wallbrunn A, Holtke C, Zuhlsdorf M, Heindel W, Schafers M, Bremer C. In vivo imaging of integrin alpha nu beta(3) expression using fluorescence-mediated tomography. Eur J Nucl Med Mol I 2007;34(5):745-754.

15. Maeda H, Sawa T, Konno T. Mechanism of tumor-targeted delivery of macromolecular drugs, including the EPR effect in solid tumor and clinical overview of the prototype polymeric drug SMANCS. J Control Release 2001;74(1-3):47-61.

16. Weissleder R, Pittet MJ. Imaging in the era of molecular oncology. Nature 2008;452(7187):580-589.

17. Zhang SR, Merritt M, Woessner DE, Lenkinski RE, Sherry AD. PARACEST agents: Modulating MRI contrast via water proton exchange. Accounts Chem Res 2003;36(10):783-790.

18. Sun SH, Zeng H, Robinson DB, et al. Monodisperse MFe2O4 (M = Fe, Co, Mn) nanoparticles. Journal of the American Chemical Society 2004;126(1):273-279.

19. Torchilin VP. Multifunctional nanocarriers. Adv Drug Deliver Rev 2006;58(14):1532-1555.

20. Henkelman RM, Huang XM, Xiang QS, Stanisz GJ, Swanson SD, Bronskill MJ. Quantitative Interpretation of Magnetization-Transfer. Magnetic Resonance in Medicine 1993;29(6):759-766.

21. Morrison C, Henkelman RM. A Model for Magnetization-Transfer in Tissues. Magnetic Resonance in Medicine 1995;33(4):475-482.

22. Wolff SD, Balaban RS. Magnetization Transfer Contrast (Mtc) and Tissue Water Proton Relaxation Invivo. Magnetic Resonance in Medicine 1989;10(1):135-144.

CHAPTER FIVE

Investigation of In Vivo Targeting Kinetics of αvβ3-Targeted SPPM Nanoprobes Using T2*-weighted High Temporal Resolution (HTR) MRI

5.1 - Introduction

Recent advances of ultrasensitive nanoprobes have greatly broadened the capability of MRI in cancer molecular imaging applications. Compared to small molecular T1 agents, superparamagnetic nanoparticles (i.e. Fe_3O_4, $MnFe_2O_4$, FeCo) have substantially larger molar relaxivities with a detection limit in the nanomolar to picomolar concentration range.[1-6] Imaging of various cancer-specific biomarkers, such as αvβ3 and αvβ5 integrins, Her2-Neu, transferrin receptors and folate have been reported.[5,7-13] In most of these applications, nanoprobes were first injected and after a certain time, post-contrast images were acquired by conventional T2/T2*-weighted or off-resonance saturation methods to evaluate the accumulation of nanoprobes in the targeted tissues. Despite many successful reports on such contrast changes between pre- and post-injection images, very few studies have examined the fundamental kinetic processes of molecular targeting in vivo.

Dynamic contrast enhancement (DCE) MRI has established its application in the clinical setting in cancer detection, diagnosis, stratification and the assessment of anti-angiogenic therapy.[14] By capturing T1-wieghted images at a temporal resolution of seconds to minutes during the administration of small molecular weight T1-weighted contrast agents (e.g. Gd-DTPA, Magnevist®), it allows DCE-MRI to noninvasively report blood volume dynamics, vascular permeability and other transport kinetics in benign and malignant tissues.[15,16] Although Gd-based small molecular weight agents

work well in tumor permeability studies, these agents are not very sensitive, requiring millimolar (10^{-3} M) concentrations, and therefore are ineffective for the visualization of protein biomarkers in vivo.[17]

In this study, we describe the use of T2*–weighted high temporal resolution (HTR) -MRI method with 1.3 s temporal resolution over 30 minutes to investigate the targeting kinetics of an αvβ3-specific ultrasensitive T2 contrast agent in different tumor xenografts in athymic nude mice. The T2 contrast agent is based on the superparamagnetic polymeric micelles (SPPM) that have been previously established in our lab as αvβ3 integrin specific molecular imaging nanoprobes.[5] Integrin αvβ3 is an established biomarker of angiogenesis, which is expressed on active endothelial cells during angiogenesis and is quiescent in non-angiogenic endothelial cells. Using nanoprobes conjugated with a cyclic RGDfK peptide (cRGD), an αvβ3-specific ligand, and a non-targeting cRAD control, we evaluated the change of MR signal intensity over time at different angiogenic "hotspots" in subcutaneous tumor xenografts of lung, breast and glioblastoma cancers. Comparison of the targeted and non-targeted SPPM data allows for the subtraction of signal intensity contributions from blood concentration, clearance and the enhanced permeability and retention (EPR) effect. The subtracted HTR-MRI temporal profiles allow for the assessment of the specific targeting kinetics of cRGD-encoded SPPM to αvβ3-expressing tumor endothelial cells *in vivo*.

5.2 Materials and Methods

5.2.1 Synthesis and fabrication of cRGD- and cRAD-SPPM

Methoxy- and maleimide-terminated poly(ethylene glycol)-b-poly(D,L-lactide) (MeO-PEG-PLA and Mal-PEG-PLA) and tetramethylrhodamine (TMR) conjugated

MeO-PEG-PLA-TMR copolymers and SPIO nanoparticles were synthesized using previously published procedures.[5,10,18,19] All copolymers had a molecular weight of 10kD with 5 kD PEG and PLA blocks. The diameter of SPIO nanoparticles was 9.0 ± 0.9 nm by transmission electron microscopy (JEOL 1200 EX at 120 KeV). SPPM were prepared by a solvent evaporation method. [10] Briefly, a mixture of MeO-PEG-PLA, MeO-PEG-PLA-TMR, Mal-PEG-PLA and SPIO in THF was added dropwise to 0.05 M HEPES buffer containing 0.01 M EDTA (pH 7.4) under sonication. The micelle suspension was then equally divided into two parts, and then shaken on an orbital shaker for 4 h to allow THF to evaporate. A solution of either thiol-terminated cRGDfK or cRADfK was added to the micelle solution. The solutions were then shaken overnight to complete conjugation of peptides to maleimide-terminated micelles. Thiol-terminated cRGDfK and cRADfK were obtained by deprotections of thioacetate cRGDfK and cRADfK (Peptides International, Louisville, KY), followed by preparative HPLC purifications. All SPPM formulations were filtered through 1.0 μm nylon syringe filters and concentrated using centrifugal filters (100 kDa cutoff, Millipore, Billerica, MA).

5.2.2 Animal model and preparation

Animal studies were approved by the Institutional Animal Care and Use Committee at UT Southwestwen Medical Center in Dallas and carried out according to its guidelines. Female athymic nude mice (27-30g) were utilized.

The subcutaneuos tumor xenografts were formed from non-small cell A549 lung cancer, MDA-MB-231 breast cancer, or U87 glioblastoma cell lines. All cell lines were injected subcutaneously into the dorsal flank of the mouse. Five million A549, five million matrigel supplemented (20%) MDA-MB-231, and one million U87 cells were

injected in 100 μL of phosphate buffered saline (PBS) to start tumor formation in their respective groups. Tumors were allowed to grow to 300-500 mm^3 at which time they were randomized into cRGD- and cRAD-SPPM treatment groups (n = 3 each) for MR imaging.

5.2.3 MR imaging

MR studies were conducted in a 7T horizontal bore small animal MRI scanner (Varian Inc., Palo Alto, CA). All mice were anesthetized with 1-2% isoflurane mixed with pure oxygen via a nose cone and were placed in a stretched supine position with a respiratory sensor. SPPM was administered via a tail vein catheter at a concentration of 10 mg Fe/kg. The catheter was made in-house with a 27G 0.5 inch butterfly needle with PE10 tubing (~50 cm in length) to allow for injection during the HTR-MR imaging acquisition. The average dead volume of the catheter was 100-125 μL.

Axial and coronal two-dimensional (2D) fast spin-echo sequence images were firstly acquired to ensure the position of the implanted tumor as scout imaging. The imaging parameters were: TR/TE =1000/5.3 ms, band width = 100 kHz, FOV = 35 x 35 mm, matrix size = 128 x 128, slice thickness = 1 mm, and NEX = 1. Subsequent HTR-MRI images were acquired. Multiple T2*-weighted images with a temporal resolution of 1.3 s make up the 30 minute HTR-MRI dataset. The T2*-w parameters were: TR/TE = 10/3 ms; flip angle = 45°; FOV = 35 x 35 mm; matrix size = 128 x 128, NEX = 1. Thirty seconds after the start of the 30 min HTR-MRI sequence a SPPM bolus was administered manually over 30 – 45 s, after which the line was flushed with saline (total injection time about 1.25 min). The dataset images, $I_{n,}$ were normalized by dividing each image by an averaged image (created from the averaging of 5 pre-injection images collected in the

first 15 seconds of the HTR-MRI sequence). Regions of interest (ROIs) were selected to measure the temporal change of the signal intensity (SI) and graphed against time using Prism (Graphpad). Images were analyzed using ImageJ software (National Institutes of Health, NIH).

5.2.4 In vivo pharmacokinetic and TEM studies of SPPM

Experiments involving radioactive materials were approved by the Radiation Safety Committee at UT Southwestern Medical Center. ^{3}H (or T)-labelled cRGD encoded and cRGD-free SPPMs were prepared from 75% MeO-PEG-PLA-C(O)CT_3 and 25% MAL-PEG-PLA. In a second cohort of mice (n=3), ^{3}H labeled SPPM solutions were injected via the tail vein. Blood was collected via ocular vein at 1 min, 1, 2 , 4 , 8 , 12, and 24 hrs after the injection. Plasma was isolated from red blood cells by centrifugation at 1000 rpm for 10 min. The plasma was subsequently mixed with a tissue solubilizer solution (1 mL, BTS-450, Beckman, CA) at room temperature for 5 hrs followed by an addition of a liquid scintillation cocktail (10 mL, Ready Organic™, Beckman, CA) for 12 hrs. Amount of radioactive isotope was measured by a liquid scintillation counter (Beckman LS 6000 IC).

In a third cohort of mice (n=4), 20 μL plasma samples from the mouse were taken at 1, 10, 20, 40 and 60 mins after injection of SPPM (10 mg Fe/kg). Samples were digested in concentrated HCl and analyzed for Fe content using atomic absorption spectroscopy (Varian SpectrAA 50, Varian). Plasma samples for transmission electron microscopy (TEM) analysis were collected 40 minutes post-injection and placed on the carbon grid, blotted and imaged using JEOL 1200 EX at 120 kV. The TEM samples were stained with 2% phosphotungestic acid (PTA) prior to analysis.

5.2.5 Histological analysis

After MR imaging, mice were injected with Hoechst 33342 (10mg/kg) via the tail vein. The dye was allowed to circulate for 1 minute. The tumor tissue was resected and embedded in optimal cutting temperature medium and flash frozen. The tissue was sectioned on a Leica cryostat (model 3050S) at 8 μm. Sections were fixed with -20 °C acetone, mounted and coverslipped. Fluorescent micrographs were taken on an upright Leica 5500DM with a monochrome camera using a mercury lamp and proper excitation (ex) and emission (em) filters for TMR (ex bandpass 515-560 nm; em longpass 590 nm) and Hoechst (ex bandpass 340-380 nm; em bandpass 450-490 nm) fluorescence.

5.3 Results

5.3.1 SPPM characterization

Spherical SPPM nanoprobes encoded with cRGD- or cRAD peptide ligands were produced and characterized according to published procedures (Figure 5.1). Nanoprobes had a size distribution of 57±12 and 53±10 nm for cRGD- and cRAD-FSPPM, respectively by dynamic light scattering analysis. All formulations of FSPPM had a mean transverse relaxivity of 406.6 ± 9.1 Fe $mM^{-1}s^{-1}$ at 20° C and similar fluorescent properties.

5.3.2 SPPM phantom study for optimization of HTR-MRI parameters

Precluding in vivo imaging, a phantom with varying concentrations of SPPM (0.1 to 100 μM Fe) in phosphate buffered saline was analyzed to find the optimal TE and flip angle to image SPPM at a high temporal resolution. The results showed that an increase in the flip angle increased the contrast-to-noise ratio (CNR) at the SPPM concentrations examined, while an increase in TE time decreased the CNR at high

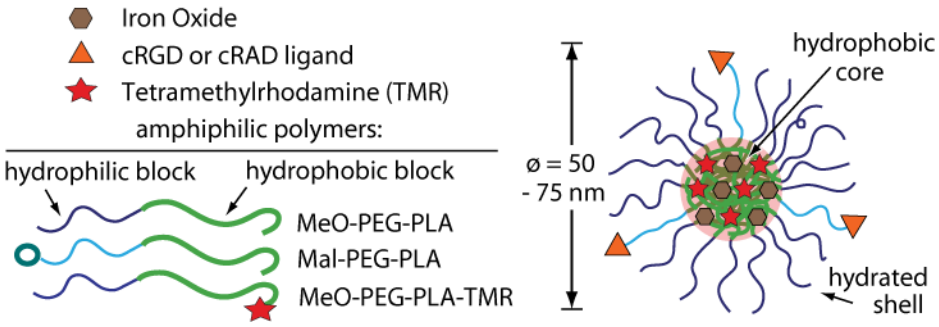

Figure 5.1 - Schematic of superparamagnetic polymeric micelles (SPPM).

concentrations of SPPM (50 and 100 μM) but had no effect on samples at low concentrations (2, 5 and 10 μM). Based on the phantom study, flip angles between 45 and 90 degrees were chosen for in vivo animal studies with a TR of 10 ms and a TE of 3 ms. *In vivo* imaging of a mouse bearing an A549 subcutaneous tumor using 45, 60 and 90° flip angles were compared by the contrast-to-noise ratio (CNR) produced after one excitation (NEX =1). The 45° flip angle showed the highest CNR and was used for the remainder of the study (data not shown).

5.3.3 Representative in vivo HTR-MRI data and quantification

Figure 5.2 illustrates representative data in mice bearing A549 non-small cell lung cancer subcutaneous xenografts. The images are marked with color-coded regions-of-interest (ROIs) that correspond to the like-colored signal intensity curves (Figure 5.2, lower panel). Baseline images showed little to no SI difference among other images before injection. After injection (Figure 5.2, lower panel, dashed line), major blood vessels (systemic circulation) showed a maximum SI loss for both cRGD- (Figure 5.2, green line) and cRAD-FSPPM (Figure 5.2, purple line) treated mice. These vascular ROIs continued to show similar SI curves for the entire study, returning to ~ 50% normalized SI at 30 minutes. An initial decrease of SI in tumor ROIs was observed in both cRGD- (Figure 5.2, red line) and cRAD-FSPPM (Figure 5.2, blue line) treated animals. cRGD-SPPM tumor ROI showed decrease to 40% SI and a sustained negative slope over the 30 minute dataset indicating more accumulation of SPPM in that ROI, whereas the cRAD-SPPM tumor ROI showed an initial decrease to 70% SI and then a positive slope trending towards returning to baseline. This could be due to the clearance

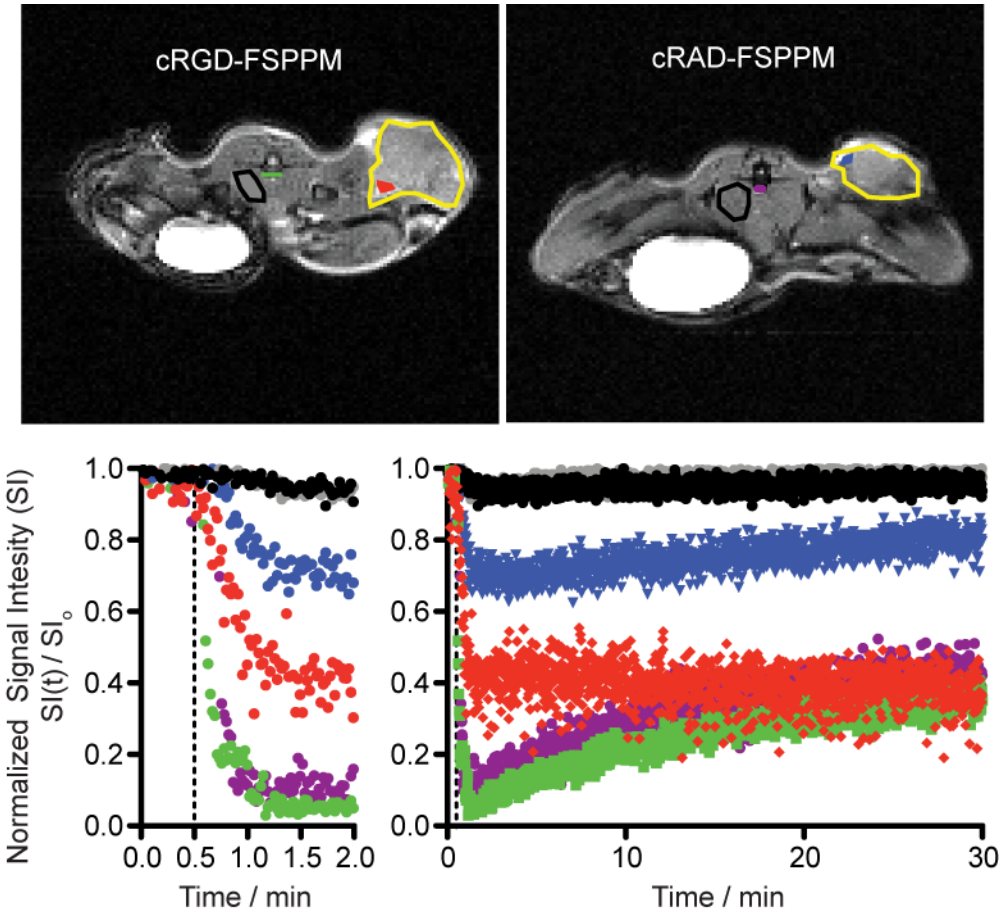

Figure 5.2 - T2-weighted images of a representative cRGD- or cRAD-SPPM treated animal. Images are color coded with tumor margins (yellow outline), major blood vessels (green and purple), tumor ROIs (red and blue) and muscle (black/gray and black outline). The corresponding signal intensity curves show the varied responses recorded by each ROI over a period of 30 mins. Dashed lines indicate start of the SPPM bolus (10 mg Fe/kg).

of the particle from the blood and the tumor tissue at that ROI. Muscle tissue in cRGD- and cRAD-FSPPM treated animals showed smaller initial deceases in SI and then a return to baseline over the 30 minute imaging period (Figure 5.2 lower panel, black and gray lines, respectively).

5.3.4 Blood clearance half-lives of SPPM using ^{3}H polymers and Fe

We modified the hydroxyl (-OH) terminal group of MeO-PEG-PLA copolymer with a ^{3}H radioactive moiety ($-C(O)CT_3$) for the quantitative measurement of SPPM pharmacokinetics in vivo. Two groups of animals were injected with cRGD-encoded SPPM and cRGD-free SPPM. Plasma clearance studies showed a two-phase behavior over 24 h using ^{3}H labeled polymers. The plasma half-lives ($t_{1/2,\alpha}$) for the α-phase were 0.41±0.11 and 0.32±0.08 hrs for the cRGD- and cRAD-SPPM (n=3 for each SPPM formulation), respectively. The $t_{1/2,\beta}$ values for the β-phase were 2.26±0.32 and 3.85±0.5 hrs for the cRGD- and cRAD-SPPM (n=3), respectively (Figure 5.3). Pharmacokinetics of the Fe content in the plasma also validated the clearance of the SPPM from the blood, corroborating with the kinetic profiles seen in the vascular ROIs in the HTR-MRI dataset (Figure 5.4A). TEM analysis of plasma collected 40 minutes post–injection showed a spherical cluster of SPIO. The core-shell architecture was maintained and elucidated in the 2% phosphotungstic acid negatively stained plasma sample showing SPIO encapsulated in the white hydrophobic core of the SPPM (Figure 5.4B). Together all blood clearance and TEM studies validate the SI curves observed in the HTR-MRI datasets, and indicates that the SPPM nanoprobe is still intact 40 mins post-injection in the blood. It is important to note that the differences in cRGD-SPPM and cRAD-SPPM blood vessel curves from both HTR-MRI (Figure 5.2) and radiolabeled polymer

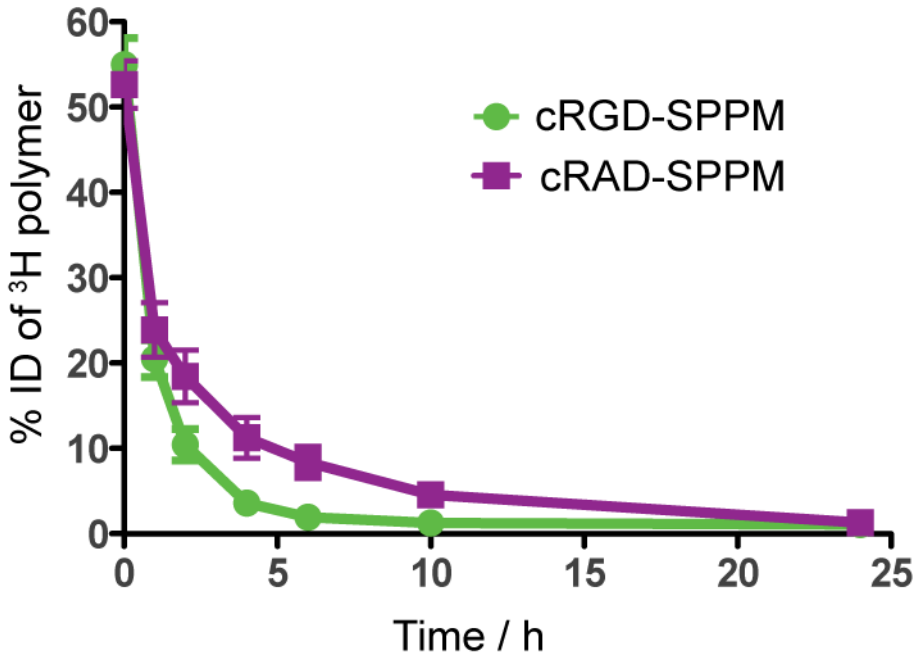

Figure 5.3 - Plasma concentration-time relationships (n=3 for each SPPM group) for cRGD-SPPM (green line) and cRAD-SPPM (purple line) using ^{3}H-labeled polymers. The plasma half-lives ($t_{1/2,\alpha}$) for the α-phase were 0.41±0.11 and 0.32±0.08 hrs for the cRGD- and cRAD-SPPM (n=3 for each SPPM formulation), respectively. The $t_{1/2,\beta}$ values for the β-phase were 2.26±0.32 and 3.85±0.5 hrs for the cRGD- and cRAD-SPPM (n=3), respectively.

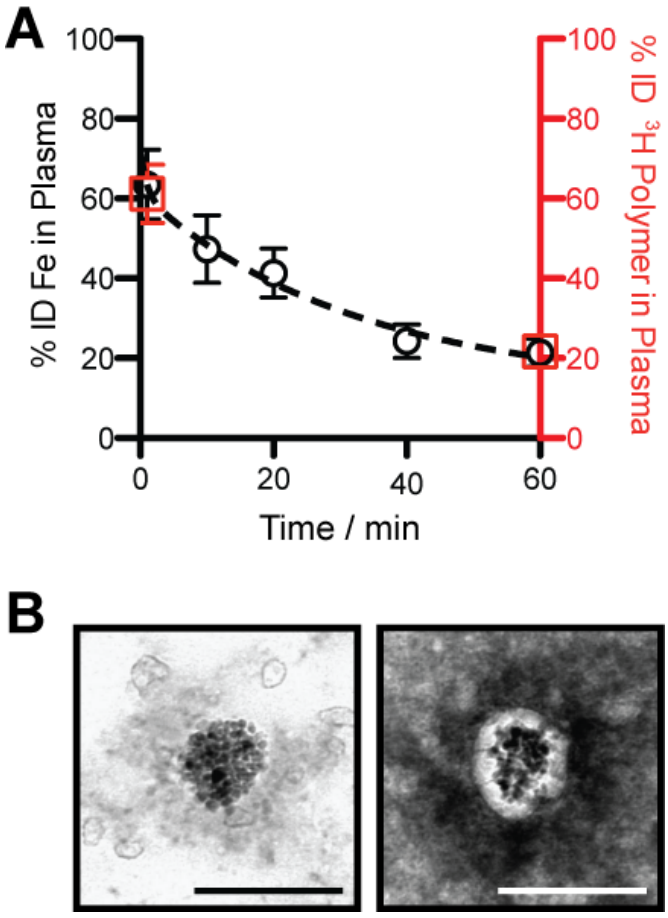

Figure 5.4 - (A) Plasma concentration-time relationships after a bolus of 10 mg Fe/kg of cRGD-SPPM, measured in tumor bearing animals, Fe content represented by black open circle, Radiolabeled polymer from Figure 5.3 (1 min and 60 min) represented by red open square. (B) TEM micrographs of plasma collect at 40 mins after bolus of SPPM. The plasma sample was negatively stained with 2% PTA solution (right micrograph). Scale bar = 100 nm.

pharmacokinetic experiments (Figure 5.3) are not significantly different with P-values of 0.36 and 0.15, respectively.

5.3.5 Targeting kinetics of αvβ3-targeted SPPM in lung, breast and brain tumor xenografts

Further dynamic MRI studies of SPPM in multiple subcutaneous xenografts were examined and quantified. Tumor ROIs from human A549 lung cancer, MDA-MB-231 breast cancer and U87 glioblastoma cancer cell lines showed similar SI curves with cRGD- (black line, averaged tumor ROI from n = 3 animals, Figure 5.5) having a greater decrease in SI compared to cRAD-SPPM (gray line, Figure 5.5) treated animals. cRGD-SPPM treated animals showed similar trends with a continuing decreasing SI over the 30 minute imaging time. All animals showed similar mean tumor ROI profiles in their respective groups. cRAD-SPPM animals showed a returning trend to baseline SI or a constant SI (U87 model) over the 30-minute imaging time.

To assess the targeting kinetics of the cRGD-SPPM to αvβ3 expressing tumor endothelium, a pharmacokinetic compartmental model was established to assess the targeting kinetics (k_a or $k_{accumulation}$) to the angiogenic endothelium compartment (Figure 5.6). Specifically, the targeting kinetics of the cRGD-SPPM (Figure 5.7) was calculated by subtracting the mean cRGD-SPPM tumor ROI SI curve (black line, Figure 5.5) in all tumor models from the mean cRAD-SPPM tumor ROI SI curve (gray line, Figure 5.5). When fitted to a one compartment physiological model of distribution, cRGD-SPPM showed accumulation rates of 0.21 (R^2=0.48), 0.28 (R^2=0.87) and 0.26 (R^2=0.83) min^{-1} in A549, MDA-MB-231 and U87 tumor models, respectively (Figure 5.7). The slopes of the linear fit (linear regression) from data points after 5 mins also indicate a continued

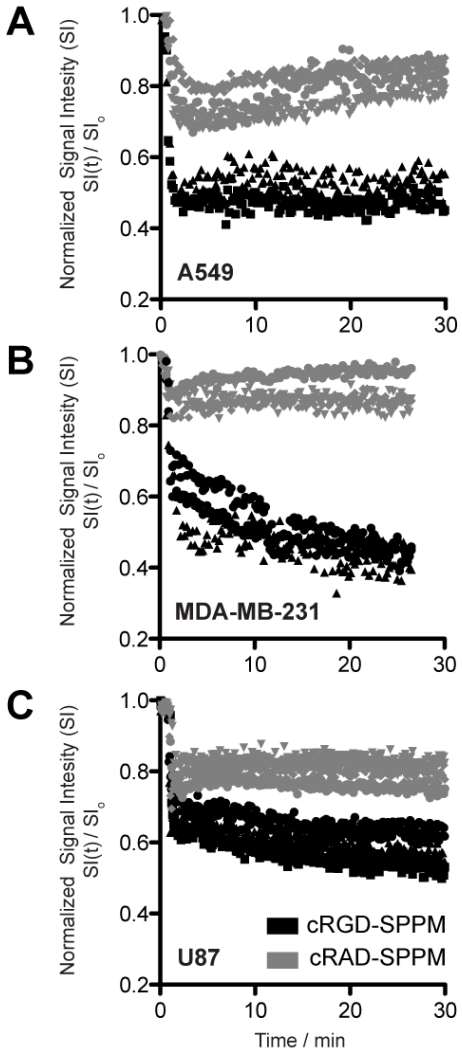

Figure 5.5 - Mean tumor ROI signal intensity curves from cRGD- (black symbols) and cRAD-SPPM (gray symbols) treated animals bearing either A549, MDA-MB-231 or U87 subcutaneous xenografts. cRGD-SPPM tumor hot-spot ROIs (black symbols) show a continued decrease in SI over 30 minutes, indicating continued accumulation. In cRAD-SPPM treated animals (gray symbols) the SI values are maintained or trend upwards back to baseline indicating wash-out or clearance from the tumor tissue.

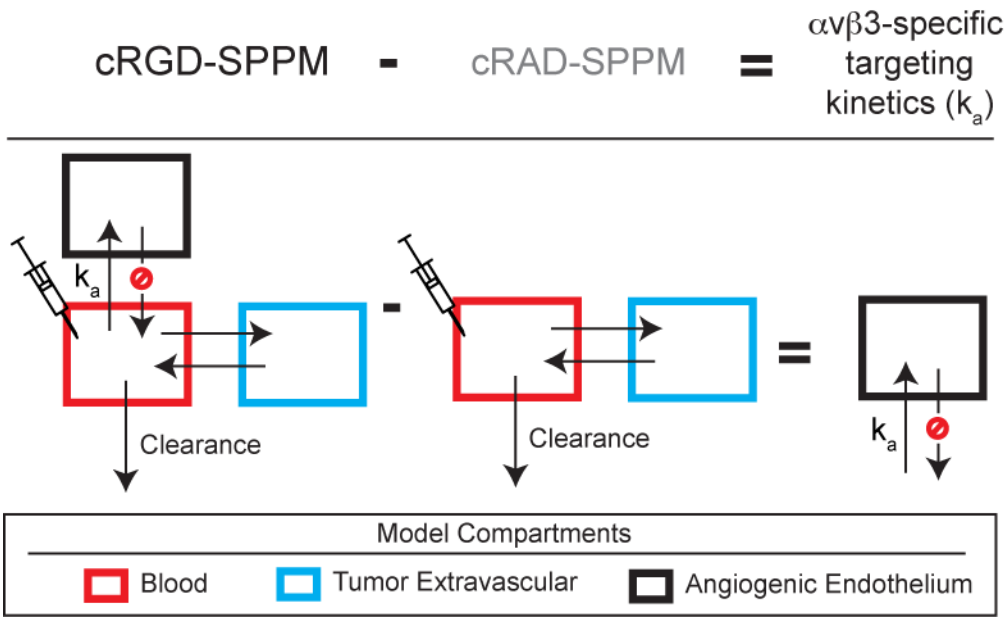

Figure 5.6 - Scheme of the pharmacokinetic model used to define the angiogenic endothelial cell compartment (black box) and elucidate the targeting kinetics of cRGD-SPPM in angiogenic endothelium, or $k_{accumulation}$ (k_a). Assuming that the cRGD-SPPM has a third compartment not present in cRAD-SPPM treated animals, the tumor extravascular compartment (blue box) and blood compartment (red box) can be subtracted out of the kinetic curves leaving only the angiogenic endothelium compartment for analysis.

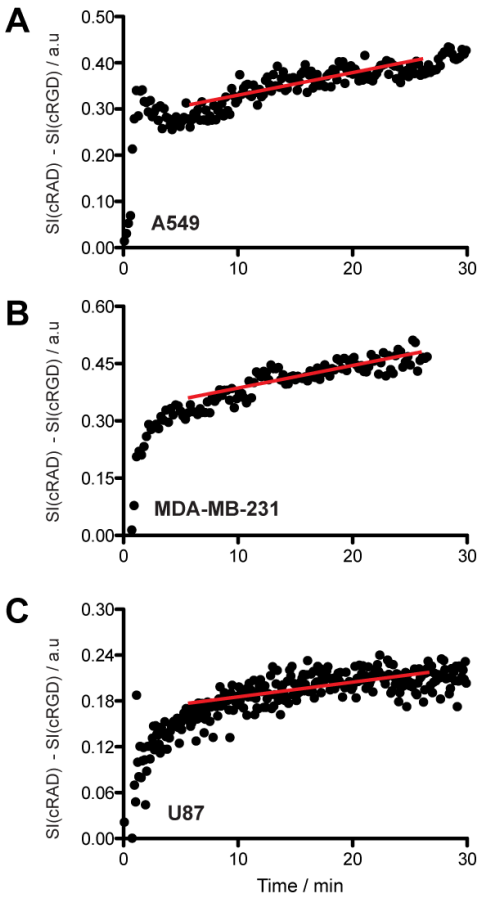

Figure 5.7 - cRGD-SPPM targeting kinetic curves in all three tumor, A549 (A), MDA-MB-231 (B) and U87 (C) models. When fitted to a one compartment physiological model of distribution, cRGD-SPPM showed accumulation rates (k_a) of 0.21 (R^2=0.48), 0.28 (R^2=0.87) and 0.26 (R^2=0.83) min^{-1} in A549, MDA-MB-231 and U87 tumor models, respectively. The slopes of the linear fit (red lines) from data points after 5 mins also indicate a continued accumulation of the cRGD-SPPM in these tissues, with slopes of 0.010 (R^2=0.75), 0.010 (R^2=0.98) and 0.005 (R^2=0.89) min^{-1} for A549, MDA-MB-231 and U87 models, respectively.

accumulation of the cRGD-SPPM in these tissues over the 30 minute HTR-MRI acquisition, with slope of 0.010 (R^2=0.75), 0.010 (R^2=0.98) and 0.005 (R^2=0.89) min^{-1} for A549, MDA-MB-231 and U87 models, respectively. Various tumor pathological factors could determine the total SI change in each tumor model such as MVD, blood flow and αvβ3 expression levels at the time of imaging.

To verify the DCE-MRI data histologically, fluorescent micrographs of the tumor ROIs were investigated. By secondarily injecting Hoechst 33342 intravenously, nuclei of well-perfused vessels could be identified (blue, Figure 5.8). Red fluorescence was seen in close proximity to vessels in the tumor ROIs of cRGD-SPPM treated tumors (Figure 5.8A) whereas a more diffuse punctate staining of the cRAD-SPPM treated animals. Close association of cRAD-SPPM with vessels was not seen in the ROIs examined. The qualitative accumulation of cRGD-SPPM was also greater in comparison to cRAD-SPPM (Figure 5.8B).

5.4 Discussion

In this study, we measured the targeting kinetics of the cRGD-SPPM and cRAD-SPPM to αvβ3 integrins in three tumor xenograft models in vivo using T2*-w HTR-MRI after intravenous injection of an ultrasensitive T2 MRI contrast agent, SPPM. Conventional MRI kinetic studies are conducted using T1-weighted DCE-MRI protocols along with the injection of small molecular Gd-based contrast agents. The kinetic datasets collected from DCE-MRI sequences when processed and fit to well established pharmacokinetic models based on small molecular weight contrast agents can give information on the vascular permeability, blood volume, and density of the tissue of interest as well as the agents perfusion kinetics. However the DCE-MRI protocol is

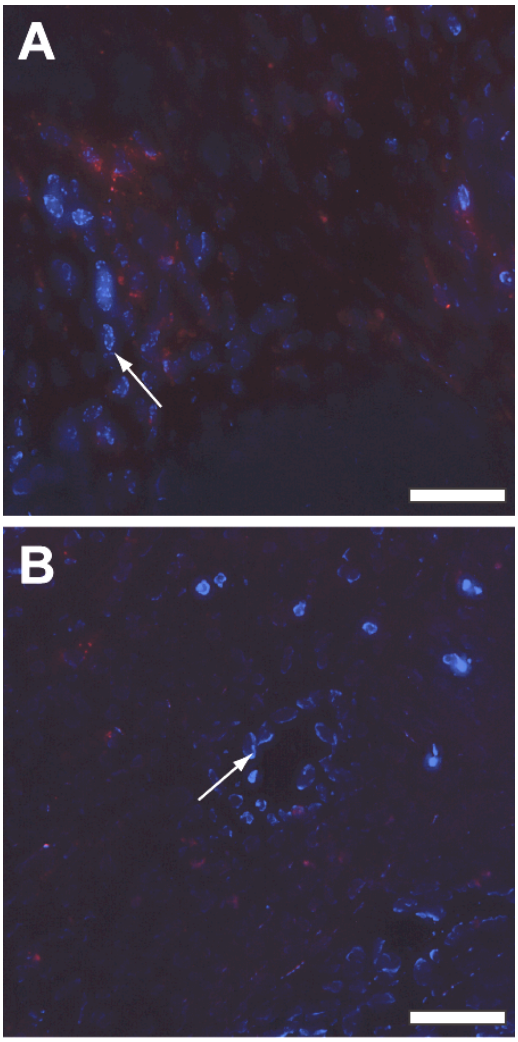

Figure 5.8 - Fluorescent micrographs of cryosectioned tumor xenografts from cRGD- (A, red) and cRAD-SPPM (B, red) treated animals. Highly perfused vessels (white arrows) are stained with Hoechst (blue). This staining is caused by the limited time for the Hoechst dye to circulate (1 min) thus it only stain vessels. cRGD-SPPM are shown tightly associated with these vessels (A, red fluorescence), whereas in the cRAD-SPPM treat animals they are dispersed around throughout the tumor parenchyma (B, red fluorescence).

limited in its application to report binding kinetics of contrast agents to in vivo biomarkers due to the relative insensitivity of T1-weighted contrast agents that require millimolar concentration for detection.[17] In contrast, superparamagnetic nanoparticles (i.e. SPIO-based contrast agents) have shown to be detected at nanomolar to picomolar concentrations by drastically reducing the T2 relaxation times of nearby water protons and that its susceptibility effects can clearly exceed the voxel at which it is located.[5,6] Recent studies on the use of SPIO nanoparticles in a clustered format have shown to further increase the T2 relaxivity of the particle over clinically approved single SPIO nanoparticles.[20,21] This MR ultrasensitivity of SPPM is vital for its detection at concentrations equivalent to in vivo biomarker expression levels, which enables the assessment of their in vivo targeting to αvβ3 and the detection of angiogenic hot-spots in tumor tissues.

SPPM nanoprobes are considered high molecular weight contrast agents with the size around 10^6-10^7 Da. Supramolecular structures, such as SPPM, are limited in the diffusion, extravasation and penetration from blood vessels into tumor tissues due to their size, and are therefore, well suited to target angiogenic endothelium compartments. Hence, cRGD-SPPM localize into and around the angiogenic vasculature allowing the specific detection of these areas and not bulk tumor cells that may also express αvβ3.

Although the current HTR-MRI computational and pharmacokinetic models are not as refined or robust as conventional T1 DCE-MRI analysis, the dynamic contrast profiles recorded allowed for the analysis of targeted versus non-targeted T2 contrast agents. By being able to collect images at a high temporal resolution (i.e. 1.3 s), we were able to visualize the earliest differences in cRGD-SPPM's active $\alpha_v\beta_3$ targeting kinetics

versus cRAD-SPPM passive targeting processes, which is further compared to the blood clearance profiles in the same data set.[9] Although MRI SI is unable to report the concentration of the SPIO nanoparticles in vivo, kinetic analysis based on wash-in, wash-out and accumulation rate models can still yield invaluable targeting data in vivo. Other studies have attempted to use DCE-MRI protocols to study the kinetics of $\alpha_v\beta_3$ targeting but lack the temporal resolution gained by injecting the contrast agent directly via an iv catheter, thus, eliminating the need for replacing the animal into the MR scanner after injection.[9]

Interestingly, the targeting of $\alpha_v\beta_3$ integrins by cRGD-SPPM showed a significantly different kinetic profile than the non-targeted cRAD-SPPM in all three tumor models. Tumor ROI analysis indicated an accumulation of the cRGD-SPPM and an insistent decrease or maintenance of the SI over the 30 minute image acquisition time period (Figure 5.5). The cRAD-SPPM profile, however, showed an initial decrease in SI and then a clearance from the tumor ROI that matched the slope of the blood vessel ROI (purple and blue, Figure 5.2, lower panel), indicating cRAD-SPPM clearance from the blood contributes to the wash-out of the non-targeted SPPM from the tumor ROI. In comparison, in cRGD-SPPM treated animals, blood clearance is similar to that of cRAD-SPPM but the cRGD-SPPM tumor ROI continues to decrease in SI throughout the 30 min HTR-MRI study, indicating a continual accumulation of targeted SPPM in the tumor tissue, possibly a result of αvβ3 recycling and sustained αvβ3-mediated endocytosis. Control ROIs from muscle tissues showed a slight decrease in SI that returned to baseline after 7-9 minutes, which indicates that the perfusion of normal tissue does not cause similar kinetic profiles as observed in the tumor tissue. Moreover, the targeted and non-

targeted SPPM treated animals had similar patterns of wash-in kinetics between three different tumor models, although these tumor models have been shown to have differing vascular architectures (e.g microvascular densities (MVD)).[22-24] By analyzing the tumors with constant ROI areas (546 μm^2), it is assumed that the analysis would be influenced by these differing architectures of the tumors, however the kinetic profiles are comparable between A549, MDA-MB-231, and U87. Although between cRGD-SPPM and cRAD-SPPM in the A549 xenograft model, a slight difference in the tumor wash-in rates can be seen (Figures 5.5A and 5.7A). This difference could be due to varied bolus injection times or the perfusion of the A549 tumor at this ROI. These types of offset can hamper the accuracy, e.g. R^2=0.48 in A549 analysis, of the kinetic analysis to analyze the cRGD-SPPPM targeting in vivo.

To quantify the targeting kinetics of cRGD-SPPM to αvβ3 integrins in vivo, we subtracted the non-targeted SI curve from the cRAD-SPPM from the targeted, cRGD-SPPM SI curves to yield a pure targeting kinetic curve for the cRGD-SPPM. By subtracting the non-targeted SI data, we hypothesized that blood concentration and clearance, extravascular-extracellular and other passive accumulation mechanisms (e.g. EPR effect) are excluded (Figure 5.7). The use of a single compartment model showed similar accumulation rates (k_a) between tumor models with first-order rate constants of 0.21, 0.28 and 0.26 min^{-1} in A549, MDA-MB-231 and U87 tumor models, respectively. This is consistent with the fact that the angiogenic endothelial cells in tumor vasculature are mouse endothelial cells in origin (i.e. independent of the injected human cancer cells), which may share similar expression levels of αvβ3 integrins. As a result, similar kinetics in αvβ3 binding and cell uptake of cRGD-SPPM are anticipated among the different

tumor models. Linear regression analysis from 5-30 mins showed an increasing trend in the cRGD-SPPM targeting kinetic profile (Figure 5.7, red lines), indicating a continuation in cRGD-SPPM uptake in tumor endothelial cells over 30 mins. This two-phase analysis, e.g. k_a and 2nd phase linear fit, can be used to describe the initial binding and uptake of the nanoparticles when they are first seen by the angiogenic endothelial compartment, i.e. k_a, and the possibly continued uptake of nanoparticles via αvβ3 recycling and sustained αvβ3-mediated endocytosis. Longer time HTR-MRI studies could yield interesting kinetic information that is currently absent in the conventional pre- and post-contrast MRI experiments.

In summary, this study demonstrates the feasibility to carry out and quantitatively evaluate the targeting kinetics of cRGD-SPPM in vivo using T2*-w HTR-MRI sequence. Histological analysis corroborates the avb3-specific targeting of cRGD-SPPM where the decrease in SI from the "hot spot" ROIs correlates with the avb3-expressing tumor vasculature. Further physiological analysis using T2*-w HTR-MRI method with SPPM nanoprobes will shed further lights on the vascular permeability and perfusion information from these nanoprobes.

5.5 References

1. Bulte JWM, Kraitchman DL. Iron oxide MR contrast agents for molecular and cellular imaging. NMR Biomed 2004;17(7):484-499.
2. Thorek DLJ, Chen A, Czupryna J, Tsourkas A. Superparamagnetic iron oxide nanoparticle probes for molecular imaging. Ann Biomed Eng 2006;34(1):23-38.
3. Lee JH, Huh YM, Jun Y, et al. Artificially engineered magnetic nanoparticles for ultra-sensitive molecular imaging. Nat Med 2007;13(1):95-99.

4. Seo WS, Lee JH, Sun X, et al. FeCo/graphitic-shell nanocrystals as advanced magnetic-resonance-imaging and near-infrared agents. Nat Mater 2006;5(12):971-976.

5. Khemtong C, Kessinger CW, Ren J, et al. In vivo off-resonance saturation magnetic resonance imaging of alphavbeta3-targeted superparamagnetic nanoparticles. Cancer Res 2009;69(4):1651-1658.

6. Mills PH, Ahrens ET. Theoretical MRI contrast model for exogenous T2 agents. Magn Reson Med 2007;57(2):442-447.

7. Artemov D, Mori N, Okollie B, Bhujwalla ZM. MR molecular imaging of the Her-2/neu receptor in breast cancer cells using targeted iron oxide nanoparticles. Magn Reson Med 2003;49(3):403-408.

8. Hogemann-Savellano D, Bos E, Blondet C, et al. The transferrin receptor: a potential molecular imaging marker for human cancer. Neoplasia 2003;5(6):495-506.

9. Mulder WJ, Strijkers GJ, Habets JW, et al. MR molecular imaging and fluorescence microscopy for identification of activated tumor endothelium using a bimodal lipidic nanoparticle. FASEB J 2005;19(14):2008-2010.

10. Nasongkla N, Bey E, Ren J, et al. Multifunctional polymeric micelles as cancer-targeted, MRI-ultrasensitive drug delivery systems. Nano Lett 2006;6(11):2427-2430.

11. Schmieder AH, Caruthers SD, Zhang H, et al. Three-dimensional MR mapping of angiogenesis with alpha5beta1(alphavbeta3)-targeted theranostic nanoparticles in the MDA-MB-435 xenograft mouse model. FASEB J 2008;22(12):4179-4189.

12. Sonvico F, Mornet S, Vasseur S, et al. Folate-conjugated iron oxide nanoparticles for solid tumor targeting as potential specific magnetic hyperthermia mediators: synthesis, physicochemical characterization, and in vitro experiments. Bioconjug Chem 2005;16(5):1181-1188.

13. Zhang C, Jugold M, Woenne EC, et al. Specific targeting of tumor angiogenesis by RGD-conjugated ultrasmall superparamagnetic iron oxide particles using a clinical 1.5-T magnetic resonance scanner. Cancer Res 2007;67(4):1555-1562.

14. O'Connor JP, Jackson A, Parker GJ, Jayson GC. DCE-MRI biomarkers in the clinical evaluation of antiangiogenic and vascular disrupting agents. Br J Cancer 2007;96(2):189-195.

15. Tofts PS, Brix G, Buckley DL, et al. Estimating kinetic parameters from dynamic contrast-enhanced T(1)-weighted MRI of a diffusable tracer: standardized quantities and symbols. J Magn Reson Imaging 1999;10(3):223-232.

16. Su MY, Wang Z, Carpenter PM, Lao X, Muhler A, Nalcioglu O. Characterization of N-ethyl-N-nitrosourea-induced malignant and benign breast tumors in rats by using three MR contrast agents. J Magn Reson Imaging 1999;9(2):177-186.

17. Ahrens ET, Rothbacher U, Jacobs RE, Fraser SE. A model for MRI contrast enhancement using T1 agents. Proc Natl Acad Sci U S A 1998;95(15):8443-8448.

18. Luo L, Tam J, Maysinger D, Eisenberg A. Cellular internalization of poly(ethylene oxide)-b-poly(epsilon-caprolactone) diblock copolymer micelles. Bioconjug Chem 2002;13(6):1259-1265.

19. Sun S, Zeng H. Size-controlled synthesis of magnetite nanoparticles. J Am Chem Soc 2002;124(28):8204-8205.

20. Ai H, Flask C, Weinberg B, et al. Magnetite-loaded polymeric micelles as ultrasensitive magnetic-resonance probes. Adv Mater 2005;17(16):1949-+.

21. Barcena C, Sra AK, Chaubey GS, Khemtong C, Liu JP, Gao J. Zinc ferrite nanoparticles as MRI contrast agents. Chem Commun (Camb) 2008(19):2224-2226.

22. Mukherjee P, Abate LE, Seyfried TN. Antiangiogenic and proapoptotic effects of dietary restriction on experimental mouse and human brain tumors. Clin Cancer Res 2004;10(16):5622-5629.

23. Matsui J, Funahashi Y, Uenaka T, Watanabe T, Tsuruoka A, Asada M. Multi-kinase inhibitor E7080 suppresses lymph node and lung metastases of human mammary breast tumor MDA-MB-231 via inhibition of vascular endothelial growth factor-receptor (VEGF-R) 2 and VEGF-R3 kinase. Clin Cancer Res 2008;14(17):5459-5465.

24. Jarzynka MJ, Guo P, Bar-Joseph I, Hu B, Cheng SY. Estradiol and nicotine exposure enhances A549 bronchioloalveolar carcinoma xenograft growth in mice through the stimulation of angiogenesis. Int J Oncol 2006;28(2):337-344.

CHAPTER SIX

T2-weighted and ORS MRI in Orthotopic Lung Cancer Models Using αvβ3-Targeted SPPM

6.1 - Introduction

Lung cancer is a devastating disease and is currently the leading cause of cancer-related deaths in men and women over other types of cancer in the US.[1] Although the incidence rate of lung cancer has started to decline recently, five-year survival rates for local, regional, and distant diseases have remained constant at 52.9%, 24.0%, and 3.5%, respectively.[2] At diagnosis, most lung cancers are at an advanced state (56%), i.e. regional or distant (metastatic) stage.[2] In light of the disparaging statistics, it is apparent that early stage lung cancer patients have a much higher five-year survival rate. Early detection and therapeutic invention such as surgical resection and adjuvant chemotherapy may provide a cure and strengthen the potential benefit of lung cancer screening. Based on the premise that early detection of lung cancer may save lives, numerous randomized screens using chest x-rays (CXR) and low dose helical computed tomography (LDCT) have been designed and executed. From these studies, lung cancer could be detected in asymptomatic patients, although some studies reported 10-20% false positive screening rates.[3-7] High false positive rates often lead to significant concerns in healthy individuals. In some cases, the follow-up lung biopsy may result in further complications including partial collapse of the lung, bleeding, and infection as well as unnecessary medical costs. In addition to x-ray based methods for detecting lung cancer, positron emission tomography (PET) and ^{18}F-fluorodeoxyglucose (FDG) are clinically utilized for the staging of lung cancers. PET/FDG has proved to permit diagnosis of lung cancer nodules

greater than 1 cm but also suffers from high false negative rates in nodules less than 1 cm as well as 90% of well-differentiated lung tumors larger than 1 cm.[8-11] This combined with poor spatial resolution in clinical scanners (7-8 mm) are major limitations in the use of PET for early detection of lung cancer.[12]

Therefore, new tools and technologies that are less invasive and can detect malignant lesions from benign lung structures are necessary for the proper diagnosis and/or for the follow up after a positive initial screening for lung cancer. Recently, molecular imaging of cancer biomarkers in preclinical models has shown great promise in reporting molecular and physiological parameters in vivo. New discoveries of novel biomarkers for cancer and specifically lung cancer such as αvβ3 and αvβ6, respectively, hold potential for the specific treatment and stratification of lung cancers in vivo.[13-15] Advances in clinical imaging modalities have also been made, mainly supplemented by concurrent advances in imaging probes and their applications. One such modality is magnetic resonance imaging (MRI), where the introduction of Gd(III)-based T1 contrast agents has allowed the implementation of dynamic contrast enhanced (DCE) - MRI protocols in the clinics to report on vascular permeability and transfer kinetics in tumorigenic tissues. The discovery and application of superparamagnetic iron oxide (SPIO)-based T2 contrast agents has contributed to the advancement of MRI as a molecular imaging modality capable of capitalizing on its superb spatial resolution and soft tissue contrast to image biomarkers such as αvβ3, folate receptor, Her2-Neu, and others noninvasively.

Over the past decade, multifunctional nanosized theranostic platforms that allow for highly specific and quantitative detection of angiogenesis-specific biomarkers have

been under intensive investigation for their ability to noninvasively target, treat and detect cancer. In this study, we report the use of T2-weighted (T2-w) and off-resonance saturation (ORS) MRI and integrin αvβ3-specific superparamagnetic polymeric micelles (cRGD-SPPM, Figure 6.1) for the detection of tail-vein induced orthotopic lung xenografts in vivo. Integrin αvβ3 is a well-established biomarker of angiogenesis, and should facilitate the detection of angiogenesis in lung cancer nodules.

6.2 Materials and Methods

6.2.1 Synthesis and fabrication of cRGD- and cRAD-SPPM

Methoxy- and maleimide-terminated poly(ethylene glycol)-b-poly(D,L-lactide) (MeO-PEG-PLA and Mal-PEG-PLA) and tetramethylrhodamine (TMR) conjugated MeO-PEG-PLA-TMR copolymers and SPIO nanoparticles were synthesized using previously published procedures.[16-18] All copolymers had a molecular weight of 10kD with 5 kD PEG and PLA blocks. The diameter of SPIO nanoparticles was 9.0 ± 0.9 nm by transmission electron microscopy (JEOL 1200 EX at 120 KeV). SPPM were prepared by a solvent evaporation method. [19] Briefly, a mixture of MeO-PEG-PLA, MeO-PEG-PLA-TMR, Mal-PEG-PLA and SPIO in THF was added dropwise to 0.05 M HEPES buffer containing 0.01 M EDTA (pH 7.4) under sonication. The micelle suspension was then equally divided into two parts, and then shaken on an orbital shaker for 4 h to allow THF to evaporate. A solution of either thiol-terminated cRGDfK or cRADfK was added to the micelle solution. The solutions were then shaken overnight to complete conjugation of peptides to maleimide-terminated micelles. Thiol-terminated cRGDfK and cRADfK were obtained by deprotections of thioacetate cRGDfK and cRADfK (Peptides International, Louisville, KY), followed by preparative HPLC purifications. All

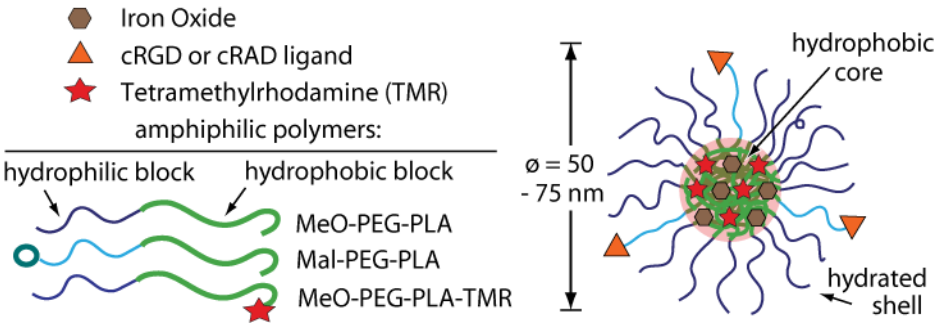

Figure 6.1 - Schematic of superparamagnetic polymeric micelles (SPPM).

SPPM formulations were filtered through 1.0 μm nylon syringe filters and concentrated using centrifugal filters (100 kDa cutoff, Millipore, Billerica, MA).

6.2.2 Tail-vein induced orthotopic lung cancer model and preparation

Animal studies were approved by the Institutional Animal Care and Use Committee at UT Southwestern Medical Center at Dallas and carried out according to its guidelines. For this study both female athymic nude, and SCID-NOD mice weighting 24-27 g and 22-24 g were utilized, respectively. In athymic nude mice, mouse 3LL Lewis lung carcinoma cells were injected ($5x10^5$ cells in 100 μL PBS) via the tail vein, whereas the SCID-NOD mice received human non-small cell lung cancer A549 cells ($5x10^5$ cells in 100 μL PBS). The 3LL and A549 cells were infected with a lentivirus construct that contained the luciferase gene with a cytomegalovirus promoter, to enable their noninvasive tracking via bioluminescence imaging (BLI). Lung colonization and tumor growth were monitored using Xenogen IVIS Lumina and Spectrum imager. For BLI, animals were placed under 1-2% isoflurane anesthesia and 2.5 mg D-luciferin was subcutaneously administered 5 mins prior to imaging. BLI images were acquired with 30 or 60 s exposures. Tumor growth to an MRI visible size (0.5 to 1 mm) took on an average of 7-9 days and 21-30 days for 3LL and A549 inoculated mice, respectively.

6.2.3 T2-w and ORS MRI imaging of lung cancer in mice

All MRI experiments were conducted on a 7T Varian small animal horizontal bore MRI scanner using a 40 mm i.d. Millipede coil. T2-weighted images were collected using a fast spin echo sequence with the following parameters: TR/TE = 3s/40ms; FOV = 30 x 30 mm; Matrix = 128 x 128; NEX = 4; slice thickness 1 mm. T2-weighted images

were collected using gate-triggered acquisition software and instruments by Small Animal Instruments, Inc. where the mouse was positioned in a shed with integrated ECG electrodes and a respiration pillow. MRI acquisition was gated on both cardiac and respiratory signals. Resultant images were with minimal motion artifact of the lungs and heart compared to non-gated images. Mice were injected with 6 mg Fe/kg of SPPM via tail-vein catheter after acquisition of the pre-injection images for T2-w analysis. Post-injection T2-w images were taken 1 h after injection.

ORS experiments were carried out also using a fast spin echo pulse sequence (TR = 3.6 s; TE = 8.94 ms; ETL = 8; NEX = 4; DS =10; FOV = 35 x 35 mm; Matrix = 128 x 64; zero reconstruction = 256 x 256; thickness = 1 mm), with an additional pre-saturation RF pulse at a B_1 power of 2.6 μT (75.22 Hz at 7T) for 0.5 s. The saturation frequencies were ±15, ±1.5, ±1.2, ±0.9, ±0.6, ±0.3, or 0 kHz from bulk water. The image obtained with the off-resonance frequency of 15 kHz (50 ppm) was used as a reference image. ΔORS images were obtained from subtraction of +600 Hz images from the reference image. Under anesthesia with 1.5-2% isoflurane mixed in 100% oxygen, each mouse was tracheaostomized using a 20-gauge 1 cm non-metallic cannula. The cannulated animal was then connected to a small animal ventilator (flexiVent, SCIREQ, Quebec, Canada) with an approximately ~6 m tube in the supine position with the thorax position at the center of the radiofrequency (RF) coil. The animal was mechanically ventilated at 33 breaths/min in which the durations of inhalation were set at 0.3 s and end-expiration at 1.5 s, respectively. The intrapulmonary pressure at end-inspiration was limited to 20 cm H_2O. Mice were then injected with Avertin (500 mg/kg) i.p. to suppress spontaneous respiration. Image acquisition was performed during exhalation hold and was triggered

by respiration only using SAII instrumentation discussed above. The heart beat was not gated in ORS imaging. Shimmed linewidth was on average 300 - 350 Hz for ORS imaging. Mice were injected with 6 mg Fe/kg of SPPM prior to ORS imaging. ORS image acquisition was at 1 h post-injection.

6.2.4 Histological Analysis

After MRI imaging mice were sacrificed and the lungs were filled with formalin, resected and placed in a 50 ml conical filled with 4% formalin for 24 h. After fixation, the tissues were cryoprotected in a sucrose gradient and flash frozen in optimal cutting temperature (OCT) for cryosectioning. Sections 10 μm in thickness were stained by H & E and Prussian blue. Micrographs were taken on a Leica inverted microscope (DMI 6000).

6.3 Results

6.3.1 SPPM characterization

SPPM nanoprobes were the same cRGD-SPPM and cRAD-SPPM formulations used in Chapter 5. Briefly, the spherical SPPM nanoprobes have hydrodynamic diameters of 57±12 and 53±10 nm for cRGD- and cRAD-SPPM, respectively by dynamic light scattering analysis (data not shown). Due to the cluster of superparamagnetic iron oxide (SPIO) in the core of the micelle, all formulations had a mean transverse relaxivity of 406.6 ± 9.1 Fe $mM^{-1}s^{-1}$ at 20° C at 7T, which is 4 fold higher then clinically used SPIO-based Feridex.

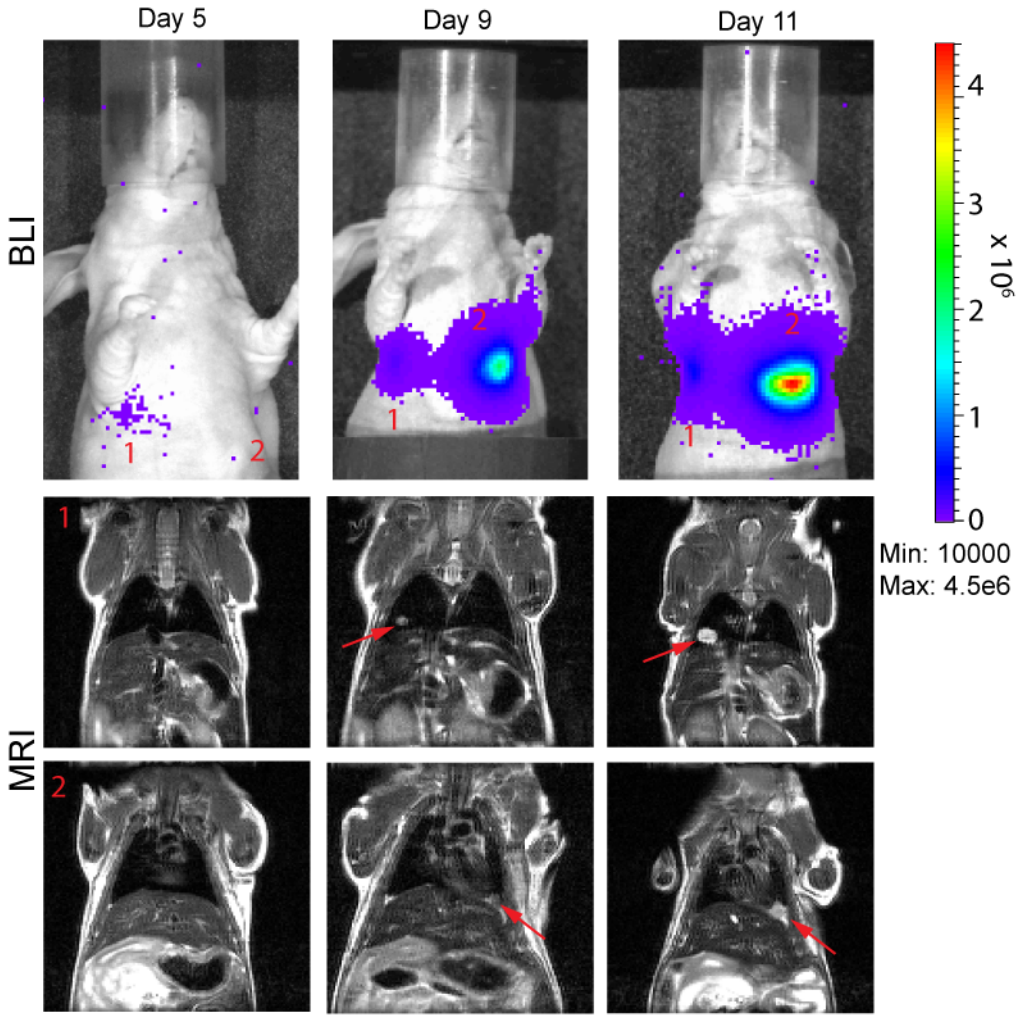

Figure 6.2 - Representative dataset of BLI and T2-w MRI images collected to monitor tumor growth before SPPM experiments. Coronal T2-w images with a 1 mm thickness show tumors location. Red arrows indicate the locations of tumors in the lungs. Middle panels labeled, 1, show the right tumor growth at a coronal depth posterior to the second tumor, 2, depicted in the bottom panels. Tumor 2 is located near the heart structure and on the left side of the mouse.

6.3.2 BLI and MRI monitoring of lung tumor burden

Figure 6.2 illustrates a representative set of BLI and MRI images for the tumor growth in a mouse over time and clearly shows that a positive BLI signal (tumor 1, area photon flux = 4.6 x 10^4) is not indicative of a visible lung tumor nodule in MRI. All BLI and MRI were performed with on the same day. On day 9 post-inoculation with 3LL cells, the BLI can detect two separate tumors with photon fluxes of 18.6 x 10^4 and 428 x 10^4 area photon flux for tumors 1 and 2, respectively (Figure 6.2, red numbers 1 and 2). Tumor volumes calculated from MRI on day 9 were 2.0 mm^3 and 3.2 mm^3 for tumors 1 and 2, respectively. Continued growth of the tumor nodules recorded fluxes of 40.7 x 10^4 and 1300 x 10^4 with tumor volumes of 3.2 mm^3 and 16.5 mm^3 for tumors 1 and 2, respectively (Figure 6.2, Day 11). Based on the BLI and MRI analysis, photon flux is not correlative with MRI tumor volume between tumors in the same animal but is correlative from day to day of the same tumor (Figure 6.2 and data not shown, n = 6). This phenomenon can be attributed to the position of the tumor in the lung. For example, tumor 1, according to MRI, is equidistant to the outside surface of the mouse in three directions (right, ventrally and dorsally) whereas tumor 2 is located very close to the ventral surface of the mouse. This difference in tumor depth has an effect on the transmission of light, created by the luciferase reaction in the presence of luciferin, oxygen and ATP, to the CCD camera. More specifically, more light can escape from tumor 2 due to the short distance and lesser light scattering as it travels through the body. This phenomenon is apparent in the representative mouse in Figure 6.2 where the tumor size at day 9 was 2.0 and 3.2 mm^3 for tumors 1 and 2, respectively, while the flux difference was 23 fold but the tumor volume

difference was only 1.6 fold. Due to this difference in flux and tumor volume each mouse was examined by both BLI and MRI, where the decision to continue with injection of SPPM was based on MRI dataset alone.

6.3.3 T2-w imaging of cRGD- and cRAD-SPPM targeting to A549 lung tumor nodules

In this study, SCID-NOD mice with A549 lung tumor nodules were imaged pre- and 1 h post-injection of cRGD- or cRAD-SPPM via a tail vein catheter (Figure 6.3). Images were acquired under ECG and respiratory gating to minimize motion artifacts from breathing and the heart beat. This setup permitted for the pixel-by-pixel subtraction of pre- and post-injection images due to the fact that the subject was not moved during the whole study. This subtraction allowed the visualization of only the areas where the SPPM particle had accumulated, where it caused a darkening in the signal intensity (SI) in the post-injection image compared to the pre-injection image. The red arrows indicate probable lung tumor nodules in the pre-injection image (Figure 6.3). Animals treated with the αvβ3-specific SPPM (cRGD-SPPM, Figure 6.3) showed a significant increase in SI in the lung tumor subtracted image over the non-targeted cRAD-SPPM with a mean ΔSI of 77.9 ± 17.2 and 43.2 ± 12.1, respectively (Figure 6.4, P-value < 0.001, mean ± s.d.). Liver also showed SI in the subtraction image although lower than the cRAD-SPPM tumor nodule SI. This is consistent with the fact that SPPM do accumulate in the liver tissue after systemic administration.[16] The enhancement seen in the subtraction images of the lung tumor nodules was seen in over 40 tumors across both groups with tumor cross-sections around 700 μm to < 3 mm, already smaller than clinically detected unclassified lung nodules (1-9 mm) using CT and much smaller than confirmed 1 cm malignant lung tumor nodules.[8-11]

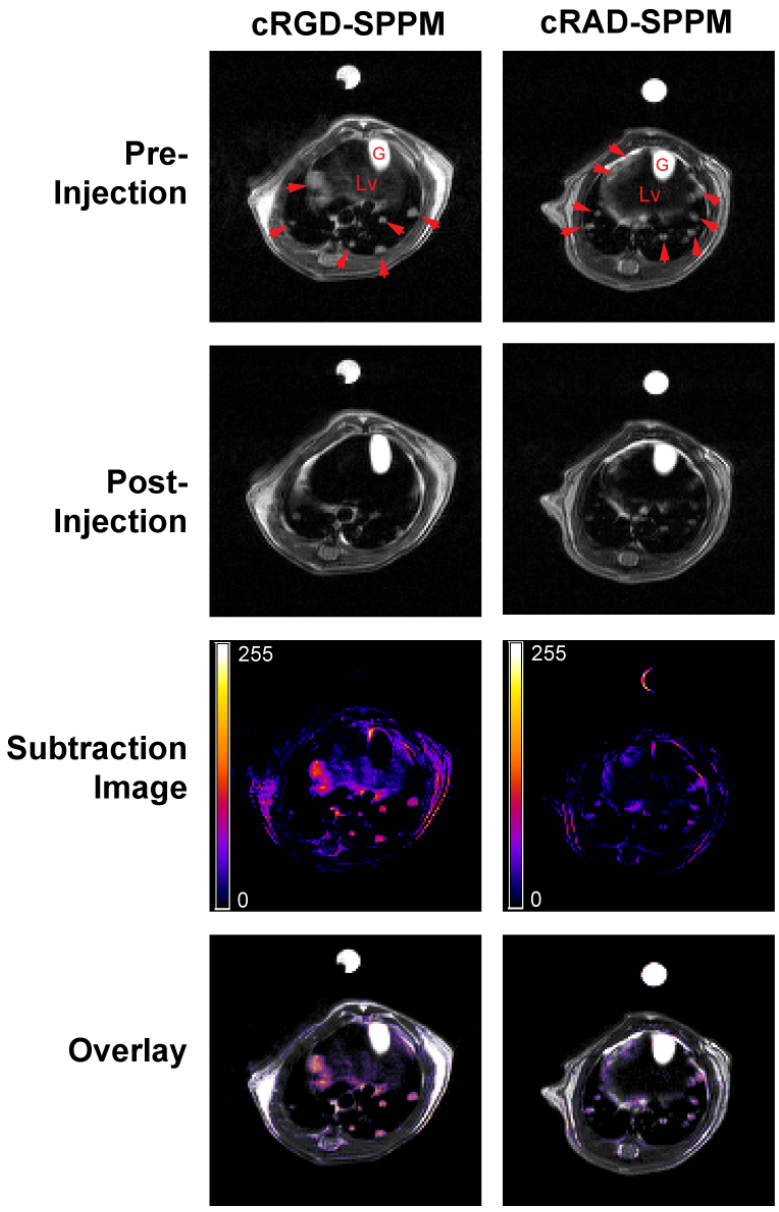

Figure 6.3 - T2-w axial images of mice with A549 lung cancer pre- and post-injection of cRGD-SPPM or cRAD-SPPM. Subtraction images are produced from same slice subtraction of pre- and post-injection images. Red arrows indicate tumors in the lung; Lv: Liver; G: gallbladder.

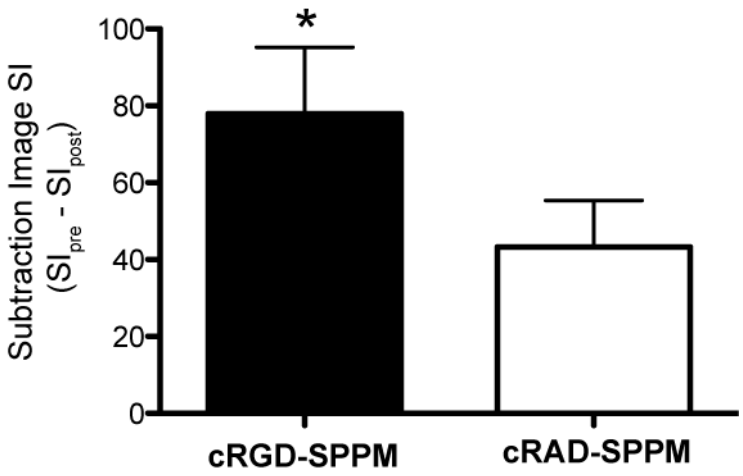

Figure 6.4 - Signal intensity quantification of lung tumors from T2-w contrast images in mice injected with cRGD- or cRAD-SPPM (black and white bar, respectively). n = 20+ tumors across 3 mice per treatment group. *P-value < 0.001.

6.3.4 ORS method MRI of 3LL Lewis Lung tumor nodules

In this study, athymic nude mice with 3LL lung tumor nodules were utilized for their observed ability to grow quickly and form large tumor nodules in the lung.[20] Mice in this group were imaged using ORS method 1 h post-injection of either targeted cRGD-SPPM or non-targeted cRAD-SPPM (n = 3 per group). Compared to T2-w imaging, the ORS acquisition parameters relied on the use of a small animal ventilator to complete the study. The steady respiratory rate provided by the ventilator is necessary to achieve the proper pre-saturation of the mouse at the specific off-resonance frequency and mouse position. Without the use of the ventilator differing slices or areas of the mouse would possibly receive differing pre-saturation energy, thus confusing the ORS image output with false positives or false negatives. Briefly, ORS method is reliant on the acquisition of images with and without an off-resonance pre-saturation RF pulse that selectively decrease the water signal in areas where SPIO are present. Then images from with or without pre-saturation RF pulse, or ON and OFF images, respectively, are subtracted to produce ΔORS contrast images. Figures 6.5 and 6.6 display all animals from the cRGD- and cRAD-SPPM treatment group, respectively, with red arrows indicating probable lung tumor nodules. In both Figure 6.5 and 6.6 it is apparent that there is positive ORS contrast in all the ΔORS images. Only one false positive positive ΔORS contrast was seen in mouse 3 of cRAD-SPPM treatment group (Figure 6.6), as well as a false negative was seen in mouse 1 of cRGD-SPPM treatment group (Figure 6.5, mouse 2 left tumor). Other positive ORS contrast tumors showed partial or total coverage of the tumor cross-section with ORS contrast in tumors as small as 700 μm (Figure 6.5, mouse 1). ORS contrast was also seen in two animals (Figures 6.5 and 6.6, mouse 2) around the

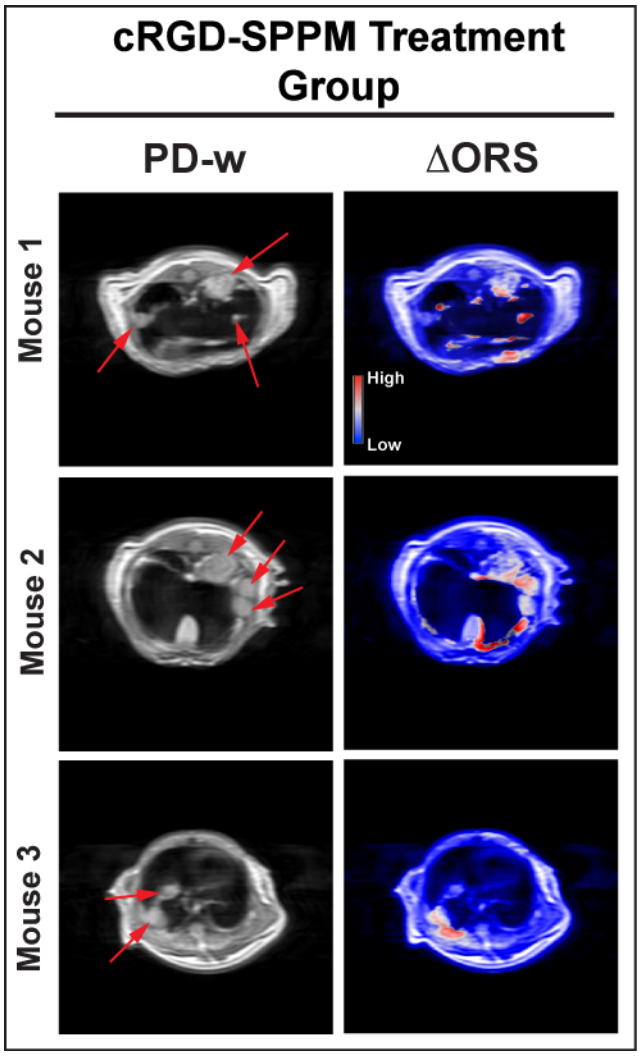

Figure 6.5 - ORS contrast images of cRGD-SPPM treated animals with 3LL lung tumors. Red arrows indicate tumors; PD-w: proton density - weighted images. ΔORS images are overlays of ORS contrast image and PD-w images.

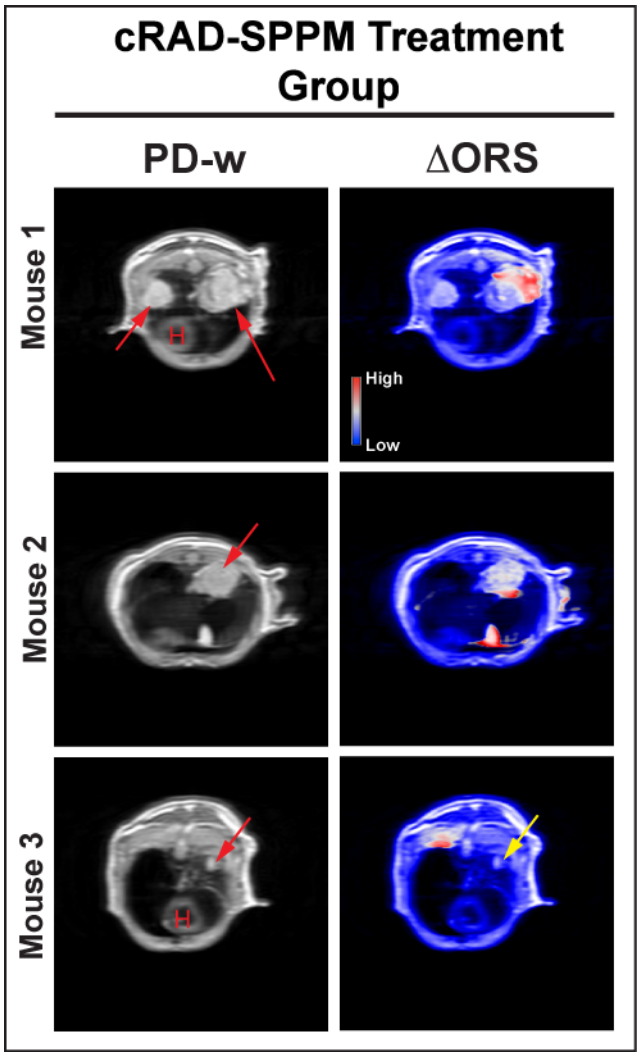

Figure 6.6 - ORS contrast images of cRAD-SPPM treated animals with 3LL lung tumors. ΔORS images are overlays of ORS contrast image and PD-w images. Red arrows indicate tumors; PD-w: proton density - weighted images; H: heart.

gallbladder, this could be due to accumulation at these locations or false positive signals. The histology from these regions was not collected and consequently was not examined. Quantification of the ORS contrast in lung tumors from cRGD-SPPM and cRAD-SPPM treated animals showed values of 101.6 ± 12 and 84.3 ± 30. These values were not significantly different with a P-value of 0.58 (Figure 6.7).

6.3.5 Histological analysis of lung cancer models

All lung tissues were fixed in formalin after MR imaging and were subsequently cryosectioned at a thickness of 10 μm. SPIO was stained by Prussian blue, i.e. forming blue precipitates, with adjacent sections by H&E. Figure 6.8 illustrates a representative dataset of an MRI image, H&E and Prussian blue stained tissue section with 2 tumor nodules, red arrows in Figures 6.8A and B. These types of datasets allow for the matching of the SPIO location in the tumor with the corresponding positive MR contrast in either T2-w subtraction images or ORS contrast images. Blue precipitates found in Prussian blue stained sections matched positive contrast areas in MR images (Figure 6.9). Although a quantitative difference was found between cRGD-SPPM over cRAD-SPPM in T2-w subtraction images and not in ORS contrast images both treatment groups showed qualitative positive blue staining in the lung tumors at locations matching the MRI data (Figure 6.9A, B).

6.4 Discussion

Clinically, lung cancer is detected by x-ray based methods such as CXR and LDCT and staged in tandem with PET/FDG analysis, which provides identification and stratification for surgical and therapeutic intervention of lung nodules with cross-sections

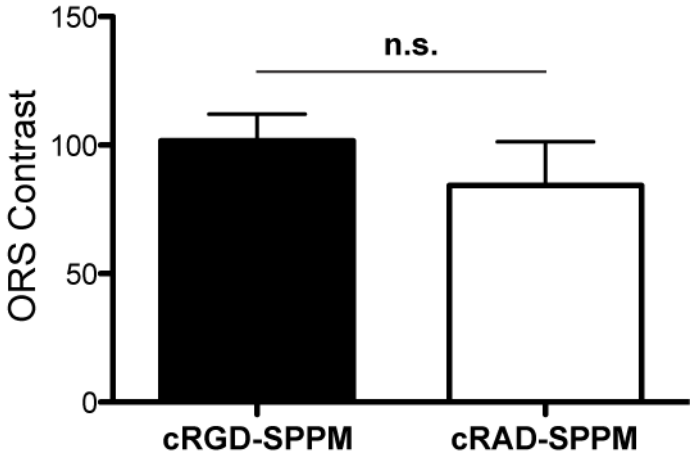

Figure 6.7- Signal intensity quantification of lung tumors from ORS contrast images in mice injected with cRGD- or cRAD-SPPM (black and white bar, respectively). n = 3 mice per group. n.s. = non-significant; P-value = 0.587.

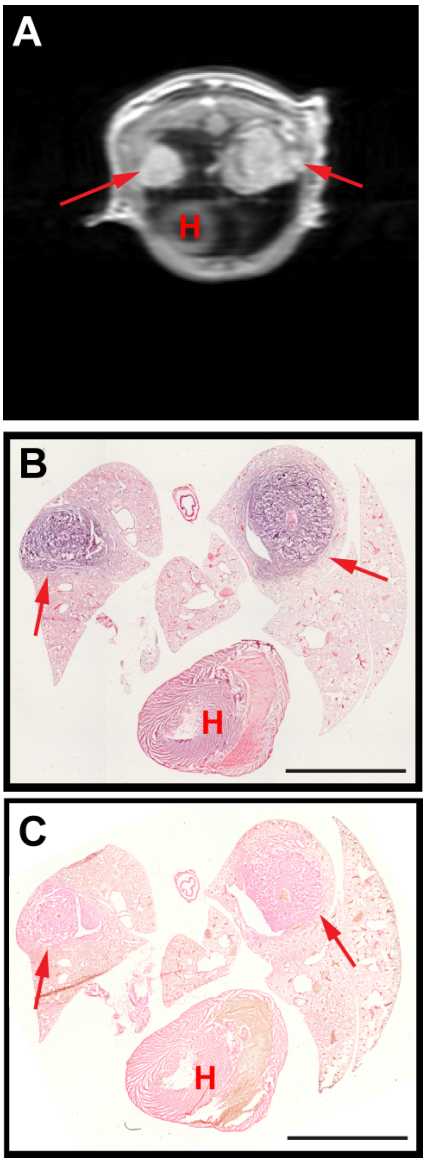

Figure 6.8 - Representative correlation of MRI axial images with histologically stained whole mount cryosections. Shown above is a T2-w MR image (A) with H & E (B) and Prussian blue stained adjacent cryosections (C). Red arrows indicate the tumors. Scale bar = 5 mm. H: heart.

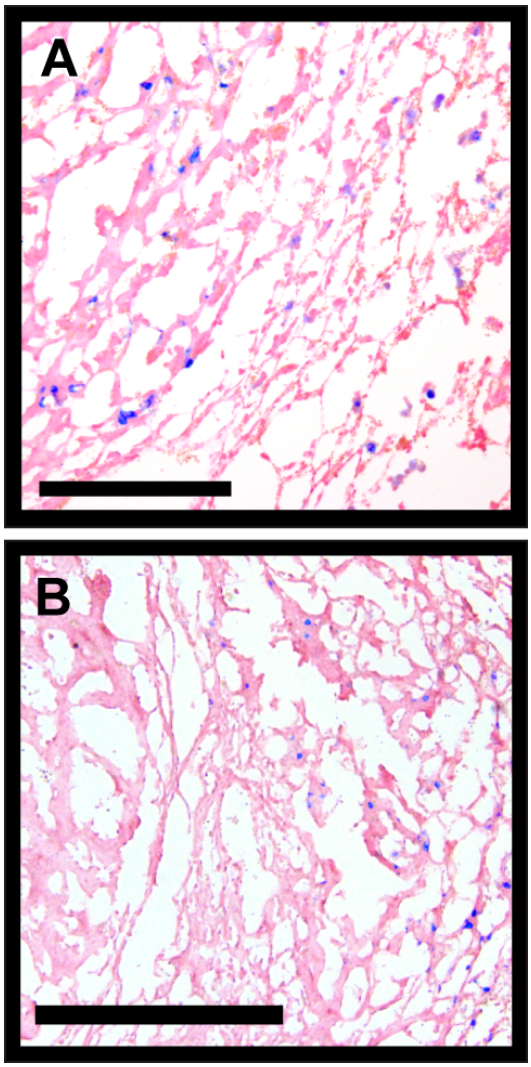

Figure 6.9 - Prussian blue staining of lung tumors treated with cRGD-SPPM (A) and cRAD-SPPM (B). SPPM accumulate in both lung tumors of cRGD- and cRAD-SPPM treated animals. Scale bar = 500 µm.

greater than 1 cm. [3-11] Currently greater than 50% of patients that present with lung cancer have metastatic disease and have a five year survival rate less than 4%, however, if the disease is caught in the local stage of lung cancer their five survival increases over twelve fold.[2] Therefore, the need for imaging protocols capable of assessing the malignance of lung nodules below 1 cm is paramount to possibly decreasing mortality rates from this disease.

MRI is emerging as a potential imaging modality capable of visualizing small lung nodules in vivo due to its excellent soft tissue contrast, but it lacks the molecular or physiological information to discern a nodule's maligancy. Recently, molecular imaging platforms based on SPIO nanoparticles have increased the sensitivity of detection to nanomolar and picomolar concentrations making it capable for these contrast agents to image cancer biomarker expressions in vivo.[16,21-23]

Indeed, results from this study demonstrated detection of lung cancer nodules as small as 400 μm (2 pixels across) using $\alpha v\beta 3$-specific SPPM by MRI in two distinct lung cancer models using a conventional T2-w pre- and post-injection imaging and novel ORS MRI methods over non-targeted SPPM. However it is important to note that non-target cRAD-SPPM also detected small lung nodules in both T2-w and ORS imaging, albeit with significantly less SI of 43.2 ± 12.1 compared to 77.9 ± 17 of cRGD-SPPM treated animals in T2-w analysis (Figures 6.3 and 6.4, P-value < 0.001). In ORS imaging cRAD-SPPM treated animals had equal ORS contrast compared to cRGD-SPPM with ORS contrast values of 84.3 ± 30 and 101.6 ± 12, respectively (Figures 6.5-6.7, P-value=0.58).

To our knowledge this is the first study describing a nanosized targeted T2 contrast agent to specifically detect lung cancer with T2-w imaging, with only one other

study utilizing Gd(III)-based agents in a liposome nanoplatform to visualize lung cancer in a mouse model. In that study, Pirollo and coworkers used single-chain antibody fragments specific for transferrin receptor to decorate the surface of the liposome to target and successfully image small lung cancer nodules (< 400 μm) over non-targeted liposome.[24] However both our T2-w and their T1-w studies rely on the acquisition of pre- and post-injection of contrast agent images to detect lung cancer nodules. This approach can be hard to implement asking the patient to receive contrast agent in the magnet to obtain pre- and post-injection images while also remaining still so as not to cause a misalignment of the pre- and post-injection images for their final subtraction. This movement would specifically hamper the correct detection of very small lung nodules that are less than a few millimeters.

Although T2*-weight (T2*-w) imaging is the gold standard of visualizing SPIO-based particle accumulation, its application in the detection of lung cancer is difficult due to its inherent sensitivity to B_0 inhomogeneity and magnetic susceptibility at air-tissue interfaces, such as those in the lung. This property of T2*-w imaging would possibly lend itself to false negatives and the same pre- and post- injection image acquisition scenarios. However in this study and another subcutaneous tumor study from our group, we reported a novel ORS method where a pre-contrast injection image is not needed to image SPIO-containing tissues. Based on ORS one can take a far off-resonance saturation image, i.e. 50 ppm or 15 kHz, that is not affected by SPIO in the tissue, and an off-resonance saturation image near the bulk water peak, i.e. 2ppm or 600 Hz, where the SPIO causing a darkening in tissue where it is present, simultaneously and then subtract the two to gain a single acquisition ORS contrast image. In Figures 6.5 and 6.6, the ORS

method was applied to visualize a syngeneic lung cancer model with targeted and non-targeted SPPM, and the results showed the ability to detect lung cancer in both models. Histological analysis of the lung samples from both cRGD- and cRAD-SPPM verified that the contrast seen was indeed from the accumulation of SPPM, specifically SPIO, in those areas.

In conclusion, T2-w and ORS imaging methods in concert with the injection with cRGD- and cRAD-SPPM showed the ability to image lung cancer in a human xenograft and mouse syngeneic model. cRGD-SPPM did show significantly higher accumulation at the lung cancer nodules in T2-w analysis but the cRAD-SPPM treated animals also showed contrast in both T2-w and ORS imaging methods 1 h post-injection. Although these results indicate that the visualization of lung tumors can be achieved with either targeted or non-targeted SPPM formulations at 1 h, previous studies have shown greater cRGD-SPPM targeted accumulation in multiple subcutaneous tumor models.[16] This could be due to the need to optimize the post-injection image acquisition time where longer times will increase the accumulation difference in targeted versus non-targeted SPPM. Another explanation could be based on the different organ architecture of the lung compared to subcutaneous locations and the immune cells present at these locations. In subcutaneous models, macrophages are thought to travel to and extravagate into the tumor tissue, whereas in the lung a subset of macrophages, i.e. alveolar macrophages, are always present. Macrophages are part of the reticuloendothelial system and are known to uptake nanoparticles and other foreign particles from the blood, and could be the source of localization of cRAD-SPPM at the site of the tumor. Moreover, the lung is densely packed with blood vessels to facilitate gas exchange. Due to the increased magnetic

susceptibility in the lungs caused by the large air-tissue interface, the lungs appear as void space in all MR images. However, tumors in the lungs have less air-tissue interface and show up as bright spots in T2-w images. Therefore, the addition of a T2-w contrast agent would further increase the magnetic susceptibility in the lung and may cause all tissues in the lung to become darkened. This effect could influence T2-w imaging less due to the decreased sensitivity of SPPM in T2-w images over ORS method images, albeit a small one, i.e. nanomolar versus picomolar concentrations, respectively.[16,21,25]

Future work in the above mentioned areas is the current focus of this project and are essential to developing the ORS method and SPPM nanoprobes for the accurate detection of lung cancer nodules below 1 cm. Other work comparing the detection of benign lesions, such as small nodular scars in the lungs, and lung cancer with SPPM nanoprobes are also necessary for clinical translation.

6.5 References

1. Jemal A, Siegel R, Ward E, Hao Y, Xu J, Thun MJ. Cancer statistics, 2009. CA Cancer J Clin 2009;59(4):225-249.
2. Altekruse SF KC, Krapcho M, Neyman N, Aminou R, Waldron W, Ruhl J, Howlader N, Tatalovich Z, Cho H, Mariotto A, Eisner MP, Lewis DR, Cronin K, Chen HS, Feuer EJ, Stinchcomb DG. SEER Cancer Statistics Review, 1975-2007. In: BK E, editor. National Cancer Institute. Bethesda, MD; 2010.
3. Sone S, Takashima S, Li F, et al. Mass screening for lung cancer with mobile spiral computed tomography scanner. Lancet 1998;351(9111):1242-1245.

4. Henschke CI, McCauley DI, Yankelevitz DF, et al. Early Lung Cancer Action Project: overall design and findings from baseline screening. Lancet 1999;354(9173):99-105.

5. Swensen SJ, Jett JR, Sloan JA, et al. Screening for lung cancer with low-dose spiral computed tomography. Am J Respir Crit Care Med 2002;165(4):508-513.

6. Gohagan JK, Marcus PM, Fagerstrom RM, et al. Final results of the Lung Screening Study, a randomized feasibility study of spiral CT versus chest X-ray screening for lung cancer. Lung Cancer 2005;47(1):9-15.

7. Gohagan J, Marcus P, Fagerstrom R, Pinsky P, Kramer B, Prorok P. Baseline findings of a randomized feasibility trial of lung cancer screening with spiral CT scan vs chest radiograph: the Lung Screening Study of the National Cancer Institute. Chest 2004;126(1):114-121.

8. Gould MK, Maclean CC, Kuschner WG, Rydzak CE, Owens DK. Accuracy of positron emission tomography for diagnosis of pulmonary nodules and mass lesions: a meta-analysis. JAMA 2001;285(7):914-924.

9. Nomori H, Watanabe K, Ohtsuka T, Naruke T, Suemasu K, Uno K. Evaluation of F-18 fluorodeoxyglucose (FDG) PET scanning for pulmonary nodules less than 3 cm in diameter, with special reference to the CT images. Lung Cancer 2004;45(1):19-27.

10. Allen-Auerbach M, Yeom K, Park J, Phelps M, Czernin J. Standard PET/CT of the chest during shallow breathing is inadequate for comprehensive staging of lung cancer. J Nucl Med 2006;47(2):298-301.

11. Knoepp UW, Ravenel JG. CT and PET imaging in non-small cell lung cancer. Crit Rev Oncol Hematol 2006;58(1):15-30.

12. Townsend DW. Physical principles and technology of clinical PET imaging. Ann Acad Med Singapore 2004;33(2):133-145.

13. Elayadi AN, Samli KN, Prudkin L, et al. A peptide selected by biopanning identifies the integrin alphavbeta6 as a prognostic biomarker for nonsmall cell lung cancer. Cancer Res 2007;67(12):5889-5895.

14. Brooks PC, Montgomery AM, Rosenfeld M, et al. Integrin alpha v beta 3 antagonists promote tumor regression by inducing apoptosis of angiogenic blood vessels. Cell 1994;79(7):1157-1164.

15. Brooks PC, Clark RA, Cheresh DA. Requirement of vascular integrin alpha v beta 3 for angiogenesis. Science 1994;264(5158):569-571.

16. Khemtong C, Kessinger CW, Ren J, et al. In vivo off-resonance saturation magnetic resonance imaging of alphavbeta3-targeted superparamagnetic nanoparticles. Cancer Res 2009;69(4):1651-1658.

17. Luo L, Tam J, Maysinger D, Eisenberg A. Cellular internalization of poly(ethylene oxide)-b-poly(epsilon-caprolactone) diblock copolymer micelles. Bioconjug Chem 2002;13(6):1259-1265.

18. Sun S, Zeng H. Size-controlled synthesis of magnetite nanoparticles. J Am Chem Soc 2002;124(28):8204-8205.

19. Nasongkla N, Bey E, Ren J, et al. Multifunctional polymeric micelles as cancer-targeted, MRI-ultrasensitive drug delivery systems. Nano Lett 2006;6(11):2427-2430.

20. Blanco E, Bey EA, Khemtong C, et al. Beta-lapachone micellar nanotherapeutics for non-small cell lung cancer therapy. Cancer Res 2010;70(10):3896-3904.

21. Mills PH, Ahrens ET. Theoretical MRI contrast model for exogenous T2 agents. Magn Reson Med 2007;57(2):442-447.

22. Sonvico F, Mornet S, Vasseur S, et al. Folate-conjugated iron oxide nanoparticles for solid tumor targeting as potential specific magnetic hyperthermia mediators: synthesis, physicochemical characterization, and in vitro experiments. Bioconjug Chem 2005;16(5):1181-1188.

23. Artemov D, Mori N, Okollie B, Bhujwalla ZM. MR molecular imaging of the Her-2/neu receptor in breast cancer cells using targeted iron oxide nanoparticles. Magn Reson Med 2003;49(3):403-408.

24. Freedman M, Chang EH, Zhou Q, Pirollo KF. Nanodelivery of MRI contrast agent enhances sensitivity of detection of lung cancer metastases. Acad Radiol 2009;16(5):627-637.

25. Ai HF, C.; Weinberg, R.; Shuai, X.; Pagel, M.; Farrell, D.; Duerk, J.; Gao, J. Magnetite-Loaded Polymeric Micelles as Novel Magnetic Resonance Probes. Adv Mat 2005;17:1949-1952.

CHAPTER SEVEN

Summary and Future Work

7.1 - Summary of work

Currently, lung cancer is the leading cause of cancer-related deaths in men and women in the US and worldwide.[1,2] Advances in early detection of the disease with the advent of low dose helical computed tomography (LDCT) and application of positron emission tomography (PET) and ^{18}F-fluorodeoxyglucose (FDG) has proven successful in diagnosing lung nodules greater than 1 cm as cancerous but is unable to accurately assess the malignancy of lesions less than 1 cm. Tumors 1 cm^3 contain roughly 10^9 cancer cells and are capable of shedding over 10^6 cells per day leading to metastatic disease in major organs such as the brain, liver and bone.[3] Current five year survival rates for lung cancer diagnosed at the metastatic stage is less than 4%, but this is improved 14 fold if the disease is caught at its earliest stage.[2] Therefore, new technologies and methods for the accurate identification of early stage lung cancer nodules are necessary and should play a beneficial role in the clinical management of lung cancer, helping physicians stratify and recommend the most advantageous treatment regiments for their patients.

Our objective was to develop a molecular imaging nanoprobe that could effectively target αvβ3 as well as develop novel imaging methods to noninvasively report on angiogenesis in tumorigenic tissues in the lung. Hence, in Chapter 2 of this dissertation, we fabricated a fluorescent cRGD-labeled polymeric micellar nanoprobe loaded with a cluster of SPIO in its core, referred to as FSPPM. MR and fluorescent characterization showed a nanoprobe that was 4-fold more sensitive to MRI detection over clinically used SPIO-based contrast agents, as well as fluorescent. In vitro cRGD-

SPPM showed increased uptake in overexpressing αvβ3 SLK cells using both MR and fluorescence endpoints over control non-targeted cRAD-SPPM. In vivo cRGD-FSPPM allowed for the detection and 3D mapping of angiogenic hot-spots in subcutaneous xenografts.

In Chapter 3, we proposed and validated a novel MRI imaging method, ORS, showing that an off-resonance saturation RF-pulse turned on and off can report on the presence of SPIO-based nanoprobes in aqueous solutions at 4.7T and 7T magnetic field strengths. Continuation of this work was reported in Chapter 4, where αvβ3-targeted SPPM and ORS MRI was utilized for the detection of angiogenesis in a subcutaneous lung cancer tumor xenograft in vivo. Moreover, SPPM was detectable using ORS MRI at concentration as low as 22 pM (10^{-12}) where conventional T2-w detection is in the nM (10^{-9}) concentration range. The ORS method also showed to be more specific for SPIO compared to the current gold-standard for SPIO detection, T2*-w imaging, and biodistribution of the cRGD-SPPM in the tumor was 2 fold greater than control SPPM groups.

In Chapter 5 of this work, T2*-w HTR-MRI was utilized to analyze the targeting kinetics of αvβ3-targeted SPPM in vivo. With a temporal resolution of 1.3 s, HTR-MRI was able to report accumulation rates into the angiogenic endothelium compartment, a first for noninvasive targeted nanoparticle analysis. In Chapter 6 we applied, both the ultrasensitive SPPM nanoprobe and MRI (conventional T2-w and novel ORS MRI) to image human A549 and syngeneic 3LL tail-vein induced othrotopic lung cancer model. Here we showed that both T2-w and ORS MRI in concert with SPPM could image lung tumor nodules as small as 400 μm.

Taken together, results from this study demonstrate the potential of αvβ3-targeted SPPM nanoprobes and ORS MRI for lung cancer detection sub 1 cm.

7.2 Future work

In the immediate future comprehensive and in-depth validation of the cRGD-SPPM nanoprobe platform with ORS MRI in a malignant and benign lung models should be carried out. Further examination of the nanoprobe's imaging efficacy in other orthotopic cancer models in small animals as well as including higher order species, is necessary prior to the clinical translation of the nanoprobe and imaging technologies. However, the ORS method is currently translatable to the clinic with only minor MR sequence modifications needed for the imaging of clinically approve SPIO-based contrast agents. Other future work, discussed below, can aim to take advantage of the theranostic platform of the SPPM with the functionalization of the micelle with other ligands specific novel cancer biomarkers or the incorporation of therapeutic agents. Other novel MRI methods to quantify the amount of SPPM in tissue have been proposed and could be examined in the context of noninvasively following anti-angiogenesis therapy. [4-6]

7.2.1 Functionalization of SPPM with NSCLC binding peptides for MR imaging and stratification of lung cancer

Due to the multifunctional nature of the SPPM nanoplatform targeting ligands can freely be functionalized to the SPPM surface by maleimide chemistry. Recently, Brown and coworkers have shown the ability to identify selective and specific NSCLC binding peptides, H2009.1, H1299.1 and .2, HCC15.1 and .2, using an M13 phage biopanning process.[7] These ligands may be useful in the stratification of patients due to their cell line specificity. Specifically the H2009.1 peptide has been shown to bind the

integrin αvβ6, which is a prognostic marker for NSCLC.[8] Gao and coworker in collaboration with the Brown lab, have been able to e functionalize a theranostic micelle formulation with the H2009.1 peptide for the specific delivery of doxorubicin and SPIO to αvβ6-expressing cells in vitro.[9] Extension of this work is currently ongoing in the lab, but application of the technology to specific imaging of lung cancer should also be investigated. In this strategy, lung cancer peptide-encoded SPPM can be utilized in concert with ORS imaging in a orthotopic model to distinguish between different type of lung cancer. Therapeutic agents could also be incorporated into the SPPM platform to allow for the specific delivery and noninvasive imaging of targeted SPPM over time, thus allowing one to follow the amount of drug reaching the target and the efficacy of the treatment over time.

7.2.2 Magnetic susceptibility MRI for noninvasive T1 and T2 contrast agent quantification angiogenesis in vivo

Currently quantitative MRI of contrast agents has been mainly correlative with endogenous or exogenous standards, such as CNR comparisons with muscle tissue or water/Gd(III) phantoms placed outside the animal, respectively. However, recent work by Yang and coworkers have utilized gradient echo MR imaging to report on the exact amount of Gd(III) or Fe, i.e. SPIO, in a specific voxel.[4-6] This technology, magnetic susceptibility MRI (msMRI), is similar to 3D gradient echo acquisition with the addition of multiple acquisitions at increasing TE values. The specific equations derived by their work analyze the magnetic susceptibility generated in MR phase images. Preliminary studies have already shown that the SPPM nanoprobe is compatible with the

quantification method, but an in-depth study and proper biological application are needed.

One clinically relevant application would be the implementation of the msMRI method to quantitatively assess angiogenesis utilizing the cRGD-SPPM targeting of αvβ3 integrin pre- and post- anti-angiogenesis therapy using clinically available or preclinically available agents, such as bevacizumab or 2C3.

7.3 References

1. Jemal A, Siegel R, Ward E, Hao Y, Xu J, Thun MJ. Cancer statistics, 2009. CA Cancer J Clin 2009;59(4):225-249.
2. Altekruse SF KC, Krapcho M, Neyman N, Aminou R, Waldron W, Ruhl J, Howlader N, Tatalovich Z, Cho H, Mariotto A, Eisner MP, Lewis DR, Cronin K, Chen HS, Feuer EJ, Stinchcomb DG. SEER Cancer Statistics Review, 1975-2007. In: BK E, editor. National Cancer Institute. Bethesda, MD; 2010.
3. Butler TP, Gullino PM. Quantitation of cell shedding into efferent blood of mammary adenocarcinoma. Cancer Res 1975;35(3):512-516.
4. Kressler B, de Rochefort L, Liu T, Spincemaille P, Jiang Q, Wang Y. Nonlinear regularization for per voxel estimation of magnetic susceptibility distributions from MRI field maps. IEEE Trans Med Imaging 2010;29(2):273-281.
5. Liu T, Spincemaille P, de Rochefort L, Kressler B, Wang Y. Calculation of susceptibility through multiple orientation sampling (COSMOS): a method for conditioning the inverse problem from measured magnetic field map to susceptibility source image in MRI. Magn Reson Med 2009;61(1):196-204.

6. Wang Y, de Rochefort L, Liu T, Kressler B. Magnetic source MRI: a new quantitative imaging of magnetic biomarkers. Conf Proc IEEE Eng Med Biol Soc 2009;2009:53-56.

7. Oyama T, Sykes KF, Samli KN, Minna JD, Johnston SA, Brown KC. Isolation of lung tumor specific peptides from a random peptide library: generation of diagnostic and cell-targeting reagents. Cancer Lett 2003;202(2):219-230.

8. Elayadi AN, Samli KN, Prudkin L, et al. A peptide selected by biopanning identifies the integrin alphavbeta6 as a prognostic biomarker for nonsmall cell lung cancer. Cancer Res 2007;67(12):5889-5895.

9. Guthi JS, Yang SG, Huang G, et al. MRI-visible micellar nanomedicine for targeted drug delivery to lung cancer cells. Mol Pharm 2010;7(1):32-40.

APPENDIX A
Protocols

Cryosectioning

- Tissue Processing Protocol -

To produce thin, high-quality frozen sections, the tissue must be well prepared, the conditions of the cryostat must be optimal, and the block temperature must be correct for the tissue being cut. The best quality frozen sections are produced from fresh unfixed tissue that has been rapidly frozen. However, fixed tissue can provide quality sections as well. Herein, are provided protocols for fixation and freezing the tissue for cryosectioning. This is not the absolute protocol and much more can be learned though experimenting with conditions, and online resources such as, Histonet Archives.

Below are outlined protocols that describe the preparation of fresh unfixed tissue and fixed tissue for cryosectioning.

Preparation of Tissue

Preparation of Fixed Tissue:

1. Resect tissue(s) of interest
2. Cut tissues into smaller pieces (< 1 cm^3)†
3. Put tissue in 10% Formalin
4. Shake at RT (O/N)
5. Wash 1 x PBS, 3x, at 4°C
6. Immerse in 10% Sucrose (8h, 4°C)
7. Immerse in 18% Sucrose (O/N, 4°C)
8. Snap-freeze tissues

Preparation of Fresh Unfixed Tissue:

1. Resect tissue(s) of interest
2. Cut tissues into smaller pieces (< 1 cm^3)†
3. Snap-freeze tissues

⚠ CAUTION
Avoid having to section skin, fat or bone. All are difficult to section along with tissue of interest.

Snap-freezing of Tissue

There are numerous ways to snap-freeze tissue (Table 1). To obtain quality sections without freezing artifact the tissue needs to be rapidly frozen. Freeze artifact happens when ice crystals form and then thaw after sectioning, the ice melts and leaves a hole in the tissue section. To decrease this artifact fixed tissue are cryoprotected with sucrose and snap-frozen, and never thawed and re-frozen. Below are two protocols for storage of tissue with and without OCT. OCT is a polymer-water mixture that is liquid at RT and a hard white matrix at -10°C and below, that helps support the tissue when being sectioned.

Techniques for suitable freezing include:

Liquid nitrogen	-190°C
Isopentane cooled by liquid N_2	-150°C
Dry ice	-70°C
Dry ice slurries*	~ 70°C

*Dry ice w/Acetone,MeOH, or EtOH

Table 1: Snap-Freezing Options

⚠ CAUTION
Isopentane is extremely flammable but is noted to be the standard, high quality method. Dry ice slurries can fix the tissue while freezing which could mask your antigen of interest in IF or IHC. Some tissues require different application of freezing methods, consult online references.

Snap-freezing of Tissue (continued)

Liquid Nitrogen Methods††

1. Pour into proper bowl container

Storage in cryovial without OCT:

1. Blot Tissue
2. Place tissue, fixed or fresh, into cryovial
3. Submerge in liquid nitrogen until frozen
4. Store at -80°C

⚠ CAUTION
Over-freezing can crack OCT & tissue!!!

Storage in cryomold with OCT:

1. Blot Tissue
2. Place tissue into cryomold with OCT
3. Place plastic petri dish on top of liquid nitrogen, so that it floats
4. Place cryomold in the dish
5. Wait until OCT is completely white
6. Store at -80°C

Preparing Tissue for Sectioning

Now that you have frozen tissue or tissue blocks, you will need to optimize the cryostat cabinet and specimen holder temperature for sectioning. As well as embed your tissue in OCT if it is not already. Provided is a table of optimal cutting temperatures based on the type of tissue (Table 2). Set the cryostat to the proper temperature and place the frozen tissue and tissue blocks, chucks, and blade into the chamber so the tissue and equipment's temperature can equilibrate.

Embedding Tissue in OCT:

1. Place a bead of OCT on the chuck.
2. Before the bead freezes place the tissue on the bead, using pre-cool tweezers.
3. Next use the OCT to cover all sides of the tissue. Go slow, so that the OCT has time to soldify and then build the OCT up to completely cover the tissue.
4. Be patient! Step 3 can get very messy.
5. Once solidified you are ready to cut.

Mounting Cryomold OCT embedded tissue:

1. Remove tissue block from cryomold.
2. Place a bead of OCT on the chuck.
3. Before the bead freezes place the block on the bead, using pre-cool tweezers.
4. Once solidified you are ready to cut.

Tissue	10 - 15	15 - 25	25 - 50
Tumor	X	X	
Liver			X
Spleen	X	X	
Kidney			X
Brain		X	
Intestinal		X	
Heart		X	
Muscle		X	
Fat			X
Lung†††		X	

Table 2. Reference for temperature settings (in minus °C)

† Small tissue chucks allow for homogenous diffusion of formalin through the tissue. However, in my experience this doesn't need to be done in most cases.
†† Other methods for freezing tissue are used in the cryosectioning field, i.e. Table 1.
††† Lung tissue should be inflated with an 1:1 OCT:Water mixture before freezing and sectioning.

Hematoxylin and Eosin

- Tissue Staining Protocol -

Hematoxylin and Eosin stain, H&E stain or HE stain, is a standard staining method in histology. It is widely used in medical diagnosis of biopsies of a suspected cancer. Its popularity is based on its comparative simplicity and ability to demonstrate clearly an enormous number of different tissue structures. Essentially, the hematoxylin component stains the cell nuclei blue-black, while the eosin stains cell cytoplasm and most connective tissue fibers in varying shades and intensities of pink, orange, and red.

Below is an outlined protocol that describes the staining of formalin fixed and fresh cryosectioned tissue.

Preparation

Supplies

1. Tissue sections on slides.†
2. Hematoxylin (Harris)
3. Eosin (Eosin Y)
4. Bluing Agent
5. 95% EtOH, 100% EtOH
6. Xylene or Xylene Substitute
7. Mounting Media
8. Glass Cover Slips, No. 1 or 1.5
9. Coplin Jar(s)

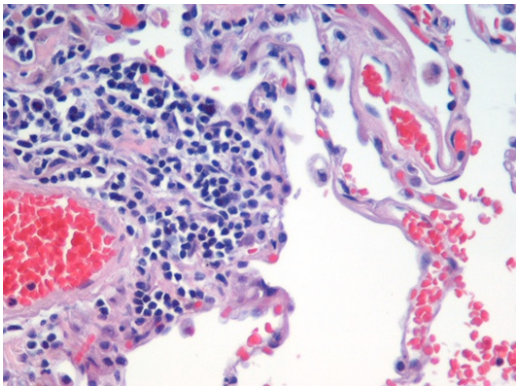

H&E stained paraffin-embedded lung section.

Slide Preparation

Before starting staining the tissue should be fixed. Outlined below is a common way of fixing unfixed cryosections.

1. Prepare -20°C Acetone
2. Pour -20°C Acetone into coplin jar that is on, and surrounded by ice.
3. Incubate slide(s) in acetone for 2 - 10 mins.
4. Remove slides and let dry completely.
5. Rinse slides dH_2O, this will remove OCT that surrounds the section.

H&E Staining Protocols

One the following pages are two different H&E staining protocols. One is a standard protocol and the other is a rapid protocol. Both produce similar staining patterns. I have included both for completeness. **If your sections were paraffin embedded. Please follow procedure below before starting staining protocol.

Deparaffinize and Rehydration of Paraffin Embedded

1. 3 x 2' Xylene
2. 3 x 2' 100% EtOH
3. 1 x 2' 90% EtOH
4. 1 x 2' 85% EtOH
5. 1 x 5' dH_2O

⚠ CAUTION
Only paraffin embed tissues need to be deparaffinized and rehydrated.

⚠ CAUTION
Xylene has harmful fumes, use in hood. It will melt gloves.

†Charged slides are preferred because the charge interaction with the sections holds the section to the slide.

Rapid Hematoxylin and Eosin Protocol

1. Slide mounted section are washed briefly in tap water.
2. Stain in hematoxylin solution for 2 minutes.
3. Rinse in tap water - 2 changes.
4. Differentiate in 1% acid alcohol.
5. Immediately dip slides in tap water, 3x, to rinse.
6. Blue the slides in Bluing Agent for 30 seconds.
7. Counterstain in 1% eosin for 30 seconds
8. Rinse in tap water.
9. 3 x 2' 95% EtOH
10. 3 x 2' 100% EtOH
11. 3 x 2' Xylene
12. Mount in synthetic mounting medium.

Hematoxylin and Eosin Protocol

1. Slide mounted section are washed briefly in tap water.
2. Stain in hematoxylin solution for 1 minutes.
3. Rinse in tap water - 2 minutes.
4. Dip 8 - 12x in acid alcohol to differentiate.
5. Rinse in tap water - 2 minutes.
6. Blue the slides in Bluing Agent for 2 minute.
7. Rinse in dH2O - 2 minutes
8. Counterstain in 1% eosin for 1 minute.
9. 3 x 2' 95% EtOH
10. 3 x 2' 100% EtOH
11. 3 x 2' Xylene
12. Mount in synthetic mounting medium.

Prussian Blue Method

- Iron Staining of Tissue Section or Fixed Cells -

Prussian blue reaction involves the treatment of samples with an acid solution of ferrocyanides. Any ferric ion (Fe^{3+}) present in the sample combines with the ferrocyanide and results in the formation of a bright blue pigment called Prussian blue, or ferric ferrocyanide. This and other variations (DAB-PrussianBlue) are the most sensitive histochemical tests for iron.

Solutions and Reagents (Make fresh) :

Nuclear Fast Red Solution - from FisherSci

20% Aqueous Solution of Hydrochloric Acid:
Hydrochloric acid, concentrated 37% _____ 20 mL
Distilled water _____ 80 mL
Mix well.

10% Aqueous Solution of Potassium Ferrocyanide:
Potassium ferrocyanide, Trihydrate _____ 10 grams
$(K_4Fe(CN)_6 \bullet 3H_2O$
Distilled water _____ 100 mL
Mix to dissolve.

Working Solution:
Mix equal parts of 20% hydrochloric acid and 10% potassium ferrocyanide solutions JUST before use. Mixed working solution is good only for immediate use, DO NOT let solution sit for 10 minutes before use, after 10 minutes the solution may give false positives. The solution will produce blue precipitates due to it reacting with itself.

Sample Fixation/Prep:

Cells: Procedure has worked with -20C acetone, 70%MeOH/30%Acetone (-20C), formaldehyde, and formalin fixed samples.

Tissue: Sections from formalin or fresh-frozen tissue samples will work.
For frozen sections fix in -20C acetone for at least 2-5 minutes. Acid can deform tissue sample if not fixed for long enough time. After fixation let air dry then follow staining procedure

Prussian Blue Staining Procedure:

1. Hydrate samples - Put slides to distilled water (1x for 2 min).
2. Immerse slides in the working solution for 20-30 minutes.
3. Wash in distilled water (3x changes)
4. Counterstain with nuclear fast red for 5 minutes.
5. Rinse twice in distilled water.
6. Coverslip with mounting medium.

Results:
Iron = bright blue
Nuclei = Red
Cytoplasm = red/pink

Wheat Germ Agglutinin

- Cell Membrane Staining Protocol -

Wheat germ agglutinin (WGA) is a lectin that selectively binds to sialic acid and N-acetylglucosaminyl residues. (Cell membranes) In solution, WGA exists as a heterodimer with a moelcular weight of approximately 38,000 daltons and is normally cationic under physiological conditions. (www.probes.com)

This staining can be combined to the end of any extracellular fluorescent staining protocol.

Protocol:

1. Wash cells with 1x PBS (3 x 2 min)
2. Fix cells with freshly made 4% paraformaldehyde in PBS (30 min or O/N @ 4°C or 10 min @ RT)
3. Rinse with Tris/PBS (3 x 2 min), 1mL of 1M Tris in 49mL 1x PBS (50mL total)
4. Stain with WGA solution (10 min @ RT)- 1:100 dilution of WGA stock in PBS
    1. WGA Stock Prep
        1. Comes as powder
        2. Add sterile PBS to make 1 mg/mL concentration
        3. Store 4°C
5. Wash cells with 1x PBS (3 x 2 min)
6. Mount with or without DAPI

Available in lab WGA conjugates as of 1/2009:

1. Blue-fluorescent AlexaFluor 350 WGA
2. Oregon Green 488 WGA
3. TMR WGA
4. Texas Red WGA

Dry powder stored in -20C
Stock solution stored in 4C

Hoechst 33342

- Nuclear Staining Protocol for Live-Cell or Fixed Imaging -

Hoechst 33342 nucleic acid stain is a popular cell-permeant nuclear counterstain that emits blue fluorescence when bound to dsDNA. This dye is often used to distinguish condensed pycnotic nuclei in apoptotic cells and for cell cycle studies in combination with BrdU. (www.probes.com)

This staining can be combined to any fluorescent staining protocol.

Live-Cell Protocol:

1. Wash cells with 1x PBS (3 x 2 min)
2. Incubate cells with Hoechst/PBS solution for 10-15 minutes.(1µg/mL Hoechst/PBS, ~ 1:1000 Dilution from Hoechst 33342 stock)
3. Wash cells with 1x PBS (3 x 2 min)
4. Image cells or fix cells

Hoechst 33342 Stock Preparation

1. Comes as powder
2. Add sterile dH_2O to make 1 mg/mL concentration
3. Store 4°C

CD31 & CD61 Immunohistochemical Staining Procedure for Frozen Sections

- IHC Vascular Marker Staining Protocol -

Immunohistochemistry, IHC, is a technique for identifying cellular or tissue antigens by means of antigen-antibody interactions. In this application, we are staining for CD31 and CD61 or PECAM-1 and $\alpha_V\beta_3$ - integrin, respectively. CD31 is a vascular marker, and CD61 is considered an angiogenesis marker. These protocols are used to analyze the vessel density, and angiogenesis of a given tissue. Caveat: CD61 expression is found on many different cell types.

Below is an outlined protocol that describes the IHC staining of unfixed cryosectioned tissue. This protocol has been done on subQ and mammary fat pad tumor tissues, and spleen tissues.

Preparation

Supplies

1. Tissue sections on slides.†
2. Eosin
3. Hematoxylin (Harris)
4. Bluing Agent
5. 95% EtOH, 100% EtOH
6. Xylene or Xylene Substitute
7. Mounting Media
8. Glass Cover Slips, No. 1 or 1.5
9. Coplin Jar(s)

Slide Preparation

Before starting staining the tissue should be fixed. Outlined below is a common way of fixing unfixed cryosections.

1. Prepare -20°C Acetone
2. Pour -20°C Acetone into coplin jar that is on, and surrounded by ice.
3. Incubate slide(s) in acetone for 2 - 10 mins.
4. Remove slides and let dry completely.
5. Rinse slides dH_2O, this will remove OCT that surrounds the section.

⚠ CAUTION
Xylene has harmful fumes, use in hood. It will melt gloves.

†Charged slides are preferred because the charge interaction with the sections holds the section to the slide.

Streptavidin-Horseradish Peroxidase IHC Staining Protocol

1. Label slides with a solvent resistant pen and demarcate the tissue.
2. Rinse slides 3x - 2' in 1x PBS, to remove tissue-freezing matrix, OCT.
3. Block endogenous peroxidase activity by incubating the slides in 0.3% H_2O_2 solution in PBS for 10 minutes.
4. Rinse slides 3x - 2' in 1x PBS.
5. Dilute the antibody to 1:50 for CD31 and 1:30 for CD61 in the Antibody Diluent. Apply the diluted antibody to the tissue sections on the slide. Incubate O/N in a humidified chamber.
6. Rinse slides 3x - 2' in 1x PBS.
7. Dilute the provided biotinylated anti-Ig secondary antibody 1:50. Anti-Rat for CD31 and Anti-Hamster for CD61. Apply to the tissue sections on the lside and incubate for 30 minutes at RT.
8. Rinse slides 3x - 2' in 1x PBS.
9. Apply the Streptavidin-HRP to the tissue sections on the lside and incubate for 30 minutes at RT.
10. Rinse slides 3x - 2' in 1x PBS.
11. Prepare DAB substrate solution by adding 1 drop of DAB chromogen to every 1 mL of DAB buffer. **DAB is a suspected carcinogen.**
12. Drain PBS from slides and apply the DAB substrate solution. Allow slides to incubate for 5 minutes or until the desired color intensity is reached.
13. Rinse slides 3x - 2' in 1x PBS.
14. Counter Stain slides:
    1. Stain in hematoxylin solution for 60 seconds
    2. Rinse slides thoroughly in tap water.
    3. Dip slides twice in Bluing reagent
    4. Rinse slides thoroughly in tap water.
15. Dehydrate and Mount.
    1. 3 x 2' 95% EtOH
    2. 3 x 2' 100% EtOH
    3. 3 x 2' Xylene
    4. Mount in synthetic mounting medium.

Nikon Confocal

- Imaging Protocol -

Laser Scanning Confocal Microscopy (LSCM) offers several advantages over conventional optical microscopy, including controllable depth of field, the elimination of image degrading out-of-focus information, and the ability to collect serial optical sections from thick specimens. The key to the confocal approach is the use of spatial filtering to eliminate out-of-focus light or flare in specimens that are thicker than the plane of focus.

Source - Molecular Expressions™ Website

- "The" Nikon Confocal -

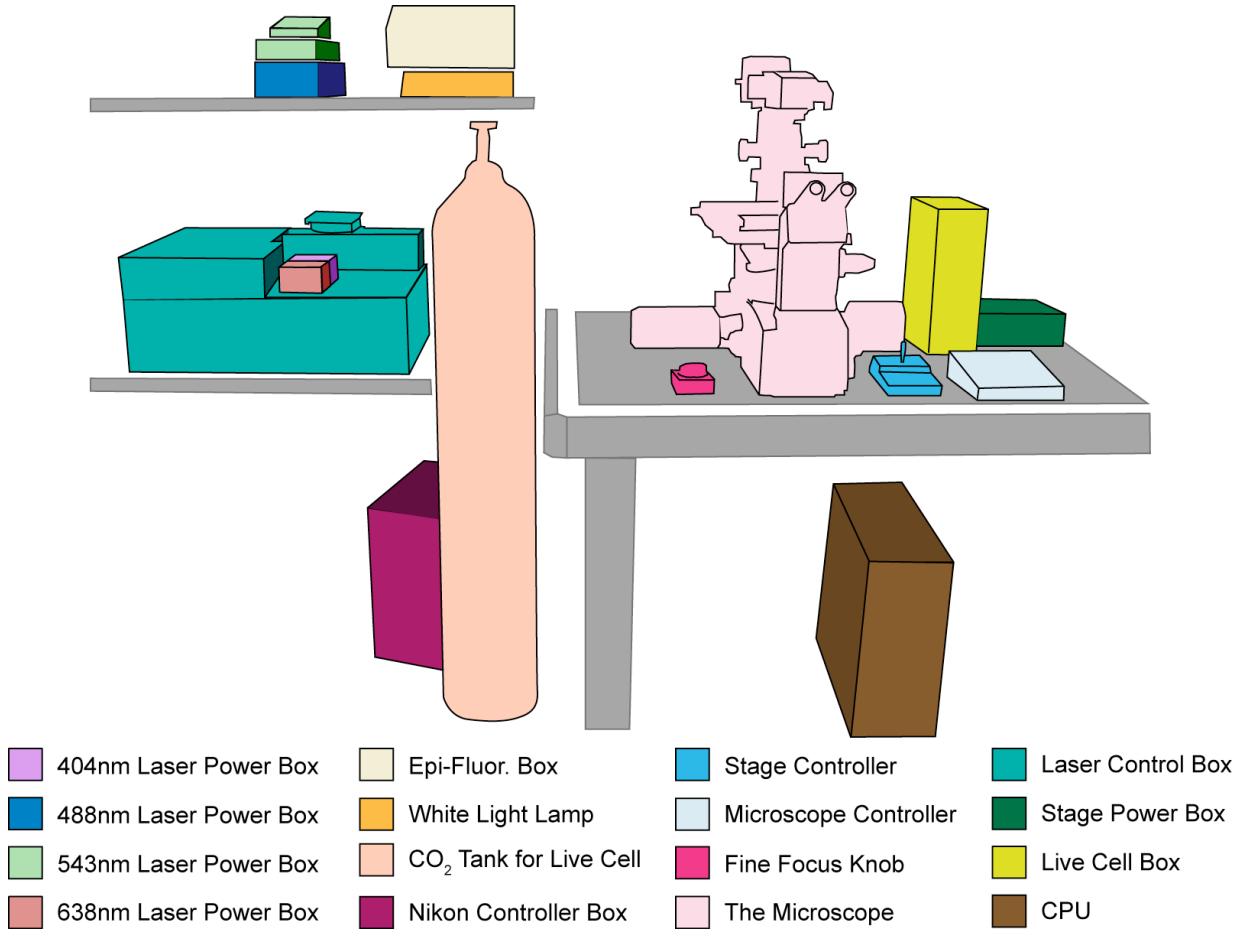

The Nikon confocal microscope setup is equipped with 4 lasers, Epi-fluorescence lamp and filters along with a live cell imaging chamber and motorized stage (detailed below). Although equipped with 4 lasers the microscope is only equipped with 3 photomultiplier tube (PMT) detectors, thus enabling three color confocal imaging.

- The Vitals -

Lasers

404 nm
488 nm
543 nm
638 nm

Confocal Setups:

Primary Setup: 404, 488, 543 nm lasers

Detectors:
432 - 467 nm (blue)
500 - 530 nm (green)
567 - 642 nm (red)

Far Red Setup: 488, 543, 638 nm lasers

Detectors:
500 - 530 nm (green)
565 - 615 nm (red)
650 nm Long Pass (far red)

Epi-fluorescence Setup:

Filter cubes:

UV: ex:340-380 nm; bp:435-485 nm
B: ex:465-495 nm; bp: 515-555 nm
Y: ex:540-580 nm; bp:600-660 nm
R: ex:590-650 nm; bp:663-738 nm
DFT (M): N/A
---: Empty, selected when using confocal acquisition

Objectives (Nikon):

- 10x -	- 20x -	- 60x -	- 100x -
PLAN 10x/0.25 inf / -WD 10.5	PLAN FLUOR 20x/0.75 MImm DIC M	PLAN APO VC 60x/1.40 Oil inf / 0.17 WD 0.13	PLAN APO VC 100x/1.40 Oil inf / 0.17 DIC N2

Specimen Holders:

(1) Slide; (2) Dishes (up to 10 cm); (3) Standard Plates (96, 48, 24, 12, 6 wells)

Live Cell Chamber:

Custom Chamber with Temp/CO_2 controller.

Motorized Stage (X,Y)

- Microscope Controller -

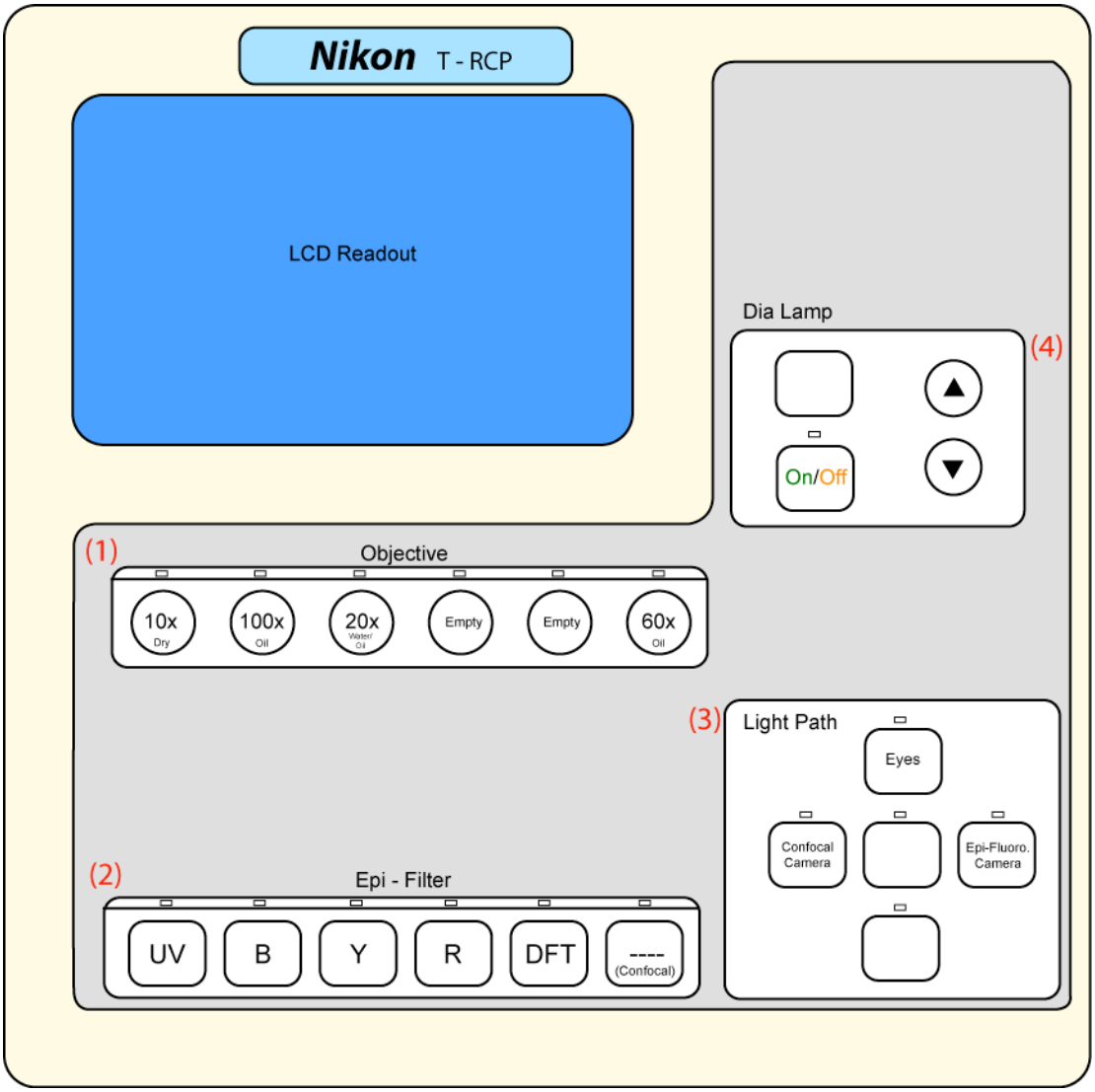

Microscope Controller

Description: The box controls the objectives, epi-filters, White-light lamp, and light path for the microscope. Other controls are also present that control the analyzer and other figures but will not be discussed here.

(1) Objective selection buttons
(2) Epi-Filter selection buttons
(3) Light Path selection buttons
(4) White light (Dia Lamp) controller buttons

- Getting Started -

STEP 1) Power On the microscope and its components. ⚠ **CAUTION** Power up sequence is critical to the use of the microscope and its software. Please follow power up sequence outlined below :

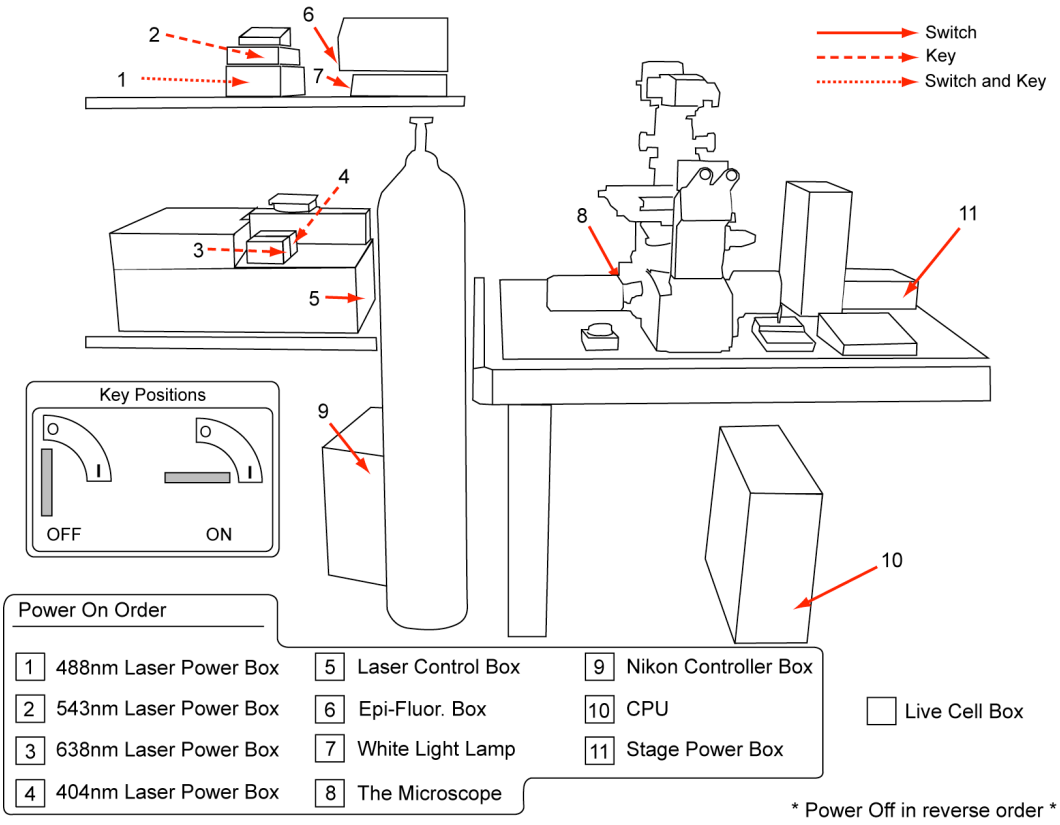

STEP 2) Allow lasers and components to warm up and stabilize for 30 - 45 minutes before imaging. This applies mainly to the lasers.

STEP 3) Change the sample holder on the motorized stage to the proper sample holder. ⚠ **CAUTION** Two screws hold the holders in place on the motorized stage. they are located on the left side of the holder. Do not lose these screw and do not over-tighten.

STEP 4) Log in to the computer under your lab. If your lab is not listed as a user, please contact the floor manager (a.k.a. Mark Thompson) to add you to the list. If you forgot your password, ask the floor manager.
STEP 5) Start the confocal software by clicking the program EZ - C1 3.40.

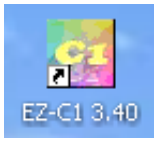

- Basics of the Nikon Confocal Software -

Laser and Detector Controller Panel

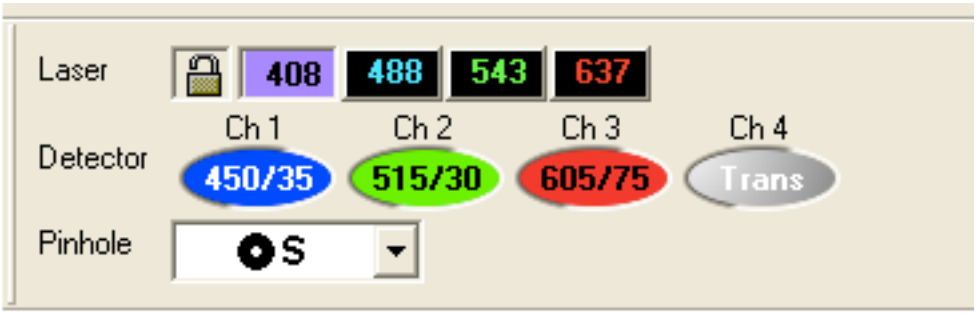

Description: This Panel allows the user to toggle the Lasers and Detectors "ON" and "OFF". Buttons highlighted in BLACK means "OFF". For example if we were to image with the above setting and all other microscope setting were optimal, the 408 nm is "ON" while all others are "OFF", and a detectors are "ON". This means that the 408nm laser is exciting the sample and we are examining all channels for fluorescence. The pinhole has setting of small (S), medium (M), large (L) and open (O). For our purposes, the pinhole should be kept as small as possible. The larger the pinhole the greater the noise.

Laser Power Control Panel

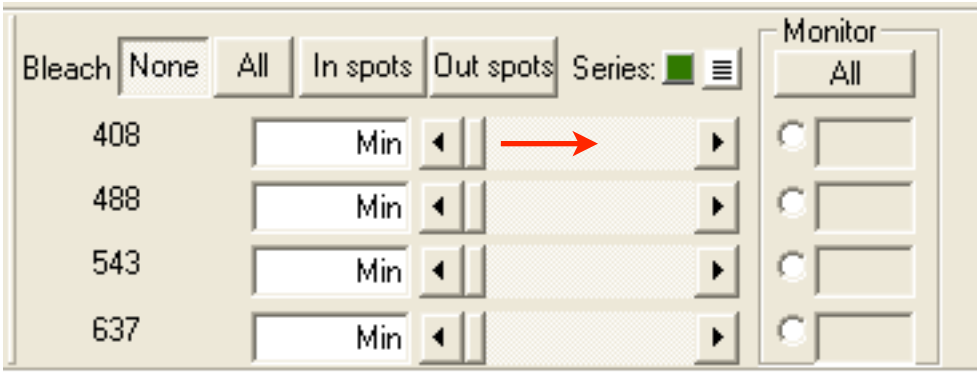

Description: This panel allows the user to control the output power of the lasers. The default setting are "Min". To achieve optimal results with the 408nm laser keep the power below 30%. This is to keep the hotspot of the laser less visible in final images. However, if you need to you can increase the 408nm laser to 100%. All other lasers can be increased to 100% without drawbacks, to my knowledge.

Detector Gain Controller Panel

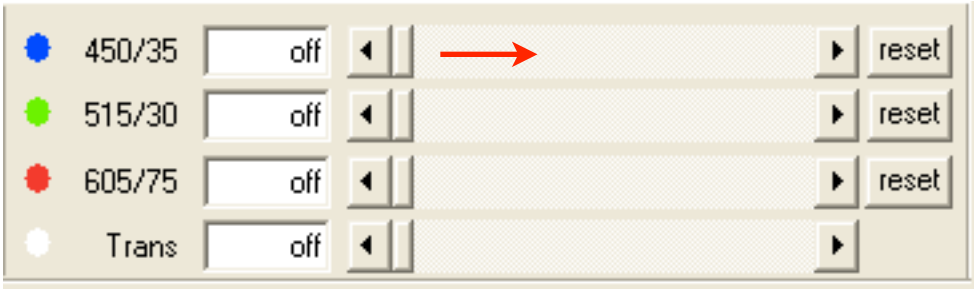

Description: This panel allows the user to control the gain of each detector. Remember that imaging above 7 to 7.50 dB will introduce noise into your image. If you are imaging above those gains, then you should change another parameter so that you can use a lower gain setting.

Image Capture Panel

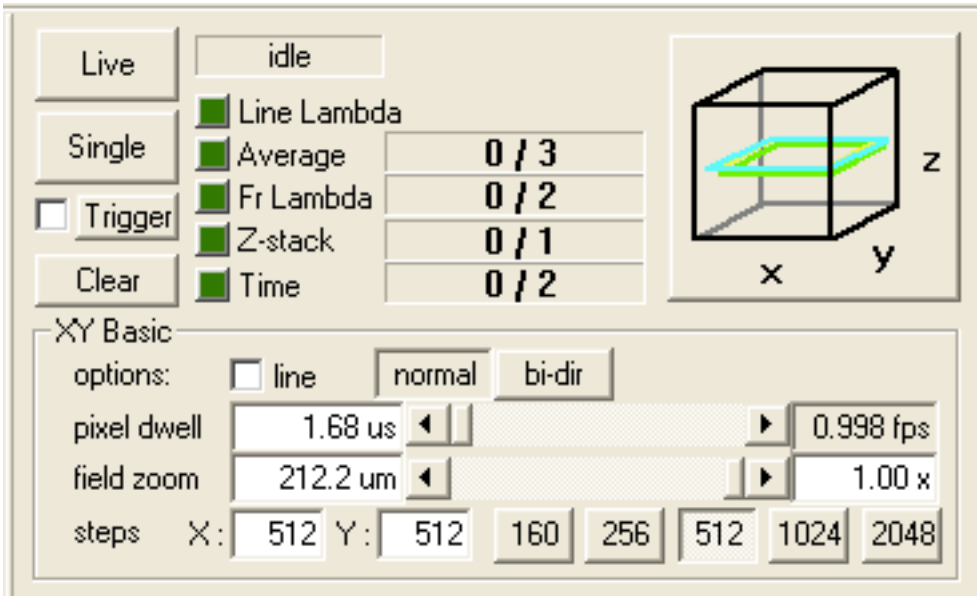

Description: This panel allows the user to capture an image. It can control the size of the image taken, 160 x 160, 256 x 256, 512 x 512, 1024 x 1024, and 2048 x 2048 pixels. Also the amount of time the laser excites and gathers light from each pixel (pixel dwell, it can also be thought of as exposure time). Field of zoom allows the user to zoom in and scan an area of the screen. Defaults for the microscope are 512 x 512, 1.68 us pixel dwell, 1.00x field zoom. The dark green buttons are for special image acquisitions explained in later sections. If dark buttons are "ON" they will be a "neon" green. If you click "Live" the microscope will continually scan the area that you are looking at. If you click single only one pass over the area will be taken. I have never used "Trigger" or "Clear.

Special Imaging Acquisition Panel

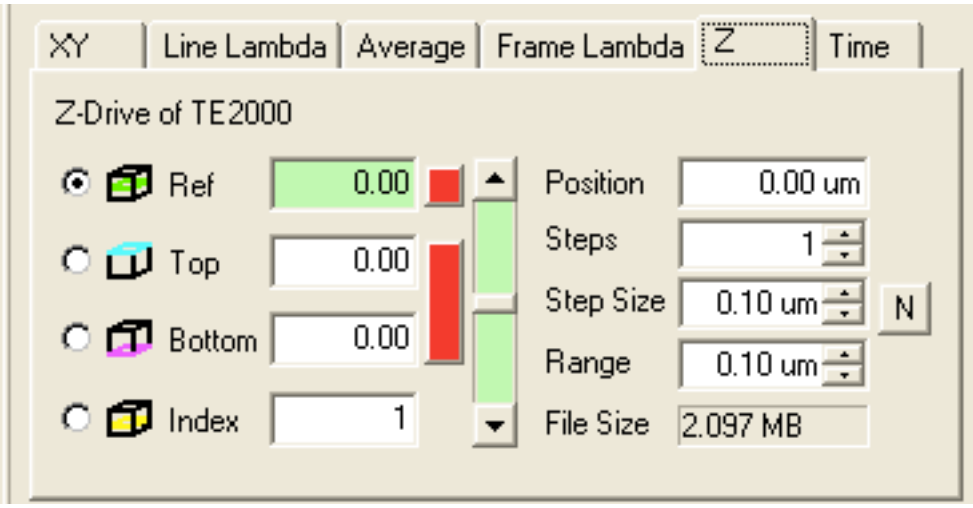

Z Stack Panel

Description: This panel allows the user to capture a Z stack of the sample. To begin a Z stack acquisition: 1) Click "Live" on the Image Acq Panel; (2) Move the imaging section to the middle of the sample; (3) Make sure "Ref radio button" is selected; (4) Click small Red box and then the tall Red box. This will reset the the measurements to 0.00; (5) Click "Top radio button" and navigate to the top of the sample using fine focus; (6) Click "Bottom radio button" , the microscope will automatically go to the Ref value, then navigate to the bottom of the sample, if you go the wrong way the microscope will return to Ref value until you navigate to the bottom; (7) Turn off "Live"; Set Up for collecting an image and press "Single".

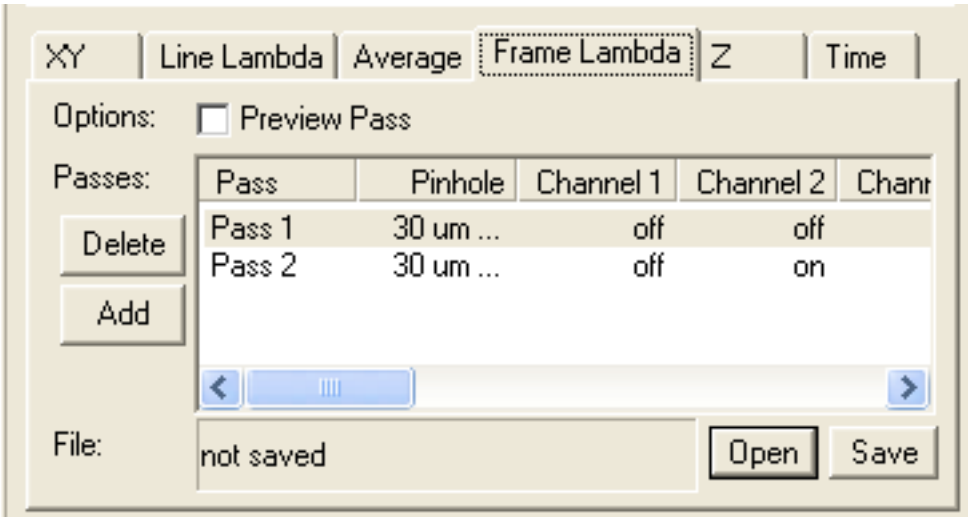

Frame Lambda Panel

Description: This panel allows the user to collect separate images of each excitation and emission, for each dye in the sample. The need to use this option comes whenever the dyes you are imaging have the possibility of spectral overlap with the other fluorophores. Here the use can setup different "Passes" for a sample. Each pass is made up of user defined setting for the "Laser and Detector, and the Detector Gain Controller Panel". Basically, the user can set up the settings to take only Blue images with one pass and only green with another. To activate the Frame Lambda click the dark green box to neon green in the Image Capture Panel. Please note that if the Preview Pass box is checked then the Pass that is highlighted will be the only one run and during the image capture.

Window Display Options

Description: These buttons allow the user to display all or one color in a single window at once, when the four circles button is depressed. The other display option (that I find useful) is the vertical rainbow button. This button is used to display a psuedocolored display of the fluorescent intensity of the single color selected.

- Taking an image -

Please understand that to take an image all parameters must be optimized for the sample of interest. With that said, outlined below are necessary steps to obtaining a simple image using the microscope and its software. These steps take for granted that you have already turned on the microscope and are ready to take an image.

Focusing on the sample -

Step 1 - Choose the objective you will be using on the *microscope controller box (1)*. If you are imaging use an oil immersion objective, i.e. 100x, 60x or 20x*, add a single drop to the lens of the objective.

Step 2 - Put your sample in the proper holding tray.

Step 3 - Change the epi-filter to **---** on the *microscope controller box (2)*. **If you have a stable fluorescent sample with a specific fluorophore, i.e. Dapi, use can select to focus the sample using epi-filter UV and epi-fluorescence. Other steps must be taken to open and close the epi-fluorescence's light source shutter located below the stage on the right. These steps are not detailed herein.

Step 4 - Change the light path to **eyes** on the *microscope controller box (3)*.

Step 5 - Turn on the white light using the *microscope controller box (4)*. My personal preference is to immediately decrease the light intensity using the down arrow on the *microscope controller box (4)*. Then move the shutter to open position, e.g. pull it out, at the top of the microscope. **If your sample is super light sensitive you can skip this step or do Steps 5-8 very quickly to decrease light exposure.

Step 6 - If using an oil/water immersion objective bring the objective up towards the sample using the coarse focus knob until the oil/water touches the sample. You should see the oil/water spread on the sample.

Step 7 - Use the coarse focus to slowly bring the objective towards the sample while looking through the oculars. You will notice the sample come into focus, when this happens begin to use the fine focus knob. **DO NOT touch the objective to the sample, this is noticeable when the sample and sample holder begin to move upward from the stage. If you are having trouble finding your sample, relax and take deep breath and using the coarse focus knob move the objective away from the sample and try again. Instances can occur where the sample has lost cells as well and the sample no longer has cells on the dish.

Step 8 - Once in focus, turn **off** the white light (*microscope controller box (4))* and close the shutter at the top of the microscope, e.g. push it in. Change the light path to **confocal** on the *microscope controller box (3)*. Verify the epi-filter is **---**.

Taking an image -

Step 1 - With the confocal software open, set the software settings for your experiment. These would include turning the lasers and detectors on or off, adjusting their power and gain, respectively.

Step 2 - Take scout images making sure to find the appropriate position of the sample (x,y) and depth (z) using your understanding of the software elements. Changes in x and y directions can be done by using the *stage controller* joystick (to the right of the microscope)

Step 3 - Adjust and take your images

Step 4 - Turn off instrument and components in reverse order as power on protocol outlined above.

Tail Vein Hoechst 33342

- Perfusion Staining Protocol -

Hoechst 33342 nucleic acid stain is a popular cell-permeant nuclear counterstain that emits blue fluorescence when bound to dsDNA. This dye is often used to distinguish condensed pycnotic nuclei in apoptotic cells and for cell cycle studies in combination with BrdU. When given i.v. via tail vein injection and allowed to circulate for 1 min, it stains the nuclei of higly perfused blood vessels only. (www.probes.com)

Protocol:

1. Hoechst 33342 dose is 10 mg/kg (injection volume can vary from <100 to 200 uL)
2. Inject and allow to circulate for 1 min
3. Sacrifice mouse and harvest tissue of interest

Hoechst 33342 Stock Preparation

1. Comes as powder
2. Add sterile PBS or saline to make 2.5 mg/mL concentration
3. Store 4°C

MRI Tail-Vein Catheter

- Instructions for constructing catheter for 7T MRI scanner -

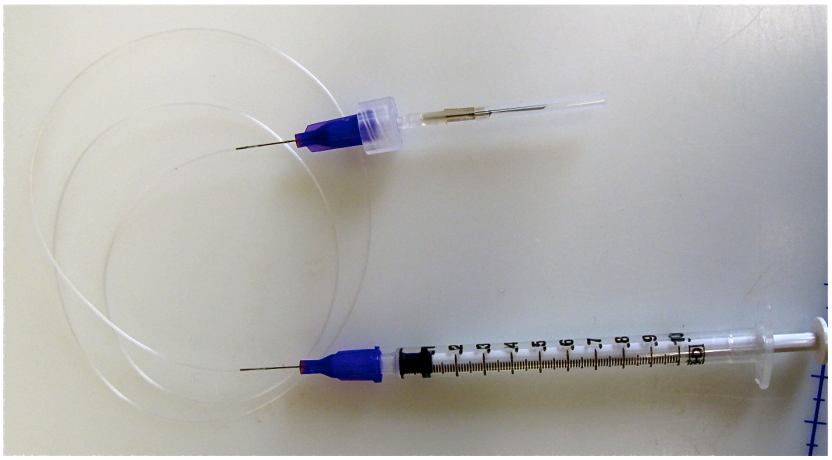

Materials:

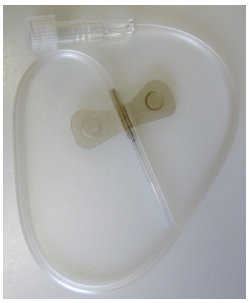

Terumo® SURFLO WINGED INFUSION SET 27G X 1/2" (8")

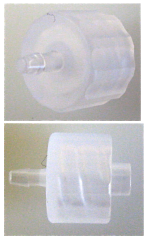

Cole-Parmer: Male Luer Integral Lock ring to 200 Series Barb, 1/16" ID Tubing, Natural Polypropylene

INTRAMEDIC™ Non-radiopaque Polyethylene Tubing Non-toxic PE10 ID 0.28mm (.011") OD 0.61mm (.024") 30.5m (100')

SAI: Blunt Needle 30G 0.5" 100 Bulk; B30-50; Non-sterile

Construction instructions:

1) Obtain all materials listed above.

2) Cut Infusion set's butterfly wings off both sides and trim the tube length has shown:

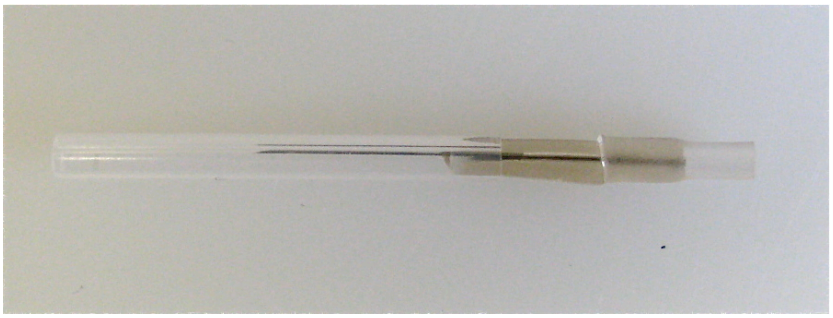

3) Insert the barb end of the luer to barb into the cut tubing end of the infusion set.

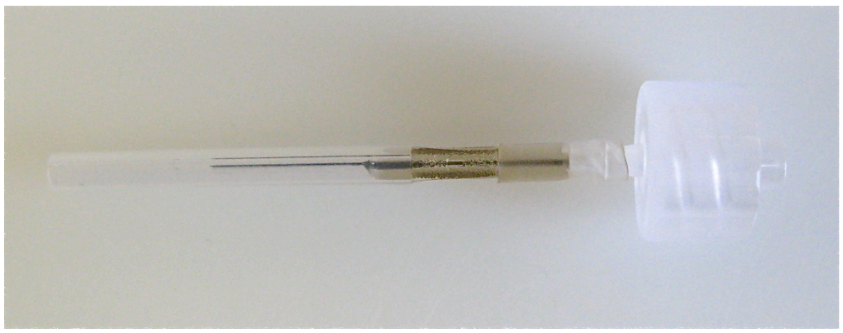

4) Cut the PE10 tubing to 54-55 cm in length.

5) Insert the blunt needle into the PE10 tubing (both ends). **Note tubing should go at least 5 mm or more down the shaft of the blunt needle.

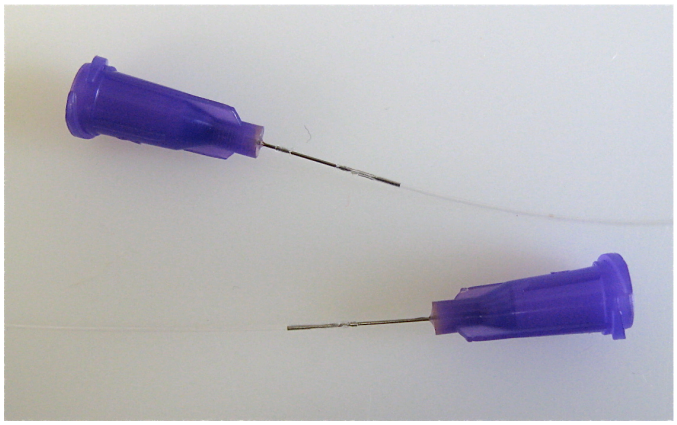

6) Attach elements together.

7) Measure dead volume (usually 100-125 uL) and flush with heparin.

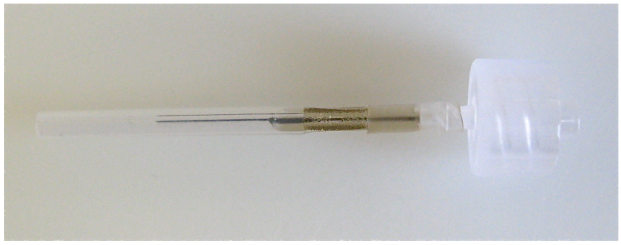

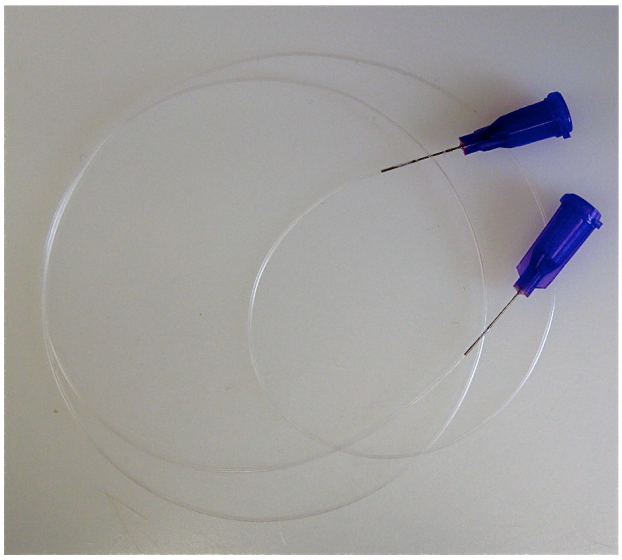

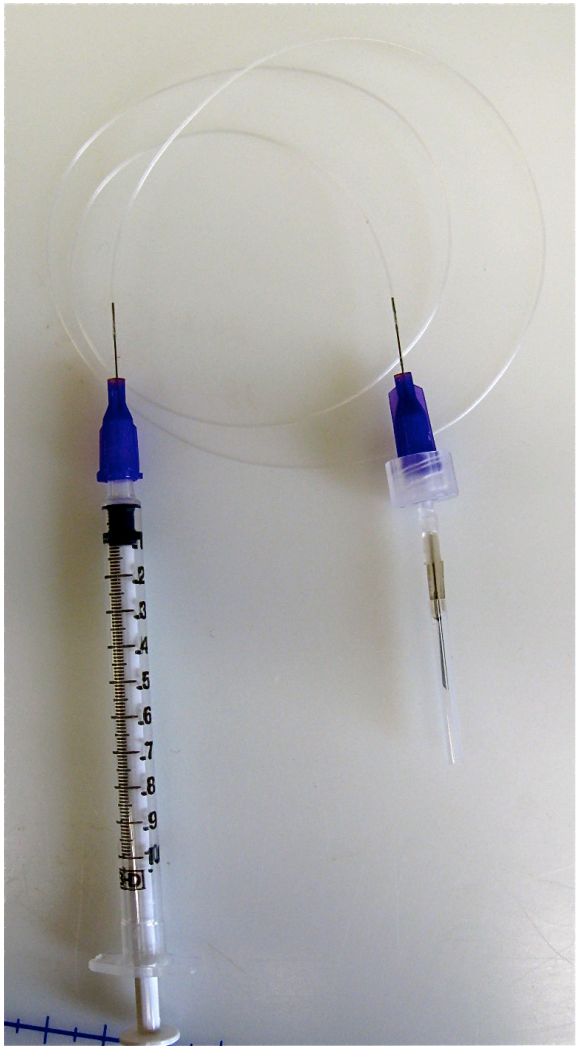

Optional Construction:

To decrease dead volume from syringe, you can use of tuberculin/insulin syringes (28G) by inserting it directly into the PE10 tubing. **Note: Caution needle is sharp in this example, USE CARE.***Air bubbles are easily introduced using this setup.

BIBLIOGRAPHY

Adams ML, Lavasanifar A, Kwon GS. Amphiphilic block copolymers for drug delivery. J Pharm Sci 2003;92(7):1343-1355.

Ahrens ET, Rothbacher U, Jacobs RE, Fraser SE. A model for MRI contrast enhancement using T1 agents. Proc Natl Acad Sci U S A 1998;95(15):8443-8448.

Ai H, Flask C, Weinberg B, et al. Magnetite-loaded polymeric micelles as ultrasensitive magnetic-resonance probes. Adv Mater 2005;17(16):1949-1952.

Aime S, Delli Castelli D, Terreno E. Novel pH-reporter MRI contrast agents. Angew Chem Int Ed Engl 2002;41(22):4334-4336.

Allen-Auerbach M, Yeom K, Park J, Phelps M, Czernin J. Standard PET/CT of the chest during shallow breathing is inadequate for comprehensive staging of lung cancer. J Nucl Med 2006;47(2):298-301.

Alric C, Taleb J, Le Duc G, et al. Gadolinium chelate coated gold nanoparticles as contrast agents for both X-ray computed tomography and magnetic resonance imaging. J Am Chem Soc 2008;130(18):5908-5915.

Altekruse SF KC, Krapcho M, Neyman N, Aminou R, Waldron W, Ruhl J, Howlader N, Tatalovich Z, Cho H, Mariotto A, Eisner MP, Lewis DR, Cronin K, Chen HS, Feuer EJ, Stinchcomb DG. SEER Cancer Statistics Review, 1975-2007. In: BK E, editor. National Cancer Institute. Bethesda, MD; 2010.

Artemov D, Mori N, Okollie B, Bhujwalla ZM. MR molecular imaging of the Her-2/neu receptor in breast cancer cells using targeted iron oxide nanoparticles. Magn Reson Med 2003;49(3):403-408.

Aumailley M, Gurrath M, Muller G, Calvete J, Timpl R, Kessler H. Arg-Gly-Asp constrained within cyclic pentapeptides. Strong and selective inhibitors of cell adhesion to vitronectin and laminin fragment P1. FEBS Lett 1991;291(1):50-54.

Bader BL, Rayburn H, Crowley D, Hynes RO. Extensive vasculogenesis, angiogenesis, and organogenesis precede lethality in mice lacking all alpha v integrins. Cell 1998;95(4):507-519.

Barcena C, Sra AK, Chaubey GS, Khemtong C, Liu JP, Gao J. Zinc ferrite nanoparticles as MRI contrast agents. Chem Commun (Camb) 2008(19):2224-2226.

Beer AJ, Haubner R, Sarbia M, et al. Positron emission tomography using [18F]Galacto-RGD identifies the level of integrin alpha(v)beta3 expression in man. Clin Cancer Res 2006;12(13):3942-3949.

Beer AJ, Schwaiger M. Imaging of integrin alphavbeta3 expression. Cancer Metastasis Rev 2008;27(4):631-644.

Blanco E, Bey EA, Khemtong C, et al. Beta-lapachone micellar nanotherapeutics for non-small cell lung cancer therapy. Cancer Res 2010;70(10):3896-3904.

Brooks PC, Clark RA, Cheresh DA. Requirement of vascular integrin alpha v beta 3 for angiogenesis. Science 1994;264(5158):569-571.

Brooks PC, Montgomery AM, Rosenfeld M, et al. Integrin alpha v beta 3 antagonists promote tumor regression by inducing apoptosis of angiogenic blood vessels. Cell 1994;79(7):1157-1164.

Brooks PC, Stromblad S, Klemke R, Visscher D, Sarkar FH, Cheresh DA. Antiintegrin alpha v beta 3 blocks human breast cancer growth and angiogenesis in human skin. J Clin Invest 1995;96(4):1815-1822.

Bulte JWM, Kraitchman DL. Iron oxide MR contrast agents for molecular and cellular imaging. Nmr Biomed 2004;17(7):484-499.

Butler TP, Gullino PM. Quantitation of cell shedding into efferent blood of mammary adenocarcinoma. Cancer Res 1975;35(3):512-516.

Cai QY, Kim SH, Choi KS, et al. Colloidal gold nanoparticles as a blood-pool contrast agent for X-ray computed tomography in mice. Invest Radiol 2007;42(12):797-806.

Cai W, Chen K, Mohamedali KA, et al. PET of vascular endothelial growth factor receptor expression. J Nucl Med 2006;47(12):2048-2056.

Cai W, Chen X. Multimodality molecular imaging of tumor angiogenesis. J Nucl Med 2008;49 Suppl 2:113S-128S.

Chandrachud LM, Pendleton N, Chisholm DM, Horan MA, Schor AM. Relationship between vascularity, age and survival in non-small-cell lung cancer. Br J Cancer 1997;76(10):1367-1375.

Chen M, Liu JP, Sun S. One-step synthesis of FePt nanoparticles with tunable size. J Am Chem Soc 2004;126(27):8394-8395.

Chen X, Conti PS, Moats RA. In vivo near-infrared fluorescence imaging of integrin alphavbeta3 in brain tumor xenografts. Cancer Res 2004;64(21):8009-8014.

Chen X, Hou Y, Tohme M, et al. Pegylated Arg-Gly-Asp peptide: 64Cu labeling and PET imaging of brain tumor alphavbeta3-integrin expression. J Nucl Med 2004;45(10):1776-1783.

Cheng Z, Wu Y, Xiong Z, Gambhir SS, Chen X. Near-infrared fluorescent RGD peptides for optical imaging of integrin alphavbeta3 expression in living mice. Bioconjug Chem 2005;16(6):1433-1441.

Cheresh DA, Stupack DG. Integrin-mediated death: an explanation of the integrin-knockout phenotype? Nat Med 2002;8(3):193-194.

Collins LG, Haines C, Perkel R, Enck RE. Lung cancer: diagnosis and management. Am Fam Physician 2007;75(1):56-63.

Delgado C, Francis GE, Fisher D. The uses and properties of PEG-linked proteins. Crit Rev Ther Drug Carrier Syst 1992;9(3-4):249-304.

Dijkgraaf I, Kruijtzer JA, Liu S, et al. Improved targeting of the alpha(v)beta (3) integrin by multimerisation of RGD peptides. Eur J Nucl Med Mol Imaging 2007;34(2):267-273.

Dubertret B, Skourides P, Norris DJ, Noireaux V, Brivanlou AH, Libchaber A. In vivo imaging of quantum dots encapsulated in phospholipid micelles. Science 2002;298(5599):1759-1762.

Elayadi AN, Samli KN, Prudkin L, et al. A peptide selected by biopanning identifies the integrin alphavbeta6 as a prognostic biomarker for nonsmall cell lung cancer. Cancer Res 2007;67(12):5889-5895.

Ellegala DB, Leong-Poi H, Carpenter JE, et al. Imaging tumor angiogenesis with contrast ultrasound and microbubbles targeted to alpha(v)beta3. Circulation 2003;108(3):336-341.

Fontana RS, Sanderson DR, Woolner LB, Taylor WF, Miller WE, Muhm JR. Lung cancer screening: the Mayo program. J Occup Med 1986;28(8):746-750.

Freedman M, Chang EH, Zhou Q, Pirollo KF. Nanodelivery of MRI contrast agent enhances sensitivity of detection of lung cancer metastases. Acad Radiol 2009;16(5):627-637.

Friedlander M, Brooks PC, Shaffer RW, Kincaid CM, Varner JA, Cheresh DA. Definition of two angiogenic pathways by distinct alpha v integrins. Science 1995;270(5241):1500-1502.

Frost JK, Ball WC, Jr., Levin ML, et al. Early lung cancer detection: results of the initial (prevalence) radiologic and cytologic screening in the Johns Hopkins study. Am Rev Respir Dis 1984;130(4):549-554.

Gilad AA, McMahon MT, Walczak P, et al. Artificial reporter gene providing MRI contrast based on proton exchange. Nat Biotechnol 2007;25(2):217-219.

Gohagan J, Marcus P, Fagerstrom R, Pinsky P, Kramer B, Prorok P. Baseline findings of a randomized feasibility trial of lung cancer screening with spiral CT scan vs chest radiograph: the Lung Screening Study of the National Cancer Institute. Chest 2004;126(1):114-121.

Gohagan JK, Marcus PM, Fagerstrom RM, et al. Final results of the Lung Screening Study, a randomized feasibility study of spiral CT versus chest X-ray screening for lung cancer. Lung Cancer 2005;47(1):9-15.

Gould MK, Maclean CC, Kuschner WG, Rydzak CE, Owens DK. Accuracy of positron emission tomography for diagnosis of pulmonary nodules and mass lesions: a meta-analysis. JAMA 2001;285(7):914-924.

Guthi JS, Yang SG, Huang G, et al. MRI-visible micellar nanomedicine for targeted drug delivery to lung cancer cells. Mol Pharm 2010;7(1):32-40.

Hainfeld JF, Slatkin DN, Focella TM, Smilowitz HM. Gold nanoparticles: a new X-ray contrast agent. Br J Radiol 2006;79(939):248-253.

Hanahan D, Weinberg RA. The hallmarks of cancer. Cell 2000;100(1):57-70.

Hashizume H, Baluk P, Morikawa S, et al. Openings between defective endothelial cells explain tumor vessel leakiness. Am J Pathol 2000;156(4):1363-1380.

Haubner R, Kuhnast B, Mang C, et al. [18F]Galacto-RGD: synthesis, radiolabeling, metabolic stability, and radiation dose estimates. Bioconjug Chem 2004;15(1):61-69.

Haubner R, Wester HJ. Radiolabeled tracers for imaging of tumor angiogenesis and evaluation of anti-angiogenic therapies. Curr Pharm Des 2004;10(13):1439-1455.

Haubner R, Wester HJ, Burkhart F, et al. Glycosylated RGD-containing peptides: tracer for tumor targeting and angiogenesis imaging with improved biokinetics. J Nucl Med 2001;42(2):326-336.

Haubner R, Wester HJ, Reuning U, et al. Radiolabeled alpha(v)beta3 integrin antagonists: a new class of tracers for tumor targeting. J Nucl Med 1999;40(6):1061-1071.

Henkelman RM, Huang XM, Xiang QS, Stanisz GJ, Swanson SD, Bronskill MJ. Quantitative Interpretation of Magnetization-Transfer. Magnetic Resonance in Medicine 1993;29(6):759-766.

Henkelman RM, Stanisz GJ, Graham SJ. Magnetization transfer in MRI: a review. Nmr Biomed 2001;14(2):57-64.

Henschke CI, McCauley DI, Yankelevitz DF, et al. Early Lung Cancer Action Project: overall design and findings from baseline screening. Lancet 1999;354(9173):99-105.

Hinton DP, Bryant RG. 1H magnetic cross-relaxation between multiple solvent components and rotationally immobilized protein. Magn Reson Med 1996;35(4):497-505.

Hodivala-Dilke KM, McHugh KP, Tsakiris DA, et al. Beta3-integrin-deficient mice are a model for Glanzmann thrombasthenia showing placental defects and reduced survival. J Clin Invest 1999;103(2):229-238.

Hoge RD, Franceschini MA, Covolan RJ, Huppert T, Mandeville JB, Boas DA. Simultaneous recording of task-induced changes in blood oxygenation, volume, and flow using diffuse optical imaging and arterial spin-labeling MRI. Neuroimage 2005;25(3):701-707.

Hogemann-Savellano D, Bos E, Blondet C, et al. The transferrin receptor: a potential molecular imaging marker for human cancer. Neoplasia 2003;5(6):495-506.

Hood JD, Cheresh DA. Role of integrins in cell invasion and migration. Nat Rev Cancer 2002;2(2):91-100.

Horak ER, Leek R, Klenk N, et al. Angiogenesis, assessed by platelet/endothelial cell adhesion molecule antibodies, as indicator of node metastases and survival in breast cancer. Lancet 1992;340(8828):1120-1124.

Hu G, Lijowski M, Zhang H, et al. Imaging of Vx-2 rabbit tumors with alpha(nu)beta3-integrin-targeted 111In nanoparticles. Int J Cancer 2007;120(9):1951-1957.

Huang X, Griffiths M, Wu J, Farese RV, Jr., Sheppard D. Normal development, wound healing, and adenovirus susceptibility in beta5-deficient mice. Mol Cell Biol 2000;20(3):755-759.

Hynes RO. Integrins: versatility, modulation, and signaling in cell adhesion. Cell 1992;69(1):11-25.

Janssen M, Oyen WJ, Massuger LF, et al. Comparison of a monomeric and dimeric radiolabeled RGD-peptide for tumor targeting. Cancer Biother Radiopharm 2002;17(6):641-646.

Janssen ML, Oyen WJ, Dijkgraaf I, et al. Tumor targeting with radiolabeled alpha(v)beta(3) integrin binding peptides in a nude mouse model. Cancer Res 2002;62(21):6146-6151.

Jarzynka MJ, Guo P, Bar-Joseph I, Hu B, Cheng SY. Estradiol and nicotine exposure enhances A549 bronchioloalveolar carcinoma xenograft growth in mice through the stimulation of angiogenesis. Int J Oncol 2006;28(2):337-344.

Jemal A, Siegel R, Ward E, Hao Y, Xu J, Thun MJ. Cancer statistics, 2009. CA Cancer J Clin 2009;59(4):225-249.

Jin H, Varner J. Integrins: roles in cancer development and as treatment targets. Br J Cancer 2004;90(3):561-565.

Kattumuri V, Katti K, Bhaskaran S, et al. Gum arabic as a phytochemical construct for the stabilization of gold nanoparticles: in vivo pharmacokinetics and X-ray-contrast-imaging studies. Small 2007;3(2):333-341.

Khemtong C, Kessinger CW, Ren J, et al. In vivo off-resonance saturation magnetic resonance imaging of alphavbeta3-targeted superparamagnetic nanoparticles. Cancer Res 2009;69(4):1651-1658.

Kim D, Park S, Lee JH, Jeong YY, Jon S. Antibiofouling polymer-coated gold nanoparticles as a contrast agent for in vivo X-ray computed tomography imaging. J Am Chem Soc 2007;129(24):7661-7665.

Knoepp UW, Ravenel JG. CT and PET imaging in non-small cell lung cancer. Crit Rev Oncol Hematol 2006;58(1):15-30.

Koole R, van Schooneveld MM, Hilhorst J, et al. Paramagnetic lipid-coated silica nanoparticles with a fluorescent quantum dot core: a new contrast agent platform for multimodality imaging. Bioconjug Chem 2008;19(12):2471-2479.

Korpanty G, Carbon JG, Grayburn PA, Fleming JB, Brekken RA. Monitoring response to anticancer therapy by targeting microbubbles to tumor vasculature. Clin Cancer Res 2007;13(1):323-330.

Kressler B, de Rochefort L, Liu T, Spincemaille P, Jiang Q, Wang Y. Nonlinear regularization for per voxel estimation of magnetic susceptibility distributions from MRI field maps. IEEE Trans Med Imaging 2010;29(2):273-281.

Kubik A, Polak J. Lung cancer detection. Results of a randomized prospective study in Czechoslovakia. Cancer 1986;57(12):2427-2437.

Lee HY, Li Z, Chen K, et al. PET/MRI dual-modality tumor imaging using arginine-glycine-aspartic (RGD)-conjugated radiolabeled iron oxide nanoparticles. J Nucl Med 2008;49(8):1371-1379.

Lee JH, Huh YM, Jun YW, et al. Artificially engineered magnetic nanoparticles for ultra-sensitive molecular imaging. Nat Med 2007;13(1):95-99.

Leong-Poi H, Christiansen J, Klibanov AL, Kaul S, Lindner JR. Noninvasive assessment of angiogenesis by ultrasound and microbubbles targeted to alpha(v)-integrins. Circulation 2003;107(3):455-460.

Li ZB, Cai W, Cao Q, et al. (64)Cu-labeled tetrameric and octameric RGD peptides for small-animal PET of tumor alpha(v)beta(3) integrin expression. J Nucl Med 2007;48(7):1162-1171.

Lindner JR. Microbubbles in medical imaging: current applications and future directions. Nat Rev Drug Discov 2004;3(6):527-532.

Liu T, Spincemaille P, de Rochefort L, Kressler B, Wang Y. Calculation of susceptibility through multiple orientation sampling (COSMOS): a method for conditioning the inverse problem from measured magnetic field map to susceptibility source image in MRI. Magn Reson Med 2009;61(1):196-204.

Luo L, Tam J, Maysinger D, Eisenberg A. Cellular internalization of poly(ethylene oxide)-b-poly(epsilon-caprolactone) diblock copolymer micelles. Bioconjug Chem 2002;13(6):1259-1265.

Maeda H. The enhanced permeability and retention (EPR) effect in tumor vasculature: the key role of tumor-selective macromolecular drug targeting. Adv Enzyme Regul 2001;41:189-207.

Maeda H, Sawa T, Konno T. Mechanism of tumor-targeted delivery of macromolecular drugs, including the EPR effect in solid tumor and clinical overview of the prototype polymeric drug SMANCS. J Control Release 2001;74(1-3):47-61.

Mankoff DA. A definition of molecular imaging. J Nucl Med 2007;48(6):18N, 21N.

Marshall JF, Rutherford DC, Happerfield L, et al. Comparative analysis of integrins in vitro and in vivo in uveal and cutaneous melanomas. Br J Cancer 1998;77(4):522-529.

Matsui J, Funahashi Y, Uenaka T, Watanabe T, Tsuruoka A, Asada M. Multi-kinase inhibitor E7080 suppresses lymph node and lung metastases of human mammary breast tumor MDA-MB-231 via inhibition of vascular endothelial growth factor-receptor (VEGF-R) 2 and VEGF-R3 kinase. Clin Cancer Res 2008;14(17):5459-5465.

Meitar D, Crawford SE, Rademaker AW, Cohn SL. Tumor angiogenesis correlates with metastatic disease, N-myc amplification, and poor outcome in human neuroblastoma. J Clin Oncol 1996;14(2):405-414.

Melamed MR, Flehinger BJ, Zaman MB, Heelan RT, Perchick WA, Martini N. Screening for early lung cancer. Results of the Memorial Sloan-Kettering study in New York. Chest 1984;86(1):44-53.

Mills PH, Ahrens ET. Theoretical MRI contrast model for exogenous T2 agents. Magn Reson Med 2007;57(2):442-447.

Mizejewski GJ. Role of integrins in cancer: survey of expression patterns. Proc Soc Exp Biol Med 1999;222(2):124-138.

Moghimi SM, Hunter AC, Murray JC. Long-circulating and target-specific nanoparticles: theory to practice. Pharmacol Rev 2001;53(2):283-318.

Morrison C, Henkelman RM. A Model for Magnetization-Transfer in Tissues. Magnetic Resonance in Medicine 1995;33(4):475-482.

Mukherjee P, Abate LE, Seyfried TN. Antiangiogenic and proapoptotic effects of dietary restriction on experimental mouse and human brain tumors. Clin Cancer Res 2004;10(16):5622-5629.

Mulder WJ, Koole R, Brandwijk RJ, et al. Quantum dots with a paramagnetic coating as a bimodal molecular imaging probe. Nano Lett 2006;6(1):1-6.

Mulder WJ, Strijkers GJ, Habets JW, et al. MR molecular imaging and fluorescence microscopy for identification of activated tumor endothelium using a bimodal lipidic nanoparticle. FASEB J 2005;19(14):2008-2010.

Nasongkla N, Bey E, Ren J, et al. Multifunctional polymeric micelles as cancer-targeted, MRI-ultrasensitive drug delivery systems. Nano Lett 2006;6(11):2427-2430.

Nasongkla N, Shuai X, Ai H, et al. cRGD-functionalized polymer micelles for targeted doxorubicin delivery. Angew Chem Int Ed Engl 2004;43(46):6323-6327.

Nomori H, Watanabe K, Ohtsuka T, Naruke T, Suemasu K, Uno K. Evaluation of F-18 fluorodeoxyglucose (FDG) PET scanning for pulmonary nodules less than 3 cm in diameter, with special reference to the CT images. Lung Cancer 2004;45(1):19-27.

Ntziachristos V, Yodh AG, Schnall M, Chance B. Concurrent MRI and diffuse optical tomography of breast after indocyanine green enhancement. Proc Natl Acad Sci U S A 2000;97(6):2767-2772.

O'Connor JP, Jackson A, Parker GJ, Jayson GC. DCE-MRI biomarkers in the clinical evaluation of antiangiogenic and vascular disrupting agents. Br J Cancer 2007;96(2):189-195.

Oyama T, Sykes KF, Samli KN, Minna JD, Johnston SA, Brown KC. Isolation of lung tumor specific peptides from a random peptide library: generation of diagnostic and cell-targeting reagents. Cancer Lett 2003;202(2):219-230.

Park JH, von Maltzahn G, Ruoslahti E, Bhatia SN, Sailor MJ. Micellar hybrid nanoparticles for simultaneous magnetofluorescent imaging and drug delivery. Angew Chem Int Ed Engl 2008;47(38):7284-7288.

Perazella MA. Current status of gadolinium toxicity in patients with kidney disease. Clin J Am Soc Nephrol 2009;4(2):461-469.

Pogue BW, Poplack SP, McBride TO, et al. Quantitative hemoglobin tomography with diffuse near-infrared spectroscopy: pilot results in the breast. Radiology 2001;218(1):261-266.

Rader C, Popkov M, Neves JA, Barbas CF. Integrin alpha v beta 3-targeted therapy for Kaposi's sarcoma with an in vitro-evolved antibody. Faseb Journal 2002;16(12):2000-+.

Reynolds LE, Wyder L, Lively JC, et al. Enhanced pathological angiogenesis in mice lacking beta3 integrin or beta3 and beta5 integrins. Nat Med 2002;8(1):27-34.

Schmieder AH, Caruthers SD, Zhang H, et al. Three-dimensional MR mapping of angiogenesis with alpha5beta1(alpha nu beta3)-targeted theranostic nanoparticles in the MDA-MB-435 xenograft mouse model. FASEB J 2008;22(12):4179-4189.

Schmieder AH, Winter PM, Caruthers SD, et al. Molecular MR imaging of melanoma angiogenesis with alphanubeta3-targeted paramagnetic nanoparticles. Magn Reson Med 2005;53(3):621-627.

Seo WS, Lee JH, Sun X, et al. FeCo/graphitic-shell nanocrystals as advanced magnetic-resonance-imaging and near-infrared agents. Nat Mater 2006;5(12):971-976.

Seppenwoolde JH, Viergever MA, Bakker CJ. Passive tracking exploiting local signal conservation: the white marker phenomenon. Magn Reson Med 2003;50(4):784-790.

Sipkins DA, Cheresh DA, Kazemi MR, Nevin LM, Bednarski MD, Li KC. Detection of tumor angiogenesis in vivo by alphaVbeta3-targeted magnetic resonance imaging. Nat Med 1998;4(5):623-626.

Sone S, Takashima S, Li F, et al. Mass screening for lung cancer with mobile spiral computed tomography scanner. Lancet 1998;351(9111):1242-1245.

Sonvico F, Mornet S, Vasseur S, et al. Folate-conjugated iron oxide nanoparticles for solid tumor targeting as potential specific magnetic hyperthermia mediators: synthesis, physicochemical characterization, and in vitro experiments. Bioconjug Chem 2005;16(5):1181-1188.

Stupack DG, Cheresh DA. Get a ligand, get a life: integrins, signaling and cell survival. J Cell Sci 2002;115(Pt 19):3729-3738.

Su MY, Wang Z, Carpenter PM, Lao X, Muhler A, Nalcioglu O. Characterization of N-ethyl-N-nitrosourea-induced malignant and benign breast tumors in rats by using three MR contrast agents. J Magn Reson Imaging 1999;9(2):177-186.

Sun S, Murray CB, Weller D, Folks L, Moser A. Monodisperse FePt nanoparticles and ferromagnetic FePt nanocrystal superlattices. Science 2000;287(5460):1989-1992.

Sun S, Zeng H. Size-controlled synthesis of magnetite nanoparticles. J Am Chem Soc 2002;124(28):8204-8205.

Sun S, Zeng H, Robinson DB, et al. Monodisperse MFe2O4 (M = Fe, Co, Mn) nanoparticles. J Am Chem Soc 2004;126(1):273-279.

Sutton D, Nasongkla N, Blanco E, Gao J. Functionalized micellar systems for cancer targeted drug delivery. Pharm Res 2007;24(6):1029-1046.

Swensen SJ, Jett JR, Sloan JA, et al. Screening for lung cancer with low-dose spiral computed tomography. Am J Respir Crit Care Med 2002;165(4):508-513.

Thorek DLJ, Chen A, Czupryna J, Tsourkas A. Superparamagnetic iron oxide nanoparticle probes for molecular imaging. Ann Biomed Eng 2006;34(1):23-38.

Tofts PS, Brix G, Buckley DL, et al. Estimating kinetic parameters from dynamic contrast-enhanced T(1)-weighted MRI of a diffusable tracer: standardized quantities and symbols. J Magn Reson Imaging 1999;10(3):223-232.

Torchilin VP. PEG-based micelles as carriers of contrast agents for different imaging modalities. Adv Drug Deliv Rev 2002;54(2):235-252.

Torchilin VP. Multifunctional nanocarriers. Adv Drug Deliver Rev 2006;58(14):1532-1555.

Townsend DW. Physical principles and technology of clinical PET imaging. Ann Acad Med Singapore 2004;33(2):133-145.

von Wallbrunn A, Holtke C, Zuhlsdorf M, Heindel W, Schafers M, Bremer C. In vivo imaging of integrin alpha nu beta(3) expression using fluorescence-mediated tomography. Eur J Nucl Med Mol I 2007;34(5):745-754.

Vosseler S, Mirancea N, Bohlen P, Mueller MM, Fusenig NE. Angiogenesis inhibition by vascular endothelial growth factor receptor-2 blockade reduces stromal matrix metalloproteinase expression, normalizes stromal tissue, and reverts epithelial tumor phenotype in surface heterotransplants. Cancer Res 2005;65(4):1294-1305.

Wang Y, de Rochefort L, Liu T, Kressler B. Magnetic source MRI: a new quantitative imaging of magnetic biomarkers. Conf Proc IEEE Eng Med Biol Soc 2009;2009:53-56.

Wang YX, Hussain SM, Krestin GP. Superparamagnetic iron oxide contrast agents: physicochemical characteristics and applications in MR imaging. Eur Radiol 2001;11(11):2319-2331.

Ward KM, Aletras AH, Balaban RS. A new class of contrast agents for MRI based on proton chemical exchange dependent saturation transfer (CEST). J Magn Reson 2000;143(1):79-87.

Weidner N, Semple JP, Welch WR, Folkman J. Tumor angiogenesis and metastasis--correlation in invasive breast carcinoma. N Engl J Med 1991;324(1):1-8.

Weissleder R, Pittet MJ. Imaging in the era of molecular oncology. Nature 2008;452(7187):580-589.

Weissleder R, Stark DD, Engelstad BL, et al. Superparamagnetic iron oxide: pharmacokinetics and toxicity. AJR Am J Roentgenol 1989;152(1):167-173.

WHO. The global burden of disease: 2004 update.: WHO; 2008.

Winter PM, Caruthers SD, Kassner A, et al. Molecular imaging of angiogenesis in nascent Vx-2 rabbit tumors using a novel alpha(nu)beta3-targeted nanoparticle and 1.5 tesla magnetic resonance imaging. Cancer Res 2003;63(18):5838-5843.

Winter PM, Schmieder AH, Caruthers SD, et al. Minute dosages of alpha(nu)beta3-targeted fumagillin nanoparticles impair Vx-2 tumor angiogenesis and development in rabbits. FASEB J 2008;22(8):2758-2767.

Wolff SD, Balaban RS. Magnetization Transfer Contrast (Mtc) and Tissue Water Proton Relaxation Invivo. Magnetic Resonance in Medicine 1989;10(1):135-144.

Yarnykh VL. Pulsed Z-spectroscopic imaging of cross-relaxation parameters in tissues for human MRI: Theory and clinical applications. Magnetic Resonance in Medicine 2002;47(5):929-939.

Zhang C, Jugold M, Woenne EC, et al. Specific targeting of tumor angiogenesis by RGD-conjugated ultrasmall superparamagnetic iron oxide particles using a clinical 1.5-T magnetic resonance scanner. Cancer Res 2007;67(4):1555-1562.

Zhang S, Trokowski R, Sherry AD. A paramagnetic CEST agent for imaging glucose by MRI. Journal of the American Chemical Society 2003;125(50):15288-15289.

Zhang SR, Merritt M, Woessner DE, Lenkinski RE, Sherry AD. PARACEST agents: Modulating MRI contrast via water proton exchange. Accounts Chem Res 2003;36(10):783-790.

Zhang X, Xiong Z, Wu Y, et al. Quantitative PET imaging of tumor integrin alphavbeta3 expression with 18F-FRGD2. J Nucl Med 2006;47(1):113-121.

Zurkiya O, Hu X. Off-resonance saturation as a means of generating contrast with superparamagnetic nanoparticles. Magn Reson Med 2006;56(4):726-732.